

Alma Mater Studiorum - Università Degli Studi di Bologna

DOTTORATO DI RICERCA IN
INGEGNERIA ELETTRONICA, INFORMATICA E DELLE
TELECOMUNICAZIONI

Ciclo XXIV

Settore Concorsuale di afferenza: 09/F2 TELECOMUNICAZIONI

Settore Scientifico disciplinare: ING-INF 03 TELECOMUNICAZIONI

Performance Analysis and Improvements for
the Future Aeronautical Mobile Airport
Communications System (AeroMACS)

Presentata da: Ing. Paola Pulini

Coordinatore:

Chiar.mo Prof. Ing. Luca Benini

Relatore:

Chiar.mo Prof. Ing. Marco Chiani

Correlatore:

Dr. Ing. Michael Schnell

Esame Finale Anno 2012

Contents

Acronyms, Symbols, and Notations	v
Introduction	1
1 Airport Environment	7
1.1 Overview of the Aeronautical Communications	7
1.2 Airport Channel Model	10
1.2.1 Channel Description	10
1.2.2 Channel Implementation	12
1.2.3 Channel Parameters	15
1.3 Summary	18
2 AeroMACS System	19
2.1 OFDM Based Profile	19
2.1.1 Performance	20
2.2 OFDMA Based Profiles	25
2.2.1 Performance	29
2.3 Remarks on the AeroMACS System	35
2.4 Summary	36
3 Multiple Antennas	37
3.1 Fundamentals of Multiple Antenna Techniques	37
3.1.1 Receive Diversity - SIMO	39
3.1.2 Transmit Diversity - MISO	43
3.2 Multiple Antenna in AeroMACS	46
3.2.1 Simulation Parameters	47
3.2.2 Performance Evaluation	48
3.3 A Novel Implementation of STC for AeroMACS	50
3.3.1 Simulation Parameters	52
3.3.2 Simulation Results	53
3.4 Summary	57

4	Cooperative Communications	59
4.1	Overview of the Different Techniques	60
4.1.1	Amplify and Forward	61
4.1.2	Decode and Forward	61
4.1.3	Coded Cooperation	62
4.2	Cooperation in the Airport Environment	63
4.3	AF Implementation for AeroMACS	65
4.3.1	Simulation Parameters	68
4.3.2	Simulation Results	69
4.4	DF Implementation for AeroMACS	73
4.4.1	Simulation Parameters	74
4.4.2	Simulation Results	75
4.5	Summary	78
5	Unequal Diversity Coding: A New Concept for the Relay Channel	79
5.1	Transmission Scheme	80
5.1.1	Parity-Check Matrix Structure and Diversity	81
5.2	Unequal Diversity Protographs	82
5.3	Protograph EXIT Analysis over BFC	83
5.3.1	Protograph EXIT Analysis	83
5.3.2	Outage Regions and Asymptotic Error Probability	87
5.4	Outage Analysis for the Relay Channel	89
5.4.1	On the Protograph Design	91
5.4.2	On the Decoding Strategies	95
5.5	Application to AeroMACS	95
5.6	Summary	96
6	Packet Level Coding	97
6.1	Introduction to Packet Level Coding Techniques	97
6.2	Flexible IRA Codes	99
6.2.1	Fully-Random Construction	100
6.2.2	Permutation-Based Construction	101
6.2.3	Permutation-Based Construction with an Outer Random Code	103
6.2.4	On the Signalling of the Parameters	103
6.3	Performance on the Binary Erasure Channel	103
6.4	Application to AeroMACS	108
6.5	Summary	110
7	Conclusions	111
7.1	Enhancements of AeroMACS	111
7.1.1	Conclusions and Outlook	114

7.2 Thesis Achievements	114
A Channel Estimation	117
A.1 OFDM Profile	117
A.2 OFDMA	118
A.2.1 Forward Link	118
A.2.2 Reverse Link	119
B Low-Density Parity-Check Codes	121
B.1 Basics and Iterative Decoding	122
B.1.1 The Log-Domain Sum-Product Algorithm	124
B.2 Density Evolution Analysis	126
B.2.1 The Gaussian Approximation	127
B.2.2 Extrinsic Information Transfer Charts	129
B.2.3 The Area Theorem and Its Consequences	131
B.3 LDPC Code Designs	134
B.3.1 Protograph Designs	135
B.4 On Decoding Over Erasure Channels and PLC	137
Bibliography	149

Acronyms, Symbols, and Notations

Preliminaries

Throughout this thesis, time-discrete OFDMA signals are used. We generally indicated the OFDMA symbol (time) and subcarrier (frequency) indices with i and j ($x_{i,j}$). However, in some cases, we omitted these indices, indicating the symbol transmitted on the generic subcarrier $x_{i,j}$ only with x . This omission allows a simplification of the notation, especially in MIMO or cooperative cases, where indices for the antenna and the links are required. We generally indicate with x the transmitted signal, while the received signal is represented by y . The scalars are indicated with simple characters, while bold characters are used for vectors and matrices (capital letters). The symbols $E\{\cdot\}$, $(\cdot)^*$, $(\cdot)^T$, and $(\cdot)^H$ denote respectively the statistical mean, the complex conjugation, the transpose, and the Hermitian transpose operations.

List of Acronyms

AA	architecture aware
AeroMACS	aeronautical mobile airport communications system
AF	amplify and forward
AMC	adaptive modulation and coding
AOA	autonomous operations area
APP	a-posteriori probability
APP-LLR	a posteriori probability log-likelihood ratio
ARA	accumulate-repeat-accumulate
ARQ	Automatic Repeat reQuest
ATC	air traffic control
AWGN	additive white Gaussian noise

BEC	binary erasure channel
BER	bit error rate
BFC	block fading channel
BPSK	binary phase shift keying
BSC	binary symmetric channel
BTC	block turbo codes
BW	bandwidth
CDF	cumulative density function
CDMA	code-division multiple access
CER	codeword error rate
CN	check node
CP	cyclic prefix
CRC	cyclic redundancy check
CSI	channel state information
CTC	concatenated-tree code
CTC	convolutional turbo codes
DC	down converter
DE	density evolution
DF	decode and forward
DL	down link
ENR	en route
EUROCONTROL	European Organization for the Safety of Air Navigation
EXIT	extrinsic information transfer
FAA	Federal Aviation Administration
FDD	frequency-division duplexing
FEP	fragment error probability

FER	fragment error rate
FFT	fast Fourier transformation
F-IRA	flexible irregular repeat-accumulate (IRA)
FRC	fully-random construction
FUSC	fully usage of subcarriers
GA	Gaussian approximation
GE	Gaussian elimination
GeIRA	Generalized Irregular Repeat-Accumulate
GPSD	Gaussian power spectral density
ICI	inter-carrier interference
IFFT	inverse fast Fourier transformation
IRA	irregular repeat-accumulate
ISI	inter-symbol interference
IT	iterative
LDPC	low-density parity check
LLR	log-likelihood ratio
LOS	line-of-sight
MAP	maximum a posteriori
MBMS	multimedia broadcast multicast service
MDS	maximum-distance-separable
MET	multi-edge-type
MI	mutual information
MIMO	multiple input multiple output
MISO	multiple input single output
ML	maximum likelihood
MMSE	minimum mean square error

MRC	maximal ratio combining
MUC	Munich airport Franz Joseph Strauss
NLOS	non line-of-sight
OC	optimum combining
OFDM	orthogonal frequency-division multiplexing
OFDMA	orthogonal frequency-division multiple access
ORP	oceanic remote polar
PBC	permutation-based construction
p.d.f.	probability density function
PEG	progressive edge growth
PER	packet error rate
PEXIT	protograph extrinsic information transfer
PLC	packet level coding
PSD	power spectral density
PUSC	partially usage of subcarriers
QAM	quadrature amplitude modulation
QPSK	quadrature phase shift keying
RA	repeat accumulate
RCA	reciprocal channel approximation
RCB	random coding bound
RL	reverse link
FL	forward link
r.v.	random variable
SC	selection combining
SFBC	space frequency block coding
SFC	space frequency coding

SFC	space-frequency coding
SIMO	single input multiple output
SINR	signal-to-interference noise ratio
SNR	signal-to-noise ratio
SOFDMA	scalable OFDMA
SPA	sum-product algorithm
SPC	single parity-check
STC	space time coding
STBC	space time block coding
TDD	time-division duplexing
TDM	time-division multiplexing
TDMA	time-division multiple access
TMA	terminal manoeuvring area
UEP	unequal error protection
UL	up link
UD	<i>unequal diversity</i>
UDC	<i>unequal diversity coding</i>
VDL2	very high frequency (VHF) Digital Mode 2
VHF	very high frequency
VN	variable node
WSSUS	wide sense stationary uncorrelated scattering model

List of Symbols

α	weight vector of a MISO scheme
$\alpha(t)$	generic fading process of a tap
$\alpha_1(t)$	real part of a generic fading process $\alpha(t)$
$\alpha_2(t)$	immaginary part of a generic fading process $\alpha(t)$
α_k	fading coefficient for tap k
α_R	channel coefficient relative to the relay link (R-D)
α_S	channel coefficient relative to the direct link (S-D)
γ	instantaneous SNR
$\bar{\gamma}$	average SNR
$\boldsymbol{\gamma}$	channel profile vector for the BFC
γ_i	instant SNR over the link i
Δ_f	subcarrier spacing
Δ_p	distance between two pilot subcarriers
ϵ^*	decoding threshold
ϵ	erasure probability
ζ	time variable
$\theta_{l,k}$	random phase for the l th scatterer of the tap k
λ	wavelength
λ_{MAX}	maximum eigenvalue of $\mathbf{H}^H \mathbf{H}$
$\lambda(x)$	polinomial variable node degree distribution
ν_c	3 dB cut-off frequency
$\nu_{l,k}$	Doppler frequency for the l^{th} scatterer of the tap k
$\rho(x)$	polinomial check node degree distribution
σ_α^2	mean power of $\alpha_i(\zeta)$
σ^2	noise variance
σ_R^2	noise variance at the relay
σ_{RD}^2	noise variance for the path R-D
σ_{f_D}	Doppler spread
σ_i^2	noise variance over the link i
σ_τ	delay spread
τ_k	delay of the tap k
A	area
\mathbf{B}	base matrix of a protograph
C	relay amplification factor
C_i	ceck node i
\mathcal{C}	generic code ensemble
\mathcal{C}_S	code ensemble applied at the source
\mathcal{C}_R	code ensemble applied at the relay
c	light speed
\mathcal{C}	check nodes ensemble
c_k	amplitude fading coefficient for the tap k
\mathbf{c}_s	coded block vector
d	diversity achieved by a protograph
d_c	degree of a check node

d_i	diversity achieved by the VN i
d_v	degree of a variable node
$\mathcal{D}^{(j)}$	N-dimensional convergence region of the VN j
$\overline{\mathcal{D}}^{(j)}$	N-dimensional outage region of the VN j
$\mathcal{D}_{\mathcal{G}}$	N-dimensional convergence region of a protograph \mathcal{G}
$\overline{\mathcal{D}}_{\mathcal{G}}$	N-dimensional outage region of a protograph \mathcal{G}
$\mathcal{D}^{(j)}$	convergence region of the high-priority fragment
$\mathcal{D}^{(h)}$	2-dimensional convergence region of the high-priority fragment
$\mathcal{D}^{(l)}$	2-dimensional convergence region of the low-priority fragment
\mathcal{E}	edges ensemble
E_b	energy per bit
E_s	energy per symbol
E_{tot}	total energy per bit spent by the system
f	frequency variable
f_c	carrier frequency
f_d	Doppler shift
f_{d_k}	Doppler shift for the tap k
$f_{d_{max}}$	maximum Doppler shift
$f_{\gamma}(\gamma)$	fading channel distribution for the instantaneous SNR γ
\mathbf{G}	generator matrix
\mathcal{G}	protograph
\mathcal{G}_R	relay protograph
\mathcal{G}_S	source protograph
$H(f)$	channel transfer function
\mathbf{H}	parity check matrix
h_i	generic channel coefficient relative to the antenna i
$h_{i,j}$	channel coefficient corresponding to the symbol i, j
h_{SR}	channel coefficient corresponding to the link S-R
I	generic mutual information
I_A	a posteriori mutual information
I_{ch}	channel mutual information
I_E	ecstrinsic mutual information
$J(\sigma)$	capacity of a binary-input additive Gaussian noise channel
K	Rice factor
k_S	number of coded bits at the source
$L^{(j)}(\mathbf{y})$	a posteriori log-likelihood ratio for the j^{th} bit
L_{CP}	power loss due to the cyclic prefix
L_{PB}	power loss due to pilot boosting
n	number of information bits
m_S	number of parity bits computed by the source
m_R	number of parity bits computed by the relay
n_i	thermal noise coefficient corresponding to the antenna i
n_{SD}	thermal noise coefficient corresponding to the link S-D
N_0	AWGN noise power
N_{data}	number of data subcarriers
N_{pilot}	number of pilot subcarriers
N_s	number of scatterers

N_t	number of taps
P_b	bit error probability
P_B	pilot boosting
$P_b(\gamma)$	bit error probability for a given channel profile γ
P_F	fragment error probability
$P_F^{(h)}$	fragment error probability for the high-priority fragment
$P_F^{(l)}$	fragment error probability for the low-priority fragment
p_k	power of the tap k
\mathbf{p}_s	parity bits vector
R	coding rate
$r_\alpha(\zeta)$	autocorrelation function of the signal $\alpha(t)$
$S_\alpha(\nu)$	Doppler spectrum of the signal $\alpha(t)$
t	time variable
t_1	first time slot
t_2	second time slot
T_c	sampling time
t_{coh}	coherence time
T_{CP}	cyclic prefix duration
T_f	frame duration
T_{OFDM}	time of an OFDM symbol including the cyclic prefix
T_S	symbol time
u	total signal received by the multiple antennas
\mathbf{u}	message vector
\mathbf{u}_h	high-priority fragment of the message vector
\mathbf{u}_l	low-priority fragment of the message vector
v	speed
\mathcal{V}	variable nodes ensemble
V_i	variable node i
w_1	weight of the MRC receiver
\hat{x}	detected signal
\mathbf{x}	generic transmitted signal vector
$X(f)$	Fourier transformation of $x(t)$
x_i	generic signal transmitted by the antenna i
x_I	interfering signal
x_R	signal transmitted by the relay
$x(t)$	generic transmitted signal
\mathbf{y}	generic received signal vector
y_i	generic signal received on the antenna i
$Y(f)$	Fourier transformation of $y(t)$
y_{SD}	signal received corresponding to the link S-D
$y(t)$	generic received signal
z	random variable uniformly distributed between $(0, 1]$

Introduction

The aeronautical traffic has been subjected to an exponential growth in the last years. Following this trend, the air traffic control (ATC) infrastructure has seen a growing demand for communication, navigation and surveillance services. The airport area is a focal point, with an elevated concentration of aircraft and a high capacity demand. However, the current communications infrastructure is not able to satisfy all the requirements of capacity, efficiency, robustness, and security. Hence, a new system, able to provide an efficient solution to all the requests, must be developed. The IEEE standard 802.16 (WiMAX) [1–3] has been chosen by European Organization for the Safety of Air Navigation (EUROCONTROL) and Federal Aviation Administration (FAA) as the baseline for the up-coming airport communications [4]. The WiMAX standard provides a large variety of profiles for physical layer coding and modulation, and hence enables the choice of the one which may be most tailored to the airport environment. The standard includes three different physical layer modes, one based on single-carrier transmission and the other two on multi-carrier transmission, namely on orthogonal frequency-division multiplexing (OFDM) and orthogonal frequency-division multiple access (OFDMA), respectively. The multi-carrier modes offer a strong resistance against the multi-path effects. Hence, they represent an appealing solution for the airport scenarios, which are characterized by multi-path propagation conditions. Beyond the congested VHF band used nowadays, new frequency bands have to be considered in order to satisfy the capacity requirements. At the World Radio Conference in 2007 [5], new frequencies in C band (between 5.091 GHz and 5.150 GHz) were allocated to aeronautical airport surface operations.

This thesis deals with the development of the upcoming aeronautical mobile airport communications system (AeroMACS) system. We analyzed the performance of AeroMACS and we investigated potential solutions for enhancing its performance. Since the most critical results correspond to the channel scenario having less diversity¹, we tackled this problem investigating potential solutions for increasing the diversity of the system and therefore improving its performance. We accounted different forms of diversity as space diversity and time diversity.

Multiple antennas represent an interesting and promising innovation in wireless com-

¹This case is due by no mobility and non line-of-sight (NLOS) conditions with the control tower.

munications. The addition of one or more antennas may create independent multiple channels and introduce space diversity without reducing the spectral efficiency. However, in the aeronautical domain, the introduction of multiple antenna systems, especially on-board aircraft, is seen to be critical, limiting the applicability of MIMO.

Cooperative communication techniques can represent a valid alternative, since they allow single antenna systems to exploit spatial diversity (or more specifically, cooperative diversity). Cooperative communications represent a new paradigm based on the utilization of heterogeneous resources in order to increase the overall performance of the system. A virtual antenna array may be created by the combination of antennas of different users, obtaining cooperation diversity. The classic relay system can be seen as an example of cooperative communication, where a user of the system acts as a relay forwarding the received signal. The main drawback related with the adoption of cooperative schemes consists in an efficiency reduction. Though, new methods [6] can be adopted for mitigating this problem.

The application of error control codes to protocol stack layers different from the physical one gained a large interest during the past decade [7–11]. Such coding techniques deal with the use of a linear (block) code applied to *encoding units* (symbols) that are usually packets with constant size. In this context, a packet level encoder receives as input a set of k packets, and produces as output $n > k$ packets. Assuming systematic encoding, the final set of packets comprises the k information packets together with $m = n - k$ parity packets. At the receiver, after the physical layer decoding, the packets that have been validated (e.g. by an error detection code) are forwarded to the packet level decoder. The corrupted packets are discarded. Therefore, the upper layers deal with packet erasures. The packet level decoder may recover the erased packets by means of the parity packets. Packet level codes are employed in multimedia wireless broadcasting systems (see for example the DVB-H/SH standards [12, 13]), in multicast scenarios [14], and are currently investigated in space communication systems [15–17]. Packet level coding can be still categorized as a form of time diversity. Hence, it may suffer (as other interleaver-based solutions) for relatively-large delays.

It is thus clear that all the above-mentioned diversity techniques represent in principle appealing solutions to the diversity problem in the airport domain. Though, they all bring tradeoffs that have to be analyzed w.r.t. the system requirements. In this thesis, we analyzed the techniques mentioned so far, in the context of the airport communications.

The thesis organization and the main contributions are summarized in the following.

Airport Environment

Chapter 1 provides a general introduction to the aeronautical communications, with particular attention to the airport case. A brief summary of the data traffic and the relevant requirements is also included. A novel airport channel model based on the Bello model [18] and adapted to the peculiarities of the airport scenarios is proposed. The

model is based on four typical airport scenarios as parking, apron, taxi and runway. We illustrate the implementation of the stochastic model and we provide the channel parameters obtained from a measurement campaign carried out at the Munich airport Franz Joseph Strauss (MUC).

AeroMACS

Chapter 2 is dedicated to the performance evaluation of the new standard for the airport surface communications system (AeroMACS). We analyzed two candidate profiles, showing their performance by simulations. An analysis of the performance of the OFDM and OFDMA profiles of the IEEE 802.16e standard is provided in a realistic airport scenario. The system performances are evaluated for the apron, parking, taxi and runway scenarios. We indicated then the best candidate for becoming the baseline of AeroMACS. The OFDMA mode provides generally better results with respect to the OFDM one. Moreover, it includes a large variety of possible bandwidths, number of sub-carriers, modulations and coding schemes, out of which selecting the best ones for airport communications.

Multiple Antennas

Chapter 3 is dedicated to the multiple antennas systems. After a brief description of the main MIMO schemes, simple schemes which foresee multiple antennas only on the base station are analyzed. A 1×2 MRC scheme is applied to the reverse link of AeroMACS, while in the forward link case is used a 2×1 space-time coding scheme. Simulation results show the large performance improvement introduced by the increase of diversity. We also propose a novel space-time coding realization which preserves the original frame structure of WiMAX, analyzing its performance in a realistic airport environment.

Cooperative Communications

In Chapter 4, we analyze low-complexity cooperative communications protocols in the context of AeroMACS. Decode and forward, amplify and forward and coded cooperation methods are investigated, analyzing their properties in the aeronautical context. We propose two different realizations of simple cooperative communication schemes for improving the performance of AeroMACS in the reverse link (RL). The first scheme proposed, based on the amplify and forward method, increases the reliability of the system by means of a relay which simply forwards the source signal to the destination. In our investigation, the relay can be an aircraft. In this way the introduction of a new (ad-hoc) relay network is avoided. The resulting system can benefit from a spatial diversity of order two, which is equivalent to the result obtained with a multiple-antenna system with two antennas. The receiver can perform a simple selection combining of the two

received signals or can adopt a more sophisticated algorithm (e.g. maximal ratio combining), which allows exploiting all the received power. However, in order to perform maximal ratio combining (MRC), all the channel components must be known. Hence, it is necessary to estimate not only the resulting channel coming from the combination of the route source-relay-destination, but also the channel relative to the relay-destination segment. In order to properly estimate all the channels, we insert some pilot tones at the relay before amplifying the signal, allowing the destination to coherently sum all the received signals and maximize the performance of the system. The second scheme implemented is decode and forward. Also this scheme allows to obtain diversity of order two. Performance results in terms of bit error rate (BER) versus signal-to-noise ratio (SNR) are provided for both the implementations. The simulation results show large performance improvement in both the schemes.

Unequal Diversity Coding: a New Concept for the Relay Channel

In Chapter 5, a new cooperative scheme which provides a solution to the typical efficiency reduction related to the distributed diversity is introduced. High system efficiency is reached, while offering diversity two to the most important part of the message. A novel protograph-based construction of low-density parity check (LDPC) codes for the relay channel is proposed, which provides an enhanced unequal error protection (named *unequal diversity*) property. The focus is on quasi-static fading channels and on the high-code-rate ($R > 1/2$) regimes, for which (according to the Singleton bound) no full diversity can be achieved. In the proposed construction, some nodes (and the corresponding codeword fragment) associated with the code graph enjoy the diversity provided by the relay, whereas the remaining nodes do not experience any diversity. The proposed approach can be thus tailored to transmit information blocks with different priority levels. A specific extrinsic information transfer analysis is developed, which allows an accurate performance prediction over the considered channel model, and more in general over block-fading channels.

Packet Level Coding

In Chapter 6, we investigate an alternative method to improve the performance of the system. We increase the time diversity of the system by means of packet level coding. In many applications erasure correcting codes are used to recover packet losses at high protocol stack layers. The objects (e.g. files) to be transmitted often have variable sizes, resulting in a variable number of packet to be encoded by the packet-level encoder. We investigate algorithms for the (on-line) flexible design of parity-check matrices for irregular-repeat-accumulate codes. The proposed algorithms allow designing in fast manner parity-check matrices that are suitable for low-complexity maximum-likelihood decoding. The code ensembles generated by the proposed algorithms are analyzed via

extrinsic information transfer charts. Numerical results show how the designed codes can attain codeword error rates as low as 10^{-5} without appreciable losses w.r.t. the performance of idealized maximum-distance separable codes. We then apply the proposed construction to AeroMACS, showing large performance improvement and proving at the same time the efficiency and the flexibility of the method.

Conclusions and Appendices

Finally, Chapter 7 concludes this thesis. The main outcomes of this work are summarized and final conclusions are drawn. Advantages and drawbacks of the proposed methods are illustrated, delineating the best solutions for the airport environment.

The channel estimation algorithms developed and used throughout this thesis are illustrated in the Appendix. Fundamentals concerning the topics addressed in this work are also included in the Appendices. Low-density parity-check codes principles are introduced, together with principle of iterative decoding and the description of the EXIT chart analysis. A brief overview of the unequal error protection concepts is also provided.

Part of this work has been published and submitted to the following conferences and journals [6, 19–26].

Chapter 1

Airport Environment

The main airport communication target is the guidance and control of the aircrafts. However, also service vehicles (e.g. for luggage handling, fueling, or catering) constitute an important part of the traffic and require a significant data transmission capacity. Moreover, additional fixed/portable applications are foreseen, e.g. for connecting remote sensors to the surveillance network of the airport. Nowadays, the only communication infrastructures available at the airports are based on analog systems for voice communications, and the so called VHF Digital Mode 2 (VDL2), serving the ATC data links. However, the supported data rates are scarce, and the available spectrum in the VHF band is very limited. Therefore, a modern and efficient data link technology in another frequency band is required for the airport area, which allows higher data rates.

In order to determine the best solution for the airport data link, a good knowledge of the characteristics of the communication channel is extremely important. The airports differ one to each other for size and structure. Nevertheless, they are all characterized by the presence of typical communication scenarios. We implemented a novel stochastic airport channel model with parameters obtained from a measurement campaign carried out at the airport of Munich. Multi-path and Doppler effects with the potentially resulting inter-symbol interference and inter-carrier interference have been taken into account, respectively.

In this chapter we recall the main aeronautical communications characteristics, and in particular the peculiarities of the airport domain. We illustrate the stochastic airport channel model developed for the analysis of AeroMACS and its implementation. The channel parameters of the different scenarios are also provided.

1.1 Overview of the Aeronautical Communications

The aeronautical environment may be divided in different domains according to the aircraft position. We can distinguish:

- The airport (APT) domain is an area of 10 miles in diameter and up to 5000 ft altitude, composed by the airport surface and the immediate vicinity of the airport.

- The terminal manoeuvring area (TMA) corresponds to the airspace surrounding the airport, with an altitude spanning between 5000 and 245 ft and with a radius of 50 nautical miles.
- The en route (ENR) zone corresponds to the continental and domestic airspace.
- The oceanic remote polar (ORP) area is similar to the ENR one, but is associated to remote areas.
- The autonomous operations area (AOA) domain constitutes specific areas where the aircraft is supposed to operate in an autonomous way.

Each domain is characterized by specific characteristics and different propagation conditions, hence would require a different communication system and a different bandwidth. Following this approach, EUROCONTROL, FAA and different airline companies have started the development of a new communication concept based on the combination of heterogeneous systems (as illustrated in Figure 1.1). The combination of air-ground, air-to-air, satellite and airport communications can bring very high performance. In the Future Communications Study Final Conclusions and Recommendations Report [27], different technologies have been selected as the baseline for the development of the links of each domain.

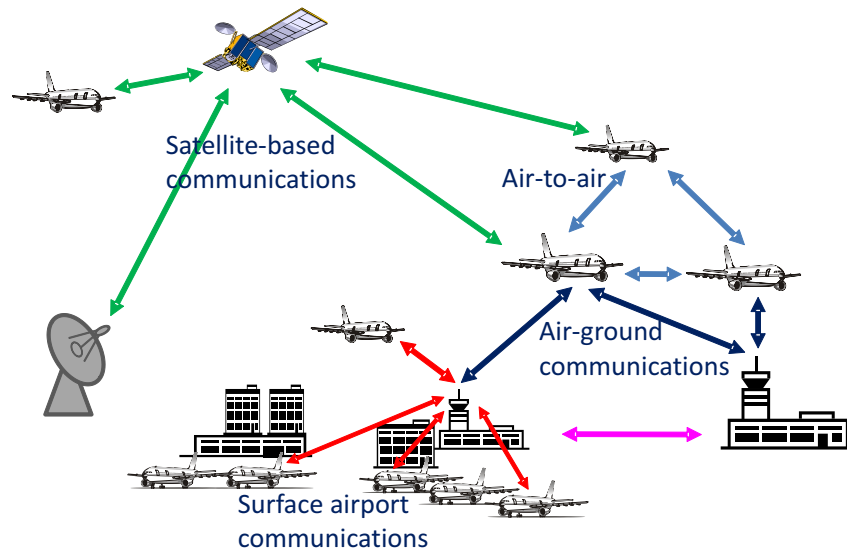


Figure 1.1: Design of the future aeronautical communications based on different heterogeneous links. The global system is composed by air-ground, air-to-air, satellite and airport communications. Each link is based on a different technology, in order to provide a solution to the requirement of the specific link.

In this thesis we target the airport domain, and we neglect all the other links. In particular, we focus on the surface airport communications. Hence, all the communications related to the aircraft on the ground, but also the ones concerning the vehicles

operating on the airport area (as vehicles providing fuels or luggage) will be tackled. The high concentration of entities requiring to communicate generates an high traffic demand. The VHF band is highly congested and cannot satisfy these requirements; hence, a new frequency band, between 5.091 and 5.150 GHz has been assigned to AeroMACS ¹.

We review next some basic notations that we will use through this thesis. In common wireless/cellular communication systems, the links from the base station to the mobile station are usually called down link (DL), as the base station occupies a higher position with respect to the mobile terminals. Accordingly, the communication from mobile terminal to base station is called up link (UL). However, in the aeronautical context, the aircraft may be on air or on the ground, and the above definition doesn't hold anymore. Thus, in order to avoid misunderstanding, the DL and the UL naming are replaced by forward link (FL) and reverse link. The FL is usually referred to the link from the control tower to the aircraft, as illustrated in Figure 1.2. In this context, the traffic can be of

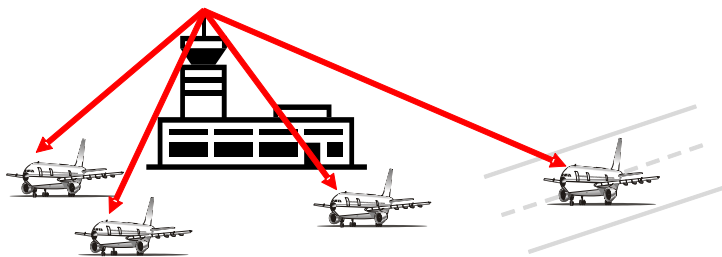


Figure 1.2: Forward link representation.

broadcast, multicast and unicast types. The RL represents the link from the aircraft to the control tower. In this case, the type of traffic is mainly unicast.

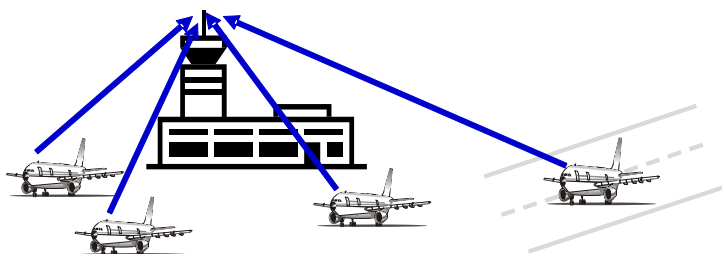


Figure 1.3: Reverse link representation.

The airport domain is generally divided in four areas called apron, taxi, parking and runway. The apron scenario represents the area in front of the terminals, with line-of-sight (LOS) condition for most of the time and limited aircraft mobility (~ 30 km/h). The parking area is also close to the buildings, but here the control tower is in NLOS condition with the vehicles for most of the time. In this scenario the aircraft have very low

¹This portion of the C band has been allocated to the airport surface communications at the ITU World radio conference [28].

speeds or are not moving at all. Last, the taxi and runway scenarios represent the phases during which the aircraft is traveling toward or from the terminals and feature LOS with the control tower. These zones are characterized by different propagation conditions that will be explained more in detail in the next section.

1.2 Airport Channel Model

In order to determine the best solution for the airport data link, a good knowledge of the characteristics of the communication channel is extremely important. The characterization of the channels may be focused on two different aspects. The large-scale models describe the path loss and the shadowing. They are useful for link budgets, coverage planning or traffic models. The small-scale models hold within some wavelengths and are characterized by the scattering function. They are appropriate to validate system performances and running simulations. Hence, for evaluating the performance of our system, we focused on the last aspect. We developed a novel stochastic airport channel model with parameters based on measurement results carried out at the airport of Munich [29].

The airports differ one to each other for size, structure and geography conditions. Nevertheless, they are all characterized by the presence of typical communication scenarios. In virtue of this characteristics, we developed a channel model based on different scenarios and we assumed the channel parameters obtained from measurements at the airport of Munich as characteristic of other airports with similar conditions.

1.2.1 Channel Description

The developed channel is based on the wide sense stationary uncorrelated scattering model (WSSUS) model [18], adapted to the peculiarities of the airport environment. The multi-path phenomena are implemented through a tapped delay line with N_t taps. Moreover, the fading processes are independent among taps. Each tap is characterized by an amplitude c_k , $k = 1 \dots N_t$, a delay τ_k and a discrete-time correlated fading process $\alpha_k(nT_c)$, with T_c being the sampling period of the received signal. As shown in Figure 1.4, the received signal $y(nT_c)$ results from the sum of all the tap components, obtained by multiplying the delayed transmitted signal $x(nT_c)$ by the different fading coefficients $\alpha_k(nT_c)$. The received signal is hence given by

$$y(nT_c) = \sum_{k=0}^{N_t-1} x(nT_c - \tau_k) \cdot \alpha_k(nT_c), \quad (1.1)$$

where nT_c represents the generic n^{th} sample time.

The fading coefficients are given by samples of correlated Rayleigh and Rice processes, generated with the sum of sinusoids method [30–32], which obtains the fading by super-

posing a finite number of scatterers. The k^{th} tap coefficient is provided by

$$\alpha_k(nT_c) = c_k(nT_c) \cdot \sqrt{\frac{1}{N_s}} \sum_{l=0}^{N_s-1} e^{j[2\pi(\nu_{l,k} + f_{d_k})nT_c + \theta_{l,k}]}, \quad (1.2)$$

$$k = 0, \dots, N_t - 1, \quad n = 0, 1, 2, \dots$$

The fading amplitude is given by the tap gain c_k and by a normalization coefficient, inversely proportional to the number of scatterers N_s . The tap gain is given by

$$c_k = \sqrt{\frac{p_k}{\sum_{j=0}^{N_t-1} p_j}}, \quad (1.3)$$

where p_k represents the power of the k^{th} tap and has an exponential decaying power delay profile

$$p_k = \begin{cases} e^{-\tau_k/\sigma_\tau}, & 0 < \tau_k < \tau_{max} \\ 0, & \tau_k \leq 0 \end{cases}. \quad (1.4)$$

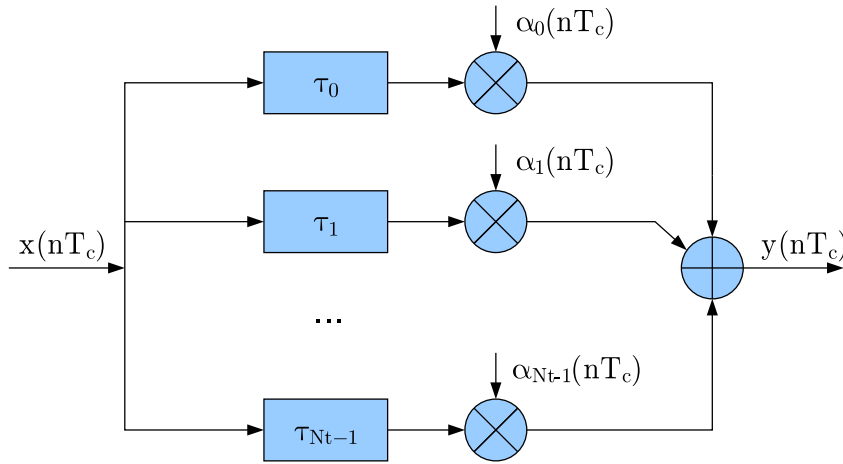


Figure 1.4: Time domain multi-path channel model scheme.

The maximum delay τ_{max} and the delay spread σ_τ depend on the specific channel scenario. The phase $\theta_{l,k}$ is chosen as a random variable uniformly distributed between 0 and 2π , while the frequency is given by the sum of the Doppler frequency shift f_{d_k} of the k^{th} tap, and a variable Doppler frequency $\nu_{l,k}$, following a certain power spectral density (PSD) distribution depending on the different scenario characteristics. Figure 1.5 describes the generation of a fading coefficient.

For the LOS component (tap $k = 0$), the fading coefficients $\alpha_0(nT_c)$ are given by

$$\alpha_0(nT_c) = c_0(nT_c) \cdot \sqrt{\frac{1}{N_s}} e^{j(2\pi f_{d_0} nT_c)}, \quad (1.5)$$

i.e., the LOS component is affected by a rigid Doppler shift only. We have chosen the Doppler shift f_{d_k} values uniformly distributed in $[-f_{d_{max}}, f_{d_{max}}]$, with

$$f_{d_{max}} = \frac{f_c \cdot v}{c}, \quad (1.6)$$

where f_c represents the carrier frequency, v is the speed of the aircraft and $c = 3 \cdot 10^8$ m/s is the speed of the light. The Doppler frequencies for the scatterers have been selected by means of the Monte Carlo method [33–35] according to a Gaussian power spectral density (GPSD). Theoretical investigations, in fact, showed that aeronautical channels are characterized by Gaussian-shaped Doppler spectrum [36].

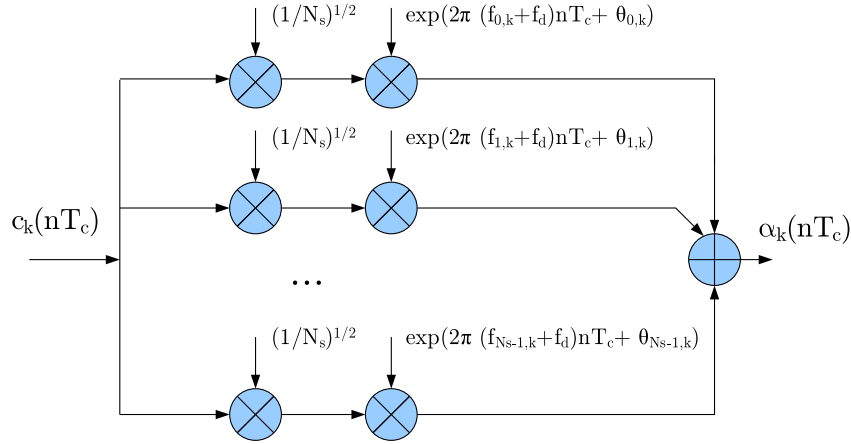


Figure 1.5: Fading generation scheme with the sum of sinusoids method.

1.2.2 Channel Implementation

We implemented the described channel model in the time domain, as depicted in Figure 1.6, and in the frequency domain. The time domain implementation allows to reproduce all the potential channel effects on the system as inter-carrier interference (ICI) and ainter-symbol interference (ISI). The signal through each tap is first delayed and then multiplied by the fading coefficients. At the end, the faded components corresponding to all the taps are added generating the received signal (Equation 1.8).

The fading coefficients α_k change every chip time T_c (and consequently the channel loses the linearity). The multiplication, in time domain, between the transmitted symbol and the fading coefficients (which are not constant anymore) can be seen, in the frequency domain, as a convolution, between the transforms of the two vectors. This introduces ICI. The fading coefficient relative to a general sample time n^{th} in a general frame i is given by

$$\alpha_k(nT_c)^{(i)} = c_k \cdot \sqrt{\frac{1}{N_s}} \sum_{l=0}^{N_s-1} e^{j[2\pi(\nu_{l,k}^{(i)} + f_{d_k}^{(i)}) \cdot n \cdot T_c + \theta^{(i)}]}. \quad (1.7)$$

The fading process is completely regenerated for every frame. The received signal is thus given by

$$y(nT_c) = \sqrt{\frac{1}{N_s}} \sum_{k=0}^{N_t-1} c_k \cdot x(nT_c - \tau_k) \sum_{l=0}^{N_s-1} e^{j[2\pi(\nu_{l,k}^{(i)} + f_{d_k}^{(i)}) \cdot n T_c + \theta^{(i)}]}. \quad (1.8)$$

Since we used an exponential power delay profile ($p_k = e^{-\tau_k/\sigma_\tau}$), the fading amplitude becomes

$$c_k = \sqrt{\frac{e^{-\tau_k/\sigma_\tau}}{\sum_{k=0}^{N_s-1} e^{-\tau_k/\sigma_\tau}}}. \quad (1.9)$$

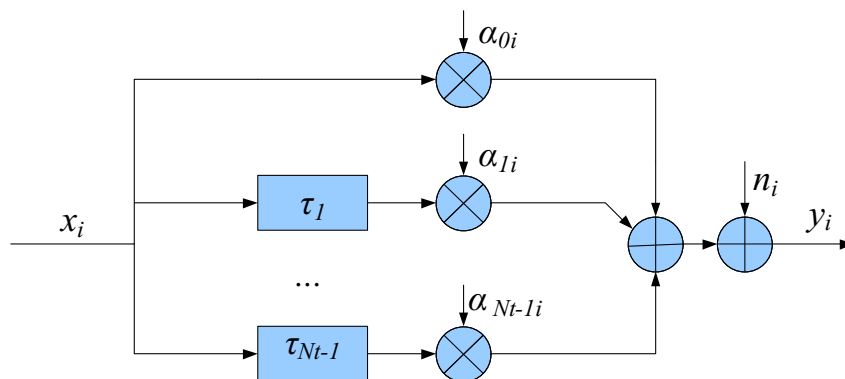


Figure 1.6: Scheme of the channel model (time domain implementation).

Frequency Domain Channel Version. The previously described channel model implementation (in the time domain) is able to account the eventual ICI and ISI. Though, a representation in time domain is computationally more expensive, since with respect to the frequencies domain one, requires the implementation of the inverse fast Fourier transformation (IFFT) and fast Fourier transformation (FFT) operations. Moreover, if the inter-carrier spacing is sufficiently bigger than the Doppler spread², there is no ICI and no necessity to implement it. Hence, a simplified channel model in the frequency domain (which provides more efficient simulations) is preferable.

The frequency domain version of the channel is the dual representation of the time domain implementation. The results provided by these two implementations are exactly the same (assuming no ICI). The channel is based on the multiplication of the transmitted signal for a channel transfer function, which is obtained by a Fourier transformation of the impulse channel response, i.e.

$$Y(f) = X(f) \cdot H(f) \quad (1.10)$$

$$H(m\Delta_f) = \sum_{k=0}^{N_{taps}-1} \alpha_k(mT_s) \cdot e^{-j2\pi m\Delta_f T_s}. \quad (1.11)$$

Considering a generic OFDM symbol m in a frame i and with T_s representing the overall OFDM symbol time, the fading coefficients and the received signal are respectively given by

²Usually, the performance of the system starts degrading for frequency values around 20% of the subcarrier spacing; hence, it should be sufficient having $\Delta_{fD} > 5 \cdot \sigma_f$ for avoiding ICI.

$$\alpha_k^{(i)}(mT_s) = c_k^{(i)} \cdot \sqrt{\frac{1}{N_s}} \sum_{l=0}^{N_s-1} e^{j[2\pi(\nu_{l,k}^{(i)} + f_{d_k}^{(i)}) \cdot mT_s + \theta^{(i)}]}, \quad (1.12)$$

$$Y(m\Delta_f) = X(m\Delta_f) \cdot \sum_{k=0}^{N_t-1} \alpha_k \cdot e^{-j2\pi m\Delta_f T_s}. \quad (1.13)$$

In this case, the channel transfer function is computed for each sub-carrier. This channel version supports a unique value of the fading coefficients during an OFDM symbol, therefore, the different signal chips see the same fading level and the channel results linear.

Doppler spectrum

Theoretical investigations in [36] have shown that aeronautical channels have a Doppler power spectral density with Gaussian shape. Although no absolute correspondence to the obtained measurements could be proved, the GPSD can in most cases very well be used as a sufficiently good approximation [37].

Indicating the generic fading process of a tap with $\alpha(t) = \alpha_1(t) + j\alpha_2(t)$, we can express the Gaussian power spectral density of the Doppler frequencies as

$$S_\alpha = S_{\alpha_i\alpha_i} = \frac{\sigma_\alpha^2}{\nu_c} \sqrt{\frac{\ln 2}{\pi}} e^{-\ln 2 \left(\frac{\nu}{\nu_c}\right)^2}, \quad i = 1, 2, \quad (1.14)$$

From Equation 1.14, it is possible to obtain the autocorrelation function r_α doing the inverse Fourier transform of the GPSD [38]. We obtain

$$r_\alpha(\zeta) = r_{\nu_i\nu_i}(\zeta) = \sigma_\alpha^2 e^{-\pi \frac{\nu_c}{\sqrt{\ln 2}} \zeta^2}, \quad (1.15)$$

where σ_α^2 denotes the mean power (variance) of the Gaussian random process α_i , ν_c is the 3 dB cut-off frequency and the index i refers to the two imaginary and real components. From the power spectral density S_α , it is possible to obtain the average frequency shift \bar{f}_d and the average spread $\bar{\sigma}_{f_D}$ that a signal experiences during a transmission as

$$B_{\alpha_i\alpha_i}^{(1)} = \frac{\int_{-\infty}^{+\infty} \nu S_{\alpha_i\alpha_i}(\nu) d\nu}{\int_{-\infty}^{+\infty} S_{\nu_i\nu_i}(\nu) d\nu} \quad (1.16)$$

$$B_{\alpha_i\alpha_i}^{(2)} = \sqrt{\frac{\int_{-\infty}^{+\infty} (f - B_{\alpha_i\alpha_i}^{(1)})^2 S_{\nu_i\nu_i}(\nu) d\nu}{\int_{-\infty}^{+\infty} S_{\nu_i\nu_i}(\nu) d\nu}}. \quad (1.17)$$

In case of $S_{\alpha_1\alpha_1}$ and $S_{\alpha_2\alpha_2}$ identical and symmetrical, using the autocorrelation function it is possible to obtain equations [38]

$$\bar{f}_d = B_{\nu_i}^{(1)} = B_{\nu}^{(1)} = 0 \quad (1.18)$$

$$\bar{\sigma}_D = \sqrt{B_{\alpha_i}^{(2)}} = \sqrt{B_{\nu}^{(2)}} = \frac{\nu_c}{\sqrt{2 \ln 2}}. \quad (1.19)$$

Applying the Monte Carlo method [38–41] to the Gaussian power spectral density 1.14, it is not possible to find a closed-form expression for the discrete Doppler frequencies ν_k . However, these values, may be determined by the zeros of the following equations, where z is a random variable uniformly distributed between $(0, 1]$ and ν_c the 3 dB cut-off frequency.

$$z - \operatorname{erf}\left(\frac{\nu_k}{\nu_c}\sqrt{\ln 2}\right) = 0, \forall k = 1, 2, \dots, N_s \quad (1.20)$$

$$\nu_k = \frac{\nu_c}{\sqrt{\ln 2}} \cdot \operatorname{erf}^{-1}(z), z \in [0, 1) \quad (1.21)$$

The choice of $\nu_c = \sqrt{\ln(2)}\nu_{max}$ leads to a Doppler spread equals to the one obtained with Jakes Doppler spectrum ($\nu = \nu_{max}/\sqrt{2}$)³.

In our simulator, in order to avoid the computational complex exact computation of the inverse error function ($\operatorname{erf}(\cdot)$) operation, we used the following approximation of the complementary inverse error function

$$\operatorname{erfc}^{-1}(x) \approx \begin{cases} \sqrt{\ln\left(\frac{1+\sqrt{1+15x}}{6.25x}\right)}, & x \leq 0.4881 \\ \frac{1-x}{1.0238}, & 0.4881 < x \leq 1 \end{cases} \quad (1.22)$$

1.2.3 Channel Parameters

The channel model parameters have been selected according to a measurement campaign carried out at the airport of Munich [29]. Although the airports have their own characteristics, they include always limited mobility scenarios, as apron and parking, and higher mobility ones, as taxi and runway. Since each scenario presents similar propagation conditions over different airports, characteristic values may be extrapolated from one single case as representative of other cases. Hence, we assumed the values extrapolated from a measurement campaign performed at a certain airport (i.e. Munich) valid also for other airports.

The power of the strongest component changes considerably between different airport areas, but is also subjected to variations within a single scenario. Therefore, the determination of a unique Rice factor ($K = p_0/\sum_{i=1}^{N_t-1} p_i$) characterizing the scenario becomes an hard task. For this reason, we decided to consider few characteristic values for each scenario. For the scenarios with frequent LOS component we chose K equal to 10 and 20 dB, while for the scenarios where the NLOS condition is predominant, we selected $K = 0$ dB and $K = -10$ dB.

We adopted an exponentially decaying power delay profile with delay spreads σ_τ chosen as the 99th percentile of the cumulative density function (CDF) obtained from the measurement results [29]. The number of taps N_t is also taken from [29].

³The simulation results illustrated in the next chapters have been obtained using this convention ($\nu_c = \sqrt{\ln(2)}\nu_{max}$).

All the fading components have a Gaussian shaped Doppler spectrum but the LOS component. We used Doppler spread values σ_{f_D} distributed between the minimum and the maximum values indicated in Table 1.1. Similarly, the main channel parameters have been picked according to Table 1.1.

Table 1.1: Channel parameters used for the different scenarios

	APRON	PARKING	TAXI	RUNWAY
K [dB]	0, 10, 20	0, -10	10, 20	10, 20
σ_τ [μ s]	0.65	1.25	1.5	1.05
$\sigma_{f_{Dmin}}, \sigma_{f_{Dmax}}$ [Hz]	20, 50	10, 40	40, 95	100, 200
f_{dmax} [Hz]	140	50	150	500
N_t	9	12	6	7
N_s	25	25	25	25

Apron Scenario

The apron scenario characterizes the area in front of the terminal building. In this phase the aircraft is moving with low speed in front of the terminals, as represented in Figure 1.7. The delay spread $\sigma_\tau = 0.65 \mu$ s corresponds to the smallest value with respect to the other scenarios. The Doppler frequency shift f_d follows an uniform distribution between the minimum and the maximum values $-f_{dmax}$ and f_{dmax} . The maximum Doppler shifts have been determined according to the typical speed profiles. Hence, considering a typical speed in the order of 30 km/h and a carrier frequency $f_c = 5$ GHz, the resulting $f_{dmax} \simeq 140$ Hz, for all $k = 0 \dots N_t - 1$. The number of tap is equal to 9. The presence of the buildings blocks the direct path for most of the time, resulting in variable LOS and NLOS conditions. The Rice factor values are accordingly set to either $K = 0$ dB or $K = 10$ dB. The number of scatterers $N_s = 25$ assures a good compromise between sufficiently accurate spectrum shape approximation and simulation complexity.

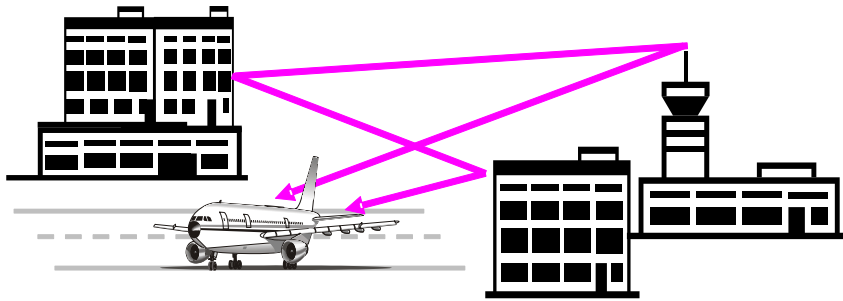


Figure 1.7: Apron scenario representation.

Parking Scenario

The parking scenario represents the phase when the aircraft is parked at the terminal or is traveling through the terminal at a very low speed. As represented in Figure 1.8, the presence of the buildings may block the LOS path between the aircraft and the control tower for the almost totality of the time. Hence, there are only reflected paths and relative low Rice factor values ($K = 0$ dB and $K = -10$ dB). The lack of speed leads to small Doppler values. The maximum Doppler shift is taken equal to 40 Hz. The delay spread is $1.25 \mu\text{s}$. The number of taps is set equal to 12. Again, the number of scatterers is assumed to be 25.

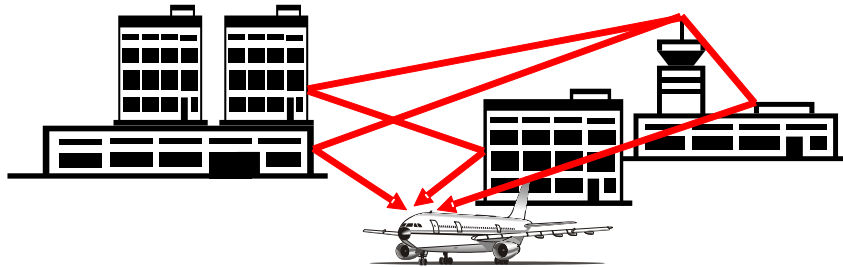


Figure 1.8: Parking scenario representation.

Taxi Scenario

The taxi scenario represents the phase during which the aircraft is traveling towards or from the gate, as illustrated in Figure 1.9. Speeds of 50 – 60 km/h are typical, as well as the presence of a LOS component. Higher Doppler and Rice factor values are assumed ($f_{d_{max}} = 150$ Hz, $K = 10$ dB and $K = 20$ dB). The delay spread of the taxi scenario has the maximum value equal to $1.5 \mu\text{s}$. The number of taps is 6.

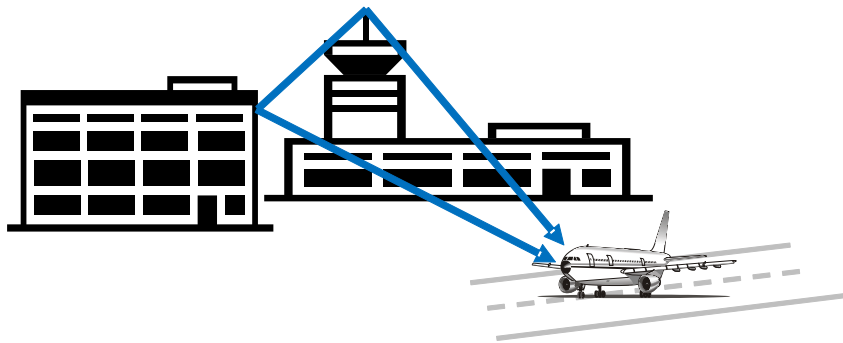


Figure 1.9: Taxi scenario representation.

Runway Scenario

Finally, the runway scenario represents the phase during which the aircraft is on the runway (Figure 1.10). This scenario is similar to the taxi case, but shows considerably

higher speeds. The maximum Doppler shift is assumed 500 Hz, the delay spread is $1.05 \mu\text{s}$ and $K = 10$ and 20 dB.

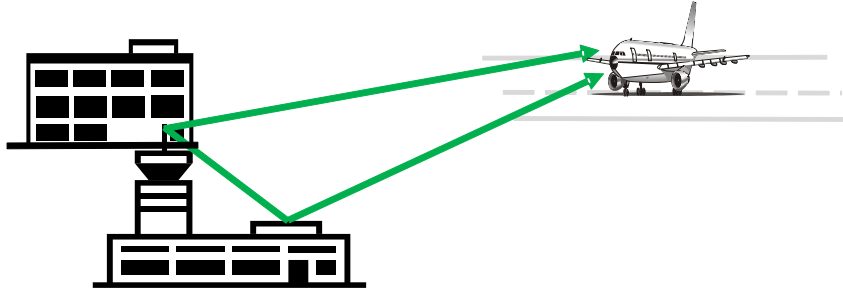


Figure 1.10: Runway scenario representation.

1.3 Summary

In this chapter, we summarized the main propagation conditions of the aeronautical communications within the airport surface. We illustrated the stochastic airport channel model that we developed for this investigation, and we provided the description of the channel model implementation. The channel parameters for the four scenarios, obtained from a measurement campaign at MUC, have also been included.

Chapter 2

AeroMACS System

The standard IEEE 802.16-2009¹ has been recommended by EUROCONTROL and FAA as the future airport data link technology. The WiMAX standard provides a large variety of profiles for physical layer coding and modulation, and hence enables the choice of the one which may be most suitable for the airport environment. The standard includes three different types of physical layer, one based on single-carrier transmission and the other two on multi-carrier transmission, namely on OFDM and OFDMA, respectively. The multi-carrier modes offer a strong resistance against the multi-path effects. Hence, they represent an appealing solution for the airport scenarios, which are characterized by frequent multi-path propagation conditions. Bandwidths, access schemes, frame structures, coding, modulation techniques are defined in the physical layer profiles.

In this chapter, we analyze the multi-carrier profiles of the WiMAX standard. We evaluate the OFDM and OFDMA modes over the airport channel model introduced in the previous chapter, showing their performance. Then, we summarize the results obtained by simulations, delineating the best profile for becoming the baseline of AeroMACS. The OFDMA based waveform shows better performance with respect to the OFDM one; moreover, it allows a large flexibility in the selection of bandwidths, number of subcarriers and coding schemes. The AeroMACS standard is still under development, however, EUROCONTROL has selected the OFDMA-PHY profile with 5 MHz BW and 512 subcarriers as the baseline of the physical layer of the system. The summary of the main AeroMACS parameters is also provided, together with an evaluation of strengths and drawbacks of the system.

2.1 OFDM Based Profile

The OFDM profile uses time-division multiple access (TDMA) and includes both time-division duplexing (TDD) and frequency-division duplexing (FDD). The OFDM

¹Initially, the previous versions of the standard 802.16-2004 [1] and 802.16e-2005 [2] were selected as the candidate technologies for the future airport surface communications system. However, in a second moment, the new 2009 release of the standard has been chosen as reference.

waveform of the WiMAX standard consists of 256 subcarriers, out of which only 200 (in the center of the bandwidth) are effectively used for data transmission and for pilot symbols (except for the DC sub-carrier, which is nulled). Two lateral guard bands of 27 and 28 subcarriers are left unused. The signal bandwidth is adjusted by scaling the sub-carrier spacing Δ_f according to the needs. The maximum bandwidth allocation is set to 5 MHz. The distance between two pilot subcarriers Δ_p is fixed to $25\Delta_f$ for all the symbols, as shown in Figure 2.1.

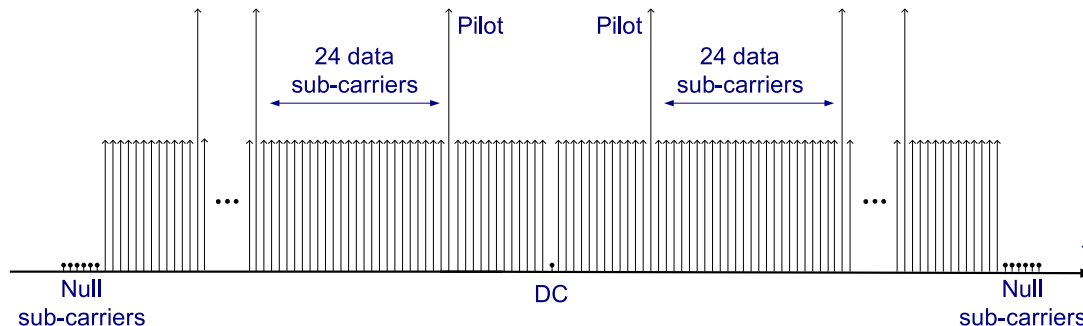


Figure 2.1: Symbol structure for the OFDM case.

The basic coding scheme for this mode is based on the concatenation of an outer Reed-Solomon code with an inner convolutional code with different coding rates. Optionally, convolutional turbo codes (CTC) and block turbo codes (BTC) can be used. The modulation set for the subcarriers includes binary phase shift keying (BPSK), quadrature phase shift keying (QPSK), quadrature amplitude modulation (QAM) with 16 constellation points (16-QAM) and optionally 64-QAM. The cyclic prefix may be selected within $1/4$, $1/8$, $1/16$ or $1/32$ of the symbol duration.

2.1.1 Performance

We provide a performance evaluation of the OFDM profile in the context of the airport environment. We selected some system parameters and we analyzed the system by simulations, using a realistic airport channel model. The next subsections provide in detail the system parameters considered and the simulation results.

Simulation Parameters

The parameters chosen for the simulations consist of a bandwidth of 5 MHz with sub-carrier spacing of almost 20 kHz, a basic coding scheme with a rate $1/2$ convolutional code and a QPSK subcarrier modulation. Given this sub-carrier spacing and the Doppler values presented in Table 1.1, the inter-carrier interference shall provide a negligible impact on the performance. The cyclic prefix has been set $1/8$ of the symbol length, therefore the total OFDM symbol time T_{OFDM} is approximatively $57.6 \mu\text{s}$. Frames of 24 OFDM

symbols have been considered, with all available subcarriers allocated to one user. Prior to the modulation, the bits at the output of the convolutional encoder are interleaved over the entire frame. We used the channel model described in the previous chapter and we evaluated the system performance in all the channel scenarios. At the receiver side we implemented a linear channel interpolation in the frequency domain (see Appendix A.1). Table 2.1 provides the main system parameters used in the simulations.

Table 2.1: Simulation system parameters

System parameters	FL - OFDM
Bandwidth	5 MHz
FFT size	256
Null guard subcarriers	56
Pilot subcarriers/ OFDM symbol	8
cyclic prefix (CP)	$1/8 \cdot T_S = 6.4 \mu s$
Frame size	24 OFDM symbols
Symbol time T_S	51.2 μs
$T_{\text{OFDM}} = T_S + \text{CP}$	57.6 μs
T_{frame}	1.38 ms
Subcarrier spacing Δ_f	$\simeq 20$ kHz
Pilot subcarrier spacing Δ_p	$25\Delta_f \simeq 500$ kHz
Coding, rate	Convolutional, 1/2
Decoding	Soft Viterbi
Modulation	QPSK
Pilot boosting	2.5 dB
Channel scenario	Parking, apron, taxi, and runway
Channel Estimation	Linear pilot interpolation (freq. domain)

Simulation Results and Potential Improvements

In the following, we present the simulation results, analyzing the performance of the above-described system on the aeronautical channel model described in Section 1.2. The results are presented separately for each scenario and are shown in terms of BER versus E_b/N_0 . In the energy per bit E_b computation, we included also the losses due to the transmission of the CP, $L_{CP}[dB] = -10 \log(1 - T_{CP}/T_S)$ and the pilot boosting P_B , $L_{P_B}[dB] = -10 \log(1 - N_{pilot} \cdot P_B / (N_{data} + N_{pilot} \cdot P_B))$. Hence, considering $CP = 1/8T_S$ and $P_B = 2.5$ dB, we obtain a total loss of almost $0.51 + 0.31$ dB.

In Figure 2.2, the results obtained for the apron scenario are provided. This case is characterized by a delay spread $\sigma_\tau = 0.65 \mu s$ and small values of Doppler spread and shift ($\sigma_{f_D} \leq 50$ Hz, $|f_D| < 140$ Hz). The plots obtained with the higher K values are encouraging while the one obtained with $K = 0$ dB presents a relatively high error floor. The parking scenario corresponds to the lowest mobility case with NLOS conditions for most of the time. This scenario is characterized by a rich multi-path with a large delay

spread, while the low mobility results in small Doppler spreads and shifts. Rice factor values of 0 and -10 dB have been chosen to reproduce the predominance of the fading components. Performances provided by Figure 2.3 show that the lack of LOS component plays a dominant role. The performance is very poor and high error floors are present.

Figure 2.4 provides the results obtained for the taxi scenario. Here, with respect to

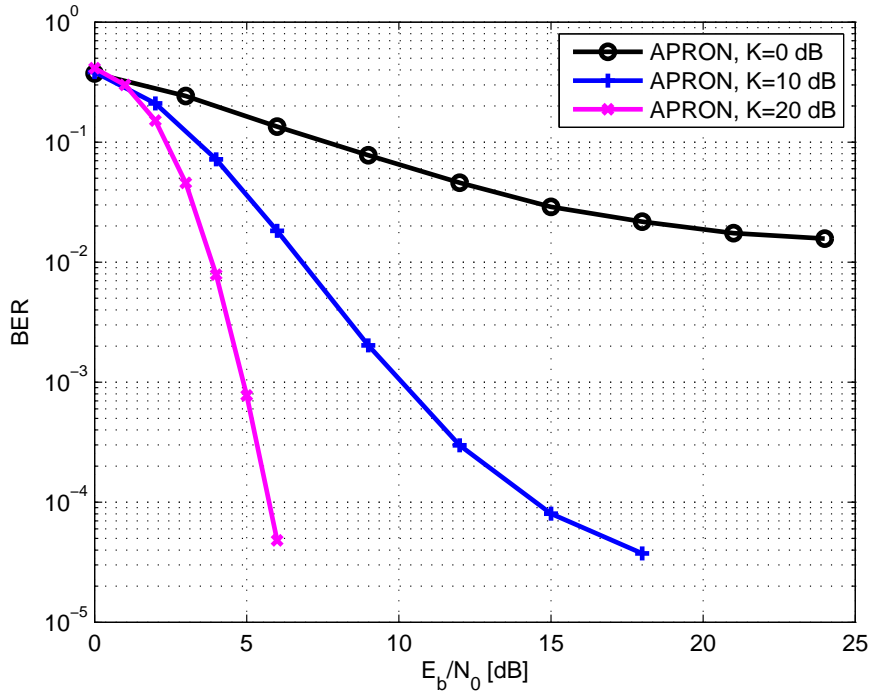


Figure 2.2: Apron scenario performance with different Rice factor values ($K = 0, 10$ and 20 dB) and linear pilot interpolation.

the previous cases, there is more mobility and typically LOS condition, which reflects on the relatively good performance for $K = 10$ dB and $K = 20$ dB. Viceversa, the (less-characteristic) $K = 0$ dB chart, included for sake of completeness, presents poor performance with the highest error floors w.r.t. the other scenarios. Figure 2.5 shows the performance obtained for the runway area. This scenario features the highest mobility and the highest Doppler values, though the large sub-carrier spacing of 20 kHz assures no appreciable degradation due to ICI. Also in this scenario the LOS component is predominant, hence the Rice factor is realistically in the range $10 - 20$ dB. This scenario presents indeed the best performance. In general in LOS conditions the performances are sufficiently good for all the scenarios. The small differences within the scenarios may be explained considering the different delay spreads and Doppler values. However, in case of Rice factor values ≤ 0 dB, the performances of the system are generally particularly poor. Considering that the cyclic prefix $CP=0.64 \mu s$ is sufficient to avoid ISI and that the sub-carrier spacing of 20 kHz should assure no ICI, this behavior can be explained considering a lack of time selectivity and, most of all, a challenging channel estimation. The distance

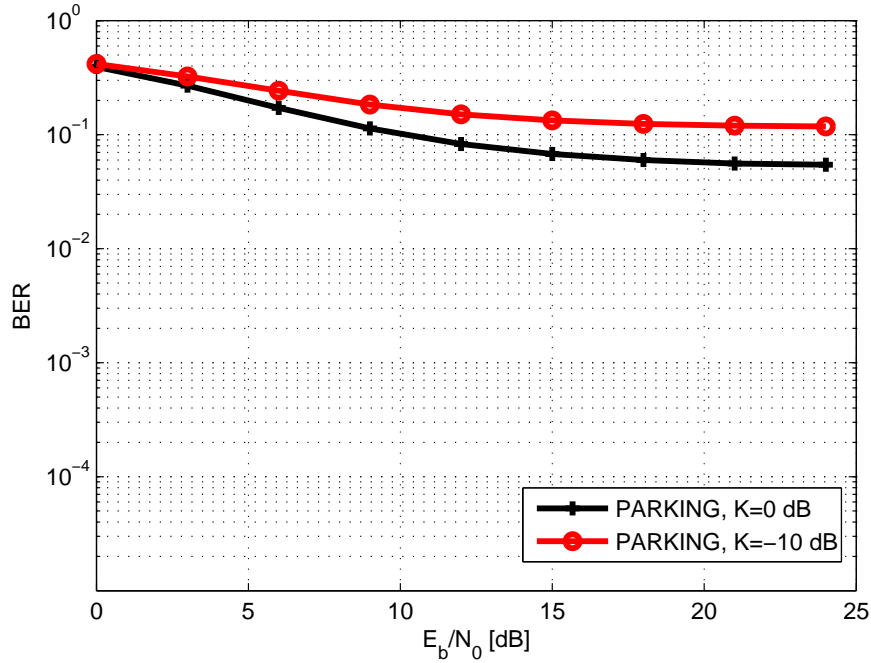


Figure 2.3: Parking scenario performances with different Rice factor values ($K = 0$ and -10 dB) and linear pilot interpolation.

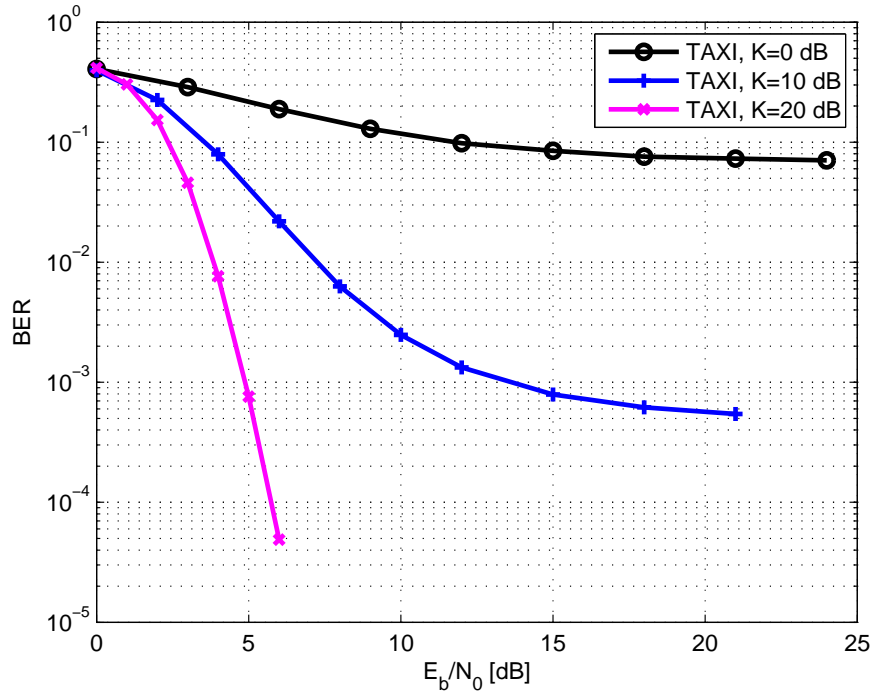


Figure 2.4: Taxi scenario performances with different Rice factor values ($K = 0, 10$ and 20 dB) and linear pilot interpolation.

between two pilot subcarriers ($\Delta_p = 25\Delta_f$) is too large for the frequency selectivity of

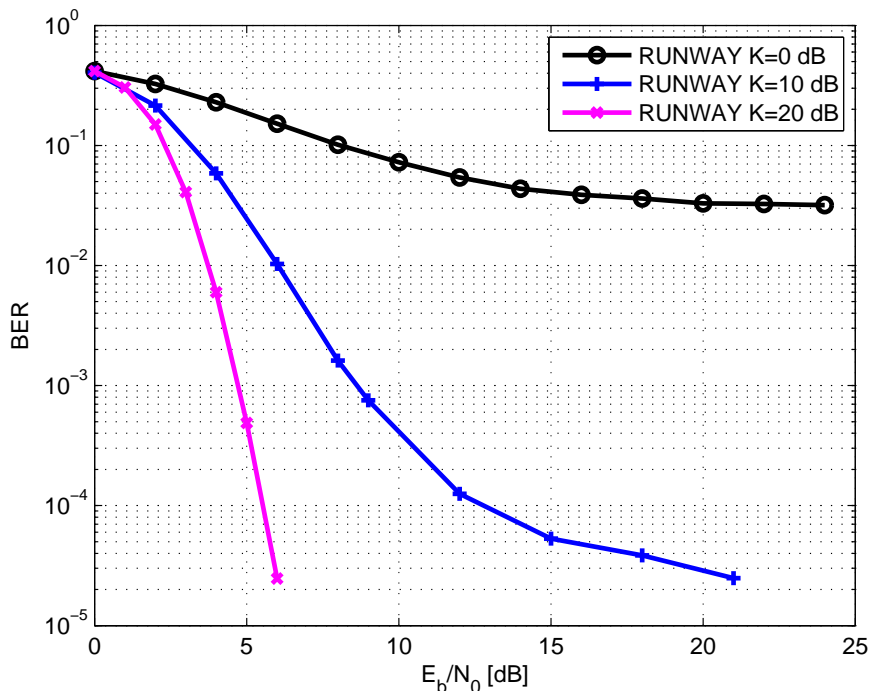


Figure 2.5: Runway scenario performances with different Rice factor values ($K = 0, 10$ and 20 dB) and linear pilot interpolation.

the channel. Therefore, the channel behavior cannot be properly tracked. The inefficient channel estimation causes the error floors and jeopardizes any eventual frequency diversity effect. Indeed, the worst performances correspond to the highest delay spread values, i.e. the taxi ($\mu_\tau = 1.5 \mu s$) and the parking ($\mu_\tau = 1.25 \mu s$) scenarios.

We decided to investigate simple techniques for enhancing the system performance², with particular emphasis to the parking scenario, which presents the major performance degradation. To this end, we briefly anticipate now some results on antenna diversity, leaving a more detailed analysis of multiple input multiple output (MIMO) schemes to Chapter 3.

As discussed before, the two main issues affecting the system performance are the too large separation between pilot subcarriers in the frequency domain and the limited time diversity provided by the channel. The problem has been thus tackled from both sides. On one hand a basic 1×2 single input multiple output (SIMO) scheme (with two antennas at the receiver side) has been introduced to enhance the diversity. On the other hand, increased pilot sub-carrier densities have been investigated to allow accurate channel estimation even in presence of large delay spreads. In Figure 2.6, the results obtained by reducing the pilot sub-carrier spacing with and without the 1×2 SIMO scheme are presented. The results are related to a parking scenario with a Rice factor $K = -10$ dB.

²As we will show better in the next sections, the OFDM profile provides worst performance with respect to the OFDMA. Though, we investigated potential way to improve its performance.

When the SIMO scheme is adopted, MRC of the received signals is performed, using the channel estimates provided by the linear interpolator. Interestingly, the introduction of the second antenna, leaving the pilot sub-carrier spacing to $25\Delta_f$, brings a moderate performance improvement. The error floor is slightly lowered, but it still appears at rather high error rates ($\text{BER} \simeq 10^{-2}$). This phenomenon is due to the insufficient carrier spacing w.r.t. to the frequency selectivity introduced by the relatively high delay spread. We thus investigated the performance of the system with an increased pilot density, i.e. with pilot sub-carrier spacing $10\Delta_f$ and $5\Delta_f$. The framing has been modified accordingly, preserving the lateral null guard bands. The results are shown in Figure 2.6 and confirm our conjecture. In particular, the reduction of the sub-carrier spacing to $5\Delta_f$ permits to remove the floors (at least, down to the error rates achieved through the simulations) and permits to highlight the diversity gain provided by the SIMO scheme.

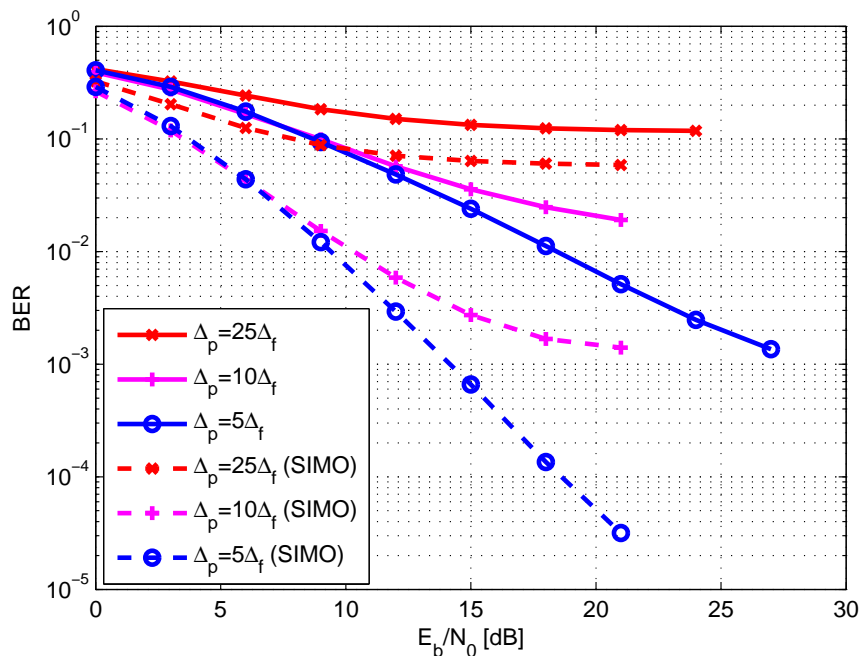


Figure 2.6: Parking scenario with $K = -10$ dB. Performance evaluation with the introduction of antenna diversity (SIMO) and with the reduction of the pilot sub-carrier spacing ($\Delta_p = 5$ and $10\Delta_f$) respect to the standard specification case ($\Delta_p = 25\Delta_f$).

2.2 OFDMA Based Profiles

The WiMAX profiles based on the OFDMA introduce a few more features w.r.t. the OFDM ones. Besides the different multiple access scheme (OFDMA against TDMA), a variable number of subcarriers and greater bandwidths are available. The system can have a numbers of subcarriers equal to 128, 512, 1024 or 2048. The number of subcarriers determines the bandwidth, because the subcarrier spacing is fixed. However, the OFDMA

mode introduces a features called scalable OFDMA (SOFDMA), which consists in the dynamic change of the bandwidth by means of the variation of the number of subcarriers. Only the central subcarriers are effectively used for data transmission and pilot symbols (except the DC sub-carrier, which is nulled). The frame is divided in FL subframe and RL subframe (see 2.7), with the ratio between subframes dynamically variable. The CP values may be set within 1/4, 1/8, 1/16 or 1/32 of the symbol duration. The unique certified values³ for the bandwidth are 5 MHz, which corresponds to a FFT size equal to 512 and 10 MHz which corresponds to 1024 subcarriers.

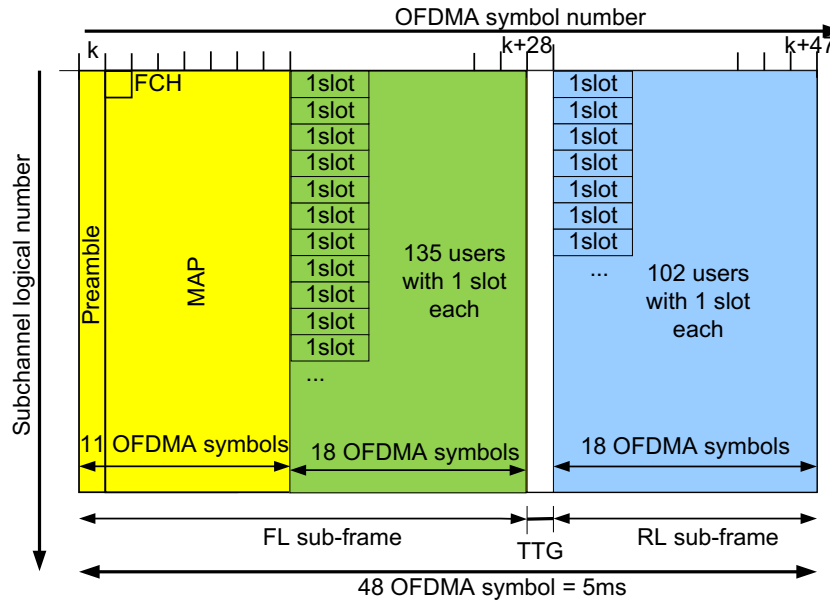


Figure 2.7: Generic scheme of an AeroMACS frame.

The basic coding scheme for this mode includes the convolutional codes and the Turbo codes with different coding rates. Optional codes are the CTC and LDPC codes. The modulation set for the subcarriers includes QPSK, QAM with 16 constellation points (16-QAM) and optionally 64-QAM.

The used subcarriers may be distributed in the frame according to different permutation modes. The main permutation mode, called partially usage of subcarriers (PUSC),

³The WiMAX standard includes a wide range of techniques and parameter sets, therefore it requires to be reduced for practical reasons of inter-operability and implementation. WiMAX Forum [42] proposes to obtain this scope defining a limited number of system profiles and certification profiles. A system profile defines the subset of mandatory and optional physical and MAC layer features selected by WiMAX Forum from the IEEE 802.16-2004 [1] or IEEE 802.16e-2005 [2] standard. The mandatory and optional status of a particular feature within a WiMAX system profile may be different from what it is in the original IEEE standard. Currently, WiMAX Forum has two different types of system profile: one based on IEEE 802.16-2004, OFDM-PHY, called the fixed system profile; the other one based on IEEE 802.16e-2005 scalable OFDMA-PHY, called the mobility system profile. A certification profile is defined as a particular instantiation of a system profile where the operating frequency, channel bandwidth, and duplexing mode are also specified. Within the mobility profiles, two profiles are certified: one with 5 MHz BW and one with 10 MHz.

organizes the FL sub-frame in *clusters* and the RL sub-frame in *tiles*. Two lateral frequency bands are left unused.

The OFDMA mode defines two families of permutation modes: *contiguous* (or adjacent) *permutations*, which use group of adjacent subcarriers, and *diversity* (or distributed) *permutations*, which distribute the subcarriers pseudo-randomly. The main advantage of distributed permutations consists in the frequency diversity and inter-cell interference mitigation. The probability of using the same subcarriers on adjacent sector is minimized and the users have the best average performance. In mobile application these advantages can be particularly helpful.

Distributed Permutation Modes: PUSC and FUSC. The distributed permutation modes include PUSC and fully usage of subcarriers (FUSC). The PUSC permutation mode is based on the concept of tile and cluster which are associated to the RL and FL subframes, respectively. A tile is a group of 12 adjacent (in frequency and time) subcarriers having the structure showed in Figure 2.8. The tile spans over three adjacent OFDMA symbols and allocates the pilot tones on the four corners (the other subcarriers are used for data). Six tiles compose a *subchannel* (or *slot*), which is the minimum quantity allocable to the user.

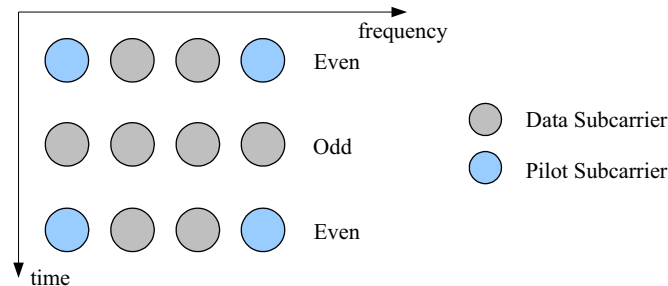


Figure 2.8: Scheme of a tile.

The cluster is the corresponding tile structure for the FL subframe. In this case the group is composed by 28 subcarriers spanning over two OFDMA symbols. Figure 2.9 illustrate the cluster structure. In this case the subchannel is composed by two clusters.

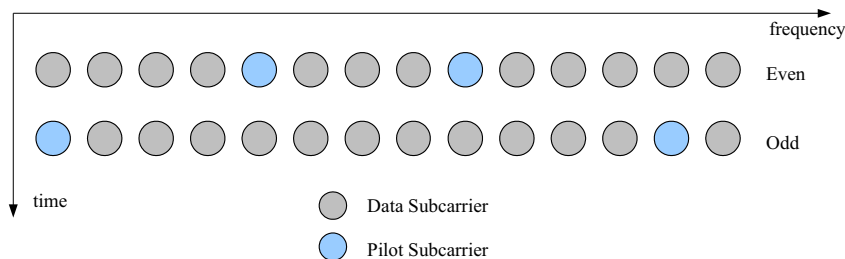


Figure 2.9: Scheme of a cluster.

In both the RL and FL cases the subchannel is composed by 48 data subcarriers. The

clusters and tiles of the subchannels are interleaved in the frame in order to provide a better frequency-time diversity to the system. Figure 2.10 illustrate a scheme of a FL subframe based on the cluster concept. According with the WiMAX framing, two lateral guard bands are left unused. The central "used" subcarriers are organized in groups called clusters. Two clusters non adjacent constitute one subchannel (or slot), which is the minimum quantity allocable to the user.

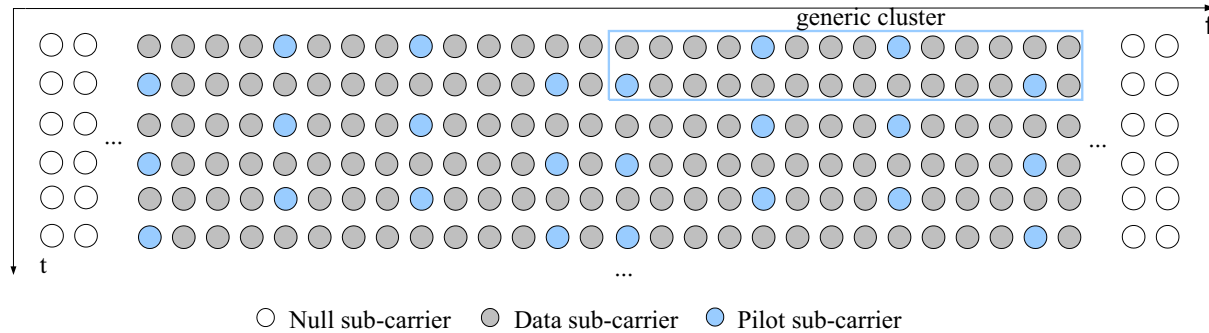


Figure 2.10: Scheme of the FL subframe based on the clusters.

Contiguous (or Adjacent) Permutation Mode: AMC. The adaptive modulation and coding (AMC) mode is based on the contiguous permutation scheme. Although respect the distributed modes frequency diversity is lost, band AMC allows system designers to exploit multiuser diversity, allocating subchannels to users based on their frequency response. Multiuser diversity can provide significant gains in overall system capacity, if the system strives to provide each user with a subchannel that maximizes its received SINR. In general, contiguous subchannels are more suited for fixed and low-mobility applications. The subchannels are made of adjacent subcarriers with the use of entities called *bins*. The bin, as shown in Figure 2.11, is a set of 9 adjacent subcarriers where the

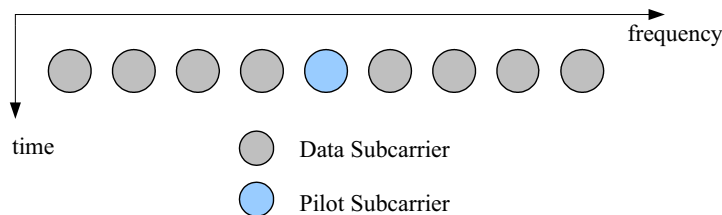


Figure 2.11: Scheme of a bin.

central one is a pilot tone. Six bins constitute a *slot* and can have four different types, as illustrated in Figure 2.12. The type of slot is determined by the configuration of the bins over the frame, and in particular, the number of OFDM symbols the slot spans over. Hence, the type 1 has six adjacent bins (in time direction) and is contained within one OFDM symbol. The type 2 spans over two symbols, while the types 3 and 4 over three and four, respectively.

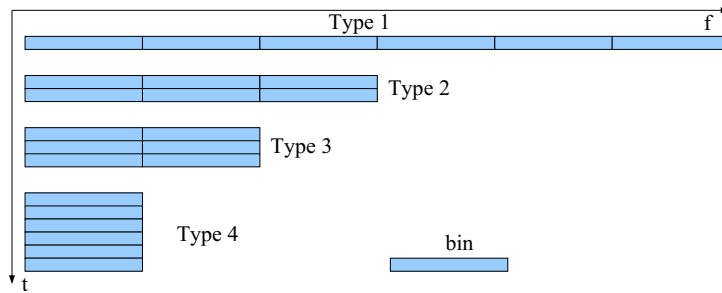


Figure 2.12: Scheme of the slot for the AMC mode. The type of slot is determined by the number of OFDM symbols the slot spans over.

2.2.1 Performance

We provide a performance evaluation of the OFDMA profile in the context of the airport environment. We selected some profile parameters and we analyzed the system performance by simulations. The next subsections provide respectively the system parameters used for the analysis and the simulation results.

Simulation Parameters

The parameters chosen for the simulations consist of a bandwidth of 5 MHz with subcarrier spacing of 10.94 KHz, a basic coding scheme with a rate 1/2 convolutional code and a QPSK subcarrier modulation. The cyclic prefix has been set 1/8 of the symbol length, therefore, the total OFDM symbol time T_{OFDM} is approximatively 57.6 μs . Frames of 26 (or 18 in the RL case) OFDMA symbols have been considered. We considered packet length of 1 and 15 slots. At the receiver side, we implemented linear pilot interpolation algorithms operating in the frequency domain and tailored to the FL and RL frame structures (see Appendix A.2). Table 2.2 summarizes the main system parameters used in the simulations. We used the channel model described in Section 1.2.

Table 2.2: Main Simulation Parameters

Parameters	Values
Multiple access	OFDMA
Bandwidth	5 MHz
FFT	512
CP	1/8 T_S
Δ_f	10.94 KHz
Modulation	QPSK
Coding, rate	Convolutional, 1/2
OFDM symbols per frame	26 (FL case), 18 (RL case)
Number of slots	1, 15
Channel scenario	Parking, apron, taxi, and runway
Channel Estimation	Ideal, linear pilot interpolation (frequency domain)

Simulation Results

The simulation results are showed in terms of BER versus E_b/N_0 . In the computation of E_b , we accounted also the power used for transmitting the CP and the pilot boosting, hence, having $CP = 1/8T_S$ and $P_B = 2.5$ dB, in the FL case, we obtain a loss of almost 0.51+1.05 dB (0.51+2.76 dB in the RL case, the loss is larger because of the bigger number of pilot tones) over the E_b of a basic OFDM system. We evaluated the performance of the system in all the airport scenarios for both FL and RL cases. The Figures 2.13 and 2.14 show the results obtained in the parking scenario for FL and RL, respectively. This scenario is characterized by slow fading and NLOS conditions for most of the time, hence, the performance of the system is particularly stressed. The actual (linear) channel estimation case (LI), indicated with a dashed line, introduces a performance degradation of roughly 1 dB with respect to the case with ideal channel estimation (ID). The curves representing the cases with Rice factor equal to $K = 0$ dB and $K = -10$ dB provide similar results especially in the RL case. The results obtained for the apron scenario

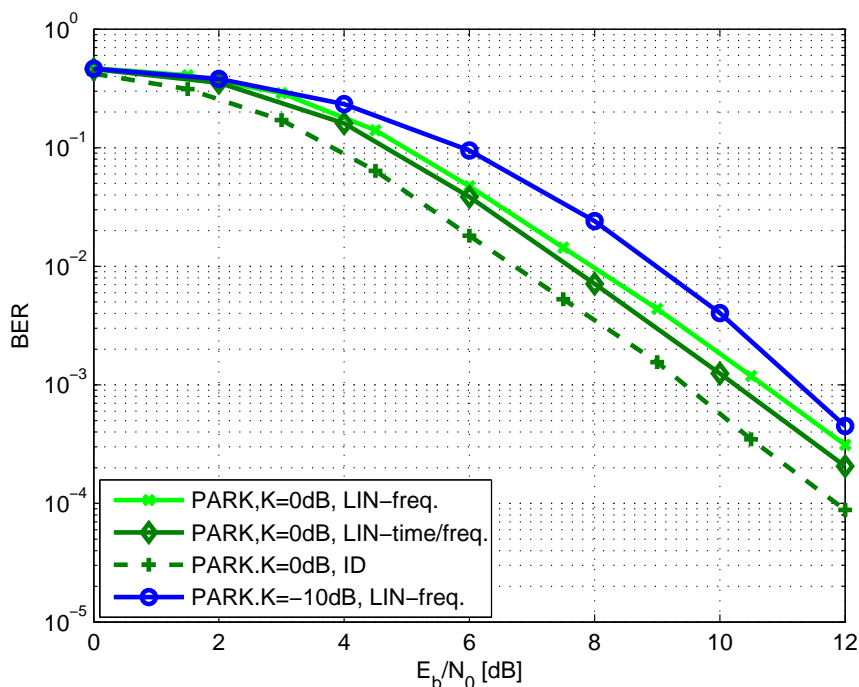


Figure 2.13: Performance of AeroMACS in the parking scenario for the FL case. Packet length of 15 slot.

are illustrated in Figures 2.15 and 2.16. Here, with respect to the parking case, there is also a LOS component. Hence, we considered also a case with $K = 10$ dB, which provides definitely better performance. Figure 2.17 and 2.18 provide the performance of the system in the taxi scenario. Here, with respect to the previous cases, there is more mobility and typically LOS conditions, which reflect on the relatively good performance for $K = 10$ dB and $K = 20$ dB. Here, the linear interpolation case introduces a penalty of 0.7 dB with

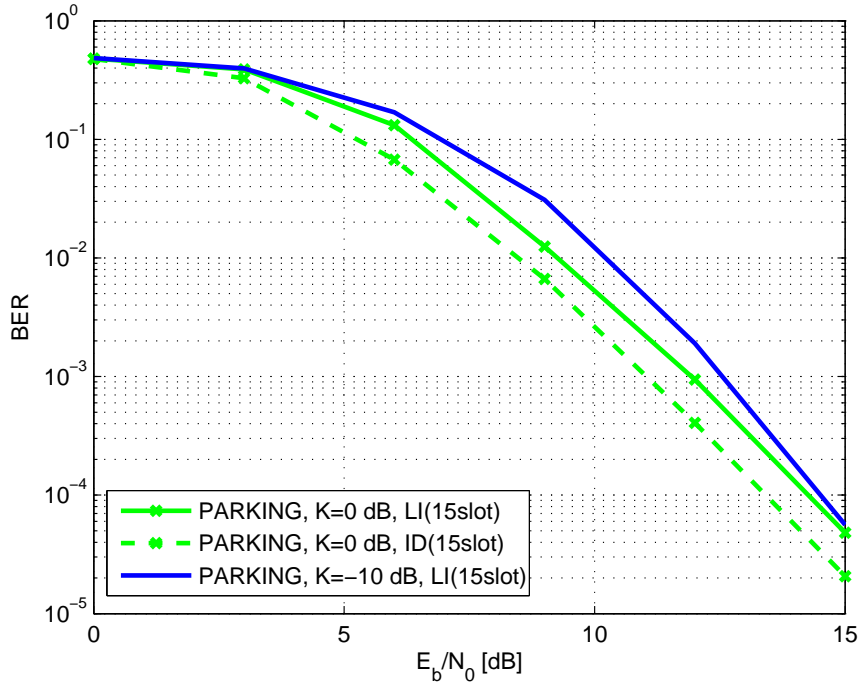


Figure 2.14: Performance of AeroMACS in the parking scenario for the RL case. Linear pilot interpolation in frequency domain using the time and frequency direction.

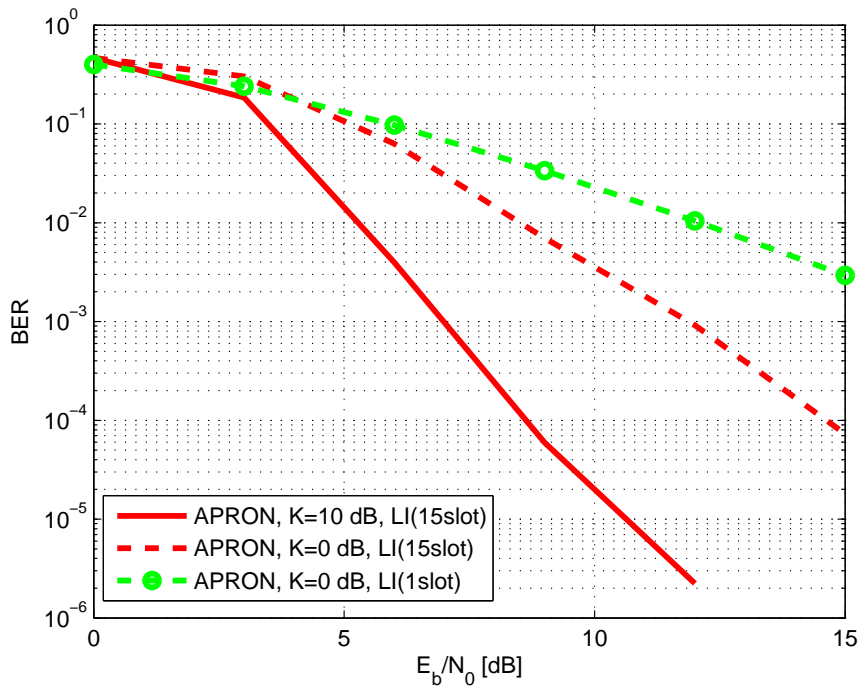


Figure 2.15: Performance of AeroMACS in the apron scenario for the FL case. Linear pilot interpolation in the frequency domain.

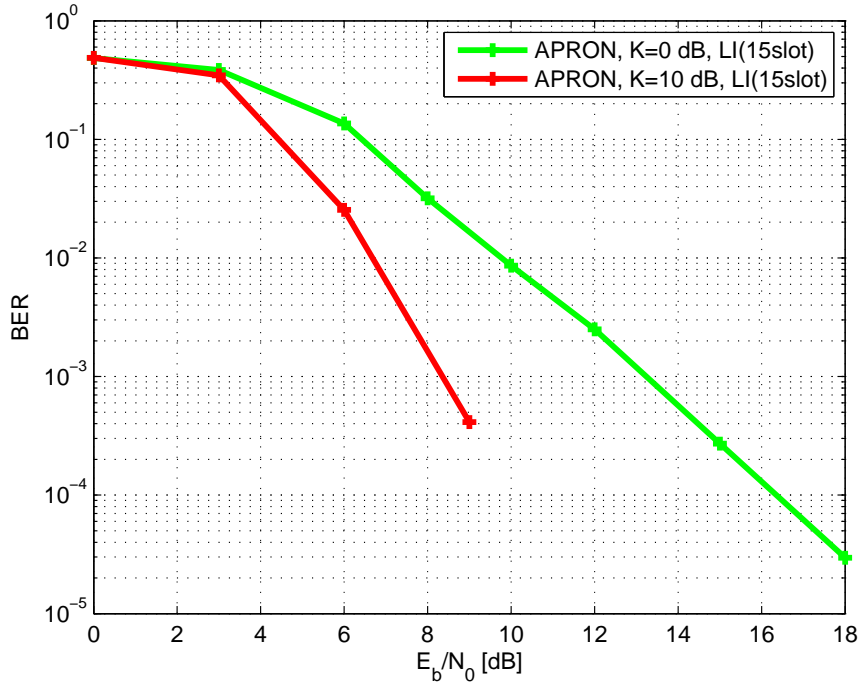


Figure 2.16: Performance of AeroMACS in the apron scenario for the RL case. Linear pilot interpolation in the frequency domain using the time and frequency direction.

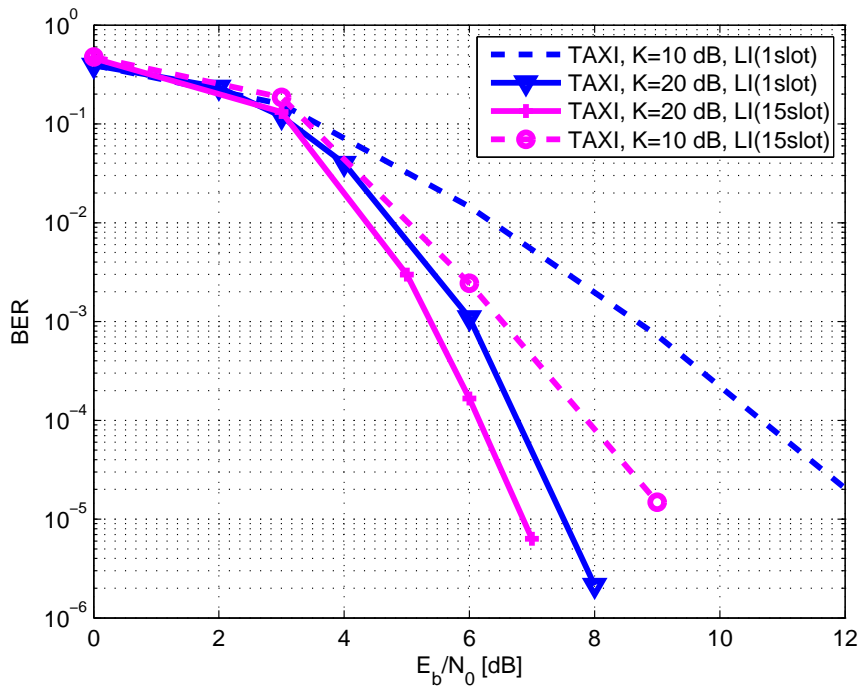


Figure 2.17: Performance of AeroMACS in the taxi scenario for the FL case. Linear pilot interpolation in the frequency domain.

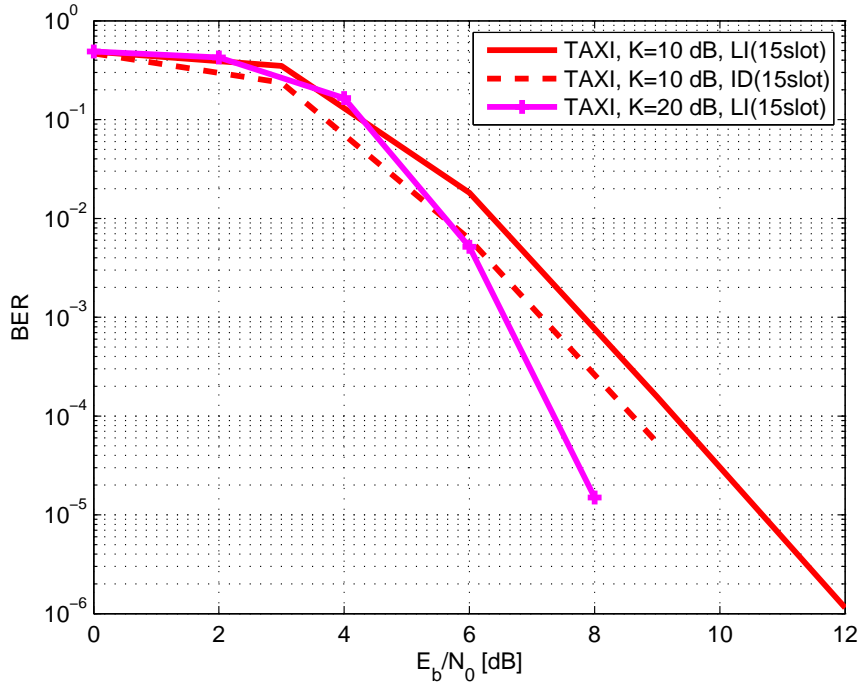


Figure 2.18: Performance of AeroMACS in the taxi scenario for the RL case. Linear pilot interpolation in the frequency domain using the time and frequency direction.

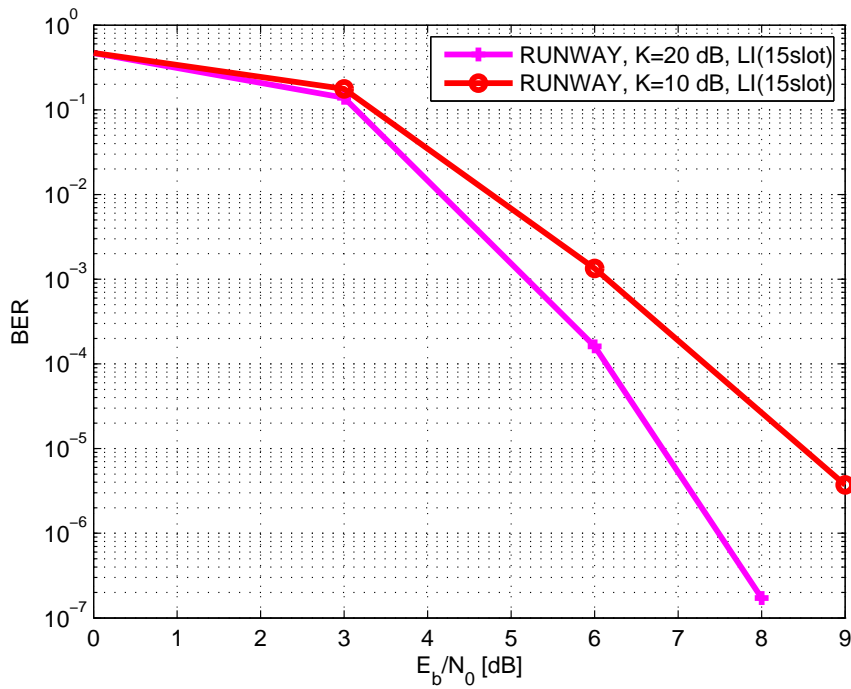


Figure 2.19: Performance of AeroMACS in the runway scenario for the FL case. Linear pilot interpolation in frequency domain.

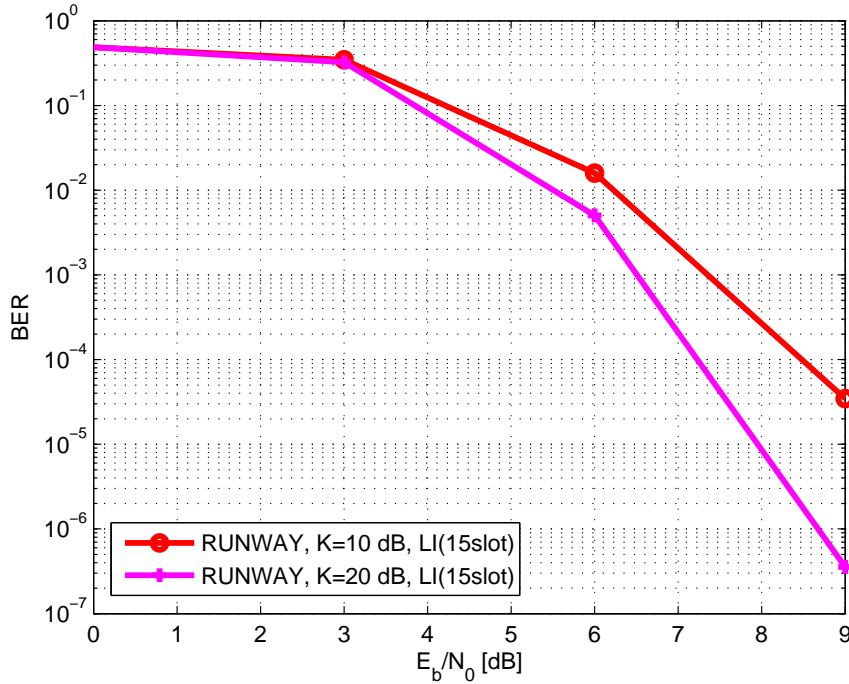


Figure 2.20: Performance of AeroMACS in the runway scenario for the RL case. Linear pilot interpolation in frequency domain using time and frequency direction.

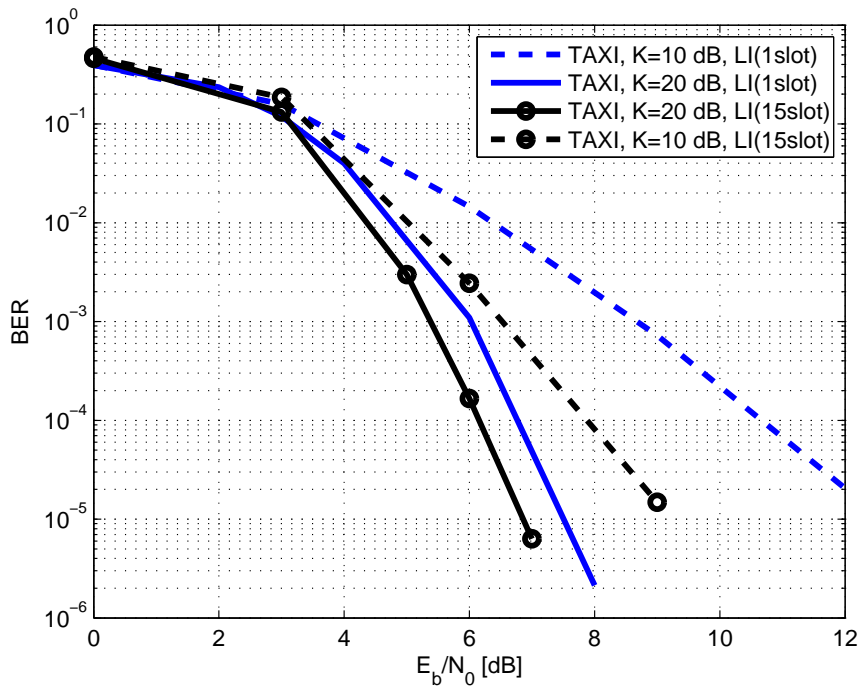


Figure 2.21: Performance of AeroMACS in the taxi scenario for the FL case. Linear pilot interpolation in frequency domain. The packet size is 15 and 1 slot.

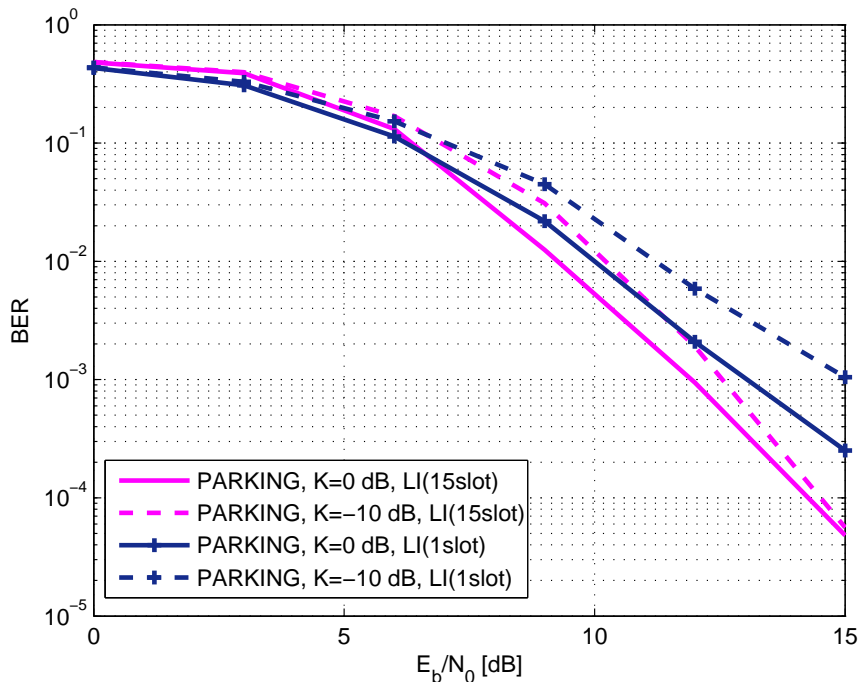


Figure 2.22: Performance of AeroMACS in the parking scenario for the RL case. Linear pilot interpolation in frequency domain. The packet size is 15 and 1 slot. The last value corresponds to the minimum length

respect to the case with perfect channel knowledge. The runway scenario presents the highest mobility and LOS conditions. The simulation results are provided in Figures 2.18 and 2.17 and show promising performance. The simulation results have been obtained considering a general packet length of 15 slot, corresponding to almost 740 bits. Besides those results, we evaluated also the case with a minimum packet length equivalent to one slot only (Figure 2.21 and 2.22). This represents a worst case, since the small number of subcarriers allocated does not allow a very efficient exploitation of frequency diversity.

2.3 Remarks on the AeroMACS System

The OFDMA profile provides generally better performance with respect to the OFDM one. Moreover, it provides more features and flexibility in terms of bandwidth (BW), FFT size, coding schemes and multiple access. Hence, it represents a better solution for the future surface airport communications system. Currently, the AeroMACS standard is still under development. However, the OFDMA-PHY profile of the standard IEEE 802.16-2009 [3] has been selected as baseline. In particular, the profile with 5 MHz BW has been taken as reference. Its waveform includes 512 subcarriers, TDD and different modulations and coding schemes (as illustrated in Table 2.3). The frame is 5 ms and is divided in FL and RL subframes, which are based on the PUSC permutation mode. The

CP is set to $1/8 \cdot T_s$. Table 2.3 summarizes the main system parameters of the AeroMACS system.

Table 2.3: Main parameters of the AeroMACS system

Parameters of the AeroMACS system	Values
Multiple access	OFDMA
BW	5 MHz
FFT size	512
Frame time T_f	5 ms
Subcarrier spacing Δ_f	10.94 KHz
Symbol time T_s	91.41 μs
CP	$\frac{1}{8}T_s$
Overall symbol time T	102.83 μs
Duplexing	time-division multiplexing (TDM)
Null guard band (FL / RL)	91 / 103
Used subcarriers per OFDM symbol (FL/RL) (FFT size - null guard - DC)	420/ 408
Coding	Convolutional coding, Turbo codes
Modulations	QPSK, 16-QAM, 64-QAM

Generally, AeroMACS provides relatively good results in the airport environment. However, in some cases, especially in NLOS conditions as in the parking scenario, a performance degradation appears and improvements are necessary to satisfy the stringent requirement of high reliability, robustness and coverage.

2.4 Summary

In this chapter, we analyzed the performance of two different WiMAX profiles in the context of the airport environment and we selected the best candidate for becoming the baseline of AeroMACS. The OFDMA based waveform provides better results and is more flexible with different possible bandwidths, number of subcarriers, modulations and coding schemes. Generally, AeroMACS provides good results in the airport scenarios. However, in some critical cases, improvements may be accounted. The ubiquitous coverage, the high reliability and robustness make the research of techniques able to improve the system performance (in the above mentioned critical scenarios) crucial.

In the next chapters, we investigate possible solutions for enhancing the performance of AeroMACS. Since the most critical results are obtained in correspondence of the parking channel scenario (and marginally for the apron), in the following, we focus only on this case. This scenario is characterized by NLOS conditions and no (or limited) mobility, with resulting slow channel (especially in time direction). In this context, we address the limited diversity of system. We analyze potential ways for increasing the diversity of the system and hence improving the performance of AeroMACS.

Chapter 3

Multiple Antennas

In modern mobile wireless communication systems the use of diversity techniques is fundamental to reach the high quality of service required. The time diversity exploitation requires interleaving and coding over several channel coherence times. In some cases however, this is not feasible due to eventual strict delay constraints (this is especially true in presence of large channel coherence times). Similarly, frequency diversity is not always achievable, especially on channels with nearly flat fading response. Hence, other forms of diversity have to be obtained. Antenna diversity can be an alternative solution. The addition of one or more antennas may create independent multiple channels and introduce space diversity without reducing the spectral efficiency.

This chapter is dedicated to the study of the applicability of MIMO techniques to the airport context. An overview of simple multiple antennas techniques is provided. Then, focusing on the AeroMACS case, an analysis of the possible solutions for the airport domain is carried out. Performance results obtained by simulations are illustrated. Furthermore, a space time coding (STC) implementation for AeroMACS is introduced, which differs from the WiMAX one and allows reusing the (conventional) AeroMACS framing. Performance results and a comparison with the standard implementation are also included.

3.1 Fundamentals of Multiple Antenna Techniques

The MIMO techniques represent a straightforward and effective solution for increasing the diversity of a system and improving its performance. It is possible to distinguish between three types of systems characterized by the allocation of the multiple antennas on the transmitter/receiver sites, as depicted in Figure 3.1. The first scheme of the figure represents a multiple receiving antennas system. This configuration, also called SIMO, represents an ideal solution for improving the performance of systems with problems of complexity at the transmitter but not at the receiver. The cellular mobile system for example doesn't allow to arbitrarily increase the number of antennas on the mobile terminal, while the base station may support the increase of the number of antennas

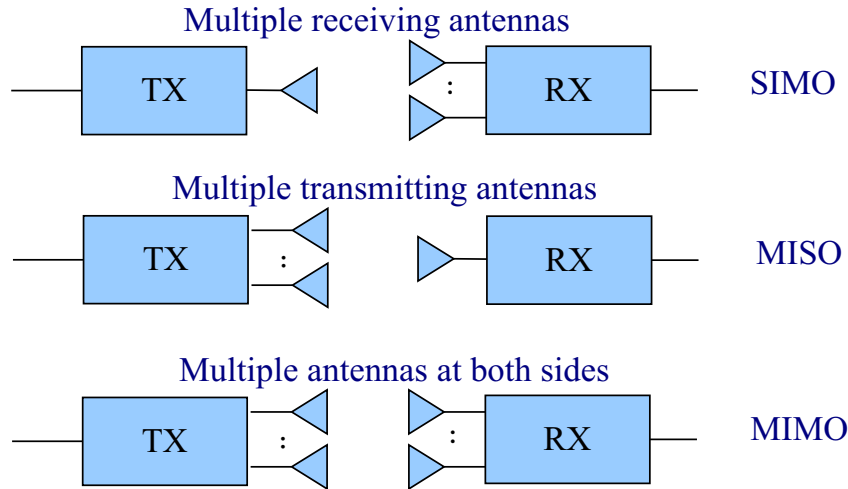


Figure 3.1: Generic multiple input multiple output system schemes.

without major problems. SIMO is therefore an optimum solution for the RL case. The second scheme of Figure 3.1 illustrates a multiple transmit antennas system, also called multiple input single output (MISO). It is the dual scheme of SIMO system with multiple antennas only at the transmitter side and represents a good solution for systems that necessitate keeping the receiver simple. The last scheme of Figure 3.1 depicts the general case with multiple antennas at both sides and we refer to this case as a MIMO antenna system. MIMO systems constitute the most complex and powerful antenna diversity scheme and can be used to increase the system reliability, the system capacity, the coverage area, etc... However, these results have to be achieved with a certain tradeoff. For example the highest capacity systems will not benefit of the strongest reliability or highest power reduction. Hence, the design of the system can be driven to reach, with the multiple antennas, the most appropriate compromise. Within the advantages introduced by MIMO the following points represent very attractive outcomes:

- Array gain (coherent sum of signals);
- Diversity gain (to counteract fading);
- Co-channel interference reduction;
- Spatial multiplexing (to achieve high spectral efficiency).

The array gain is one of the easiest forms of gain achievable by the MIMO systems. It is typical of systems with multiple receiving antennas since it comes from the coherent sum of received signals. The array gain G_A , is linearly proportional to the number of antennas (G_A [dB] = $10\log_{10}N_R$) and can be obtained also in case of statistically correlated channels. Diversity gain results from the multiple independent channels between the transmitter and the receiver. By averaging over different independent signal paths,

the probability that the overall gain is small decreases. Being a result of the statistical independence of those channels, the diversity gain disappears if the channels are correlated. The diversity gain may be obtained by all the types of configuration: SIMO, MISO and MIMO. Differently from the array gain, the diversity gain saturates with the increasing number of antennas [43].

The diversity gain can be obtained by a properly spacing of the antennas. The required distance between antennas depends on the local scattering and on the carrier frequency. For a mobile on the ground with many scatterers, a distance S between one wave length and a quarter of it may be sufficient ($S > \lambda/4$). For high towers the required distance is much bigger, up to several wavelengths. Other efficient ways of obtaining independent replicas of the signals are polarization and angle direction. These techniques produce different types of diversity and provide respectively polarization and direction (or angle) diversity. Several systems operating in congested bands suffer from co-channel interference. Multiple antennas in these cases can be used for reducing the interferences of undesired signals over the same bandwidth [44–48]. Last, but very important, MIMO may be used for achieving a high spectral efficiency system. The different "subchannels" created by the multiple antennas may be used for transmitting different data streams in parallel and creating a spatial multiplexing. Spatial multiplexing exploits the multipath richness of the environment and increases the capacity of the system. Differently from the other gains introduced by multiple antennas, spatial multiplexing can be only obtained with true MIMO systems (i.e. with multiple antennas at both sides) [49, 50].

In the following subsections the main characteristics of MIMO systems are described, focusing on the simpler cases of transmit diversity and receive diversity, since in the aeronautical context the incremental of the number of antennas on the aircraft is considered very critical. Detailed descriptions of the 1×2 SIMO and 2×1 MISO systems is also provided. For simplicity, in the equations we omitted the frequency and the time indexes.

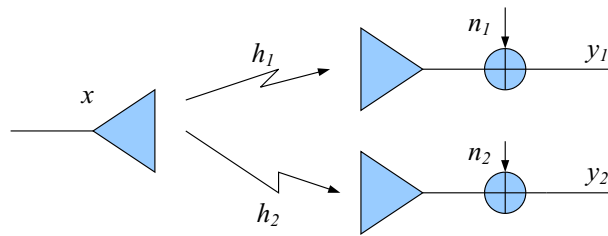
3.1.1 Receive Diversity - SIMO

One of the simplest ways to obtain antenna diversity is the addition of one or more antennas only at the receiver side of the system. This SIMO scheme permits to increase the SNR of the system combining the received versions of the signal. The simplest receive diversity case 1×2 SIMO with one antenna at the transmitter side and two at the receiver side is represented in Figure 3.2.

It is possible to characterize the system using a vector form summarizing the two received signals

$$\begin{cases} y_1 = x \cdot h_1 + n_1 \\ y_2 = x \cdot h_2 + n_2 \end{cases} \quad (3.1)$$

as $\mathbf{y} = x \cdot \mathbf{h} + \mathbf{n}$, where the vectors \mathbf{h} and \mathbf{n} represent respectively the channel gains and the noise contributions. As previously mentioned, in the multiple receiving antenna case, besides the diversity gain, there is an array (or power) gain. Being not related

Figure 3.2: 1×2 SIMO scheme.

to the statistical properties of the channels, it increases the system's SNR also in case of correlated channels as in LOS conditions. The array gain is linearly proportional to the number of antennas ($\text{SNR} \times N_r$) and doesn't have saturation. For example in the case of two antennas it introduces a 3 dB gain and for every doubling of antennas adds other 3 dB gain. The most common ways to combine the received signals are selection combining (SC) and MRC.

Selection Combining. SC represents the simplest algorithm for exploiting the antenna diversity. It instantly analyzes the received power over all the branches corresponding to the different antennas and then selects the one with highest power. Figure 3.3 depicts a scheme of SC, while Figure 3.4 shows an example of the SNR obtained from the combination of the SNRs offered by the two different links. The potentially-useful energy of the branches non-selected is lost; thus, the SC algorithm is not optimum. However, the simple implementation of this algorithm constitutes its main strength point.

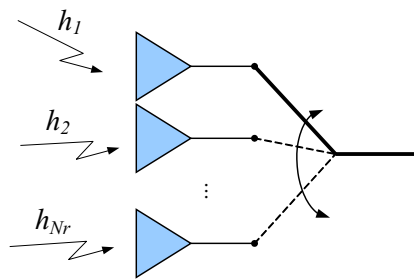


Figure 3.3: Selection combining scheme.

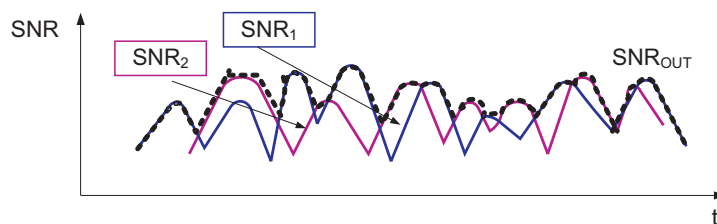


Figure 3.4: Resulting SNR with selection combining.

Weight and Combine. Weight and combine algorithms exploit better the overall received energy with respect to SC, by weighting and then adding all the signals corresponding to all the branches of the system receiver

$$y = \sum_{i=1}^{N_r} y_i \cdot w_i^*. \quad (3.2)$$

Maximal Ratio Combining. MRC is a weight and combine algorithm with the weights chosen proportional to the channel ($w_i = h_i$). A generic 1×2 SIMO system receiver with MRC is represented in Figure 3.5. The received signals y_1 and y_2 are multiplied by the conjugate values of the corresponding channel coefficients. It is therefore necessary to have at the receiver full channel information (amplitude and phase). The multiplication of the signals by h_1^* and h_2^* compensates the phase rotation introduced by the channel and the signals are coherently added. The SNR of the combined signal can be obtained

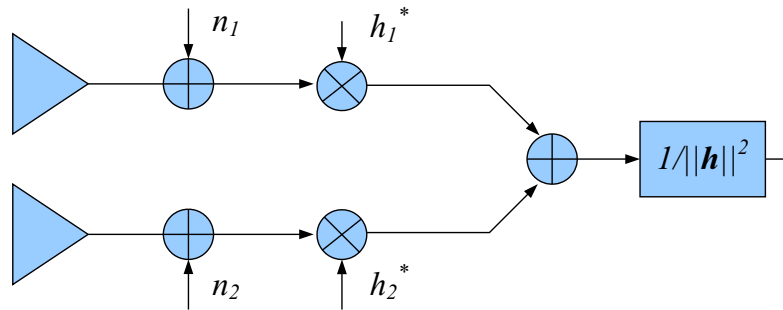


Figure 3.5: 1×2 SIMO with MRC receiver scheme.

considering the two SNRs corresponding to the two branches, SNR_1 and SNR_2 , where σ^2 is the complex noise variance,

$$SNR_1 = \frac{E\{(xh_1)(xh_1)^*\}}{\sigma^2} = E\{|x|^2\} \cdot \frac{|h_1|^2}{\sigma^2} \quad (3.3)$$

$$SNR_2 = E\{|x|^2\} \cdot \frac{|h_2|^2}{\sigma^2}. \quad (3.4)$$

The transmitted signal can be estimated by

$$\hat{x} = \frac{\mathbf{h}^H \mathbf{y}}{\|\mathbf{h}\|^2} = \mathbf{w}^H \mathbf{y}. \quad (3.5)$$

The received signal is the sum of the transmitted signal and a noise contribution distributed as a Gaussian random variable with zero mean. Hence, we can obtain the total SNR of the system from the previous equations. More specifically, we have

$$\hat{x} = x + n, \quad (3.6)$$

where $n \sim \mathcal{N}\left(0, \frac{\sigma^2}{\|\mathbf{h}\|^2}\right)$, thus,

$$SNR_{OUT} = \frac{E\{|x|^2\}}{\frac{\sigma^2}{\|\mathbf{h}\|^2}} = \frac{E\{|x|^2\}}{\sigma^2} \|\mathbf{h}\|^2. \quad (3.7)$$

The total SNR is the sum of the two SNRs corresponding to the single paths. MRC provides both array and diversity gain. In presence of correlated channel (i.e. in LOS cases) there is only the array gain that in this example amounts to 3 dB. It is possible to show that the total SNR is the maximum possible SNR; therefore this algorithm is called maximal ratio combining. Though, it should be noted that MRC may not be optimal in some cases, since it completely ignores the interference powers. In these cases other receivers may perform better. For a cellular system with interference limits, like WiMAX or AeroMACS, MRC might be strongly preferred to SC, despite its higher complexity. Although MRC and SC present similar results, since they lead indeed to the same diversity order, MRC introduces an array gain which can be very useful in some power-limited situations or LOS cases. Moreover, in frequency-selective fading channels, MRC can exploit all the frequency diversity, while a selection algorithm would simply select the best average received signal keeping potentially deep fades at certain frequencies.

SIMO with Interference

In the previous cases SIMO has been analyzed in condition of no interference. In this case a more realistic situation is considered and an interference signal x_I is added to the SIMO system as represented in Figure 3.6.

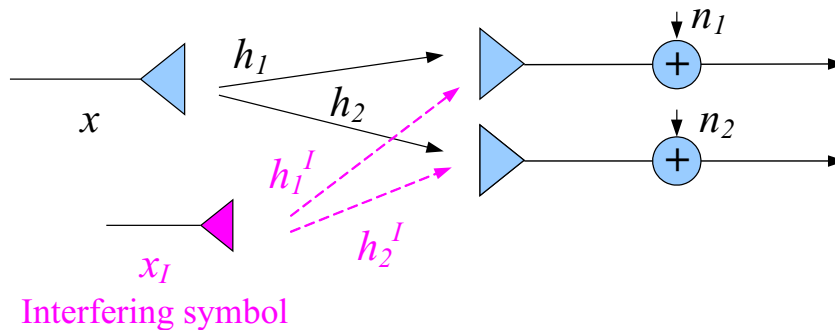


Figure 3.6: scheme of SIMO 2×1 system with interference.

The received signal \mathbf{y} is given by

$$\mathbf{y} = \mathbf{h} \cdot x + \mathbf{h}_I \cdot x_I + \mathbf{n} = \mathbf{h}x + \tilde{\mathbf{n}}. \quad (3.8)$$

We consider the case where x_I is modeled as a random variable with zero mean. The overall noise $\tilde{\mathbf{n}} = x_I \mathbf{h}_I + \mathbf{n}$ is not "white" as in the previous case and has an auto-covariance matrix equal to $R = E[|x_I|^2] \mathbf{h}_I \cdot \mathbf{h}_I^H + \sigma^2 \cdot \mathbf{I}$. In order to maximize the signal-to-interference

noise ratio (SINR) the received signal is multiplied by $\mathbf{R}^{-1/2}$, and then the MRC principle is applied. The resulting scheme is equivalent to the minimum mean square error (MMSE) receiver and is called optimum combining (OC) receiver.

3.1.2 Transmit Diversity - MISO

The multiple transmit antennas system presents multiple antennas only at the transmitter side. The MISO configuration can be particularly useful in the FL of the system where the addition of antennas is feasible on the control tower. Transmit diversity schemes offer two ways of implementation respectively based on open loop and close loop realizations. Here, close and open loop indicate the presence of a return link with channel state information (CSI) or not. The close loop scheme offers the advantage of the coherent sum of the different signals and hence an array gain, though the CSI at the transmitter side is often difficult to obtain, especially in presence of rather fast channels. The open loop scheme STC has been introduced [51] and offers a good alternative for all the systems that cannot have CSI at the transmitter side.

MISO Beamforming (Closed Loop)

The MISO closed loop system is based on the instantaneous transmission of weighted versions of the signal. The weights are proportional to the channel and therefore channel state information is required. Figure 3.7 illustrates a simple scheme of a 2×1 MISO system.

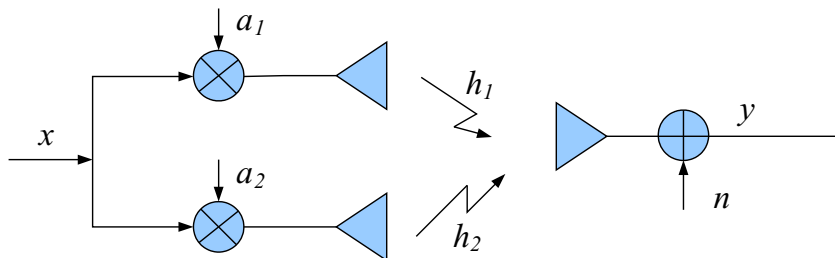


Figure 3.7: 2×1 MISO beamforming scheme.

Here, α_1 and α_2 are the weighting factors and are chosen accordingly to satisfy $|\alpha_1|^2 + |\alpha_2|^2 = 1$ in order to keep an average transmitted power $P_t = E[|x|^2] = 1$. The received signal y is given by

$$y = (\alpha_1 h_1 + \alpha_2 h_2)x + n. \quad (3.9)$$

Taking $\alpha_1 = k \cdot h_1^*$, $\alpha_2 = k \cdot h_2^*$, with $k = 1/\|h\|$ we obtain

$$y = \frac{|h_1|^2 + |h_2|^2}{\|h\|} x + n = \|h\| x + n, \quad (3.10)$$

and

$$SNR_{OUT} = \frac{E\{|x|^2\}}{\sigma^2} \|h\|^2.$$

This is exactly the same result obtained for the SIMO 1×2 MRC case. Though, in this case the transmitter must know phase and amplitude of both the channels (CSI at TX). Since the transmission vector depends on the propagation vector, this method is called beamforming.

Extensions Towards MIMO: MIMO Beamforming (Eigenbeamforming)

The MISO 2×1 beamforming case can be generalized obtaining the beamforming MIMO case depicted in Figure 3.8.

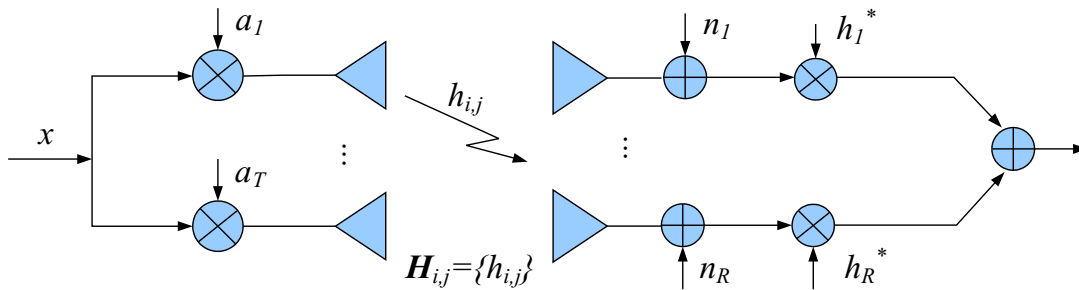


Figure 3.8: MIMO beamforming scheme.

The system with N_t transmit antennas and N_r receive antennas is described by

$$\mathbf{y} = \mathbf{x}\mathbf{H}\boldsymbol{\alpha} + \mathbf{n} \quad (3.11)$$

or

$$\mathbf{y} = \begin{bmatrix} y_1 \\ y_2 \end{bmatrix} = \mathbf{x} \cdot \mathbf{H} \cdot \boldsymbol{\alpha} = \begin{bmatrix} x_1 \\ x_2 \end{bmatrix} \cdot \begin{bmatrix} h_{11} & h_{12} \\ h_{21} & h_{22} \end{bmatrix} \cdot \begin{bmatrix} \alpha_1 \\ \alpha_2 \end{bmatrix} + \begin{bmatrix} n_1 \\ n_2 \end{bmatrix}. \quad (3.12)$$

The equation above can be rewritten as

$$\mathbf{y} = \mathbf{x} \cdot \tilde{\mathbf{h}} + \mathbf{n}, \quad (3.13)$$

where $\tilde{\mathbf{h}} = \mathbf{H}\boldsymbol{\alpha}$ and $\boldsymbol{\alpha}$ represents the transmit weighting factor vector. Imposing $\|\boldsymbol{\alpha}\| = 1$ then $E\{|x|^2\} = P_t$, if we indicate the receive weighting factors with $\mathbf{w} = k \cdot \tilde{\mathbf{h}}$, the SNR becomes

$$SNR(\boldsymbol{\alpha}) = \frac{P_t}{\sigma^2} \|\mathbf{x}\|^2 \tilde{\mathbf{h}}. \quad (3.14)$$

The $\boldsymbol{\alpha}$ that maximizes SNR is equal to the eigenvector of $\mathbf{H}^H\mathbf{H}$ corresponding to the largest eigenvalue λ_{MAX} of $\mathbf{H}^H\mathbf{H}$. The resulting SNR is given by

$$SNR_{OUT} = \frac{E\{\|\mathbf{x}\|^2\}}{\sigma^2} \lambda_{MAX}. \quad (3.15)$$

Having CSI at receiver and transmitter sides, the MIMO beamforming case provides the maximum SNR.

Space-Time Coding (Open-Loop)

The STC scheme introduced by Alamouti in [51] offers a solution for all the systems where it is impossible to have reliable CSI at the transmitter side. This open loop system transmits at the same time over the different antennas combinations of the signals to transmit and it provides the same diversity gain offered by the classical maximal-ratio receive combining scheme or the beamforming with an equal number of branches. The unique requirement of the system concerns the coherence time of the channel. It is necessary to have a sufficiently slow channel, in order to allow the decoding of the signal transmitted over two (or more) antennas and consecutive time instances. In the case 2×1 , the two transmitting antennas at a certain symbol period t_1 transmit two different signals x_1 and x_2 , respectively. In the following symbol period t_2 the first antenna transmits x_2^* , while the second one $-x_1^*$, as indicated in Figure 3.9.

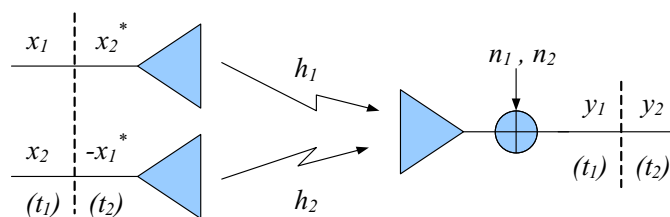


Figure 3.9: 2×1 STC Alamouti's scheme.

Assuming the channel constant over the transmission of the two symbols x_1 and x_2 ($h_1(t_1) \approx h_1(t_2) = h_1$ and $h_2(t_1) \approx h_2(t_2) = h_2$), the received signals $y_1 = y(t_1)$ and $y_2 = y(t_2)$ become

$$\begin{cases} y_1 = x_1 \cdot h_1 + x_2 \cdot h_2 + n_1 \\ y_2 = x_2^* \cdot h_1 - x_1^* \cdot h_2 + n_2 \end{cases}, \quad (3.16)$$

or, conjugating the second equation,

$$\begin{bmatrix} y_1 \\ y_2^* \end{bmatrix} = \begin{bmatrix} h_1 & -h_2 \\ -h_2^* & h_1^* \end{bmatrix} \begin{bmatrix} x_1 \\ x_2^* \end{bmatrix} + \begin{bmatrix} n_1 \\ n_2^* \end{bmatrix}. \quad (3.17)$$

The vectorial form $\mathbf{y} = \mathbf{H}\mathbf{x} + \mathbf{n}$ can be easily decomposed to obtain the transmitted signal. Being $\mathbf{H}^H\mathbf{H} = \|\mathbf{h}\|^2\mathbf{I}$, with \mathbf{I} identity matrix, we obtain $\mathbf{H}^H\mathbf{y} = \|\mathbf{h}\|^2\mathbf{x} + \mathbf{n}$, or

$$\begin{cases} \hat{x}_1 = y_1 \cdot h_1^* - y_2^* \cdot h_2 \\ \hat{x}_2 = y_1 \cdot h_2^* + y_2^* \cdot h_1 \end{cases}. \quad (3.18)$$

Focusing on the symbol x_1 , it is easy to demonstrate that the resulting SNR is the same as the one obtained for MRC.

The diversity gain is 2 for the detection of each symbol, as in a 1×2 SIMO system. However, in this case the total transmitted power is twice as that transmitted by the

1×2 MRC, so there is a loss of 3 dB (corresponding to the price paid for not having a coherent sum). There isn't in fact array gain without CSI at the transmitter. The Alamouti scheme is perfectly suitable for OFDM systems. In this case, besides the coding in time direction (STC or space time block coding (STBC)), it is possible to perform a frequency direction coding called space-frequency coding (SFC) or space frequency block coding (SFBC).

Extension Towards MIMO: MIMO STC

The MIMO 2×2 case is a generalization of the 2×1 case. In this case the total number of antennas is 4: 2 transmit and 2 receive. The receiver is composed by two "STC branches" combined with MRC. The 2×2 scheme reaches a diversity order 4, the double of the 2×1 STC scheme. As showed in [51] for a Rayleigh fading, this scheme provides a curve with a slope that is twice with respect to the 2×1 STC case. Moreover, exploiting a coherent sum of the signals, the 2×2 scheme provides an additional array gain. The result is also similar to the ones provided by a 1×4 SIMO MRC scheme. However, the SIMO case presents a larger array gain coming by the 4 receive antennas (2×2 has an array gain only over 2 antennas).

3.2 Multiple Antenna in AeroMACS

The exploitation of diversity techniques is fundamental for achieving the performance required to the next airport communications. The use of OFDM modulation (i.e. frequency diversity) is not sufficient to provide optimum results in NLOS slow fading environments as the parking scenario. Hence, MIMO techniques (which provides antenna diversity) represent a potential solution. Nevertheless, the aeronautical airport case imposes strictly constraints on the number of usable antennas and the increase of system complexity (especially on the aircraft), limiting the number of the possible solutions. Assuming impossible to increase the number of antennas on the aircraft, the unique possible solutions remain transmit diversity for the FL and receive diversity for the RL.

The simplest solution consists in the introduction of a second antenna on the base station. In this case, considering the lack of scatterers, the separation S between antennas should be up to tens of wavelengths. Hence, being in the C band and having $\lambda = 57.69$ mm, $S > n \cdot \lambda = n \cdot 57.69$ mm, where n is an integer depending on the airport configuration. Assuming $n = 100$, the distance between antennas should be $S > 0.58$ m, which doesn't represent a challenge on the base station. The presence of the second antenna on the base station permits to implement a 2×1 MISO scheme in the FL and a 1×2 SIMO scheme in the RL. Both these schemes exploit the diversity gain provided by the statistical richness of the channels between transmit and receive antennas; hence, they require uncorrelated channels. In very correlated channels, as well as in LOS conditions (ex. taxi or runway scenarios), the diversity gain disappears, making the use of antenna

diversity less efficient or even useless. The ideal case for the antenna diversity techniques is hence the parking scenario, characterized by slow fading and NLOS conditions. Note that this case is the one suffering from the worst performance and it requires large improvements to achieve the quality of service requirement. It is important to note that the array gain (which is related to the coherent sum of the signals and not to the channel) is present in all the scenarios.

FL - STC

For the MISO scheme of the FL, STC represents a preferred candidate with respect to beamforming. It provides diversity order two and avoids the requirement of channel state information at the receiver, which is a critical issue on variable channels. In AeroMACS the overall frames last 5 ms, and the coherence time $T_{coh} \approx 2$ ms [29], making the CSI not easy to obtain at the transmitter. However, STC doesn't benefit from the coherent sum of the signals and can improve the performance of the system only with uncorrelated channel, and hence, in NLOS conditions.

RL - MRC

SIMO with MRC represents a very good candidate for improving the performance of the reverse link of AeroMACS. This scheme maintains unchanged the transmitter side of the system; hence, doesn't require any modification to the standard or on the aircraft (which would represent the bigger issue). The only modifications concern the receiver side (i.e. the control tower), and are limited to the second antenna (or eventually more, depending on the chosen number), its relative chain (down converter (DC) plus IFFT blocks) and to the combiner. Keeping the increase of complexity at the minimum, 1×2 MRC case constitutes the simplest SIMO case. However, it provides a significant performance improvement with the introduction of a diversity gain of order 2 and an array gain. A 1×4 MRC scheme could also be an alternative for the RL. In this case the complexity would increase since other 2 antennas and relative chains would be necessary; though, also the outcoming improvement would be bigger. The array gain introduced by 1×4 SIMO with MRC is equal to 6 dB, while the diversity order is 4. Similarly to the forward link case, the best scenario for the use of SIMO is the parking scenario. In this case in fact it is possible to fully exploit the diversity gain for improving the performance of the system (which in this scenario is particularly poor).

3.2.1 Simulation Parameters

For our investigation we used the AeroMACS system described in Section 2.3 and the channel model illustrated in Section 1.2. We considered a bandwidth of 5 MHz with 512 subcarriers, QPSK modulation, and convolutional coding with rate 1/2. We focused only

on the most critical channel scenario, i.e the parking one. Table 3.1 and 3.2 provide the main parameters used for the simulations.

Table 3.1: Main simulation parameters

System parameters	Values
Multiple access	OFDMA
Bandwidth	5 MHz
FFT	512
CP	$1/8 T_S$
Δ_f	10.94 KHz
Modulation	QPSK
Coding, rate	Convolutional, 1/2
Decoder	Soft Viterbi
Channel scenario	Parking
Channel Estimation	Ideal, linear pilot interpolation in frequency domain

Table 3.2: Simulation parameters for FL and RL

Sub-frame	FL	RL
Diversity technique	MISO - STC	SIMO - MRC
Number of transmitting antennas	2	1
Number of receiving antennas	1	2
OFDM symbols per frame	24	18
Packet length in number of slots	15	15

3.2.2 Performance Evaluation

We applied simple MIMO schemes to the AeroMACS system, evaluating the performance by simulations. We decided to focus on the cases which foresee multiple antennas only on the control tower. Hence, SIMO for the RL and MISO for the FL. A MRC 1×2 receiver is chosen for the RL. For the FL, considering the requirement of precise CSI and its high difficulty in the obtaining, we adopted a STC scheme in place of a beam-forming one. Figure 3.10 shows the results obtained with a 1×2 SIMO scheme with MRC receiver. The performance of the system with the introduction of multiple antenna largely outperform the one of the system with single antenna. The slope of the curve is doubled (corresponding to the diversity order 2); moreover, there is a further gain of 3 dB, corresponding to the array gain. At $\text{BER} = 10^{-4}$ the gain is roughly 6 dB.

Figure 3.11 shows the performance of the system with the introduction of a 2×1 STC scheme (following the implementation proposed in the standard). The introduction of diversity provide a large performance improvement, doubling the slope of the BER curve. For example, at a $\text{BER} = 10^{-4}$ the gain is equivalent to 4 dB in the case with ideal channel estimation.

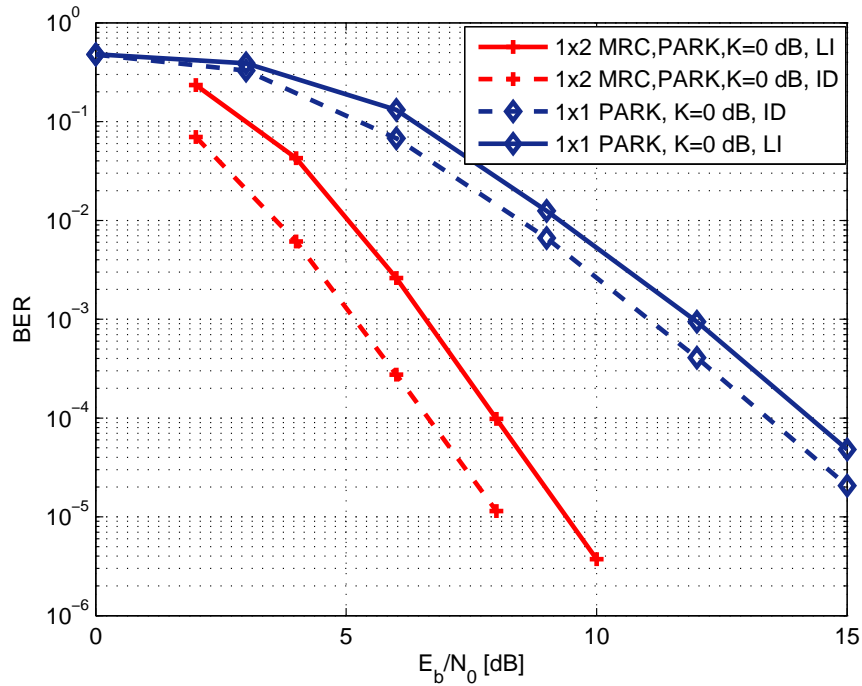


Figure 3.10: Performance of the system with the application of a 1×2 MRC scheme. Parking scenario, linear pilot interpolation in the frequency domain.

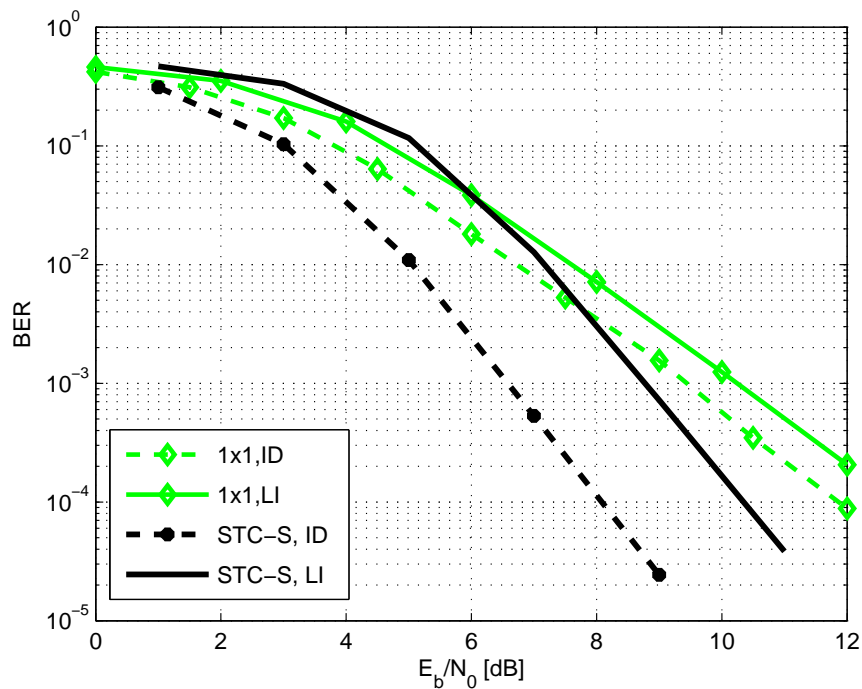


Figure 3.11: Performance of the system with the application of a 2×1 STC scheme. Parking scenario, linear pilot interpolation in the frequency domain.

3.3 A Novel Implementation of STC for AeroMACS

An OFDM system offers different possibilities for the implementation of the Alamouti scheme. The scheme may be applied in the frequency or in the time domain. In the former case the signals are combined in frequency direction, therefore the requirement on the channel is no longer on the coherence time but on the frequency selectivity. However, in all the cases, the the channel estimation constitutes a key issue for STC in OFDM systems. This is due to the fact that a combination of two different signals arrives at the receiver. Hence, a channel estimation based on the pilot tones of the standard (single antenna case) frame is then unfeasible since the pilot tones would interfere each other.

In order to apply a 2×1 diversity scheme to the WiMAX FL, the standard proposes an implementation of STC based on the modification of the FL frame trough the construction of new clusters [3]. As represented in Figure 3.12, the modified clusters have double size with respect to the normal ones (see Section 2.2 and Figure 2.9) and pilot sub-carriers in different positions. The new structure permits the STC application to consecutive OFDM symbols. Moreover, in order to solve the problem of the channel estimation the pilot symbols are shared between the two antennas, blanking the pilot tones of one antenna in correspondence of the pilot tones assigned to the other antenna.

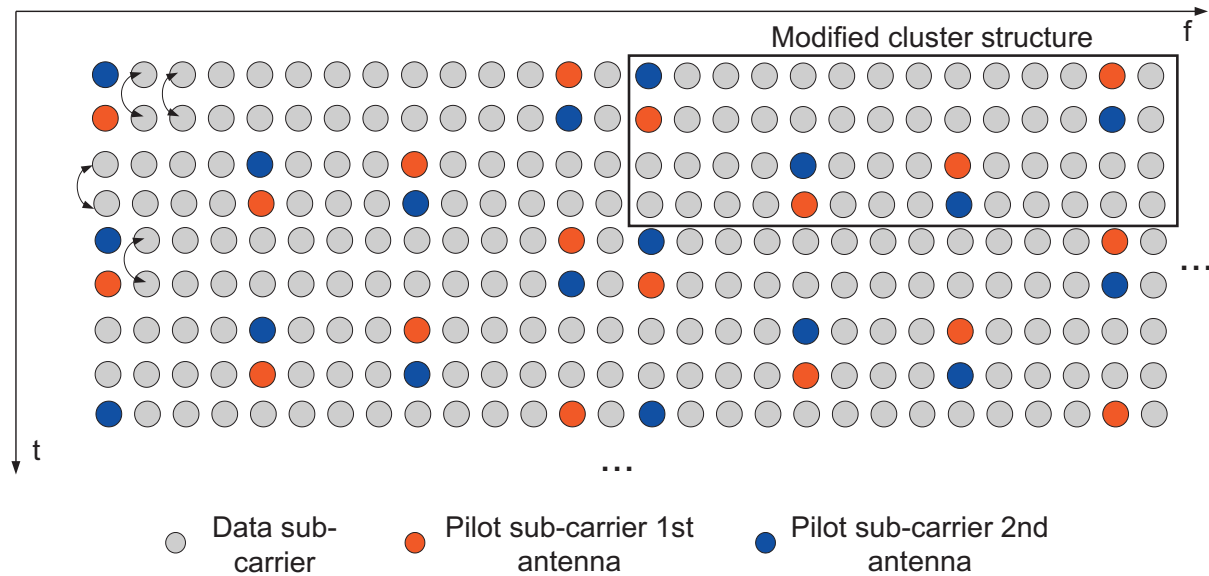


Figure 3.12: Generic WiMAX frame structure with space-time coding. The cluster structure is modified with respect to the single antenna case in order to apply STC to consecutive OFDM symbols.

We propose a different STC implementation which doesn't require the modification of the original structure of the frame and therefore also the modification of the channel estimation algorithms. In order to obtain an estimation of both channels, we assume that the channels change only slowly in time and are nearly constant over 4 OFDM symbols.

This assumption is indeed realistic, considering that for the aeronautical channel the coherence time is generally in the order of 2 ms [29], while in the AeroMACS case the OFDM symbol duration is around 115.2 μ s. Furthermore, we virtually divide the frame in subsets of 4 adjacent OFDM symbols and allocate all the pilot tones of the first two adjacent symbols to the first antenna, while the remaining ones on the other symbols to the second antenna, as showed in Fig. 3.13.

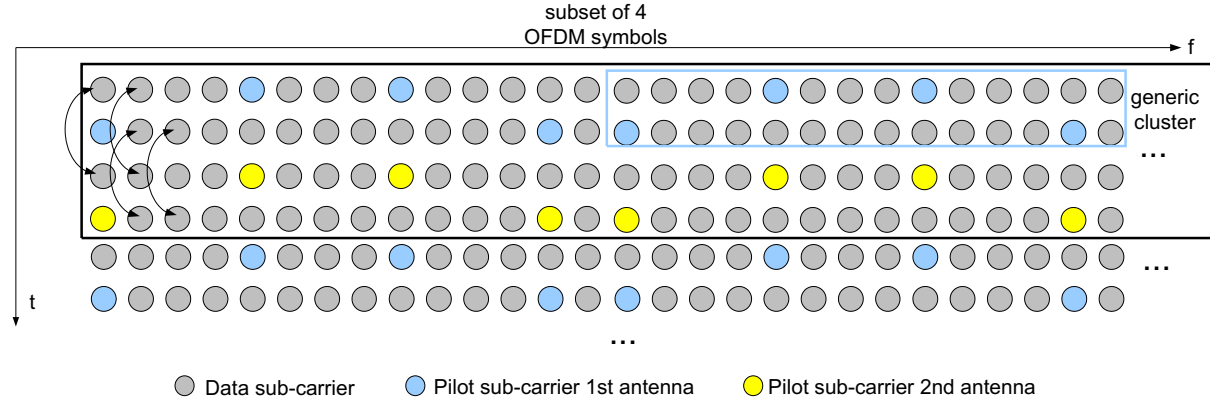


Figure 3.13: Generic frame scheme with the proposed pilot tones allocation. The pilot positions are unchanged with respect to the generic single antenna transmission (cluster scheme). The channel estimation may be performed allocating the pilot tones respectively to the first and second antennas.

Wherever the pilots of an OFDM symbol are sent through antenna 1, the corresponding sub-carriers in the OFDM symbol sent through the antenna 2 are blanked (see Figure 3.14). This assures, that in the received signal the pilot tones can be used to estimate either the channel coefficients from antenna 1 or from antenna 2.

We apply space time coding in the frequency domain between sub-carriers with same frequency position but different OFDM symbols according to the description provided in Figure 3.14 and Figure 3.13. The generic transmitting symbol $x_{i,j}$ is combined with $x_{i+2,j}$, where i and j respectively represent the time and frequency indices. Indicating $x_1 = x_{i,j}$ and $x_2 = x_{i+2,j}$, and the corresponding channels with $h_1 = h_1(i, j) \approx h_1(i + 2, j)$ and $h_2 = h_2(i, j) \approx h_2(i + 2, j)$, we can rewrite Equations 3.16 as

$$\begin{cases} y_1 = y_{i,j} = x_{i,j} \cdot h_1 + x_{i+2,j} \cdot h_2 + n_1 \\ y_2 = y_{i+2,j} = x_{i+2,j}^* \cdot h_1 - x_{i,j}^* \cdot h_2 + n_2 \end{cases} \quad (3.19)$$

and Equation 3.18 as

$$\begin{cases} \hat{x}_{i,j} = y_{i,j} \cdot h_1^* - y_{i+2,j}^* \cdot h_2 \\ \hat{x}_{i+2,j} = y_{i,j} \cdot h_2^* + y_{i+2,j}^* \cdot h_1 \end{cases} \quad (3.20)$$

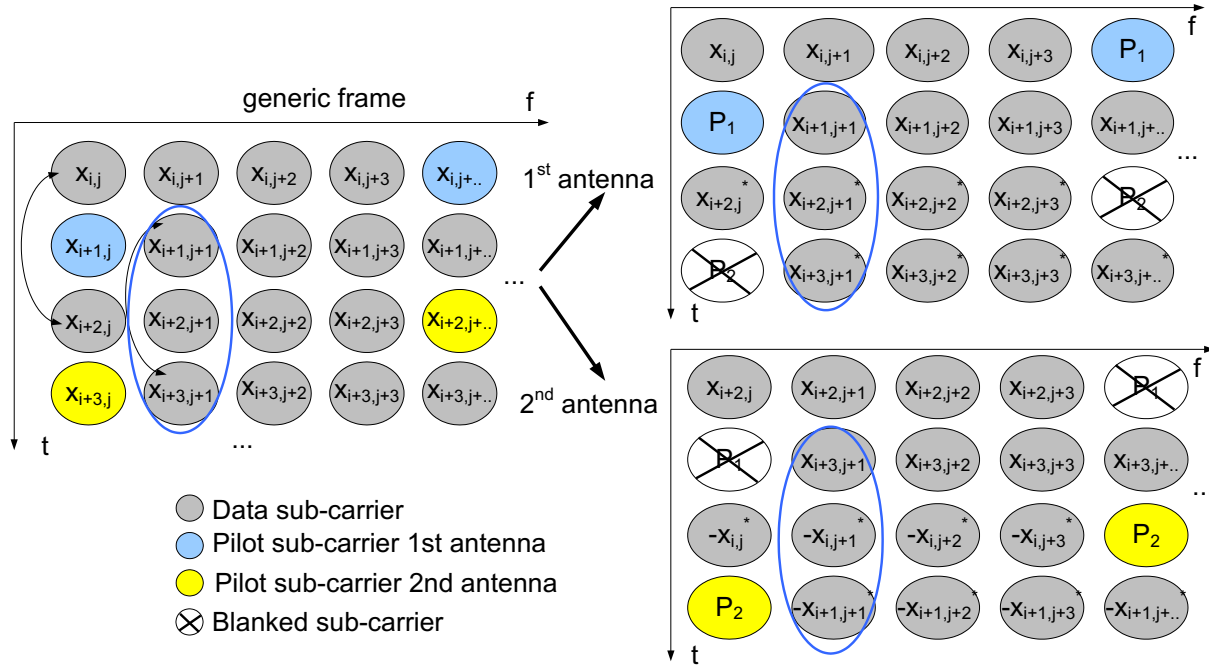


Figure 3.14: Scheme of the proposed space time coding implementation. The two frames to be transmitted on the two antennas are generated from the generic frame.

3.3.1 Simulation Parameters

The parameters chosen for the simulations consist of a bandwidth of 5 MHz with subcarrier spacing of roughly 10 KHz, a basic coding scheme with a rate 1/2 convolutional code and a QPSK subcarrier modulation. Given this sub-carrier spacing and the Doppler spread/shift values provided in Table 1.1, the inter-carrier interference shall provide a negligible impact on the performance. The cyclic prefix has been set 1/8 of the symbol length, therefore the total OFDM symbol time T_{OFDM} is approximately 115.2 μs . Frames of 24 OFDM symbols have been considered, with 17 subchannels allocated to one user. Prior to the modulation, the bits at the output of the convolutional encoder are interleaved over the entire frame.

We considered ideal channel estimation (ID) and two types of linear interpolation based on the pilot tones and tailored for the WiMAX cluster structure. The easiest algorithm performs interpolation in the frequency domain within a single cluster, using only the frequency direction (LIN-freq.). Also the other algorithm operates in the frequency domain but considers both the time and frequency dimensions over the whole frame (LIN-time/freq.). In this second case a first time direction interpolation is used to perform a second more accurate frequency interpolation. Table 3.3 provides the system parameters used in the simulations. We used the channel model described in 1.2 and the parking and apron scenarios. The main channel parameters are summarized in Table 3.4.

Table 3.3: Simulation system parameters.

System parameters	FL - OFDMA
Bandwidth	5 MHz
FFT size	512
Null guard sub-carriers	91
Cyclic prefix CP	$1/8 \cdot T_S = 12.8 \mu s$
Frame size	24 OFDM symbols
Symbol time T_S	102.4 μs
$T_{\text{OFDM}} = T_S + \text{CP}$	115.2 μs
T_{frame}	2.75 ms
Sub-carrier spacing Δ_f	$\simeq 10.94$ KHz
Coding, rate	Convolutional, 1/2
Decoding	Soft Viterbi
Modulation	QPSK
Channel Estimation	Ideal, linear pilot interpolation in freq. domain (freq. and time/freq. direction)

Table 3.4: Channel parameters of the different scenarios.

	APRON	PARKING
K [dB]	0	-10, 0
Delay spread σ_τ [μs]	0.65	1.25
Doppler spread $\sigma_{Dmin}, \sigma_{Dmax}$ [Hz]	20, 50	10, 40
Doppler shift f_{Dmax} [Hz]	140	50
Number of taps	9	12

3.3.2 Simulation Results

In the following, we present the simulation results, evaluating the performance of AeroMACS with with the above-described STC implementation. The results are obtained using the channel described in Section 1.2 and are presented separately for each scenario. All the performances are shown in terms of BER versus E_b/N_0 . The first Figures 3.15 and 3.16 represent the results obtained for the parking scenario. This scenario is characterized by a rich multi-path with a large delay spread, while the low mobility results in small Doppler spreads/shifts.

Figure 3.15 provides the results obtained with Rice factor equal to 0 dB and different channel estimations. The results obtained with linear pilot interpolation are compared with the ones obtained with ideal channel estimation. The presence of the second antenna increases the performance doubling the slope of the curves; though, the real channel estimation case with diversity loses almost 2 dB with respect to the corresponding ideal case. In Figure 3.16 the performance obtained with $K = -10$ dB and linear interpolations is shown. Also in this case the introduction of a second transmitting antenna improves the performance doubling the slope of the curves. Figure 3.17 provides the results obtained

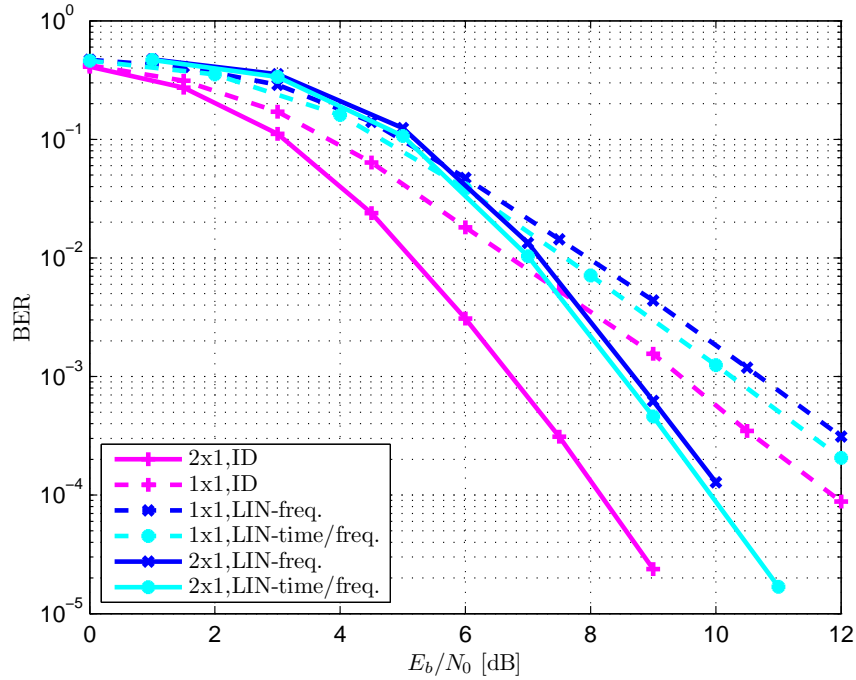


Figure 3.15: Parking scenario performance obtained with The FL of a normal OFDMA WiMAX system (no diversity) and the proposed 2×1 STC version of the system. $K = 0$ dB, evaluation of different channel interpolations w.r.t. ideal channel estimation.

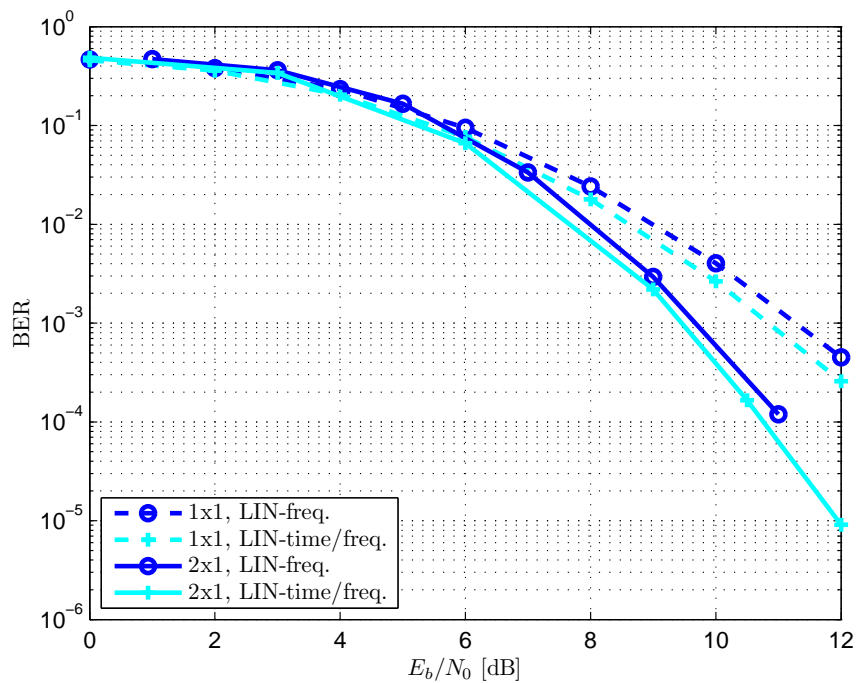


Figure 3.16: Performance obtained with the single antenna (1×1) system and the 2×1 STC system in the parking scenario ($K = -10$ dB).

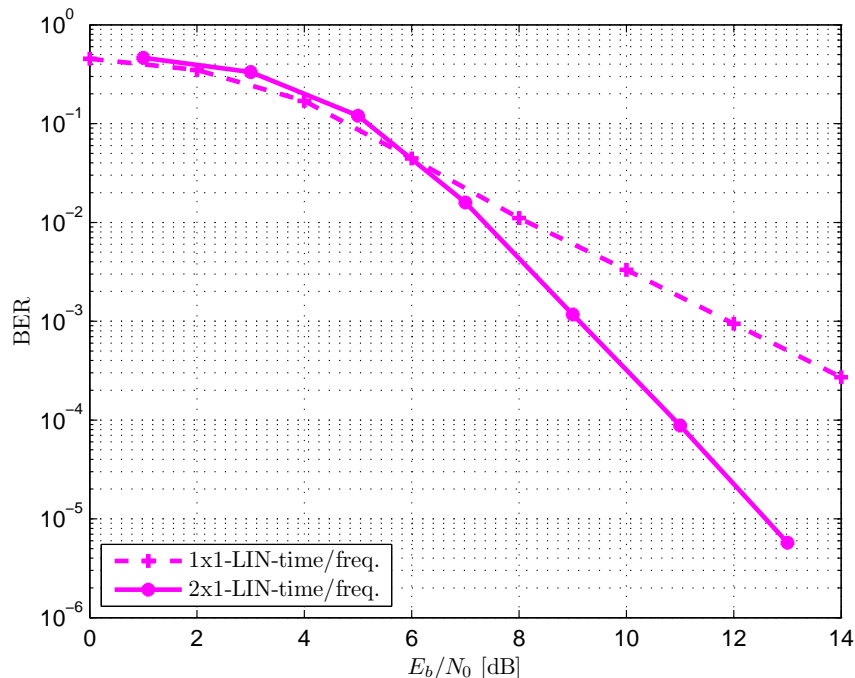


Figure 3.17: Performance obtained with the single antenna (1×1) system and the 2×1 STC system in the apron scenario ($K = 0$ dB).

with the apron scenario. This case is characterized by a delay spread $\sigma_\tau = 0.65 \mu\text{s}$ and small values of Doppler spread and shift ($\sigma_D \leq 50$ Hz, $|f_D| < 140$ Hz). We considered only $K = 0$ dB since with higher Rice factor we would not have improvement by the addition of a transmitting antenna. The results are obtained with linear interpolation in time and frequency directions and show the improvement provided by STC.

Figures 3.18 and 3.18 compare the performance provided by the above described STC implementation (here indicated for convenience with STC-N) with the implementation proposed in the standard (indicated with STC-S). Figure 3.18 shows the results for packet length equal to 15 slots. In the real channel estimation case, STC-N provides a gain of almost 1 dB (at $\text{BER}=10^{-4}$) over STC-S. In the ideal channel estimation case the performance are equivalent. Considering the similar performance in case of perfect channel estimation, the gain could be explained in a better channel estimation due to a different pilot tones structure. The case with minimum packet size (equivalent to 1 slot), illustrated in Figure 3.19, shows a stronger gain of STC-N. Indeed, the preservation of the frame structure with slots composed by 2 different clusters provides better frequency diversity exploitation and better performance, especially in the case with packet length of only 1 slot. However, the greater advantage of this alternative implementation of Alamouti STC 2×1 scheme is the preservation of the original WiMAX frame structure.

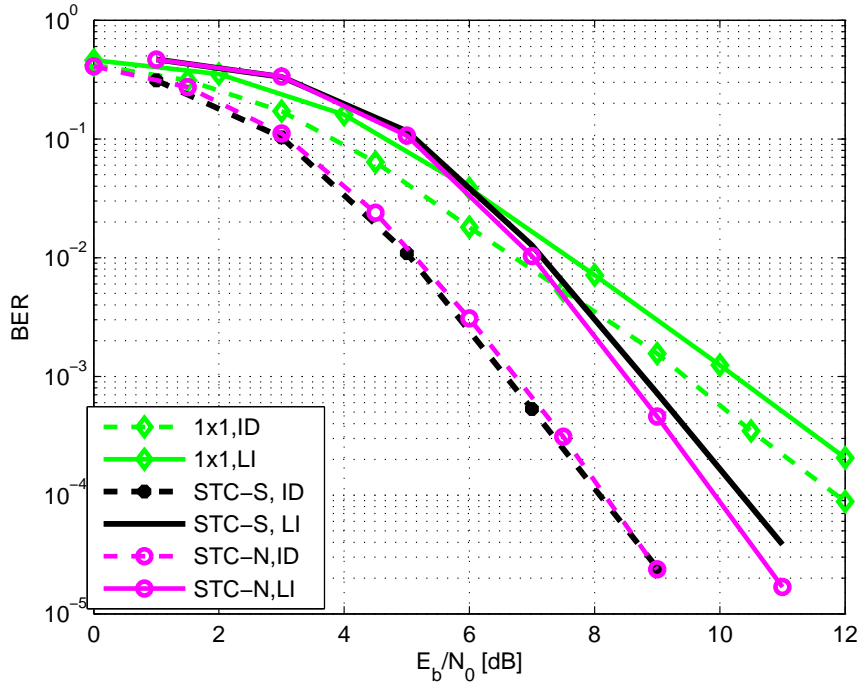


Figure 3.18: Comparison between the performance provided by the proposed implementation of STC (indicated with STC-N) and the one proposed in the standard (indicated with STC-S). Parking scenario, linear pilot interpolation, and packet size = 15 slot.

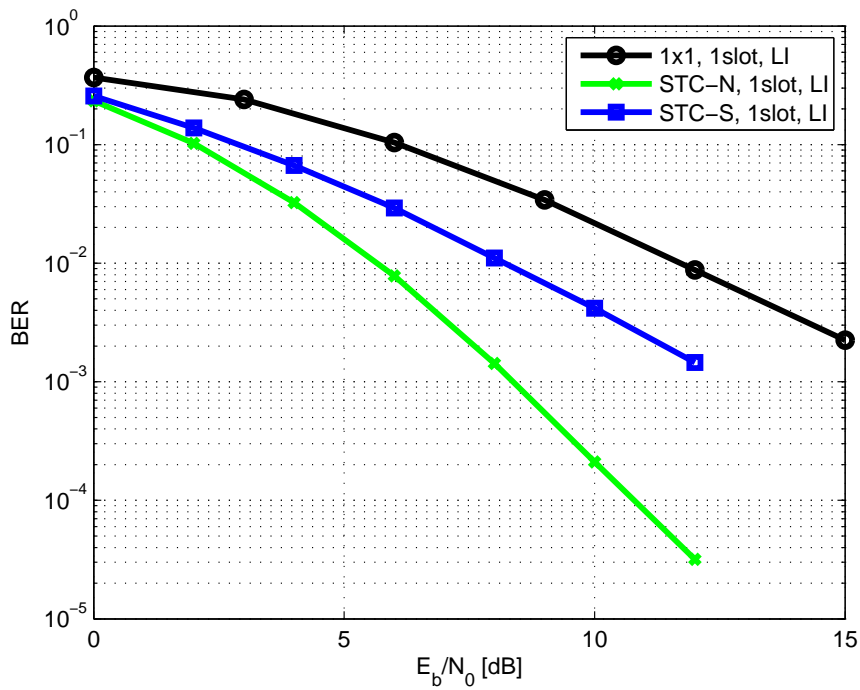


Figure 3.19: Comparison between STC-N and STC-S. Parking scenario, linear pilot interpolation, and packet size = 1 slot.

3.4 Summary

The performance gains attained by multiple antennas systems have been widely acknowledged. The case of airport communications doesn't represent an exception. Since the installation of more antennas on the aircraft is seen as critical, we focused on schemes which foresee multiple antennas only on the control tower. The simplest solution for the RL is a SIMO 1×2 scheme, which provides a diversity gain of order two (that corresponds to the maximum achievable with two antennas). Adopting a MRC receiver, as we proposed, we obtain also an additional array gain of 3 dB. Being obtained by the coherent sum of the signals, this gain is independent from the channel (hence is present also in case of correlated channels). This scheme introduces a large performance improvement with a gain of almost 6 dB at $BER = 10^{-4}$.

For the FL, we considered a MISO 2×1 STC scheme. Although STC doesn't benefit of array gain, we selected it for the airport communications because it doesn't require CSI at the transmitter (as the beamforming scheme), that is difficult to obtain. Also in this case, the diversity order is two, and the performance of AeroMACS is largely improved. For this case, beside the implementation proposed in the WiMAX standard, we proposed a different implementation of STC. This scheme preserves the original frame structure of AeroMACS, limiting the required modifications to the system and providing in some configurations even better performance w.r.t. the standard technique.

In both FL and RL, we attained large performance gains with the introduction of a second antenna. The introduction of more antennas would provide even a larger gain. For instance, having 4 antennas on the control tower, translates into a diversity gain of order 4 plus an array gain of 6 dB. Similar results could be obtained with a 2×2 MIMO scheme. However, the full potential of a MIMO scheme, with multiple antennas on both sides, is however out of reach, since in the aeronautical context the installation of multiple antennas on the aircraft is often considered critical.

In the next chapters, we discuss cooperative techniques, which allow to circumvent this limitation by creating virtual (distributed) antenna arrays on the aircraft side.

Chapter 4

Cooperative Communications

One possibility to enhance the performance of AeroMACS is the application of spatial diversity techniques. MIMO techniques represent a straightforward way to realize it, and their advantages have been widely acknowledged. However, in the aeronautical domain, the introduction of multiple-antenna systems, especially onboard aircraft, is seen to be critical, limiting the applicability of MIMO. Cooperative communication techniques can represent a valid alternative, since they allow single antenna systems to exploit spatial diversity [52–57]. Cooperative communications represent a new paradigm based on the utilization of heterogeneous resources in order to increase the overall performance of the system. A virtual antenna array may be created by the combination of antennas of different users, obtaining spatial diversity. The classic relay system can be seen as an example of cooperative communication, where a user of the system acts as a relay forwarding the received signal. However, cooperative communication methods include more possibilities. There are several fashions for cooperating and the "helping" user may elaborate the received signal in many different ways.

In this chapter, we analyze low-complexity cooperative communications protocols in the context of AeroMACS. Detect and forward, amplify and forward and coded cooperation methods are investigated, analyzing their properties in the aeronautical context. We propose a realization of a simple cooperative communication scheme for improving the performance of AeroMACS in the RL. The proposed scheme, based on the amplify and forward method, increases the reliability of the system by means of a relay which simply forwards the source signal to the destination. In our investigation, the relay can be an aircraft. In this way, the introduction of a new relay network is avoided. The resulting system can benefit of a spatial diversity of order two, which is equivalent to the result obtained with a multiple-antenna system with two antennas. The receiver can perform a simple selection combining of the two received signals or can adopt a more sophisticated algorithm (e.g. maximal ratio combining), which allows exploiting all the received power. However, in order to perform MRC, all the channel components must be known. Hence, it is necessary to estimate not only the resulting channel coming from the combination of the route source-relay-destination, but also the channel relative to the segment relay-

destination. In order to properly estimate all the channels, we insert some pilot tones at the relay before amplifying the signal, allowing the destination to coherently sum all the received signals and maximize the performance of the system. Performance results in term of BER versus SNR are also provided.

4.1 Overview of the Different Techniques

In a cooperative communication system, the transmission between the source and the destination is helped by one or more partners, which receive the transmitted signal and retransmit to the destination a copy of the signal transmitted by the source. In this way, a distributed MIMO network is created and a diversity gain is obtained. In a multi-user system, the users can act as cooperating partners creating a cooperative network. By sharing their resources, they maximize the overall performance of the system. Moreover, they keep the costs low, since the installation of an ad-hoc relay network is avoided. This solution offers the advantage of flexibility, large number of potential cooperative partners and operational efficiency. The vehicles operating on the airport surface offer furthermore sufficient power to enable complex signal processing. Again, the cooperation among users offers a wide availability of potential terminals out of which choosing the most appropriate relay (i.e. the one located in the best position with respect to the source and the destination terminals).

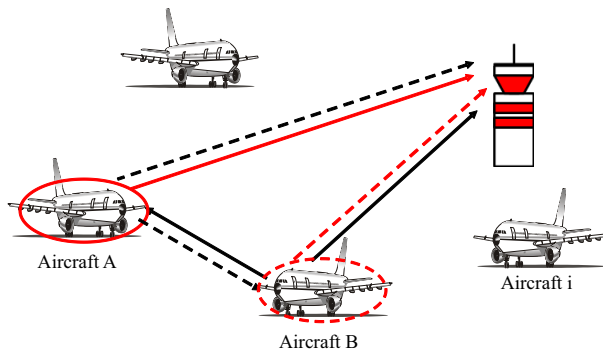


Figure 4.1: Scheme of cooperation between aircraft.

Figure 4.1 shows a scheme of cooperative communication where the users A and B collaborate. In the first case (continuous lines), the user B is helped in the communication with the base station by the user A (red line). Here, B is the source terminal and A acts as relay transmitting to the base station a replica of the signal transmitted by A. However, the roles can be exchanged and the user B can become the cooperative-terminal that helps A (dotted lines). In this example, the users A and B cooperate with each other. Though, the cooperation can take place not only with cooperating couples of users, and the partner assignation can be made in several ways according to different algorithms. The relay terminal transmits a replica of the signal transmitted by the users according to

a certain cooperation method. There are different cooperation techniques characterized by different levels of complexity and performance. However, all the methods require the receiver separating the original signal from its replicas. The easiest way to obtain the separation is to adopt time division, letting source and relay transmitting in different time slots. Table 4.1 describes an example of single-relay transmission using time division. In the first time slot (t_1), the source transmits while destination and relay receive. Then, during the second time slot (t_2), the relay transmits and the destination receives.

Table 4.1: Cooperation based on time-division

Time slot	t_1	t_2
Source	Tx	Inactive
Relay	Rx	Tx
Destination	Rx	Rx

4.1.1 Amplify and Forward

The amplify and forward (AF) method has been proposed by Laneman in [53] and constitutes a simple form of cooperation between systems. In this case, the relay device only amplifies and retransmits the noisy version of the signal received from the source. The base station receives the different versions of the signal and exploits them for improving the detection of the transmitted bits. Although the noise at the relays is amplified by the cooperation, the system receives independent replicas of the signals increasing the system diversity. For a system with two user cooperating (for example a system with a single relay), a diversity of order two is achieved. Hence, full diversity is attained.

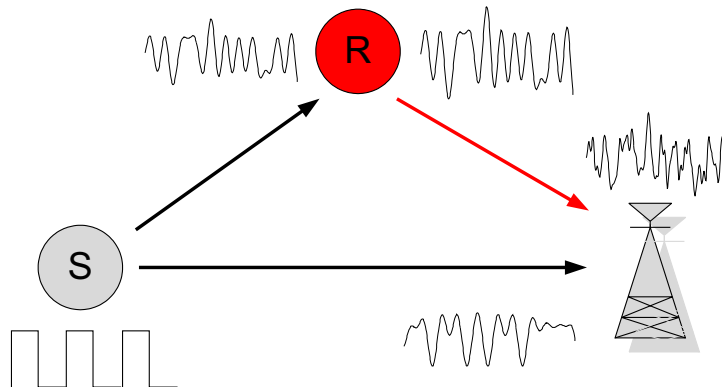


Figure 4.2: Amplify and forward scheme.

4.1.2 Decode and Forward

Within the cooperative communication methods, decode and forward (DF) is the one closest to the initial idea of relay system. As represented in Figure 4.3, the relay

detects, decodes and retransmits the signal transmitted by the source. Sedonaris in [54,55] proposed one of the first example of DF, with decode-and-forward cooperation made by code-division multiple access (CDMA). In DF, as illustrated in Figure 4.3, the relay decodes the source's signal and retransmits it after re-encoding the information. The destination receives two independent replicas of the signal that exploits for extracting the information bits. Differently from the previous method, the receiver doesn't require to know the channel between S and R to perform a coherent combination of the signals (only the channels between R-S and S-D are required, indeed).

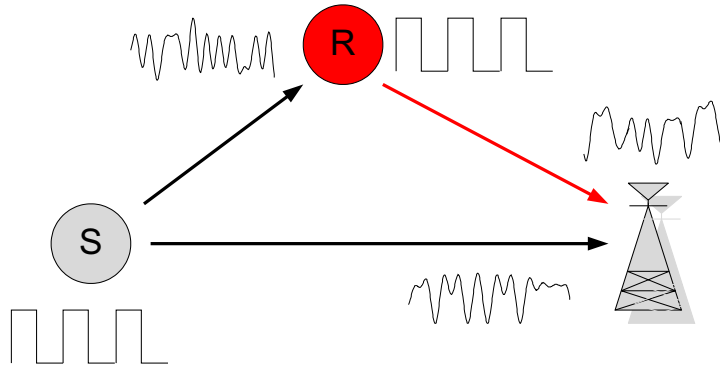


Figure 4.3: Decode and forward scheme.

4.1.3 Coded Cooperation

Coded cooperation [58,59] combines channel coding with cooperation, creating a distributed coding. The basic idea is that each partner transmits a portion of a codeword, increasing the redundancy. Figure 4.4 shows a scheme of coding cooperation between two users. Each user encodes their information (the bits of the user A are represented in grey in the figure while the ones of the user B in red) and then divides the codeword into two subsets containing N_1 and N_2 bits, respectively. The first subset is transmitted by the original user in the first frame. After decoding the first subset, the collaborating-user can obtain the second subset of the partner and transmits during the second frame. The receiver combines the fragments received by the collaborating partners and decodes them jointly obtaining the information bits. Again, including a cyclic redundancy check (CRC) code on the sub-messages, the partners can independently decide to transmit the second subset of the own message in place of the partner's. In this way, whenever the link between the partners were bad (not allowing a proper decoding and retransmission of the message) the user decides to entirely exploit its resources for itself. Thus, in this case, the system acts as non-cooperative. The partners are hence able to decide whenever it is convenient cooperating or not. This method represents an attractive cooperation option, thus it achieves gains, while preserving information rate, transmit power, and bandwidth of the non-cooperative system.

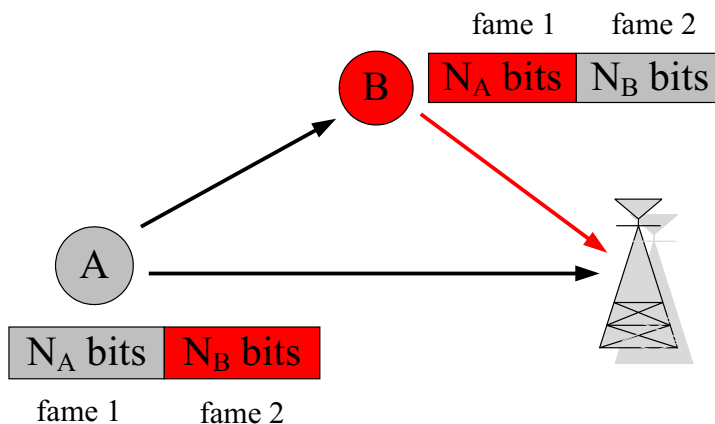


Figure 4.4: Coded cooperation scheme.

4.2 Cooperation in the Airport Environment

In a multi-user system, the users can act as cooperating partners in order to share resources and obtain better information transmissions. The creation of a cooperative network represents a convenient option for a multi-user system. In this case in fact, the installation of an expensive ad hoc relay network is avoided. Besides, the system users offer the great advantage of having already integrated all the devices necessary for transmitting and receiving signals. Hence, different types of cooperation algorithms are implicitly allowed. Again, the cooperation among users offers a large range of available terminals within choosing the most appropriate relay.

AeroMACS beneficiates of a large population of aircraft and represents a good candidate for the use of cooperative communications. Within the airport network, the aircraft could cooperate with each other increasing the performance of the system. At the airport, the ideal application scenario for cooperative communications is represented by the parking scenario. In fact, in this case the aircraft is often in non-line-of-sight with the control tower and the performance of the system tends to suffer for limited time and frequency diversity. Moreover, the network topology (including aircraft and control tower) is static, allowing reliable estimations of the relevant channel gains. Hence, the application of cooperative communications could largely improve the quality of the transmission.

The best cooperating condition is represented by a relay whose link towards the destination presents a better SNR with respect to the one provided by the direct link between source and destination. Such situation may be represented by a relay in line of sight with the user and eventually also with the control tower (and hence with a high SNR in correspondence of both the $S - R$ and $R - D$ links, as depicted in Figure 4.5).

In order to select the most appropriate aircraft-relay, the user could (independently from the control tower) exchange messages with the potential relays. Moreover, it is possible to exploit the characteristics of the airport topology. Since the airport vehicles

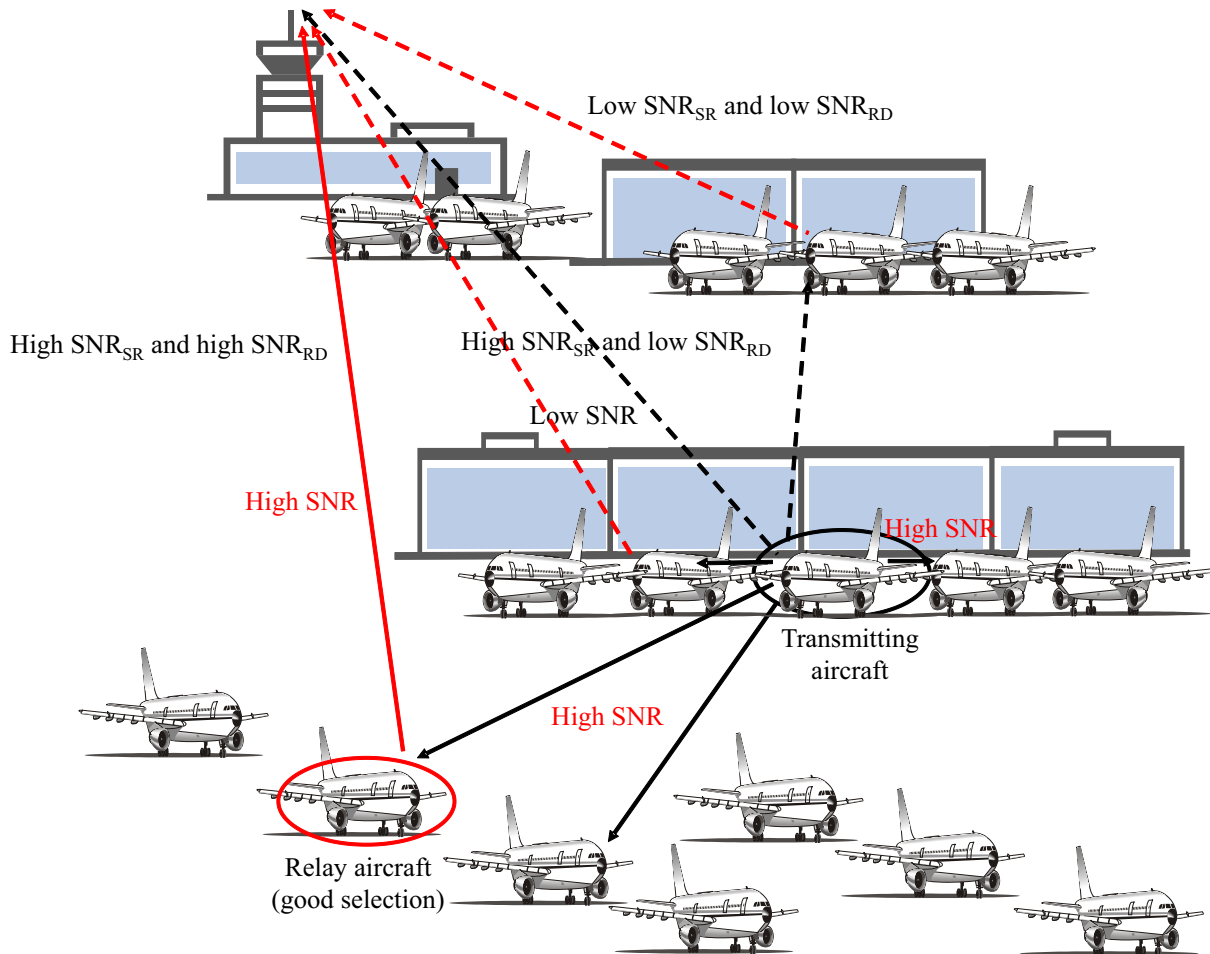


Figure 4.5: Cooperation scenarios at the airport.

are parked according to a specific scheme, this could be used to simply the selection of a good relay. In fact, aircraft parked close to each other guarantee a link between them with high SNR. Hence, it is possible to group potential cooperating-aircraft a priori and then the active user can independently choose a relay between the group's partners. The selection of the relay can also be done in a completely centralized way. In this case the base station can decide which users have to cooperate. However, the centralization of the cooperation increases the network overhead and the complexity.

The cooperative methods presented in the previous section assume that the original and the relay signals are transmitted orthogonally, hence, that the base station is able to separate them. However, except in [53], where the separation of the signals is performed by CDMA, the division of the signals represents a critical aspect. The easiest way to separate the signals is time division (see Table 4.1), that distributes the source and relay transmissions in different time interval. Another method is frequency-division. Though, many systems use different bandwidths for receiving and transmitting, making difficult the implementation of cooperation without changing the hardware.

AeroMACS is a system based on OFDMA which will operate in TDD mode. Although the frame is divided in FL and RL sub-frames, the ratio between FL and RL is variable, therefore, the relay can receive even during the RL. AeroMACS provides multiple chances of cooperation by means of time division, OFDMA sub-channel and even frequency sub-channel. In the first case the relay could transmit in a different frame but over the same OFDMA sub-channel used by the source message. Moreover, the relay has also the possibility to transmit over a different OFDMA sub-channels.

4.3 AF Implementation for AeroMACS

We implement a simple amplify and forward scheme to the AeroMACS system. We consider a single relay system, where an aircraft (partner aircraft) acts as a relay receiving and retransmitting the user's signal.

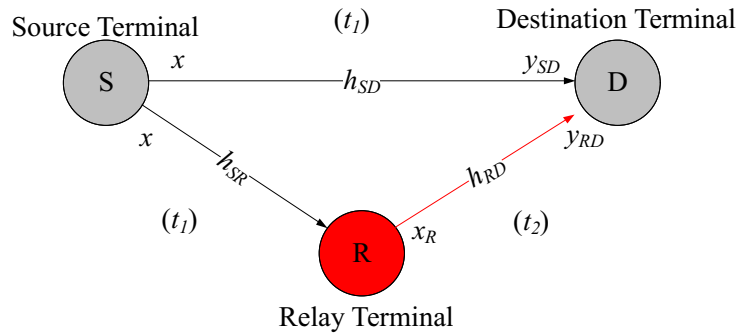


Figure 4.6: Scheme of a single relay system.

Figure 4.6 represents a simple amplify and forward scheme, where the communication between a source (S) and a destination (D) is supported by a single relay (R). The relay receives the signal transmitted by the source and retransmits it after an amplification defined by a factor C . Assuming the source transmitting only during the first slot, and the relay transmitting on the second slot, the destination receives the signals y_{SD} and y_{RD} during the first and the second slot, respectively. The system may be thus modeled as

$$\begin{cases} y_{SD} = h_{SD} \cdot x + n_{SD} \\ y_{SR} = h_{SR} \cdot x + n_{SR} \\ y_{RD} = h_{RD} \cdot x_R + n_{RD} = h_{RD} \cdot C(h_{SR} \cdot x + n_R) + n_{RD} \end{cases}, \quad (4.1)$$

where x represents the transmitted signal at the source, h_{SD} , h_{SR} and h_{RD} are the fading coefficients corresponding to the source-destination, S-R and R-D links, respectively. The signal retransmitted by the relay x_R is the received version of x amplified by a factor C , $x_R = C(x \cdot h_{SR} + n_R)$. It is convenient to call $y_1 = y_{SD}$ and $y_2 = y_{RD}$ and rewriting equation 4.1 as:

$$\begin{cases} y_1 = h_1 \cdot x + n_1 \\ y_2 = h_2 \cdot x + n_2 \end{cases}, \quad (4.2)$$

where the indices 1 and 2 represent the direct path S-D and the one provided by the relay S-R-D, respectively. Hence, the signal forwarded by the relay sees a channel $h_2 = Ch_{SR}h_{RD}$, and a noise $n_2 = Ch_{RD}n_R + n_{RD}$. All the noise components are modeled as complex Gaussian random variables with zero mean and variances $\sigma_{SD}^2 = \sigma_1^2$, σ_{SR}^2 and σ_{RD}^2 ($n_{SD} \sim \mathcal{N}(0; \sigma_{SD}^2)$; $n_{SR} \sim \mathcal{N}(0; \sigma_{SR}^2)$; $n_{RD} \sim \mathcal{N}(0; \sigma_{RD}^2)$). Normalizing the two signals by the relative noise variances σ_1^2 and σ_2^2 ¹, it is possible to obtain two signals \tilde{x}_1 and \tilde{x}_2 with the same noise variance equal to 1 ($\tilde{n}_1, \tilde{n}_2 \sim \mathcal{N}(0; 1)$),

$$\begin{cases} \tilde{y}_1 = \frac{y_1}{\sigma_1} = \tilde{h}_1 \cdot x + \tilde{n}_1 = \frac{h_1}{\sigma_1} \cdot x + \frac{n_1}{\sigma_1} \\ \tilde{y}_2 = \frac{y_2}{\sigma_2} = \tilde{h}_2 \cdot x + \tilde{n}_2 = \frac{h_2}{\sigma_2} \cdot x + \frac{n_2}{\sigma_2} \end{cases} \quad (4.3)$$

The system described by the previous equation is equivalent to a generic 1×2 single input multiple output SIMO system, hence, since the optimum weights of the MRC receiver are given by $w_1 = \tilde{h}_1^*$ and $w_2 = \tilde{h}_2^*$ (as for a 1×2 MRC system case). The resulting signal u , obtained by the combination of the two received signals y_{SD} and y_{RD} , becomes:

$$u = \tilde{h}_1^* \cdot \tilde{y}_1 + \tilde{h}_2^* \cdot \tilde{y}_2 = \frac{h_1^*}{\sigma_1^2} \cdot y_1 + \frac{h_2^*}{\sigma_2^2} \cdot y_2, \quad (4.4)$$

that can be rewritten as

$$u = \left(\frac{|h_1|^2}{\sigma_1^2} + \frac{|h_2|^2}{\sigma_2^2} \right) \cdot x + \frac{h_1^* n_1}{\sigma_1^2} + \frac{h_2^* n_2}{\sigma_2^2} = h_{tot} \cdot x + n_{tot}, \quad (4.5)$$

where the total noise coefficient and its variance are respectively given by

$$n_{tot} = \frac{h_1^* n_1}{\sigma_1^2} + \frac{h_2^* n_2}{\sigma_2^2} = \frac{h_1^* n_1}{\sigma_1^2} + \frac{h_2^* n_{RD}}{\sigma_2^2} + \frac{h_2^* C h_{RD} n_R}{\sigma_2^2} \quad (4.6)$$

$$\sigma_{n_{tot}}^2 = E\{|n_{tot}|^2\} = \frac{|h_1|^2}{\sigma_1^2} + \frac{|h_2|^2 \sigma_{RD}^2}{\sigma_2^4} + \frac{|h_2|^2 C^2 |h_{RD}|^2 \sigma_R^2}{\sigma_2^4} \quad (4.7)$$

$$\sigma_{n_{tot}}^2 = \frac{|h_1|^2}{\sigma_1^2} + \frac{\sigma_1^2 |h_2|^2 (C^2 |h_{RD}|^2 + 1)}{\sigma_2^4} = \frac{|h_1|^2}{\sigma_1^2} + \frac{|h_2|^2}{\sigma_2^2}. \quad (4.8)$$

Assuming the signal x uniformly distributed with mean power equal to 1 ($E\{|x|^2\} = 1$), the total instantaneous signal-to-noise ratio γ_{tot} becomes:

$$\gamma_{tot} = \left(\frac{|h_1|^2}{\sigma_1^2} + \frac{|h_2|^2}{\sigma_2^2} \right) = \gamma_1 + \gamma_2 \quad (4.9)$$

$$SNR_{tot} = \frac{1}{\sigma^2} \left(|h_{SD}|^2 + \frac{|h_{SR}|^2 |h_{RD}|^2}{(|h_{RD}|^2 + 1/C^2)} \right). \quad (4.10)$$

Hence, at the receiver the resulting instantaneous γ_{tot} is the sum of γ_1 and γ_2 . The first term represents the instantaneous signal-to-noise ratio relative to the direct link between the source and the destination and corresponds to the performance offered by a single

¹Note that if we assume the noise variance for all the systems identical and equal to σ^2 ($\sigma_{SD} = \sigma_{RD} = \sigma_R = \sigma$), the variances relative to the two paths become $\sigma_1^2 = \sigma_{SD}^2 = \sigma^2$ and $\sigma_2^2 = \sigma^2 (C^2 |h_{RD}|^2 + 1)$.

antenna system with no relay. The second term of the equation describes γ corresponding to the link source-relay-destination and represents the gain, in term of signal-to-noise ratio, introduced by the relay. Focusing on γ_2

$$\gamma_2 = \frac{1}{\sigma^2} \left(\frac{|h_{SR}|^2 |h_{RD}|^2}{(|h_{RD}|^2 + 1/C^2)} \right), \quad (4.11)$$

we observe that for high values of C the equation 4.11 becomes the signal to noise ratio corresponding to the S-R link γ_{SR} . Hence, the system behaves as a multiple antenna system with two receiving antennas². Vice versa, for $C = 0$, $\gamma_2 = 0$ and the system converts to a non-cooperating system. For $C = 1$, as it is reasonable to assume, γ_2 becomes

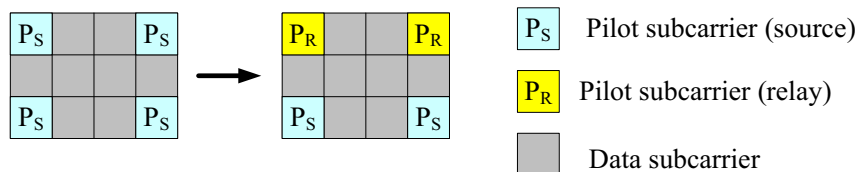
$$\gamma_2 = \frac{1}{\sigma^2} \left(\frac{|h_{SR}|^2 |h_{RD}|^2}{(|h_{RD}|^2 + 1)} \right). \quad (4.12)$$

From the previous equation it is clear to see that it is important to have the SNR relative to the link between the source and the relay (γ_{SR}) high. It is trivial to understand that a high γ_2 is fundamental for a good cooperation and to improve the performance of the system. As discussed in the previous section, it is possible to adopt some criteria in the relay selection in order to satisfy this request.

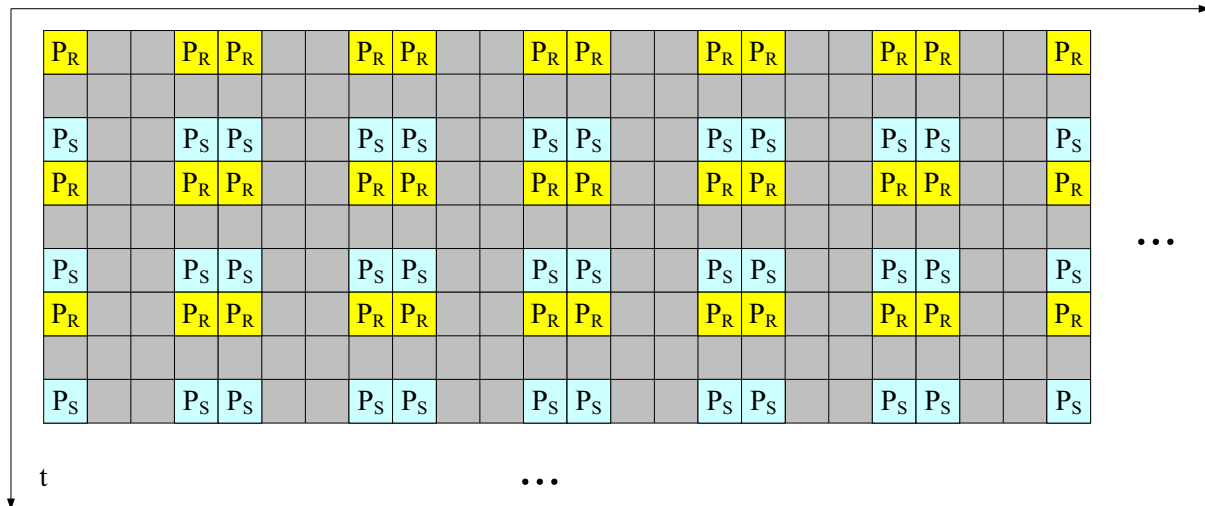
On the Channel Estimation

The previous analysis of the generic amplify and forward system shows that a coherent receiver requires to know all the three different channels (hence, the ones relative to the links S-D, S-R and R-D). In order to properly estimate all the channels, the relay could add some pilot tones, according to the scheme illustrated in 4.7. In this case, the reverse link of the WiMAX standard is considered. Hence, the frame and the pilot tones positions are based on the tile concept. The frame is divided in tiles, which consist of blocks of 12 sub-carriers with pilot sub-carriers at the corners (as illustrated in 4.7). The relay inserts two pilot values in correspondence of the first two pilots of the tile (the ones on the first frequency line) and modify the frame according to scheme presented in the figure. If the channel is sufficiently slow in time, the destination is able to estimate all the channels. In this case, the receiver may perform the channel estimation only in frequency direction, using the two pilots assigned to the link and assuming the channel constant over three consecutive OFDM symbols. The pilots inserted by the relay (P_R) to estimate the R-D channel and the pilots of the source (P_S) to estimate h_2 .

²Note that we are neglecting the power used by the relay for retransmitting the source's information. Since the relay amplification factor is directly related to the relay power consumption, in a real system, high values of C are unfeasible.



(a) Tile structure at the transmitter and at the relay



(b) Frame structure at the relay, the yellow pilot tones are inserted in order to estimate the relay channel.

Figure 4.7: Pilot tone positions for channel estimation of an AF channel.

4.3.1 Simulation Parameters

We analyzed performance of the described scheme in the context of AeroMACS and in particular on the reverse link case. For our simulations we used convolutional coding with rate $1/2$ and QPSK subcarrier modulation. We considered ideal channel estimation (ID) and linear interpolation based on the pilot tones and tailored for the WiMAX tile structure. Table 4.2 describes the relay simulation scenarios, i.e. the links between source and destination, source and relay and relay and destination. Our analysis is focused on the parking situation, therefore, we assumed the parameters typical of the parking scenario (Subsection 1.2.3). Since we account line-of-sight and non line-of-sight situations between the communicating entities, the Rice factor values are equivalent to 0 or 20 dB. Table 4.3 summarizes the main system parameters used in the simulations.

Table 4.2: Relay Simulation Scenarios

Simulation scenario	Case 1	Case 2	Case 3
Channel scenario h_{SD}	PARKING	PARKING	PARKING
K_{SD} [dB]	0	0	0
Channel scenario h_{SR}	PARKING	PARKING	PARKING
K_{SR} [dB]	20	20	0
Channel scenario h_{RD}	PARKING	PARKING	PARKING
K_{RD} [dB]	0	20	0

Table 4.3: Simulation Parameters

Parameters	Value
Link	RL
Bandwidth	5 MHz
FFT size	512
Symbol time T_S (w/o CP)	102.4 μ s
CP	$1/8T_S$
Subcarrier spacing Δ_f	10.94 kHz
Coding, rate	Convolutional, 1/2
Decoding	Soft Viterbi
Modulation	QPSK
Channel estimation	ID, LIN (freq. domain)
Relay Amplification Factor C	1, 10, 50

4.3.2 Simulation Results

In this section we present the results obtained by simulations. The first figures show the performance of the system in term of bit error rate versus average E_b/N_0 over the link S-D³. Figure 4.8 depicts the performance of a generic single relay amplify and forward system in the AeroMACS context for the third relay links configuration case. Here, the channels between the three communicating entities are assumed equal to the parking scenario and statistically independent. Therefore, the link offered by the relay doesn't provide a better SNR but only a diversity gain. The figure shows the performance with ideal channel estimation and different amplification factors. Three different relay amplification factors are showed for analyzing the system behavior. High values of C are considered as reference case, although they are unrealistic and do not lead to a fair comparison⁴. All the cooperative configurations provide a large performance improvement with respect to the non-cooperative case which is represented by the black line ($C = 0$). The cases with high C provides better performance, gaining almost 2 dB with respect to the case with $C = 1$. In fact, as showed in the previous section, increasing the C value, the system becomes equivalent to a single input multiple output system with two antennas and MRC receiver. Indeed, the performance of the cooperative system is equal to the one provided by the 2×1 MRC system. The gains provided by the cooperative schemes are remarkable. Gaining a diversity order equal to 2, they double the slope of the non-cooperative curve (exactly as the multi-antenna case).

³The power used for the relay transmission is not accounted in these figures. However, for a fair comparison it is necessary to account that the total power used for the cooperative transmission is increased with respect to the NON-cooperative system.

⁴In this work the performance of the system is shown per the link S-D, indeed. The power used by the relay for helping the user transmission is neglected. However, the total system power shall be controlled and the increase of C should be avoided.

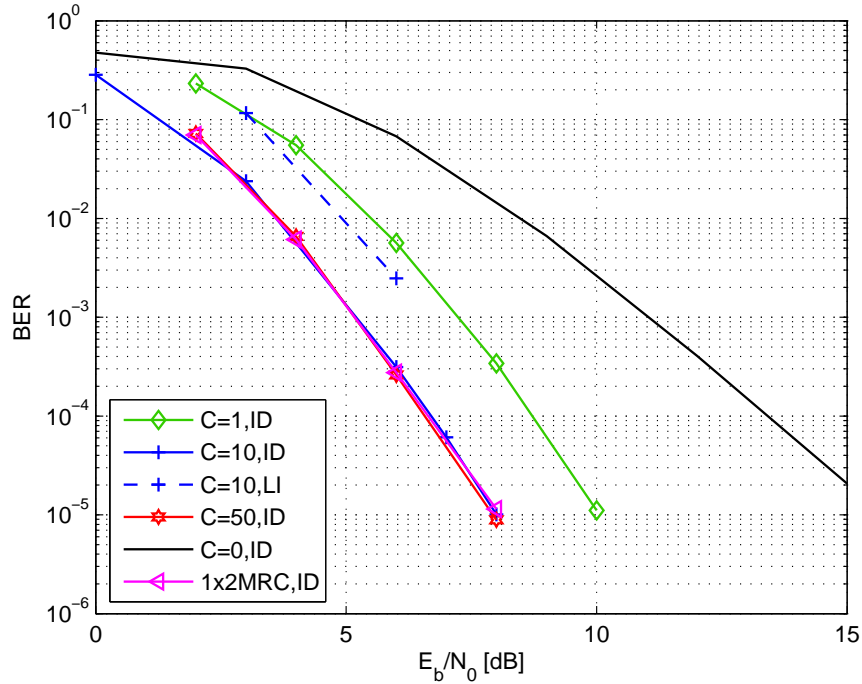


Figure 4.8: Performance of AeroMACS with AF scheme.

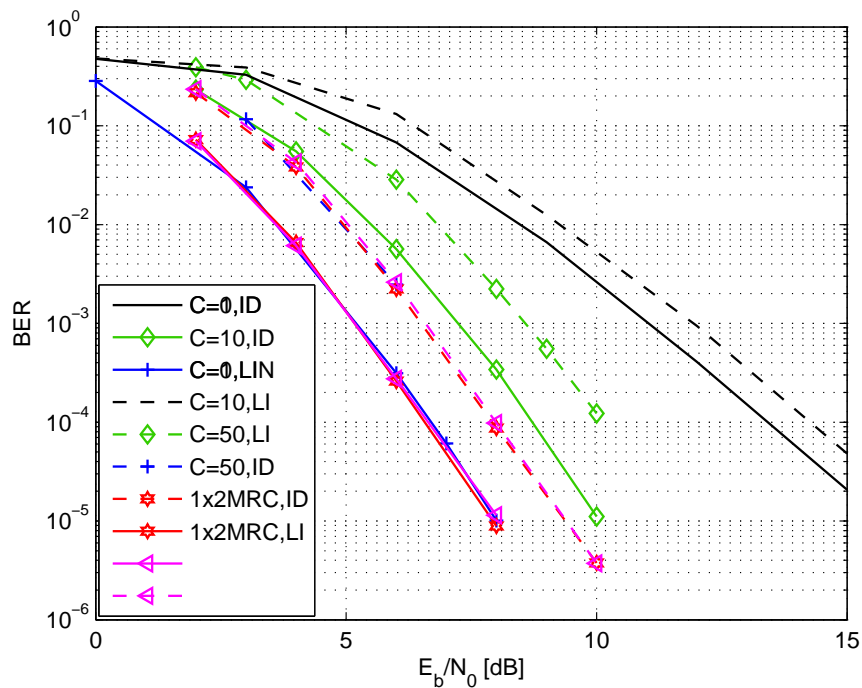


Figure 4.9: Performance of AeroMACS with AF scheme (ideal channel estimation and proposed linear interpolation algorithm).

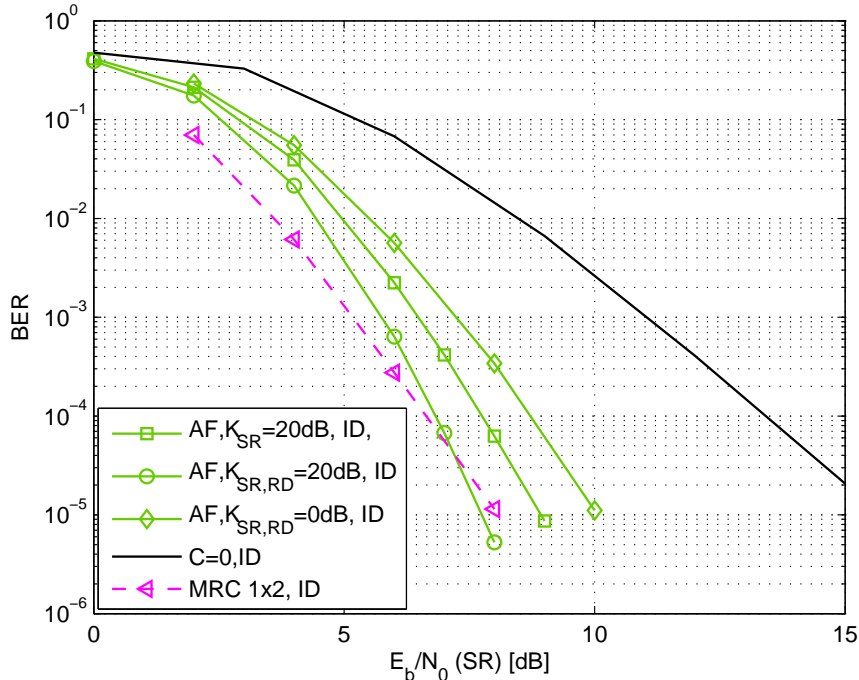


Figure 4.10: Performance of AeroMACS with AF scheme and different relay links conditions (ideal channel estimation.)

Figure 4.10 shows the performance of the system with the proposed way to perform real channel estimation for all the channel coefficients. We used linear channel interpolation based on the pilot tones. The interpolation, done in the frequency domain, is performed in time and frequency direction for the non-cooperative case and only in frequency direction (as described in the previous section) for the cooperative case. The real channel estimation cases (indicated with LI) are represented by dashed lines, while the ideal channel knowledge ones (ID) with continuous lines. The introduction of imperfect channel estimation produces a loss of almost 1.6 dB on the system performance. Figure 4.9 provides the performance of the system for different cooperation conditions (i.e. different channels between source, relay and destination). Perfect channel knowledge and relay amplification factor C equal to 1 are assumed. Besides the worst case (green curve with diamond marker) considered in the previous figures, two scenarios with different relay links conditions and hence different Rice factor K are considered. The curve with square markers represents the first case, where the source and the relay are in line-of-sight ($K_{SR} = 20$ dB). The channel between relay and destination preserves a low Rice factor $K_{RD} = 0$ dB (as the one between S and D). The second case (curve with round markers) presents high Rice factor in both the links ($K_{SR} = K_{RD} = 20$ dB), as the relay is assumed in line-of-sight with source and destination, both. All the cooperation cases provide large performance gains with respect to the non-cooperative case (black curve).

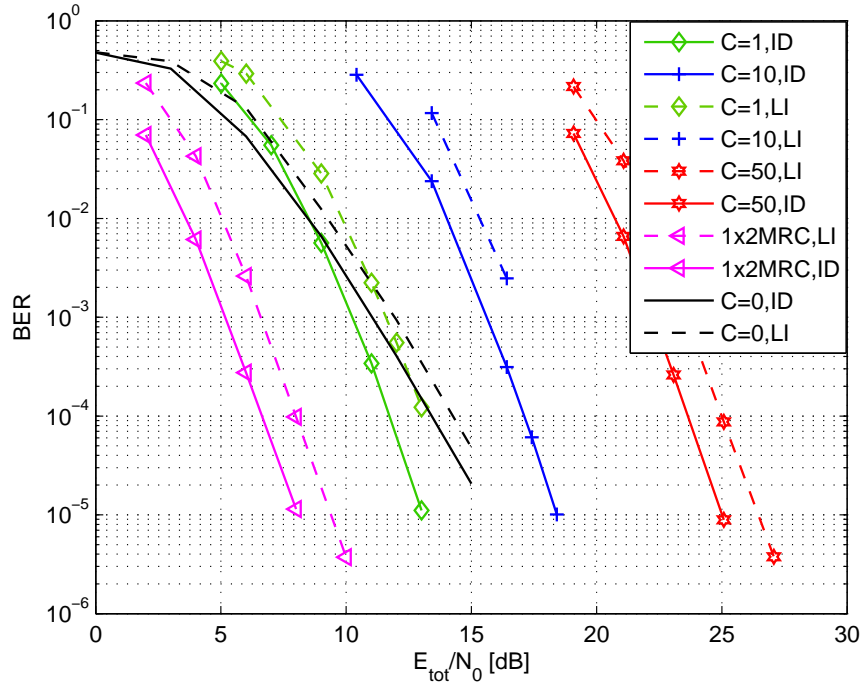


Figure 4.11: Performance of the AF scheme considering the total energy per bit.

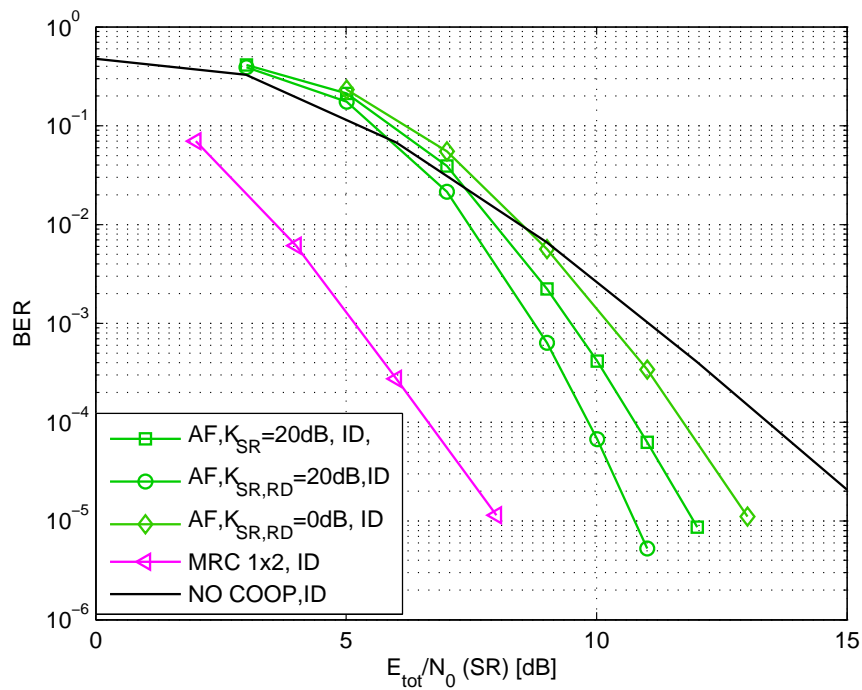


Figure 4.12: Performance of AeroMACS with AF scheme considering the total energy per bit and different Rice factor K for the relay links (ideal channel estimation).

In order to provide a fair performance evaluation of the AF scheme in the AeroMACS context, we include the behavior of the BER at the variance of the total energy per bit used by the system for the transmission ($E_{tot} = E_{b_{source}} + E_{b_{relay}}$). The following figures illustrate the performance in terms of BER versus $E_{b_{tot}}$. Figure 4.11 represents the results obtained for the worst case, i.e. the links $S-R$ and $R-D$ are not reliable with $K = 0$ dB. Figure 4.12 compares the performance obtained with different conditions of the relay links. From these figures it is clear that the use of the relay increases the total power spent by the system. Hence, certain values of the amplification factor C are completely unfeasible (as $C = 10$ and $C = 50$, respectively represented by the blue and red curves in Figure 4.11). Considering the total energy of the system, all the relay curves appear shifted to the right with respect to the previous figures. However, the slope is identical and the performance improvement still present⁵. For the case with $C = 1$, the curve is shifted of almost 3 db with respect to Figure 4.8. This implies that at BER= 10^{-4} the performance gain is almost 2 dB for the worst case ($K_{SR} = K_{RD} = 0$ dB), 3 dB for the scenario with reliable link between the source and the relay ($K_{SR} = 20$ dB, $K_{RD} = 0$), and 4 dB for the best case($K_{SR} = K_{RD} = 20$ dB).

4.4 DF Implementation for AeroMACS

Hereafter, we implemented a DF scheme with a single relay for the RL of the AeroMACS system. Again, we assume the relay being an aircraft and we use the two times transmission scheme described by Table 4.1. Considering the communication scheme represented in Figure 4.6, the control tower receives two signals during two different time slots. With respect to the previous case, the relay doesn't amplify the source's signal but decodes, re-encodes and retransmits it. We can describe the system with the following equations where the signal transmitted by the source and the relay are indicated with x_R and x , respectively,

$$\begin{cases} y_{SD} = h_{SD} \cdot x + n_{SD} \\ y_{SR} = h_{SR} \cdot x + n_{SR} \\ y_{RD} = h_{RD} \cdot x_R + n_{RD} \end{cases} \quad (4.13)$$

x_R represents the received signal ($x \cdot h$) decoded and re-encoded and we can practically indicate it with \hat{x} . Hence, if the relay can properly decode the transmitted signal, the destination will receive a useful replica of the signal. Vice versa, if the relay cannot decode the signal the destination will receive a not reliable replicas of the signal. Assuming the channel between source and relay reliable⁶ (i.e with high K factor), the behavior of the system becomes equivalent to a SIMO system. Utilizing a MRC receiver, we can maximize the total SNR_{tot} of the system. As consequence of the reliability of h_{SR} , we

⁵Assuming a realistic value for C as $C = 1$.

⁶This assumption is indeed realistic by means of the intrinsic nature of the airport, as discussed in the previous sections.

write $x_R = \hat{x} \approx x$. Hence we can write the two received signals y_{SD} and y_{RD} as

$$\begin{cases} y_{SD} = h_{SD} \cdot x + n_{SD} \\ y_{RD} = h_{RD} \cdot x + n_{RD} \end{cases} \quad (4.14)$$

This equation is equivalent to the MRC system with two receiving antennas, hence the receiver works exactly in the same way of the one illustrated in Sec. 3.1.1. Hence, the total received signal u is again obtained as

$$u = y_{SD} * h_{SD}^* + y_{RD} * h_{RD}^*. \quad (4.15)$$

The total SNR_{tot} is therefore given by the sum of the two SNRs relative to the direct path (SNR_{SD}) and the relay component (SNR_{RD})

$$\text{SNR}_{tot} = \frac{E\{|x|^2\}}{\sigma^2} (|h_{SD}|^2 + |h_{RD}|^2). \quad (4.16)$$

4.4.1 Simulation Parameters

For our simulations we used the system parameters summarized in Table 4.4. We adopted the channel model described in Chapter 1 with three different relay simulation scenarios, as summarized in Table 4.5. The first scenario reproduces the case where a reliable channel is available between the source and the relay (h_{SR}), while the other links ($S - D$ and $R - D$) are typical parking scenarios with NLOS conditions. The second simulation scenario represents a situation where the relay has not only a good h_{SR} but also a good h_{RD} . This case is obviously the ideal scenario, here the link provided by the relay outperforms the direct path. The third case constitutes the worst case, where the link provided by the relay is equivalent to the direct one. In all the cases, we assumed the typical parameters of the parking scenario, except the Rice factor K that can be either 0 dB or 20 dB.

Table 4.4: Simulation parameters

Parameters	Value
Link	RL
Bandwidth	5 MHz
FFT size	512
Symbol time T_S (w/o CP)	102.4 μ s
CP	$1/8T_S$
Subcarrier spacing Δ_f	10.94 kHz
Coding, rate	Convolutional, 1/2
Decoding	Soft Viterbi
Modulation	QPSK
Channel estimation	ID, LI (freq. domain)

Table 4.5: Relay Simulation scenarios

Simulation scenario	Case 1	Case 2	Case 3
Channel scenario h_{SD}	PARKING	PARKING	PARKING
K_{SD} [dB]	0	0	0
Channel scenario h_{SR}	PARKING	PARKING	PARKING
K_{SR} [dB]	20	20	0
Channel scenario h_{RD}	PARKING	PARKING	PARKING
K_{DR} [dB]	0	20	0

4.4.2 Simulation Results

Figure 4.13 shows the performance of the system with the introduction of a DF scheme. We considered three different simulation scenarios and perfect channel knowledge. The first case represents the situation with relay in LOS with the source but no with the destination. This case (represented by the purple curve with square markers in the figure) is the most realistic and interesting, since in the airport parking context this condition is simple to acquire. The case 2 ($K_{SR} = K_{RD} = 20$ dB, curve with round) represents the best cooperation scenario where the relay is in LOS with source and destination both. Here, the link provided by the relay is better than the direct one, and, the communication could stand only on the relay link. The case 3 ($K_{SR} = K_{RD} = 0$ dB, curve with diamond marker) foresees an unlucky situation with relay in NLOS with both source and destination. In this case, the condition of reliable channel between source and relay falls. Hence, the cooperation is ineffective. Since the link between source and relay isn't completely unreliable the performance is comparable to the one of the non cooperative system. However, in this context, it is preferable not to cooperate or, eventually, switching to an AF scheme. Figure 4.14 shows the results obtained with DF accounting linear channel interpolation. Figure 4.15 illustrates a comparison between the performance provided by AF (green curves) and DF (purple curves). The simulation results reflect the theoretical behavior. As expected, for a "not very reliable" channel between source and relay⁷, the results of AF (green curve with diamond marker) outperforms the one offered by DF (purple curves with diamond marker). The behavior changes with reliable h_{SR} , characterized by high $K = 20$ dB (curves with square and round markers); here, the performance of DF outperforms AF, since in this case the noise introduced at the relay is compensated.

In order to obtain a comprehensive evaluation of the use of the relay scheme, we include also the results in terms of BER versus the total energy per bit used by the system. Figure 4.16 shows the performance of the system with a relay DF scheme, while Figure 4.17 compare the results obtained with AF and DF. Similarly to the AF case, these curves are shifted on the right of almost 3 dB with respect to Figures 4.13 and 4.15. Therefore, the gain introduced by the relay appears for higher SNRs.

⁷We characterized this link with NLOS conditions with $K = 0$ dB.

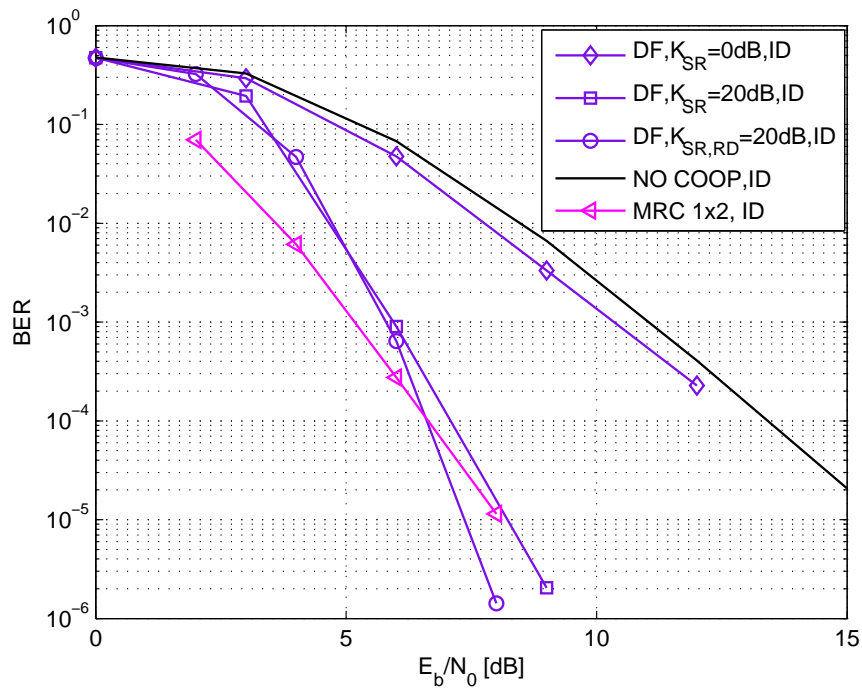


Figure 4.13: Performance of AeroMACS with DF scheme, linear pilot interpolation.

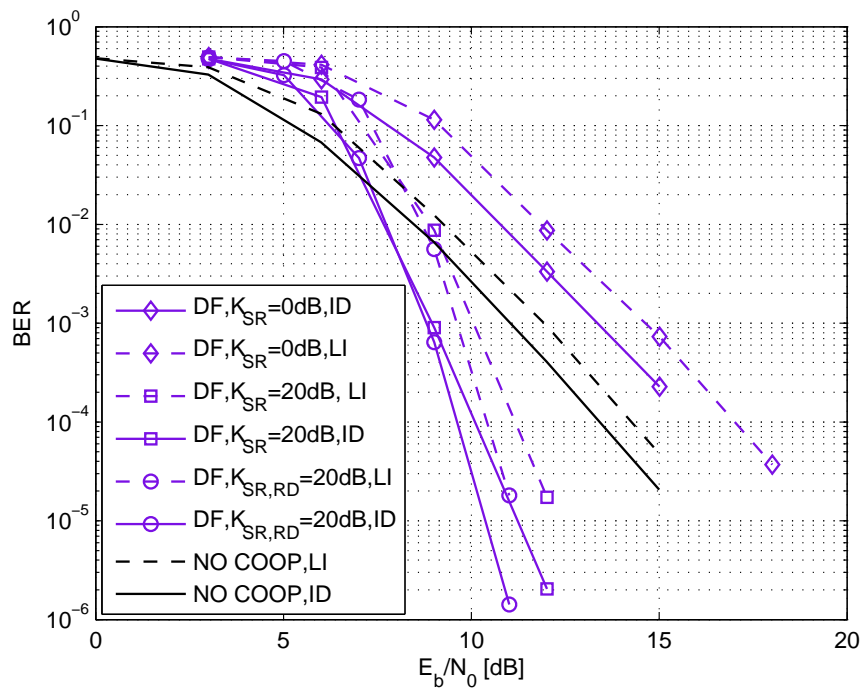


Figure 4.14: Performance of AeroMACS with DF scheme, linear pilot interpolation.

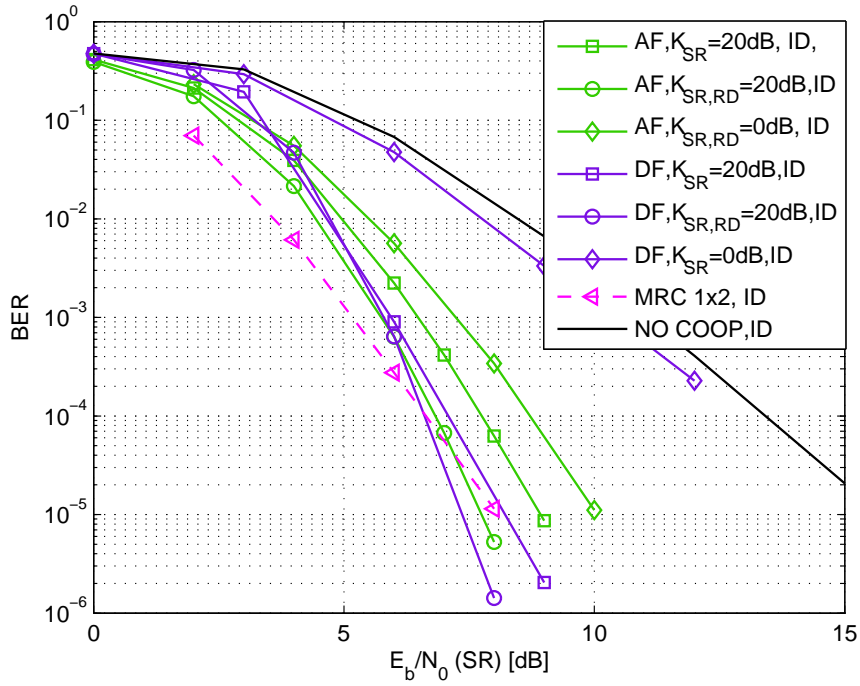


Figure 4.15: Comparison between the performance provided by AF and DF, linear pilot interpolation.

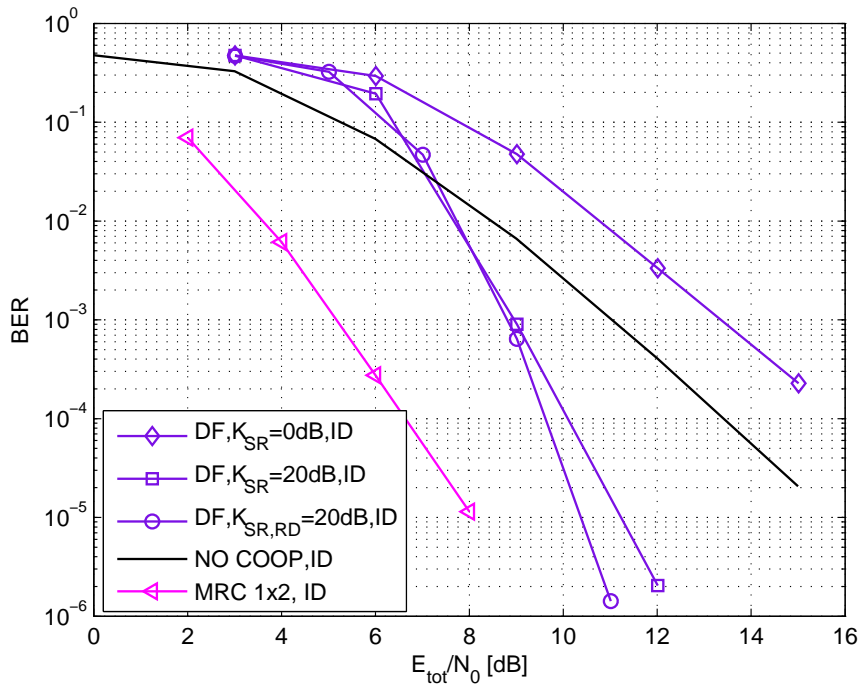


Figure 4.16: Performance of AeroMACS with DF scheme considering the total energy per bit and different Rice factor K for the relay links (ideal channel estimation.).

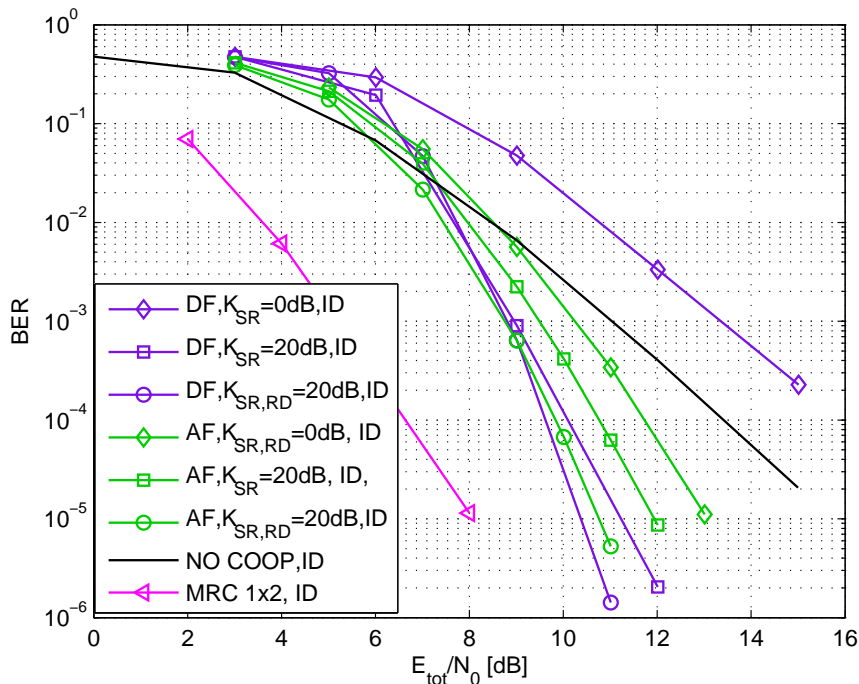


Figure 4.17: Comparison between AF and DF as function of E_{tot} .

4.5 Summary

In this chapter we investigated the use of cooperative communications schemes within AeroMACS. The use of these techniques provide spatial diversity, or more specifically cooperation diversity, even for single-antenna systems. Among the cooperation schemes, even the simpler ones, as amplify and forward and decode and forward, are able to provide large performance enhancements. More specifically, for the single-relay case, they both attain a diversity of order two. This diversity order is the maximum achievable with a single relay topology, and is the same provided by a multiple antennas system with two antennas.

However, cooperative schemes suffer from a reduction of transmission efficiency. Considering a time-division scheme (as for the schemes that we considered), where the transmission of the source and the one of the relay take place in two different time slots, the efficiency is reduced by a factor two. This is due to the fact that the transmission of a single message requires two time slots. Therefore, having assumed a code with rate $R = 1/2$ at the source, we obtain an overall rate of $1/4$. The efficiency reduction problem can be avoided using coding cooperation schemes, which allow to reach rates up to $1/2$ (that is the maximum for a system providing diversity two). Tackling the efficiency reduction problem, in the next chapter, we introduced a new coded cooperation scheme named *unequal diversity coding* (UDC) able to provide even higher rates.

Chapter 5

Unequal Diversity Coding: A New Concept for the Relay Channel

In this chapter, we tackle the problem of analyzing the performance of a high-rate ($R > 1/2$) distributed LDPC coded scheme over a quasi-static relay fading channel. The peculiarity of the proposed scheme resides in the so-called *unequal diversity* (UD) achieved by the different codeword fragments. More specifically, we design distributed LDPC codes which allow achieving full diversity (diversity-2) for some codeword fragments, whereas the remaining codeword fragments do not enjoy diversity. The proposed scheme thus trades diversity with coding rate (note in fact that diversity-2 cannot be achieved by any scheme with $R > 1/2$ over a 2-levels block fading channel (BFC)) by re-encoding at the relay a subset of the information bits encoded at the source. The proposed scheme is hence of interest for any communication system for which the unequal error protection (UEP) concept is relevant. The code construction is based on a parallel concatenation of LDPC code protographs [60]. We extend the (multi-dimensional) protograph extrinsic information transfer (PEXIT) analysis of [61, 62] to the calculation of the outage region of protograph LDPC ensembles [60] over BFCs [63]. The result is exploited for analyzing the behavior of protograph LDPC ensembles in coded cooperation schemes where each link is affected by a quasi-static Rayleigh fading. The PEXIT analysis has been previously adopted to design bilayer [64] protographs for the relay channel [65]. Nevertheless, in [65] the authors derive via PEXIT analysis the iterative decoding threshold over additive white Gaussian noise (AWGN) channel only for the designed protographs, focusing on the different point-to-point links and hence without any modification of the original analysis of [61, 62]. We extend the definition of outage regions of a code ensemble [66] to distributed protograph ensembles and to protograph variable nodes. Examples of distributed protograph ensembles are provided, which special attention to the high coding rate regime ($R > 1/2$), where diversity of order 2 cannot be achieved. For this case, ensembles exhibiting an appealing UEP properties are introduced. More specifically, some variable nodes (VNs) of the corresponding protograph achieve a diversity 2, whereas other nodes present a BER slope which is typical of a scheme without diversity. To highlight

the UD feature, we refer to the proposed codes as UD-LDPC codes. For the proposed ensembles, the codeword is assumed to be segmented into N sub-blocks, referred to as *fragments*. Each fragment is associated with a different VN in the code protograph. High-priority fragments are associated with diversity-2 VNs. Via PEXIT analysis, we develop simple yet tight bounds on the fragment error probability (FEP) associated with different codeword fragments. Numerical results confirm the accuracy of the proposed analysis.

Furthermore, we apply the developed UDC technique to AeroMACS, which represents an ideal candidate for the application of the method. The resulting performance results prove the validity of the technique.

5.1 Transmission Scheme

Following Figures 5.1(a) and 5.1(b), a rate- R_s code \mathcal{C}_s is employed at the source (S) to encode a length- k message vector \mathbf{u} which can be split into two sub-blocks (fragments, in the following) as $\mathbf{u} = [\mathbf{u}_h|\mathbf{u}_l]$, where \mathbf{u}_h represents the k_h bits long high-priority fragment and \mathbf{u}_l represents the k_l bits long low-priority fragment. The length- n_s coded block is given by $\mathbf{c}_s = [\mathbf{u}|\mathbf{p}_s]$, where \mathbf{p}_s is the $m_s = n_s - k$ bits parity vector. The coded block is then BPSK modulated, resulting in the modulated sequence \mathbf{x}_s (with $\mathbf{x}_s \in \{-1, +1\}^{n_s}$), and transmitted over the first time slot. A corrupted version of \mathbf{x}_s is received at the destination (D) as

$$\mathbf{y}_s = \alpha_s \mathbf{x}_s + \mathbf{n}_s, \quad (5.1)$$

where α_s follows a Rayleigh distribution with $\mathbb{E}[\alpha_s^2] = 1$, and where the elements \mathbf{n}_s are i.i.d. Gaussian random variables with variance $\sigma_n^2 = N_0/2$. The instantaneous SNR is given by $\gamma_s = \alpha_s^2/2\sigma_n^2$.

The same sequence \mathbf{x}_s is received at the relay (R). We will make use of a simplified assumption, i.e. we will consider the link between source and relay as reliable [67]. The assumption is justified by considering the case where the relay is selected among a set of candidate nodes in such a way the SNR on the S-R link is large enough to achieve negligible error probabilities after decoding¹. In this sense, the introduction of coding at the source (through \mathcal{C}_s) is essential to permit the selection of the relaying partner in a suitably-large area in the neighborhood of the source terminal. Note moreover that under the simplified condition the challenges in the code design remain substantially unchanged [67]. After decoding of the block \mathbf{u} , the relay extracts the high-priority fragment \mathbf{u}_h and performs encoding with a rate- R_R non-systematic code \mathcal{C}_R , producing the code block $\mathbf{c}_R = [\mathbf{p}_R]$, where \mathbf{p}_R is a n_R bits vector. The coded block is then BPSK modulated, resulting in the modulated sequence \mathbf{x}_R (with $\mathbf{x}_R \in \{-1, +1\}^{n_R}$), and transmitted over the second time

¹This assumption is realistic in many cases, e.g. assuming to have a relay close to the source (see Chapter 4).

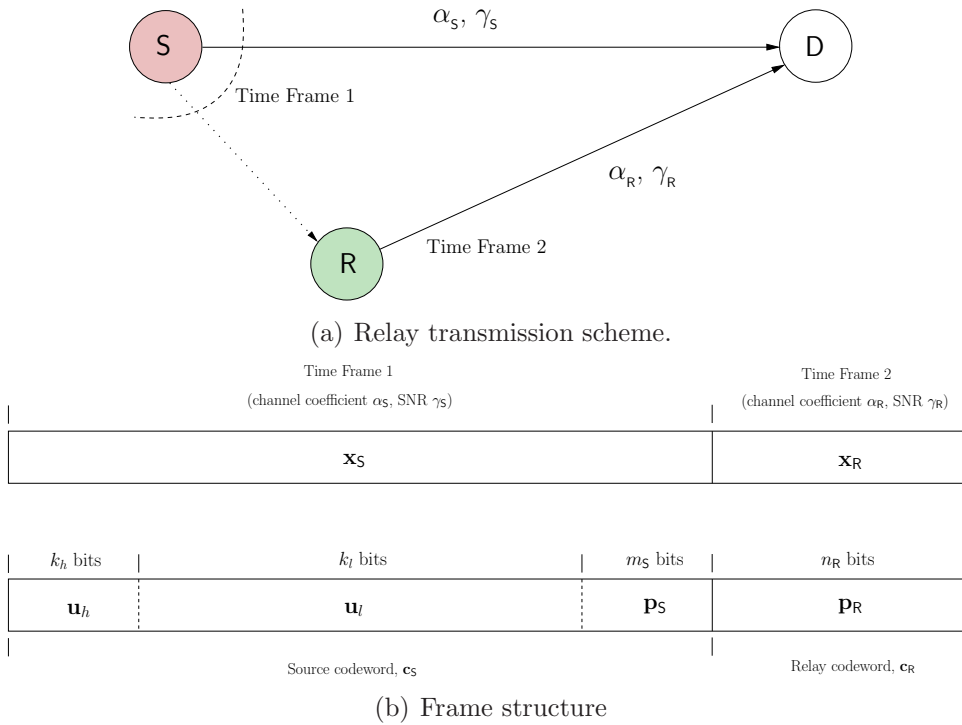


Figure 5.1: Overview of the transmission scheme and of the frame structure.

slot. A corrupted version of \mathbf{x}_R is received at the destination as

$$\mathbf{y}_R = \alpha_R \mathbf{x}_R + \mathbf{n}_R, \quad (5.2)$$

where α_R follows a Rayleigh distribution with $\mathbb{E}[\alpha_R^2] = 1$, and where the elements \mathbf{n}_R are i.i.d. Gaussian random variables with variance $\sigma_n^2 = N_0/2$. The instantaneous SNR is given by $\gamma_R = \alpha_R^2/2\sigma_n^2$.

At the receiver side, the joint observation $\mathbf{y} = [\mathbf{y}_S | \mathbf{y}_R]$ is formed and it is input to the decoder for the joint code \mathcal{C} whose task is to retrieve the code word $\mathbf{x} = [\mathbf{x}_S | \mathbf{x}_R]$, where the two blocks $\mathbf{x}_S, \mathbf{x}_R$ experience two independent fading levels α_S, α_R .

5.1.1 Parity-Check Matrix Structure and Diversity

The overall \mathcal{C} code parity-check matrix will have form

$$\mathbf{H} = \left[\begin{array}{c|c|c} \mathbf{H}_S & & \mathbf{0} \\ \hline \mathbf{M} & \mathbf{0} & \mathbf{P} \end{array} \right], \quad (5.3)$$

where the \mathbf{H}_S is the $m_S \times n_S$ parity-check matrix of the code \mathcal{C}_S and where \mathcal{C}_R has extended $n_R \times (k_h + n_R)$ parity-check matrix in the form $\mathbf{H}_R^e = [\mathbf{M} | \mathbf{P}]^2$ where \mathbf{M} is a $n_R \times k_h$ associated with the information bits in \mathbf{u}_h (which are not transmitted by the relay), and

²Note that $\mathbf{H}_R^e[\mathbf{u}_h, \mathbf{p}_R]^T = \mathbf{0}^T$, i.e. \mathbf{H}_R^e is the parity-check matrix of the augmented code obtained by concatenating \mathbf{u}_h and \mathbf{p}_R [68].

\mathbf{P} is the $n_R \times n_R$ matrix associated with the parity vector \mathbf{p}_R . Note that the final code length is $n = n_s + n_R$, and the overall code rate is $R = k/(n_s + n_R)$.

Among the possible decoding strategies, two possibilities deserve particular interest. A first (optimum) approach deals with joint decoding of the two codes $\mathcal{C}_S, \mathcal{C}_R$ composing the distributed code \mathcal{C} . A low-complexity alternative is represented by a scheme which decodes \mathcal{C}_S and \mathcal{C}_R separately,³ and depending on the decoders outcome delivers either u_h or u_l , or both (or none of them, if none of the decoders is successful).⁴ Note that in both cases the high-priority fragment achieves diversity of order 2 if $\text{rank}(\mathbf{M}) = k_h$, i.e. if each non-zero codeword of the augmented code having parity-check matrix \mathbf{H}_R^e has its support spread over \mathbf{u}_h and \mathbf{p}_R .

In the next section we will show that this behavior can be achieved by a distributed LDPC scheme under joint iterative decoding of \mathcal{C} . Consider the parity-check matrix \mathbf{H}_S of the code \mathcal{C}_S , where \mathcal{C}_S is a low-density parity-check code. Moreover, we assume \mathcal{C}_R to be a non-systematic low-density parity-check code with extended low-density parity-check matrix in the form $\mathbf{H}_R^e = [\mathbf{M}|\mathbf{P}]$. The overall \mathcal{C} code parity-check matrix will be low density. Decoding can thus be performed on the Tanner graph associated with \mathbf{H} .

5.2 Unequal Diversity Protographs

The code structure presented in the previous section can be suitably realized by means of protograph LDPC code constructions. A protograph [60, 62, 69] is a Tanner graph [70] with a relatively small number of nodes. A protograph $\mathcal{G} = (\mathcal{V}, \mathcal{C}, \mathcal{E})$ consists of a set of N variable nodes \mathcal{V} , a set of M check nodes \mathcal{C} , and a set of edges \mathcal{E} . Each edge $e_{i,j} \in \mathcal{E}$ connects a variable node $V_j \in \mathcal{V}$ to a check node $C_i \in \mathcal{C}$. Multiple parallel edges are permitted. A larger graph can be obtained by a copy-and-permute procedure: the protograph is copied q times, and then the edges of the individual replicas are permuted among the q replicas. The *derived graph* will consist of $n = Nq$ variable nodes and $m = Mq$ check nodes. A protograph can be described by a *base matrix* \mathbf{B} of size $M \times N$. The element $b_{i,j}$ of \mathbf{B} represents the number of edges connecting the variable node V_j to the check node C_i .

We introduce the concepts of source protograph \mathcal{G}_S , by which we denote the protograph for the (high-rate) code employed at the source, and of relay protograph \mathcal{G}_R , which refers to the code employed at the relay. The two protographs are connected via the VNs associated with the bits of \mathbf{u}_h . The union of the two protographs gives rise to the distributed protograph \mathcal{G} , which defines the distributed LDPC code ensemble employed by the cooperative scheme. The scheme can be seen as a distributed parallel concatenation

³Alternatively, one may consider forwarding the decision of the decoder associated with \mathcal{C}_R (if successful) to the decoder associated with \mathcal{C}_S . This has the effect of shortening \mathcal{C}_S thus facilitating the recovery of u_l

⁴We assume that an error detection mechanism provides a validation of the decoders output.

of two block codes [71] involving only a fraction of information bits.

Example 1 - Rate 7/10 protograph. A first protograph example is depicted in Figure 5.2. The protograph relates to a rate $R = 7/10$ ensemble and consists of a parallel concatenation of a rate $R_s = 7/8$ IRA protograph \mathcal{G}_s with base matrix

$$\mathbf{B}_s = [4 \ 4 \ 4 \ 4 \ 4 \ 4 \ 4 \ 2] \quad (5.4)$$

and a rate $R_r = 1/2$ non-systematic repeat accumulate (RA) protograph \mathcal{G}_r with base matrix

$$\mathbf{B}_r = \begin{bmatrix} 1 & 1 & 1 \\ 1 & 1 & 1 \end{bmatrix}, \quad (5.5)$$

The overall distributed protograph \mathcal{G} possesses a base matrix

$$\mathbf{B} = \begin{bmatrix} 4 & 4 & 4 & 4 & 4 & 4 & 4 & 2 & 0 & 0 \\ 1 & 0 & 0 & 0 & 0 & 0 & 0 & 0 & 1 & 1 \\ 1 & 0 & 0 & 0 & 0 & 0 & 0 & 0 & 1 & 1 \end{bmatrix}. \quad (5.6)$$

5.3 Protograph EXIT Analysis over BFC

In the following, we will consider protograph ensembles over non-ergodic BFCs. More specifically, we will consider a BFC with N fading levels, one for each protograph VN. Roughly speaking, the protograph VNs will *see* independent channels with different SNRs, distributed as

$$f_\gamma(\gamma) = \frac{1}{\gamma} e^{-\frac{\gamma}{\gamma}}, \quad (5.7)$$

for $\gamma \geq 0$, while $f_\gamma(\gamma) = 0$ for $\gamma < 0$. We will first modify the PEXIT of [61,62] to handle the BFC setting. Then, convergence regions will be defined and the asymptotic ensemble error probability will be analyzed. The results presented in this section will allow the analysis of protograph ensembles over the block-fading relay channel.

5.3.1 Protograph EXIT Analysis

In the following we will focus on a protograph \mathcal{G} with N variable nodes and M check nodes, and the corresponding $M \times N$ base matrix \mathbf{B} . Each variable node is allowed to see a different channel. Define $I_{ch}^{(j)}$ the channel mutual information (MI) at the input of the j -th node. Define:

$I_{Ev}(i, j)$: the MI between the message sent by V_j to C_i and the associated codeword bit, on one of the $b_{i,j}$ edges connecting V_j to C_i . ($I_{Ev}(i, j) = 0$ if $b_{i,j} = 0$)

$I_{Ec}(i, j)$: the MI between the message sent by C_i to V_j and the associated codeword bit, on one of the $b_{i,j}$ edges connecting C_i to V_j . ($I_{Ec}(i, j) = 0$ if $b_{i,j} = 0$)

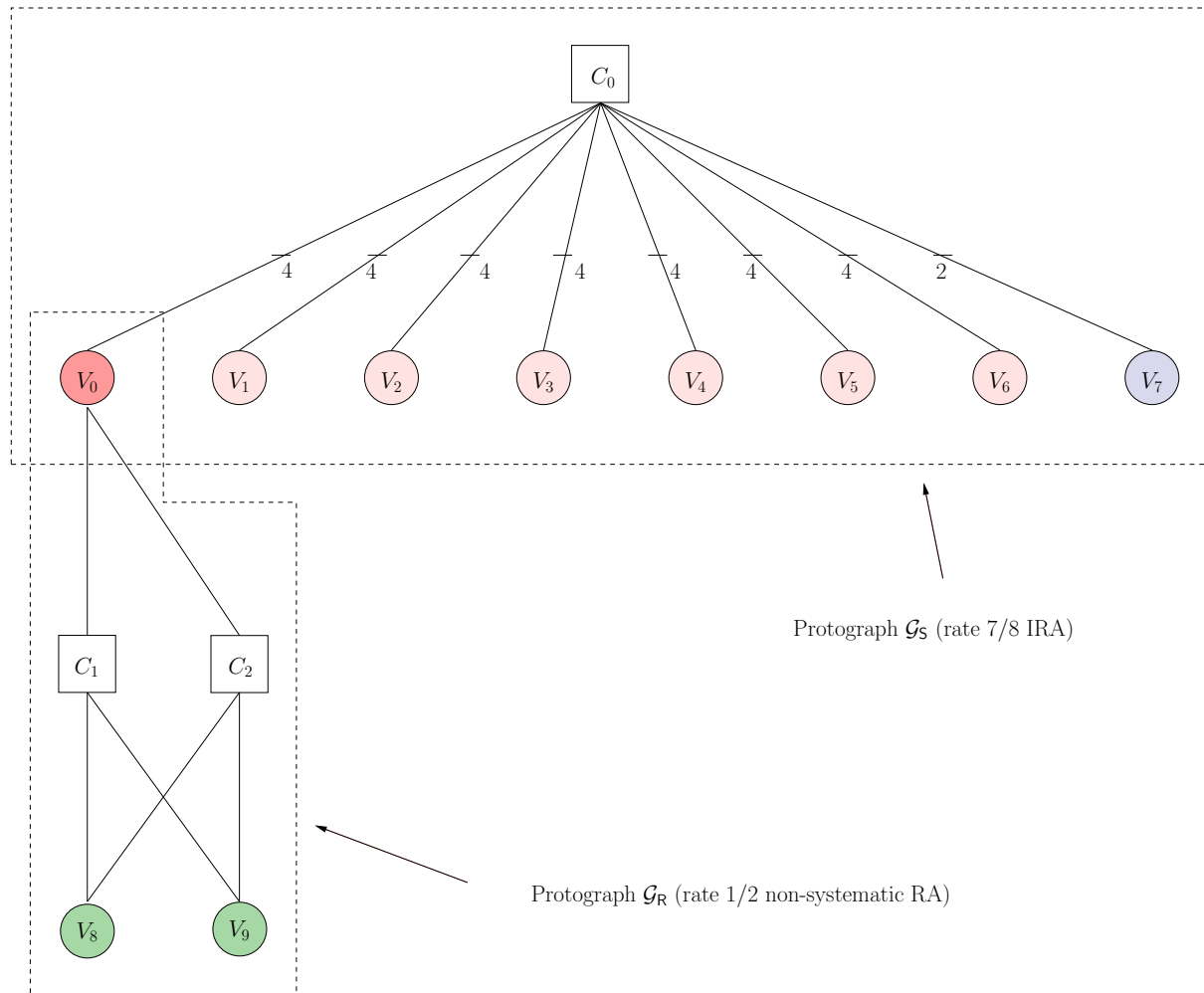


Figure 5.2: Protograph from the Example 1. The IRA code is adopted at the source, whereas the RA is used for encoding the high-priority fragment at the relay. The first column of \mathbf{B}_R is hence associated with the high-priority fragment (VN V_0 in the protograph), which is not transmitted by the relay.

$I_{APP}(j)$: the MI between the a-posteriori probability (APP) log-likelihood ratio (LLR) (modeled as a random variable)

$$L^{(j)} = \ln \frac{Pr(x_j = +1|\mathbf{y})}{Pr(x_j = -1|\mathbf{y})}, \quad (5.8)$$

evaluated by V_j and the associated codeword bit x_j .

Suppose a variable node V_j connected to C_i (i.e., $b_{i,j} \neq 0$). The mutual information between the message sent by V_j to C_i and the associated codeword bit, over one of the $b_{i,j}$ edges connecting the nodes, will be a function of

- the channel MI $I_{ch}^{(j)}$;
- the a priori MI received by V_j on each of the $b_{s,j}$ edges connecting V_j to C_s , with $s \neq i$, weighted by $b_{s,j}$;
- the a priori MI received by V_j on each of the $(b_{i,j} - 1)$ edges connecting V_j to C_i , weighted by $(b_{i,j} - 1)$.

The MI between the message sent by C_i to V_j and codeword bit associated to V_j , over one of the $b_{i,j}$ edges connecting the nodes, will be a function of

- the a priori MI received by C_i on each of the $b_{i,s}$ edges connecting C_i to V_s , with $s \neq i$, weighted by $b_{i,s}$;
- the a priori MI received by C_i on each of the $(b_{i,j} - 1)$ edges connecting C_i to V_j , weighted by $(b_{i,j} - 1)$.

The MI between the a posteriori probability log-likelihood ratio $L^{(j)}$ evaluated by V_j and the associated codeword bit will depend on the MI of all the incoming messages of V_j .

Once the above-mentioned functions have been obtained for a generic channel, and once the channel nuisance parameter has been fixed, the MI evolution along the edges of the graph can be computed iteratively, recalling that the MI on an edge connecting V_j and C_i , at the output of the variable node, is the a priori MI for C_i , i.e., $I_{Ev}(i, j) = I_{Ac}(i, j)$. Similarly, $I_{Ec}(i, j) = I_{Av}(i, j)$. At each iteration a set of $I_{APP}(j)$, with $i = 0 \dots N - 1$, is produced. The successful convergence is declared if each $I_{APP}(j)$ reaches 1 as the iteration number tends to infinity.

The extrinsic information transfer (EXIT) functions for variable/check nodes on the AWGN channel have been introduced in [72]. We denote with $J(\sigma)$ the MI between a binary random variable X , with $Pr(X = +\mu) = 1/2$ and $Pr(X = -\mu) = 1/2$, and a continuous Gaussian-distributed random variable Y with mean X and variance $\sigma^2 = 2\mu$

(symmetry condition). $J(\sigma)$ represents the capacity of a binary-input additive Gaussian noise channel, and it is given by [73]

$$J(\sigma) = 1 - \int_{-\infty}^{+\infty} \frac{1}{\sqrt{2\pi\sigma^2}} e^{-\frac{(y-\sigma^2/2)^2}{2\sigma^2}} \cdot \log_2(1 + e^{-y}) dy. \quad (5.9)$$

Note that simple polynomial approximations of functions $J(\cdot)$ and $J^{-1}(\cdot)$ are available in [72].

The PEXIT analysis presents an initialization step, which provides the channel MI for given channel parameters. A variable-to-check node update step follows. The third step provides the check-to-variable node update, and is based on the reciprocal channel approximation (RCA) [74,75]. The last step consists of the APP-LLR mutual information evaluation at each VN.

1. Initialization

Initialize $I_{ch}^{(j)} = J(\sigma_{ch,j})$, $\forall j = 0 \dots N - 1$, with

$$\sigma_{ch,j}^2 = 8\gamma^{(j)}$$

where $\gamma^{(j)}$ represents the signal-to-noise ratio associated to the channel input to the j -th variable node. We define the *channel profile* as the vector of instantaneous SNRs $\boldsymbol{\gamma} = [\gamma^{(0)}, \gamma^{(1)}, \dots, \gamma^{(N-1)}]$. Note that for punctured VNs (which may occur in capacity-approaching protographs [76]) the corresponding SNR is set to 0.

2. Variable to check update

For $j = 0, \dots, N - 1$ and $i = 0, \dots, M - 1$, if $b_{i,j} \neq 0$,

$$I_{Ev}(i, j) \approx \frac{J\left(\sqrt{\sum_{s \neq i} b_{s,j} [J^{-1}(I_{Av}(s, j))]^2} + (b_{i,j} - 1) [J^{-1}(I_{Av}(i, j))]^2 + [J^{-1}(I_{ch}^{(j)})]^2}\right)}{+ (b_{i,j} - 1) [J^{-1}(I_{Av}(i, j))]^2 + [J^{-1}(I_{ch}^{(j)})]^2}.$$

If $b_{i,j} = 0$, $I_{Ev}(i, j) = 0$.

3. For $j = 0, \dots, N - 1$ and $i = 0, \dots, M - 1$, set $I_{Ac}(i, j) = I_{Ev}(i, j)$.

4. Check to variable update

For $j = 0, \dots, N - 1$ and $i = 0, \dots, M - 1$, if $b_{i,j} \neq 0$,

$$I_{Ec}(i, j) \approx \frac{1 - J\left(\sqrt{\sum_{s \neq j} b_{i,s} [J^{-1}(1 - I_{Ac}(i, s))]^2} + (b_{i,j} - 1) [J^{-1}(1 - I_{Ac}(i, j))]^2}\right)}{+ (b_{i,j} - 1) [J^{-1}(1 - I_{Ac}(i, j))]^2}.$$

If $b_{i,j} = 0$, $I_{Ec}(i, j) = 0$.

5. For $j = 0, \dots, N - 1$ and $i = 0, \dots, M - 1$, set $I_{Av}(i, j) = I_{Ec}(i, j)$.

6. APP-LLR mutual information evaluation

For $j = 0, \dots, N - 1$,

$$I_{APP}(j) \approx J \left(\sqrt{\sum_s b_{s,j} [J^{-1}(I_{Av}(i, j))]^2 + [J^{-1}(I_{ch}^{(j)})]^2} \right).$$

The steps 2-6 are iterated until $I_{APP}(j) = 1, \forall j$, or a maximum number of iterations (I_{max}) is reached. For a given channel profile γ the convergence of a VN V_j APP to $I_{APP}(j) = 1$ means that, for the codeword bits associated with the j -th VN type, a vanishing error probability is achieved in the asymptotic setting.

5.3.2 Outage Regions and Asymptotic Error Probability

We shall adapt next the definition outage region for a code ensemble introduced in [66] to protograph ensembles. More specifically, we will introduce the concept of outage regions for the protograph nodes

Definition 1 (Convergence region of a protograph VN). *We identify by*

$$\mathcal{D}^{(j)} = \{\gamma \in \mathbb{R}_+^N | I_{APP}(j) \rightarrow 1\}$$

as the N -dimensional convergence region of the VN V_j , for $I_{max} \rightarrow \infty$.

Definition 2 (Outage region of a protograph VN). *We identify by*

$$\overline{\mathcal{D}}^{(j)} = \{\gamma \in \mathbb{R}_+^N | \exists \theta > 0 \text{ s.t. } I_{APP}(j) < 1 - \theta\}$$

the N -dimensional outage region of the VN V_j , for $I_{max} \rightarrow \infty$.

The outage region of V_j thus defines the set of SNR profiles for which an arbitrarily-small bit error probability cannot be achieved, even if the number of decoding iterations is left unbounded.

Clearly, the outage region and the convergence region of a protograph VN are complementary, i.e. $\mathcal{D}^{(j)} \cup \overline{\mathcal{D}}^{(j)} \equiv \mathbb{R}_+^N$. Similar definitions hold for the entire protograph, as follows.

Definition 3 (Convergence region of a protograph \mathcal{G}). *We identify by*

$$\mathcal{D}_{\mathcal{G}} = \{\boldsymbol{\gamma} \in \mathbb{R}_+^N | I_{APP}(j) \rightarrow 1, \forall j\}$$

the N -dimensional convergence region of \mathcal{G} , for $I_{max} \rightarrow \infty$.

Definition 4 (Outage region of a protograph \mathcal{G}). *We identify by*

$$\overline{\mathcal{D}}_{\mathcal{G}} = \{\boldsymbol{\gamma} \in \mathbb{R}_+^N | \exists j \text{ and } \exists \theta > 0 \text{ s.t. } I_{APP}(j) < 1 - \theta\}$$

the N -dimensional outage region of \mathcal{G} , for $I_{max} \rightarrow \infty$.

The outage region of a protograph thus defines the set of SNR profiles for which there is at least an VN whose bit error probability cannot be made arbitrarily small, even if the number of decoding iterations is left unbounded.

Under actual density evolution (DE), the average ensemble block error probability can be lower-bounded⁵ as [79]

$$P_B \geq \int_{\overline{\mathcal{D}}_{\mathcal{G}}} \prod_{i=0}^{N-1} f_{\gamma}(\gamma^{(i)}) d\gamma^{(i)}, \quad (5.10)$$

while the average ensemble bit error probability can be calculated as

$$\overline{P}_b = \mathbb{E}_{\boldsymbol{\gamma}} [P_b(\boldsymbol{\gamma})] \quad (5.11)$$

$$= \int_0^{\infty} \int_0^{\infty} \dots \int_0^{\infty} P_b(\boldsymbol{\gamma}) \prod_{i=0}^{N-1} f_{\gamma}(\gamma^{(i)}) d\gamma^{(i)} \quad (5.12)$$

where $P_b(\boldsymbol{\gamma})$ is the bit error probability averaged over the different protograph VNs for a given channel profile $\boldsymbol{\gamma}$,

$$P_b(\boldsymbol{\gamma}) = \frac{1}{N} \sum_{i=0}^{N-1} P_b^{(i)}(\boldsymbol{\gamma}) \quad (5.13)$$

and where the bit error probability associated with the i -th VN is obtained as

$$P_b^{(i)}(\boldsymbol{\gamma}) \approx \frac{1}{2} \operatorname{erfc} \left(\frac{1}{2\sqrt{2}} J^{-1}(I_{APP}(i)) \right). \quad (5.14)$$

Note that

$$\overline{P}_b = \frac{1}{N} \sum_{i=0}^{N-1} \int_{\overline{\mathcal{D}}^{(i)}} P_b^{(i)}(\boldsymbol{\gamma}) \prod_{j=0}^{N-1} f_{\gamma}(\gamma^{(j)}) d\boldsymbol{\gamma}. \quad (5.15)$$

⁵The convergence to a vanishing bit error probability does not represent always a sufficient condition for the convergence to a vanishing block error probability [77, 78]. Nevertheless, the bound Equation 5.10 can be confidently used to estimate the block error probability of finite length LDPC codes in many practical cases [79].

This expression can be simplified by observing that $P_b^{(i)}(\gamma) \leq 1/2 \forall \gamma \in \overline{\mathcal{D}}^{(i)}$, leading to the upper bound

$$\overline{P}_b \leq \frac{1}{2N} \sum_{i=0}^{N-1} \int_{\overline{\mathcal{D}}^{(i)}} \prod_{j=0}^{N-1} f_\gamma(\gamma^{(j)}) d\gamma^{(j)}. \quad (5.16)$$

Furthermore, observe that $\overline{\mathcal{D}}^{(i)} \subseteq \overline{\mathcal{D}}_g$, hence

$$\overline{P}_b \leq \frac{1}{2N} \sum_{i=0}^{N-1} \int_{\overline{\mathcal{D}}_g} \prod_{j=0}^{N-1} f_\gamma(\gamma^{(j)}) d\gamma^{(j)} \quad (5.17)$$

$$= \frac{1}{2} \int_{\overline{\mathcal{D}}_g} \prod_{i=0}^{N-1} f_\gamma(\gamma^{(i)}) d\gamma^{(i)}. \quad (5.18)$$

We underline that the above-derived bounds and equations hold under actual DE, whereas the EXIT analysis relies on the Gaussian approximation. Hence, all the bounds and equalities based on EXIT analysis have to be considered as approximations. We recall next the definition of diversity for a protograph code and we extend it to single protograph VNs.

Definition 5 (Diversity of a protograph). *The diversity achieved by a protograph is finally defined as [43]*

$$d = \lim_{\overline{\gamma} \rightarrow \infty} -\frac{\log \overline{P}_b}{\log \overline{\gamma}}.$$

Definition 6 (Diversity of a protograph VN). *Extending the definition of diversity, the diversity of the i -th VN is finally defined as*

$$d_i = \lim_{\overline{\gamma} \rightarrow \infty} -\frac{\log \overline{P}_b^{(i)}}{\log \overline{\gamma}}$$

where

$$\overline{P}_b^{(i)} = \mathbb{E}_\gamma \left[P_b^{(i)}(\gamma) \right] \quad (5.19)$$

$$= \int_0^\infty \int_0^\infty \dots \int_0^\infty P_b^{(i)}(\gamma) \prod_{j=0}^{N-1} f_\gamma(\gamma^{(j)}) d\gamma^{(j)}. \quad (5.20)$$

The UEP property of the protographs presented in this paper resides in assigning the high-priority fragments to the nodes with largest diversity.

5.4 Outage Analysis for the Relay Channel

The above-presented analysis can be easily adapted to the case of the relay channel with quasi-static fading. More specifically, we shall set to $\gamma^{(j)} = \gamma_s$ for all the protograph VNs associated with fragments transmitted over the source-destination channel. For the

protograph VNs associated with fragments transmitted over the relay-destination channel we shall set $\gamma^{(j)} = \gamma_{\text{R}}$. We denote by \mathcal{V}_h as the set of protograph VNs associated with high-priority fragments (thus, having the largest diversity), and by \mathcal{V}_l as the set of protograph VNs associated with low-priority fragments. The convergence regions of the variable nodes in \mathcal{V}_h , \mathcal{V}_l depend on γ_{S} and γ_{R} only. Thus, they can be conveniently represented on the 2-dimensional $\gamma_{\text{S}} \times \gamma_{\text{R}}$ plane.

Definition 7 (Convergence region of high-priority fragments for a protograph \mathcal{G}). We identify by

$$\mathcal{D}_h = \{\gamma_{\text{S}}, \gamma_{\text{R}} | I_{APP}(j) = 1, \forall V_j \in \mathcal{V}_h, I_{max} \rightarrow \infty\}$$

the 2-dimensional convergence region of the high-priority fragments for the \mathcal{G} .

Definition 8 (Convergence region of low-priority fragments for a protograph \mathcal{G}). We identify by

$$\mathcal{D}_l = \{\gamma_{\text{S}}, \gamma_{\text{R}} | I_{APP}(j) = 1, \forall V_j \in \mathcal{V}_l, I_{max} \rightarrow \infty\}$$

the 2-dimensional convergence region of the low-priority fragments for the \mathcal{G} .

The corresponding complementary non-convergence (outage) regions are given by $\overline{\mathcal{D}}_h$ and $\overline{\mathcal{D}}_l$.

The asymptotic (in the block length) FEPs associated with high and low-priority fragments can be bounded by

$$P_F^{(h)} \geq \int_{\overline{\mathcal{D}}_h} f_{\gamma}(\gamma_{\text{S}}) f_{\gamma}(\gamma_{\text{R}}) d\gamma_{\text{S}} d\gamma_{\text{R}}, \quad (5.21)$$

$$P_F^{(l)} \geq \int_{\overline{\mathcal{D}}_l} f_{\gamma}(\gamma_{\text{S}}) f_{\gamma}(\gamma_{\text{R}}) d\gamma_{\text{S}} d\gamma_{\text{R}}. \quad (5.22)$$

Example 1 - Rate 7/10 protograph. Figure 5.3(a) depicts the convergence regions for the high- and the low-priority fragments associated with the protograph of Figure 5.2 on the $\gamma_{\text{S}} \times \gamma_{\text{R}}$ plane (linear scale). A few observations follow.

- A. When fixing $\gamma_{\text{S}} = 0$, the border of the convergence region of the high priority fragment is at $\gamma_{\text{R}} = \gamma_{\text{R}}^* \simeq 1.03$ (0.142 dB, point A in the chart), which is the decoding threshold over the AWGN channel for the protograph associated with the base matrix \mathbf{B}_{R} .
- B. When fixing $\gamma_{\text{R}} = 0$, the border of the two convergence regions is given by $\gamma_{\text{S}} = \gamma_{\text{S}}^* \simeq 1.86$ (2.709 dB, point B in the chart), which is the decoding threshold over the AWGN channel for the protograph associated with the base matrix \mathbf{B}_{S} .

- C. For increasing γ_R , the border of the convergence region of the low priority fragments moves leftwards, and for sufficiently large γ_R it achieves the value $\gamma_s = \gamma'_s \simeq 1.74$ (2.42 dB, point C in the chart), which is the decoding threshold over the AWGN channel for the protograph associated with the base matrix

$$\mathbf{B}_{S'} = [4 \ 4 \ 4 \ 4 \ 4 \ 4 \ 2], \quad (5.23)$$

i.e. with a shortened version of the base matrix \mathbf{B}_s , where the first column (VN V_0 in the protograph) is removed due to the infinite reliability associated with the extrinsic information provided by the RA adopted at the relay (operated in its convergence region).

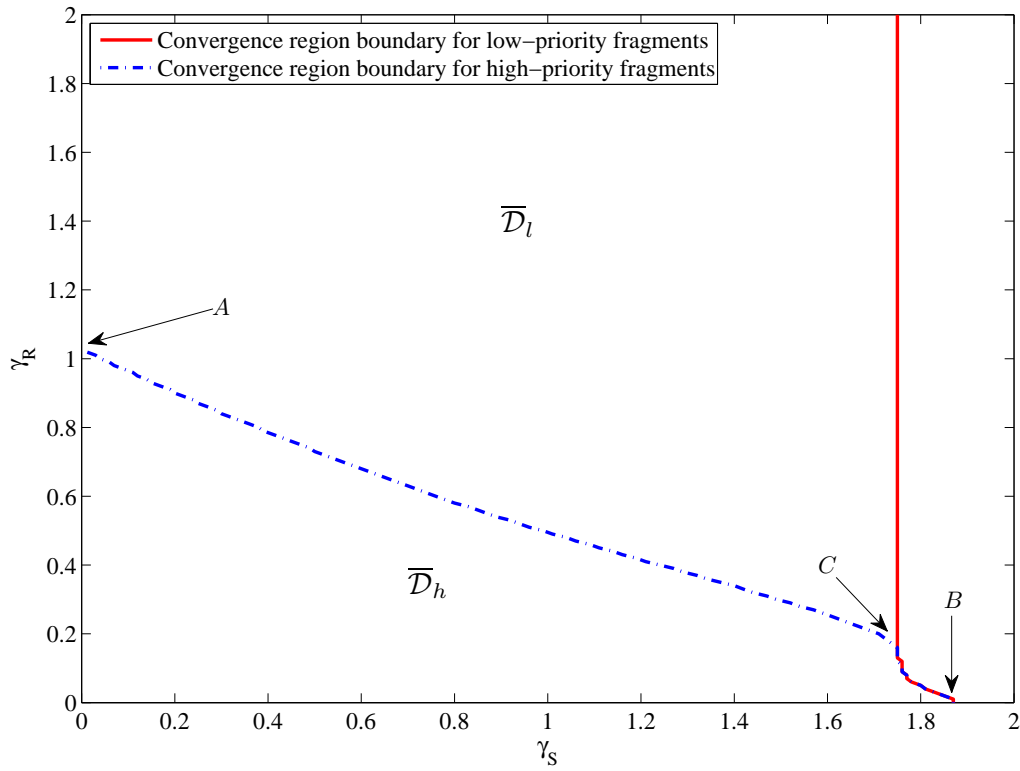
The evaluation of Equations 5.21 and 5.22 is provided in Figure 5.3(b) vs. the average SNR $\bar{\gamma}$, together with simulation results for the fragment error rate (FER) of a $n = 2560$ code obtained by a 256-fold expansion of the protograph of Figure 5.2. The expansion has been performed in 2 steps via a circulant version of the progressive edge growth (PEG) algorithm [80], leading to structured (quasi-cyclic) IRA [81] and RA [82] codes at the source and at the relay respectively. The accuracy of the analysis is evident down to the simulated FERs (10^{-5}), and confirms the different levels of diversity attained by the different node types.

5.4.1 On the Protograph Design

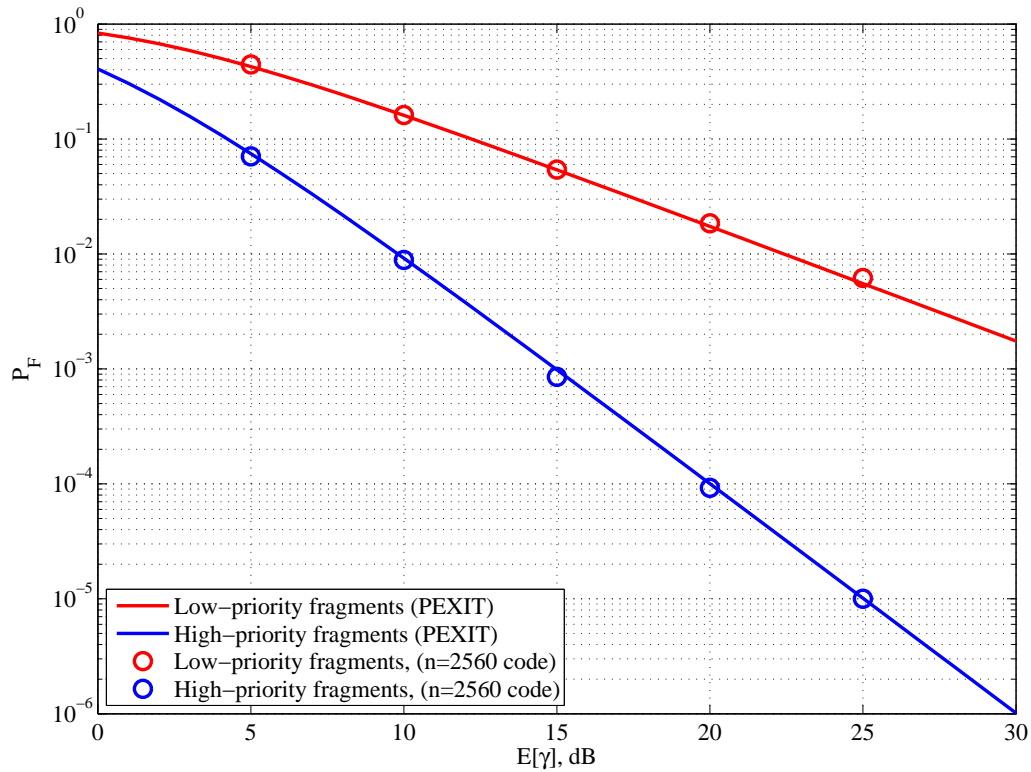
We illustrate next a sufficient condition for achieving diversity-2 high-priority fragments with the proposed protograph construction.

Proposition 1. *A sufficient condition for having diversity-2 high-priority nodes consists of having finite iterative decoding thresholds γ_s^* , γ_r^* for the protographs \mathcal{G}_s and \mathcal{G}_r , respectively.*

Proof. We resort to the sub-optimum decoding algorithm, which decodes separately the codes $\mathcal{C}_s, \mathcal{C}_r$ at the destination. Again, we assume that both γ_s, γ_r are distributed as $f_\gamma(\gamma) = \bar{\gamma}^{-1} \exp(\gamma/\bar{\gamma})$ for $\gamma \geq 0$. Denote by $P_b^{(1)}$ the bit error probability associated to the transmission with \mathcal{C}_s over the source-destination channel (averaged over all the node types of \mathcal{G}_s). Under the assumption of static fading, for large $\bar{\gamma}$, $P_b^{(1)} \sim \bar{\gamma}^{-1}$ for large $\bar{\gamma}$, since $P_b^{(1)} \leq \int_0^{\gamma_s^*} f_\gamma(\gamma) d\gamma = 1 - \exp(-\gamma_s^*/\bar{\gamma}) \sim \bar{\gamma}^{-1}$ for large $\bar{\gamma}$. Similarly, for large $\bar{\gamma}$, considering the bit error probability associated with the transmission with \mathcal{C}_r over the relay-destination channel (averaged over all the node types of \mathcal{G}_r), we have $P_b^{(2)} \sim \bar{\gamma}^{-1}$, since $P_b^{(2)} \leq \int_0^{\gamma_r^*} f_\gamma(\gamma) d\gamma = 1 - \exp(-\gamma_r^*/\bar{\gamma}) \sim \bar{\gamma}^{-1}$. For large $\bar{\gamma}$, the bit error probability associated with the high priority fragment is $P_b^{(h)} \leq (n_s/k_h) \cdot P_b^{(1)} \cdot ((n_r + k_h)/k_h) \cdot P_b^{(2)} \sim \bar{\gamma}^{-2}$. \square



(a) Outage regions for the high- and the low-priority fragments.



(b) FER performance vs. average SNR, compared with Equations 5.21 and 5.22.

Figure 5.3: Outage regions and FEP for the protograph of Example 1.

A simple design rule may thus consist in optimizing (separately) the protographs \mathcal{G}_S and \mathcal{G}_R with respect to their thresholds γ_S^* , γ_R^* .

Example 2 - Rate 7/10 protograph. In order to improve the coding gain achieved for high-priority fragments by the protograph of Example 1, we designed a second protograph with base matrix

$$\mathbf{B} = \begin{bmatrix} 16 & 6 & 3 & 3 & 3 & 3 & 3 & 2 & 0 & 0 \\ 2 & 0 & 0 & 0 & 0 & 0 & 0 & 0 & 1 & 1 \\ 1 & 0 & 0 & 0 & 0 & 0 & 0 & 0 & 1 & 1 \end{bmatrix}, \quad (5.24)$$

which is obtained by concatenating a rate 7/8 IRA code with base matrix

$$\mathbf{B}_S = [16 \ 6 \ 3 \ 3 \ 3 \ 3 \ 3 \ 2] \quad (5.25)$$

with a rate 1/2 non-systematic IRA code with base matrix

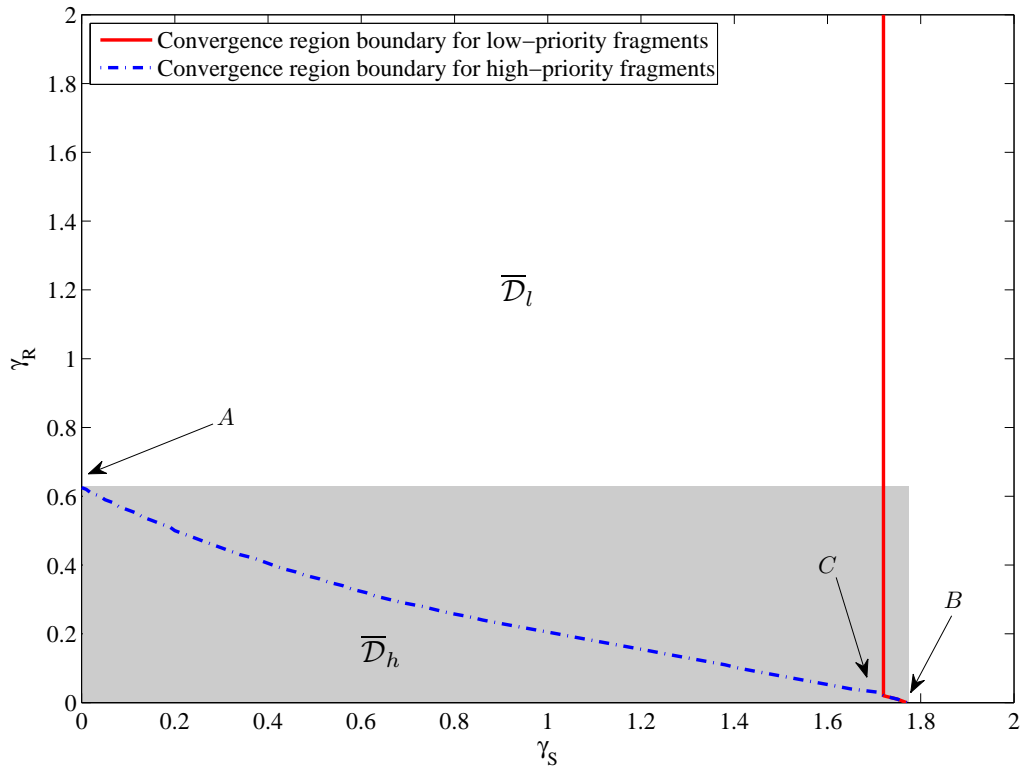
$$\mathbf{B}_R = \begin{bmatrix} 2 & 1 & 1 \\ 1 & 1 & 1 \end{bmatrix}, \quad (5.26)$$

where the first column corresponds to a punctured VN in the associated protograph \mathcal{G}_R (high-priority fragment). The new design aims at reducing the area associated with $\overline{\mathcal{D}}_h$ by lowering the iterative decoding thresholds of the protographs \mathcal{G}_S , \mathcal{G}_R , and hence by moving the points A and B of Figure 5.3(a) towards the origin of the $\gamma_S \times \gamma_R$ plane. The result is achieved in part thanks to the iterative decoding threshold of the non-systematic IRA protograph \mathcal{G}_R , that is $\gamma_R^* \simeq 0.63$ (−1.99 dB, with a $\simeq 2.1$ dB gain over the RA code of Example 1), and in part thanks to the threshold of the new IRA protograph \mathcal{G}_S , that is $\gamma_S^* \simeq 1.76$ (2.472 dB with a $\simeq 0.2$ dB gain over the IRA code of Example 1). For sake of completeness, we provide also the threshold associated with the base matrix

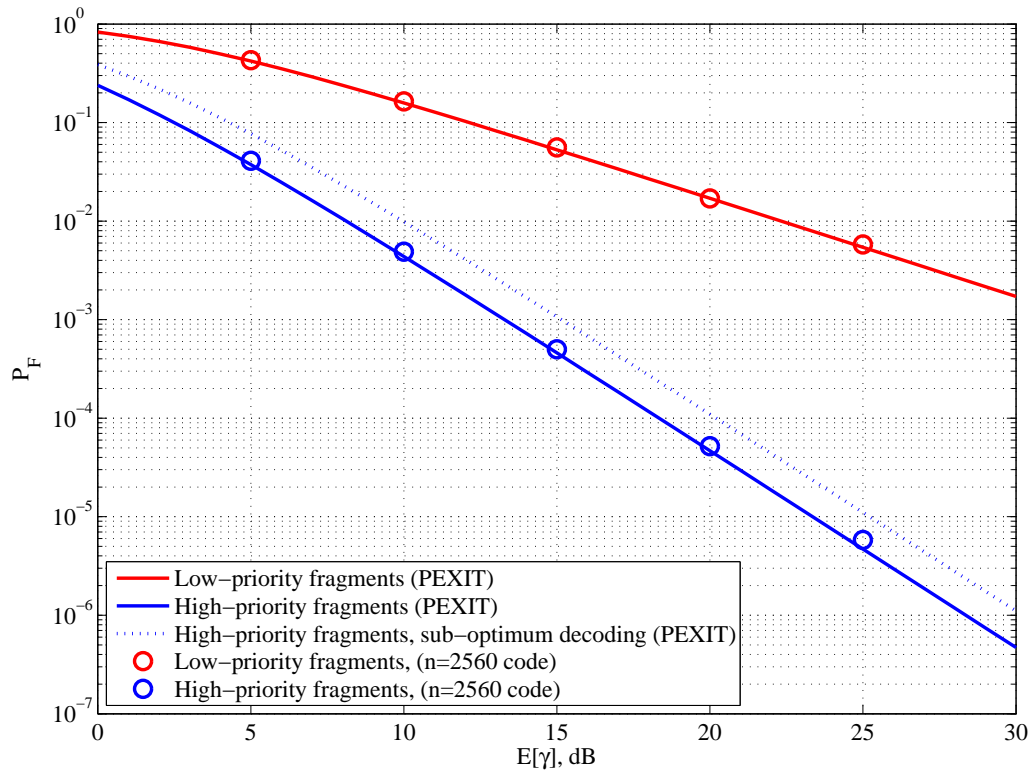
$$\mathbf{B}_{S'} = [6 \ 3 \ 3 \ 3 \ 3 \ 3 \ 2], \quad (5.27)$$

i.e. with a shortened version of the base matrix \mathbf{B}_S , where the first column is removed due to the infinite reliability associated with the extrinsic information provided by the IRA adopted at the relay (operated in its convergence region). The threshold is in this case at 2.347 dB, a slight improvement w.r.t. that of Example 1 (2.420 dB).

The convergence regions for the overall protograph are depicted in Figure 5.4(a), whereas the comparison between the evaluation of Equations 5.21 and 5.22 and the actual performance of a $n = 2560$ code is provided in Figure 5.4(b). Also for this code, the protograph expansion has been performed in 2 steps via a circulant version of the PEG algorithm [80]. The coding gain achieved by this second protograph is $\simeq 2$ dB larger w.r.t. that of the protograph of Example 1 for the high-priority fragment.



(a) Outage regions for the high- and the low-priority fragments.



(b) FER performance vs. average SNR, compared with Equations 5.21 and 5.22.

Figure 5.4: Outage regions and FEP for the protograph of Example 2.

5.4.2 On the Decoding Strategies

Consider the case where the codes \mathcal{C}_S , \mathcal{C}_R are decoded separately. Using the arguments of Section 5.3, we can argue that the fragment error probability associated with the high priority fragments bounded as

$$P_F^{(h)} \geq \int_0^{\gamma_S^*} \int_0^{\gamma_R^*} f_\gamma(\gamma_S) f_\gamma(\gamma_R) d\gamma_S d\gamma_R \quad (5.28)$$

$$= (1 - e^{(-\gamma_S^*/\bar{\gamma})}) (1 - e^{(-\gamma_R^*/\bar{\gamma})}), \quad (5.29)$$

Referring to Example 2, Equation 5.29 corresponds to the integration of $f_\gamma(\gamma_S)$, $f_\gamma(\gamma_R)$ over the rectangular gray-shaded area of Figure 5.4(a). Thus, the fragment error probability loss w.r.t. the joint decoder is given by the integration of $f_\gamma(\gamma_S)$, $f_\gamma(\gamma_R)$ over the gray-shaded area minus the non-convergence region $\bar{\mathcal{D}}_h$. The resulting coding gain loss due to the sub-optimum decoding is depicted in Figure 5.4(b), where Equation 5.29 is compared with the PEXIT prediction under joint iterative decoding. The loss is ~ 1.7 dB.

5.5 Application to AeroMACS

We applied the above-described theory to AeroMACS. The airport communications represent in fact a perfect candidate for the application of the UDC. The airport communication channel confirms the hypothesis considered in our analysis (i.e., slow Rayleigh fading). Especially in scenarios where the aircraft have a low speed or are not moving, as in the airport scenario, the channel can be approximated with a block fading channel. In this context, the communicating entities are aircraft (as illustrated in Chapter 4). Indeed, the relay terminal may be easily chosen in order to guarantee a very high SNR between source and relay, since often there is the possibility to select a relay that is standing close to the transmitting aircraft. Furthermore, the traffic profiles considered for aeronautical applications, which are defined by [83], include three different classes of messages with different priorities and requirements. Hence, the use of a method which implicitly provides different protection for different information constitutes a valuable feature.

Figure 5.5 shows the performance of AeroMACS with the proposed unequal diversity coding scheme. The results are provided in term of FER versus the average signal-to-noise ratio. Also in this case, we observe the behavior found in the previous evaluation. The packets with high-priority benefit of the diversity provided by the relay, while the low-priority ones (which don't) preserve the original performance. In this analysis, we accounted only one relay with two types of messages. However, this method can be extended to the case with more relays and messages.

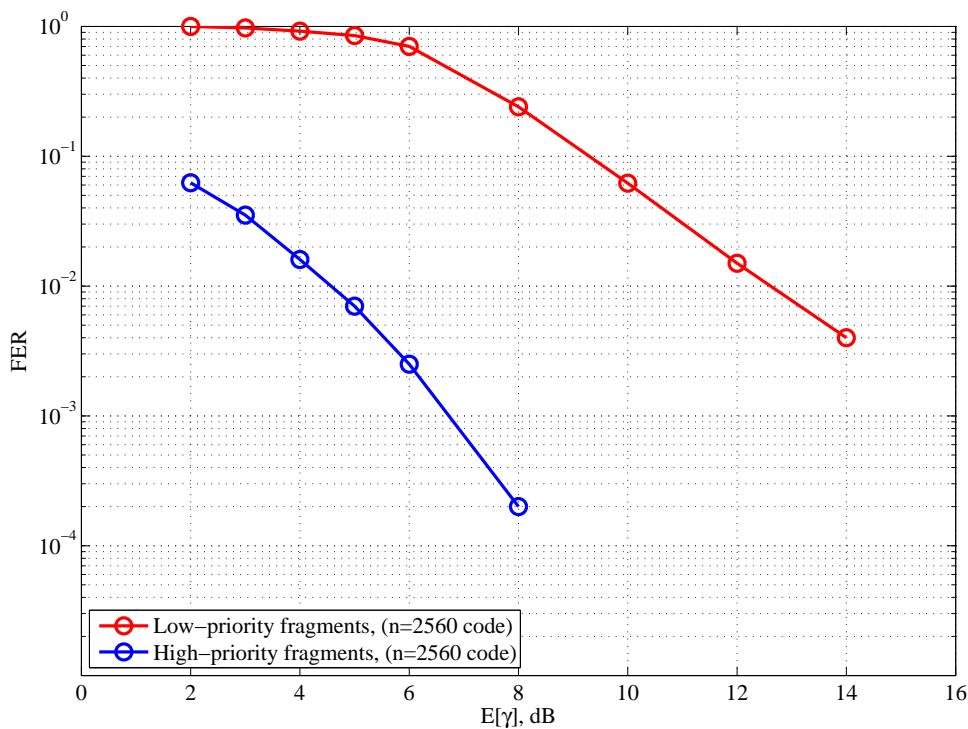


Figure 5.5: Performance of the proposed unequal diversity coding scheme in the airport context.

5.6 Summary

In this chapter, high-rate *UD* protograph LDPC code ensembles have been introduced. Their performance over the quasi-static relay fading channel has been analyzed through a novel PEXIT analysis, which allows accurately predicting the error probability associated with different codeword fragments. Protograph ensemble exhibiting the UD feature has been proposed, which are obtained via simple (parallel) concatenation of IRA/RA protographs. The proposed schemes allow combining coding efficiency (through high coding rates) with diversity for the high-priority parts of the source messages.

We applied the proposed method to AeroMACS, showing large performance gains for the high-priority part of the source message. The high-priority fragment enjoys indeed the presence of a relay link that increases the reliability of the transmission. Instead, the low-priority fragment does not benefit of any diversity and, hence, preserves the original performance⁶.

The UDC method provides a solution to the problem of the efficiency reduction of the cooperative relay techniques. Overall coding rate higher than 1/2 can be reached (in the example shown, the obtained overall rate is 7/10). However, this appealing result is achieved by sacrificing a part of the message. The low-priority segment, in fact, obtains no diversity or improvement.

⁶We refer to the performance provided by the system without any additional diversity techniques.

Chapter 6

Packet Level Coding

In many applications, erasure correcting codes are used to recover packet losses at high protocol stack layers. The objects (e.g. files) to be transmitted often have variable sizes, resulting in a variable number of packet to be encoded by the packet-level encoder.

In this chapter, algorithms for the (on-line) flexible design of parity-check matrices for irregular-repeat-accumulate codes are investigated. The proposed algorithms allow designing in fast manner parity-check matrices that are suitable for low-complexity maximum-likelihood decoding. The code ensembles generated by the proposed algorithms are analyzed via extrinsic information transfer charts. Numerical results show how the designed codes can attain codeword error rates as low as 10^{-5} without appreciable losses w.r.t. the performance of idealized maximum-distance separable codes.

The proposed packet level coding (PLC) approach is applied to the FL of AeroMACS, showing large performance improvement and proving the efficiency and the flexibility of the method. The FL represents in fact an ideal application case for the proposed packet erasure recovery scheme, due to the demand of high reliability, the airport channel characteristics (dominated by harsh fading and frequent shadowing conditions [24]), the large population of aircraft terminals and the broadcast nature of part of the traffic (which renders packet-level coding an appealing alternative to retransmission protocols [8, 84]). As a further remarkable added value, the proposed approach can be applied on top of the existing standard protocol stack, thus it does not require any expensive modification of the off-the-shelf hardware.¹

6.1 Introduction to Packet Level Coding Techniques

The application of error control codes to protocol stack layers different from the physical one gained a large interest during the past decade [7–11]. Such coding techniques deal with the use of a linear (block) code applied to *encoding units* (symbols) that are usually packets with constant size. In this context, a packet level encoder receives as input a set

¹A software implementation of maximum likelihood (ML) decoders for LDPC codes over packet erasure channels attaining data rates of 1.5 Gbps or more has been demonstrated in [85].

of k packets, and produces as output $n > k$ packets. Assuming systematic encoding, the final set of packets comprises the k information packets together with $m = n - k$ parity packets. At the receiver, after the physical layer decoding, the packets that have been validated (e.g. by an error detection code) are forwarded to the packet level decoder. The corrupted packets are discarded. Therefore, the upper layers deal with packet erasures. The packet level decoder may recover the erased packets by means of the parity packets. Packet level codes are employed in multimedia wireless broadcasting systems (see for example the DVB-H/SH standards [12, 13]), in multicast scenarios [14], and are currently investigated in space communication systems [15–17].

A specific class of powerful erasure correcting codes is that of LDPC codes [86]. It has been demonstrated that some LDPC code ensembles can asymptotically approach with an arbitrarily small gap the binary erasure channel (BEC) [87] capacity [88–90] under iterative (IT) decoding. Some problems, however, arise when constructing finite length (n, k) LDPC codes according to asymptotically optimal ensembles. Due to the sub-optimality of the IT decoder, at high error rates the performance curve, though usually good, denotes a coding gain loss with respect to that of the same code under ML decoding. At lower error rates the performance curve typically exhibits a high error floor caused by the presence of small size stopping sets [91]. In general, lowering the IT error floor implies a sacrifice in terms of coding gain at high error rates.

In [92, 93], a novel approach to the design of LDPC codes and decoders for the BEC was proposed, showing how a judicious code design together with an efficient ML decoding algorithm permits to achieve near-optimum performance (i.e., close to those of an idealized maximum-distance-separable (MDS) code, given by the Singleton bound) down to low error rates on the memory-less BEC with LDPC codes. The results were extended to correlated erasure channels in [94]. In [85] enhancements of the original LDPC ML decoding algorithm proposed in [95] were introduced, demonstrating decoding speeds up to several hundreds Mbps on an actual satellite communication link.

We address a further design aspect which was left uncovered in [92, 93]. More specifically, we aim at introducing techniques for fast, on-the-fly, algorithmic construction of the LDPC code parity-check matrix with the largest possible flexibility in the choice of the codes dimension and block length. In fact, in many applications the object (e.g., the file) to be transmitted has a variable size, resulting in a variable number of packets to be encoded. One may design a code with large input block size k and may perform code shortening for all the cases where the number of packets to be encoded is lower. In a similar manner, if the code rate has to be adapted to specific channel conditions, a low-rate code may be designed, and higher rates may be obtained by puncturing. However, shortening does not allow complete flexibility, since a maximum value of k has to be a-priori selected. Moreover, the selection of the codeword symbols to be zero-padded has to be performed in a careful manner to avoid degradations of the IT decoding threshold.² We

²Recall that a large gap between the IT decoding threshold and the BEC Shannon limit is responsible

thus investigate a flexible *on-line* code construction technique which allows designing in a fast (algorithmic) manner reasonably-good parity-check matrices for an arbitrary set of the (n, k) parameters.³ The code construction shall be based on a simple algorithm available at both the receiver and the transmitter. The adaptive packet level coding scheme may work as follows. Once the encoder receives the set of k packets to be encoded and the target code rate $R = k/n$ is selected, the set of parameters $\{n, k, \kappa\}$ is signaled to the receiver, being κ a parameter that drives the code construction (the significance of κ will be clarified in the following). On the transmitter side, a code $\mathcal{C}_{(n,k,\kappa)}$ is generated and used to encode the set of k packets. At the receiver, the $\{n, k, \kappa\}$ parameters are used to reconstruct the parity-check matrix of $\mathcal{C}_{(n,k,\kappa)}$, which is then used for the erasure decoding. The parameters $\{n, k, \kappa\}$ can be signalled, for instance, in the packets header. We propose two code constructions, both leading to IRA codes [96] whose parity-check matrix is built according to specific (code-rate dependent) degree distributions. We refer to the proposed codes as flexible IRA (F-IRA) codes. The construction of the F-IRA codes parity-check matrix is based in both cases on a pseudo-random approach. With this respect, the parameter κ can be regarded as the seed for the pseudo-random number generator used for the construction of the code parity-check matrix. We show how the proposed approach allows tightly approaching the Singleton bound on the memory-less BEC.

6.2 Flexible IRA Codes

We consider next the construction of the parity-check matrix of an (n, k) IRA code [96]. The $m \times n$ IRA code parity-check matrix is partitioned in two parts, i.e.

$$\mathbf{H} = [\mathbf{H}_u | \mathbf{H}_p], \quad (6.1)$$

with $m = n - k$ being the number of parity-check equations (and hence of check nodes (CNs) in the bipartite graph associated with \mathbf{H}). In our construction, \mathbf{H}_u is a $m \times k$ unstructured low-density (random) matrix, while \mathbf{H}_p is the usual $m \times m$ dual-diagonal matrix. The construction algorithms focus on the systematic part only (\mathbf{H}_u). In the next subsection, we make use of the following notation. We denote by Λ_i the fraction of columns of weight i in \mathbf{H} (and hence the fraction of degree- i VNs in the bipartite graph associated with \mathbf{H}), whereas Φ_i denotes the fraction of columns of weight i in \mathbf{H}_u . We denote by Ψ_i (Ω_i) the fraction of rows of \mathbf{H} (\mathbf{H}_u) with Hamming weight i . Clearly, Ψ_i is also the fraction of degree- i CNs in the bipartite graph associated with \mathbf{H} . We associate to Λ_i , Φ_i , Ψ_i , Ω_i the polynomial representations $\Lambda(x) = \sum_i \Lambda_i x^i$, $\Phi(x) = \sum_i \Phi_i x^i$, $\Psi(x) = \sum_i \Psi_i x^i$,

on one hand of poor performance under IT decoding, and on the other hand of a large decoding complexity when ML decoding is used [93].

³A similar approach has been adopted for the Raptor codes standardized in the multimedia broadcast multicast service (MBMS) [9, 14] standard.

$\Omega(x) = \sum_i \Omega_i x^i$. We refer to $\{\Lambda_i\}$ ($\{\Phi_i\}$) as the node-oriented VN degree distribution for \mathbf{H} (\mathbf{H}_u), and to $\{\Psi_i\}$ ($\{\Omega_i\}$) as the node-oriented CN degree distribution for \mathbf{H} (\mathbf{H}_u). The edge-oriented degree distributions for the complete matrix are defined as $\{\lambda_i\}$ and $\{\rho_i\}$ for VNs and CNs respectively. λ_i represents the fraction of edges in the bipartite graph representation of \mathbf{H} which are connected to VNs of degree i , while ρ_i represents the fraction of edges in the bipartite graph representation of \mathbf{H} which are connected to CNs of degree i . The polynomial representations of λ_i and ρ_i are given by $\lambda(x) = \sum_i \lambda_i x^{i-1}$, $\rho(x) = \sum_i \rho_i x^{i-1}$. Due to the structure of \mathbf{H}_p , the relations between node-perspective degree distributions for the full \mathbf{H} matrix and those for the systematic part \mathbf{H}_u are

$$\Lambda(x) = \Phi(x)R + x^2(1 - R) \quad (6.2)$$

$$\Psi(x) = \Omega(x)x^2 \quad (6.3)$$

with $R = k/n$ being the rate of the IRA code⁴. Remarkably, the techniques described next can be easily applied more generally to LDPC code classes different from the IRA one, e.g. to the class of Generalized Irregular Repeat-Accumulate (GeIRA) codes [62, 69, 97].

6.2.1 Fully-Random Construction

The first on-line construction technique works as follows. For a given VN degree distribution $\Phi(x)$ of \mathbf{H}_u , a vector $\mathbf{u} = (u_0, u_1, \dots, u_{k-1})$ of k VN degree values is derived. For the generic l -th column of \mathbf{H}_u , u_l indexes $q_0, q_1, \dots, q_{u_l-1}$ comprised between 0 and $m-1$ are generated by means of a pseudo-random number generator (e.g., a simple linear congruent generator may be used). The elements of the l -th column of \mathbf{H}_u corresponding to the indexes $q_0, q_1, \dots, q_{u_l-1}$ are hence set to 1, i.e. $\mathbf{h}_{u(q_j, l)} = 1, \forall j = 0 \dots u_l$. The construction algorithm is summarized next.

Algorithm 1 Fully-Random Construction

Calculate the column weights $\mathbf{u} = (u_0, u_1, \dots, u_{k-1})$ for the systematic part of \mathbf{H} according to $\Phi(x)$.

```

for ( $l = 0 : k - 1$ ) {
  for ( $j = 0 : u_l - 1$ ) {
    Generate a random integer number  $q \sim \mathcal{U}(0, m - 1)$ 
    while ( $(h_{u(q, l)}) == 1$ ) {
      Generate a random integer number  $q \sim \mathcal{U}(0, m - 1)$ 
    }
    Set  $h_{u(q_j, l)} = 1$ 
  }
}

```

⁴In the derivation of the relations (6.2) and (6.3) we neglected the presence of a weight-1 column in the matrix \mathbf{H}_p .

This method builds a random matrix \mathbf{H}_u whose column weights fulfill the degree distribution specified by $\Phi(x)$. Indeed, no control at all is performed on the graph girth. Even more important, there is no control on the final CN degree distribution. Hence, the ensemble is completely specified by the distribution $\Phi(x)$, the code dimension k , and the code rate $R = k/n$. We will denote this code ensemble by $\mathcal{C}_1(\Phi(x), k, R)$. The ensemble can be analyzed in the asymptotic setting for $k \rightarrow \infty$ by EXIT analysis [73]. While the VN degree distribution for the complete matrix \mathbf{H} is already available by (6.2), we need to derive the expected degree distribution for CNs. For this purpose, we define $c = \Phi'(1)$ as the average column weight of \mathbf{H}_u , and by $r = k\delta$ the average row weight of \mathbf{H}_u . It turns that a generic element of \mathbf{H}_u is a 1 with probability $\delta = c/m$. The probability that a row of \mathbf{H}_u possesses i 1s is given by

$$\Omega_i = \binom{k}{i} \delta^i (1 - \delta)^{k-i}. \quad (6.4)$$

Hence, the average CN distribution for \mathbf{H}_u is

$$\Omega(x) = \sum_i \Omega_i x^i = \sum_i \binom{k}{i} (x\delta)^i (1 - \delta)^{k-i} = (1 - \delta x)^k. \quad (6.5)$$

By letting $n \rightarrow \infty$,

$$\Omega(x) = \lim_{n \rightarrow \infty} \left(1 - \frac{r}{k}x\right)^k = \exp(-rx). \quad (6.6)$$

The knowledge of $\Omega(x)$ allows to derive the CN degree distribution for \mathbf{H} thanks to (6.3). Out of $\Lambda(x)$ and $\Psi(x)$, the iterative decoding threshold for the $\mathcal{C}_1(\Phi(x), k, R)$ ensemble can be computed and used as cost function for optimization, e.g. via differential evolution [98]. Being this construction incapable of controlling the girth of the graph, high error floors are expected. Nevertheless, we will consider the fully-random construction (FRC) as a reference for a more sophisticated construction provided in the next subsection.

6.2.2 Permutation-Based Construction

The construction method presented next does not increase the matrix generation complexity w.r.t. to the one described in Section 6.2.1. However, it permits to keep a control on the CN degree distribution, and to limit somehow the amount of short cycles. As before, the construction algorithm starts with the derivation of the vector $\mathbf{u} = (u_0, u_1, \dots, u_{k-1})$ containing the k column weights for the matrix \mathbf{H}_u , according to a specific degree distribution $\Phi(x)$. The algorithm proceeds as follows. The vector $\mathbf{v} = (0, 1, 2, \dots, m-1)$ is permuted according to a random permutation pattern, leading to the permutation vector $\pi = (\pi_0, \pi_1, \dots, \pi_{m-1})$. The values of the first u_0 elements of π are then assigned to $q_0, q_1, \dots, q_{u_0-1}$, i.e. $q_j = \pi_j$ for $j = 0 \dots u_0 - 1$, and the elements of the 0-th column of \mathbf{H}_u corresponding to the indexes $q_0, q_1, \dots, q_{u_0-1}$ are hence set to 1, i.e. $\mathbf{h}_{u(q_j, 0)} = 1, \forall j = 0 \dots u_0$. For the column with index 1, the next u_1 elements of π are

extracted, i.e. $q_j = \pi_{u_0+j}$, for $j = 0 \dots u_1 - 1$, and are used to define the elements of the column to be set at 1. For the column with index 2, the next u_2 elements of π are extracted, i.e. $q_j = \pi_{u_0+u_1+j}$, for $j = 0 \dots u_2 - 1$, and are used to define the elements of the column to be set at 1. The process continues for l steps, until the number of remaining elements in π is less than the column weight under consideration, i.e. when $\sum_{w=0}^l u_w > m$. When this happens, a new permutation vector is generated, and the above described procedure restarts from the l -column. More specifically, the first u_l elements of π are extracted, i.e. $q_j = \pi_j$, for $j = 0 \dots u_l - 1$, and are used to define the elements of the column to be set at 1. The procedure is iterated until the last column of \mathbf{H}_u has been filled.

Algorithm 2 Permutation-Based Construction

Calculate the \mathbf{H} column weights $\mathbf{u} = (u_0, u_1, \dots, u_{k-1})$ according to $\Phi(x)$.
 Generate a random permutation vector $\pi = (\pi_0, \pi_1, \dots, \pi_{m-1})$ with m elements
 Set $\mu = 0$
for ($l = 0 : k - 1$) {
 if ($\mu + u_l - 1 > m$) {
 Generate a new random permutation vector $\pi = (\pi_0, \pi_1, \dots, \pi_{m-1})$ with m elements
 Set $\mu = 0$
 }
 for ($j = 0 : u_l - 1$) {
 Set $q_j = \pi_{j+\mu}$
 Set $h_{u(q_j, l)} = 1$
 }
 Set $\mu = \mu + u_l$
}

The above-described permutation-based construction (PBC) algorithm permits to achieve a nearly-constant CN degree since, in the block of columns taking their non-null elements row indexes from the same permutation vector, the row weight is (almost) uniformly 1. The distribution $\Omega(x)$ can be derived as follows. The average column weight of \mathbf{H}_u is given by $\Phi'(1) = \sum_i i\Phi_i$, where $\Phi'(x) = \frac{d}{dx}\Phi(x)$. The average row weight of \mathbf{H}_u is hence given by $a = \Phi'(1)\frac{k}{m}$. We further define $\underline{a} = \lfloor a \rfloor$ and $\bar{a} = \underline{a} + 1$. By definition, $\exists \beta \in [0, 1]$ s.t. $a = \beta\underline{a} + (1 - \beta)\bar{a}$. It turns that $\Omega_{\underline{a}} = \beta$ and $\Omega_{\bar{a}} = 1 - \beta$, with

$$\beta = \frac{a - \bar{a}}{\underline{a} - \bar{a}} \quad (6.7)$$

and $\Omega(x) = \Omega_{\underline{a}}x^{\underline{a}} + \Omega_{\bar{a}}x^{\bar{a}}$. Note that no loops are present among the columns composing such a block. We refer to this code ensemble as $\mathcal{C}_2(\Phi(x), k, R)$.

6.2.3 Permutation-Based Construction with an Outer Random Code

The absence of a complete girth optimization may still result in error floors at moderate error probabilities, especially when short codes (e.g. $k < 500$ symbols) have to be designed. We propose hence an enhancement based on the concatenation with an outer (k, k') binary linear random block code. More specifically, the outer code parity-check matrix \mathbf{H}_o is a $(k - k') \times k$ in the form $\mathbf{H}_o = [\mathbf{H}_{ou} | \mathbf{I}]$ with \mathbf{I} being the $(k - k') \times (k - k')$ identity matrix and \mathbf{H}_{ou} being a $(k - k') \times k'$ matrix whose elements are set to 0 or 1 with uniform probability (as for the inner IRA code, the parity-check matrix of the outer code can be constructed on-line by means of the same pseudo-random number generator). The parity-check matrix of the code obtained by the concatenation of the outer random code with the inner IRA one has thus the form

$$\mathbf{H}' = \left[\begin{array}{c|c} \mathbf{H}_o & \mathbf{0} \\ \hline \mathbf{H}_u & \mathbf{H}_p \end{array} \right]. \quad (6.8)$$

We will see that the concatenation with a high-rate outer code improves significantly the error floor performance, with a limited impact on the decoding complexity.

6.2.4 On the Signalling of the Parameters

The proposed on-line construction requires that the algorithms discussed above are implemented at both the transmitter and the receiver. Furthermore, the transmitter shall signal to the receiver the (n, k) parameters together with the seed κ used to initialize the random number generator used by the algorithms. If pre-coding is used, the dimension of the pre-code k' shall be signaled too. The degree distribution $\Phi(x)$ must be known to the receiver as well. A possibility is to pre-compute capacity-approaching distributions for a range of code rates, and to store them in a tables on both the encoder and the decoder side.

6.3 Performance on the Binary Erasure Channel

In this section simulation results on the memory-less BEC with erasure probability ϵ are presented for codes constructed with the methods of Section 6.2. We will restrict to the case of coding rate 1/2. For the codes generation we will use the distribution $\Phi_1(x) = 0.543x^3 + 0.102x^4 + 0.008x^5 + 0.020x^6 + 0.008x^7 + 0.008x^8 + 0.047x^9 + 0.266x^{10}$. When used for the FRC, this distribution leads to the code ensemble characterized by an IT decoding threshold $\epsilon_{\text{IT}}^* = 0.4788$ and to an ML one $\epsilon_{\text{ML}}^* = 0.4869$ (see the ensemble EXIT function [99] in Figure 6.1(a)). When used to generate codes according to the PBC, the related ensemble possesses an IT decoding threshold $\epsilon_{\text{IT}}^* = 0.4673$ and an ML one $\epsilon_{\text{ML}}^* = 0.4954$ (see the ensemble EXIT function in Figure 6.1(b)). In both cases,

the gap between the IT and the ML thresholds is limited and hence the ML decoding complexity shall be low [85,93]. The derivation of the tight upper bound on the maximum a posteriori (MAP)/ML threshold follows the approach of [99] (note that on the BEC ML and MAP are equivalent). For a broad set of ensembles (including the regular ones and the irregular ones whose EXIT curve present a single jump [99]), the upper bound on ϵ_{ML} can be derived as follows. The EXIT function under IT decoding is derived in terms of *extrinsic erasure probability* at the output of the decoder (denoted by p_{E}) as a function of the *a priori erasure probability* input to the decoder (denoted by p_{A}). In the limit where $n \rightarrow \infty$, the EXIT function of the ensemble defined by the degree distribution pair (λ, ρ) is a function of (λ, ρ) . It can be expressed in parametric form by the pair of simultaneous equations $p_{\text{A}} = x/\lambda(1 - \rho(1 - x))$, $p_{\text{E}} = \Lambda(1 - \rho(1 - x))$, with $x \in [x_{\text{IT}}, 1]$, x_{IT} being the value of x for which $p_{\text{A}} = \epsilon_{\text{IT}}$, and where $\Lambda(x) = \sum \Lambda_i x^i$, Λ_i being the fraction of degree- i VNs. Due to the area theorem [100, Theorem 1], the area below the EXIT function under ML decoding, must equal the code rate R . Consider the extrinsic erasure probability at the output of an ML and of an IT decoder. Obviously, $p_{\text{E}}^{\text{ML}} \leq p_{\text{E}}^{\text{IT}}$. By drawing a vertical line on the EXIT function plot of the ensemble, in correspondence with $p_{\text{A}} = p_{\text{A}}^*$ and such that $\int_{p_{\text{A}}^*}^1 p_{\text{E}}(p_{\text{A}}) dp_{\text{A}} = R$ we obtain an upper bound on the ML threshold, i.e., $\epsilon_{\text{ML}} \leq p_{\text{A}}^*$.

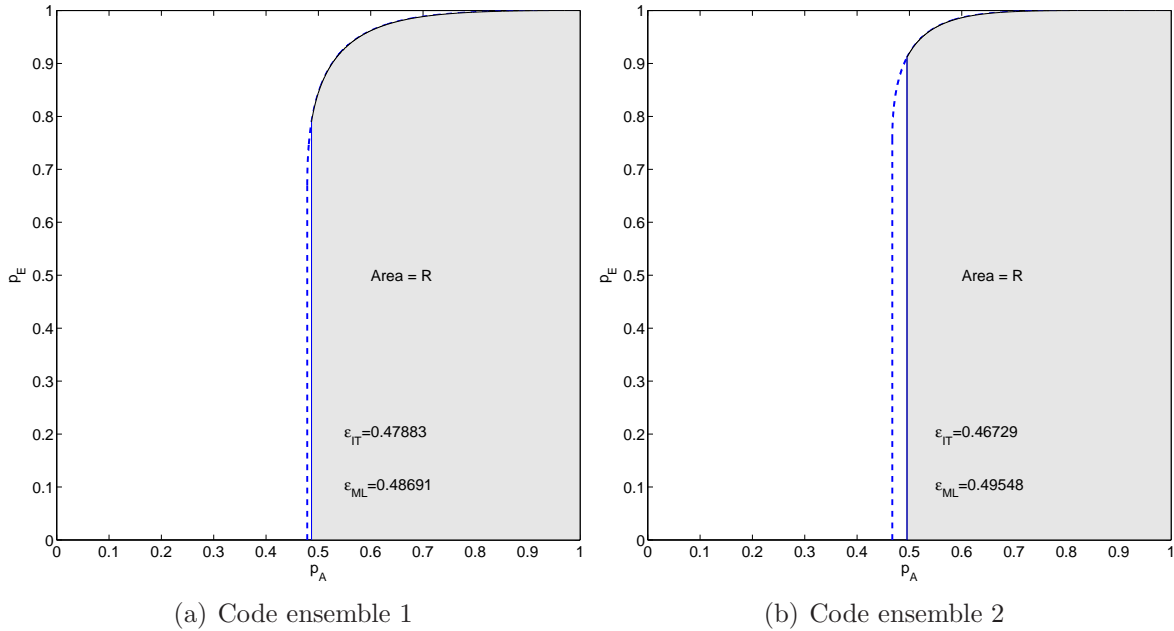


Figure 6.1: EXIT function for the FRC (left) and the PBC (right) ensembles based on $\Phi_1(x)$ with $R = 1/2$.

Two block lengths are investigated, i.e. a short one ($n = 512$) and a moderate-large one ($n = 2048$). The performance is compared with the Singleton lower bound to the block error probability of any (n, k) linear block code (representing the performance of an

idealized MDS code), given by

$$P_B^{(s)} = \sum_{i=n-k+1}^n \binom{n}{i} \epsilon^i (1 - \epsilon)^{n-i}. \quad (6.9)$$

The performance for the (512, 256) and the (2048, 1024) codes generated according to the FRC of Section 6.2.1 is depicted in Figures 6.2 and 6.3, respectively. The performance is presented in terms of codeword error rate (CER) vs. erasure probability ϵ under ML decoding. We note that in the $n = 512$ case the CER performance remains close to the Singleton bound down to $\text{CER} \simeq 10^{-1}$, while for the longer block (Figure 6.3) the performance curve follows quite closely the Singleton bound down to $\text{CER} \simeq 10^{-2}$. Below those values, in both cases the CER curves show high error floors.

The PBC permits to limit the presence of loops in the graph associated with the generated matrix, resulting in lower error floors w.r.t. the FRC. This can be observed in both Figures 6.2 and 6.3. When the short block size is considered, the floor reduction is modest (less than one order of magnitude in the CER), while it is more significant in the case of $n = 2048$. Here, the CER floor is lowered by almost 2 orders of magnitude. For sake of completeness, the performance under IT decoding is provided as well, showing the good behavior of the code also when decoded with the IT approach. A further reduction of the error floors is obtained by using an outer random code according to the approach discussed in Section 6.2.2. In Figures 6.2 and 6.3, the performance of the PBC IRA code with different (k, k') random outer codes is depicted for ML decoding. For the short block size case (Figure 6.2), we investigated the effect of (256, 251) and of (256, 246) random outer codes. In the first case, the addition of 5 parity-check equations leads to a code rate reduction to $R' = 0.490$, while in the second case the additional 10 parity-check equations lower to the code rate down to 0.480. In both cases, we provide the associated Singleton bounds as reference. The adoption of the (256, 251) outer code permits to lower the error floor of the IRA code by more than 1 order of magnitude. A large improvement is achieved by increasing the redundancy of the outer code to 10. In this case, no floors are observed down to $\text{CER} \simeq 10^{-6}$. When considering the $n = 2048$ case, we applied a (1024, 1014) random out code. Here, the code rate is reduced to $R' = 0.495$. No error floor is observed down to $\text{CER} \simeq 10^{-5}$, with a performance that is tightly approaching the Singleton bound for (2048, 1014) codes. Figure 6.4 depicts the CER performance for a family of rate-compatible F-IRA codes obtained by puncturing the (512, 246) code (given by the concatenation of a (512, 256) PBC F-IRA code with a (256, 246) random outer code). The obtained rates are $\sim 2/3$ and $\sim 4/5$. In all the cases the code performance tightly approaches the Singleton bound and almost matches the average linear random code performance given by Berlekamp's random coding bound (RCB) [101],

$$\bar{P}_B \leq \sum_{i=n-k+1}^n \binom{n}{i} \epsilon^i (1 - \epsilon)^{n-i} + \sum_{i=1}^{n-k} \binom{n}{i} \epsilon^i (1 - \epsilon)^{n-i} 2^{-(n-k-i)}. \quad (6.10)$$

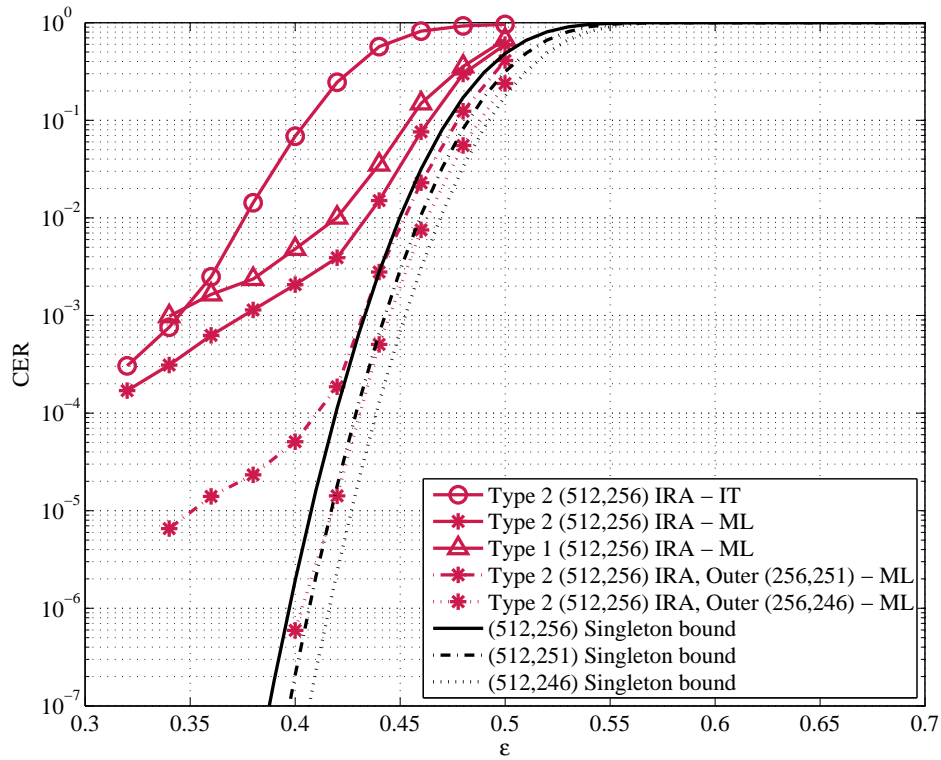


Figure 6.2: CERs for $n = 512$, $R \simeq 0.5$ FRC and PBC IRA codes.

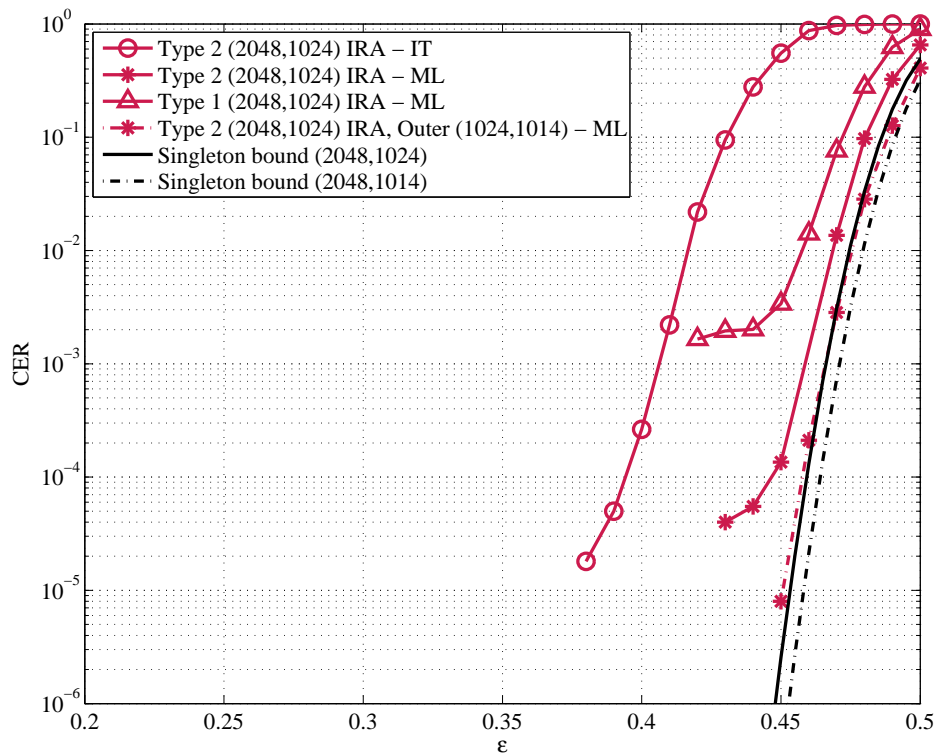


Figure 6.3: CERs for $n = 1024$, $R \simeq 0.5$ FRC and PBC IRA codes.

For our simulations, we used the efficient ML decoder described in [95] together with the Maximum Column Weight pivoting algorithm of [85]. The decoding complexity of the algorithm of [95] is dominated by the last decoding step, which consists in solving (via Gaussian elimination) a dense system of binary linear equations in α unknowns, where α unknowns are referred to as *pivots* or *reference variables*. An indirect measure of the decoding complexity is given by the average number of pivots $\bar{\alpha}$ to be solved at a certain erasure probability. Results on the average number of pivots are provided in Figure 6.5 for the case with $\epsilon = 0.5$ and on $n = 512$, the FRC leads to a lower decoding complexity w.r.t the PBC, $\bar{\alpha} = 10$ vs. $\bar{\alpha} = 12$, which is in accordance with the $\epsilon_{\text{ML}}^* - \epsilon_{\text{IT}}^*$ argument of [93]. Considering the corresponding PBC case, the concatenation with an outer code tends to increase the decoding complexity (i.e., the average number of pivots) by a factor that is related to the number of rows $k - k'$ of \mathbf{H}_ρ . However, even considering the case with $k - k' = 10$, the average number of pivots is kept small, $\bar{\alpha} = 16$, and hence high decoding speeds can be achieved.⁵

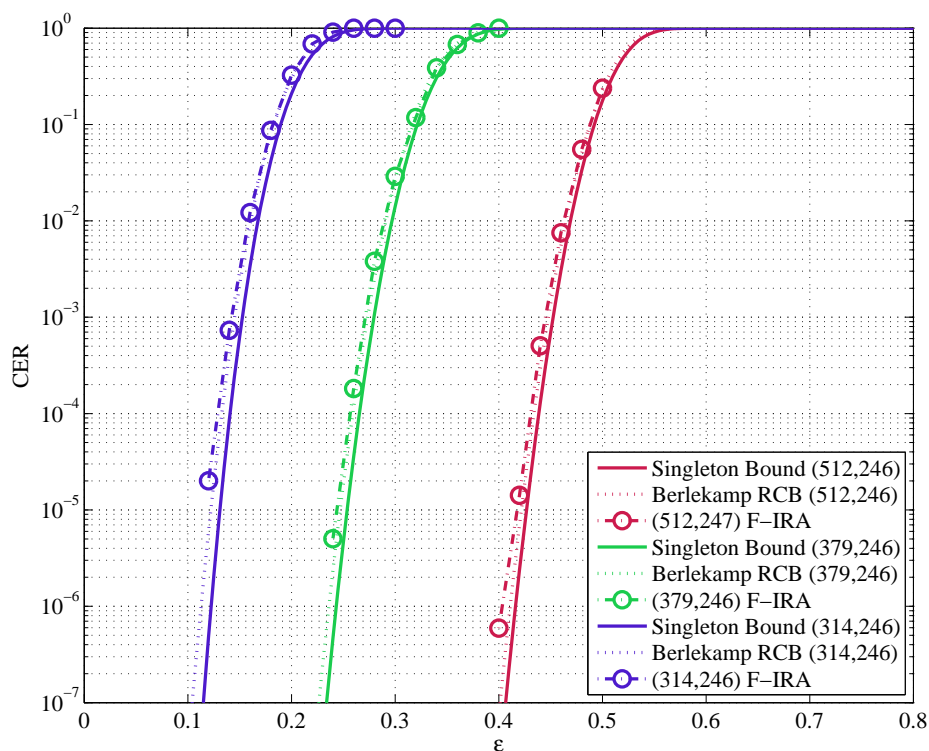


Figure 6.4: CERs for a family of rate-compatible F-IRA codes with block length $n = 512$, based on the PBC with an $(256, 246)$ random outer code.

⁵Recall that for a $(2048, 1024)$ IRA code decoding speeds higher than 1.5 Gbps via software decoder implementation of the ML decoding algorithm were demonstrated in [85].

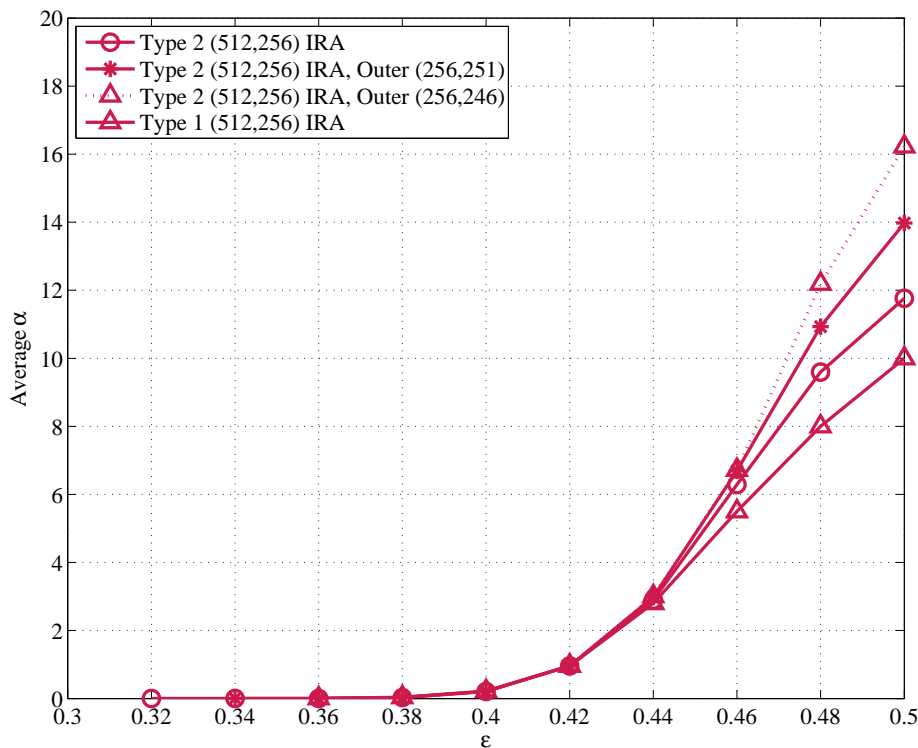


Figure 6.5: Average number of pivots vs. erasure probability for $n = 512$ F-IRA codes.

6.4 Application to AeroMACS

We applied the code construction proposed in the previous sections in the context of the wireless airport surface communications, i.e. the upcoming AeroMACS standard. This system presents in fact a large population of aircraft terminals and a traffic composed by unicast, multicast and broadcast transmissions. Packet-level coding may hence be particularly useful whenever large amounts of information have to be broadcasted to several aircrafts. In that case, the excellent performance of F-IRA rate-compatible families can efficiently complement Automatic Repeat reQuest (ARQ) protocols [8, 84], representing a valuable alternative to fountain coding schemes [8].

We focused our investigation on the most challenging airport scenario (i.e the parking one), which is characterized by NLOS conditions and slow fading. Here, packet-level coding can enhance the system performance, allowing coding on large blocks and thus exploiting time diversity. Note that an alternative approach for counteracting slow fading is provided by (long) physical layer interleavers (as for instance in the DVB-SH standard, [13]). However, being packet level coding applied on high protocol stack layers, it avoids any problematic modifications of the AeroMACS radio interface.

The AeroMACS system is based on the OFDMA mode of the WiMAX standard [3]. The OFDMA symbol comprises 512 subcarriers with a bandwidth of 5 MHz and a TDD technique with 5 ms frames divided in FL and RL sub-frames. We considered FL sub-

frames of 24 OFDM symbols, CP of 1/8 of the symbol length and QPSK sub-carrier modulation. Convolutional coding with rate 1/2 is applied to the user packets, which are assumed equal to 10 basic units (called sub-channels and corresponding to 960 bits). The channel estimation is a linear pilot interpolation in the frequency domain, tailored to the WiMAX frame structure.

The performance of the system (without packet-level coding) is depicted in Figure 6.6, in terms of packet error rate (PER) vs. E_b/N_0 . The limited time diversity leads to a

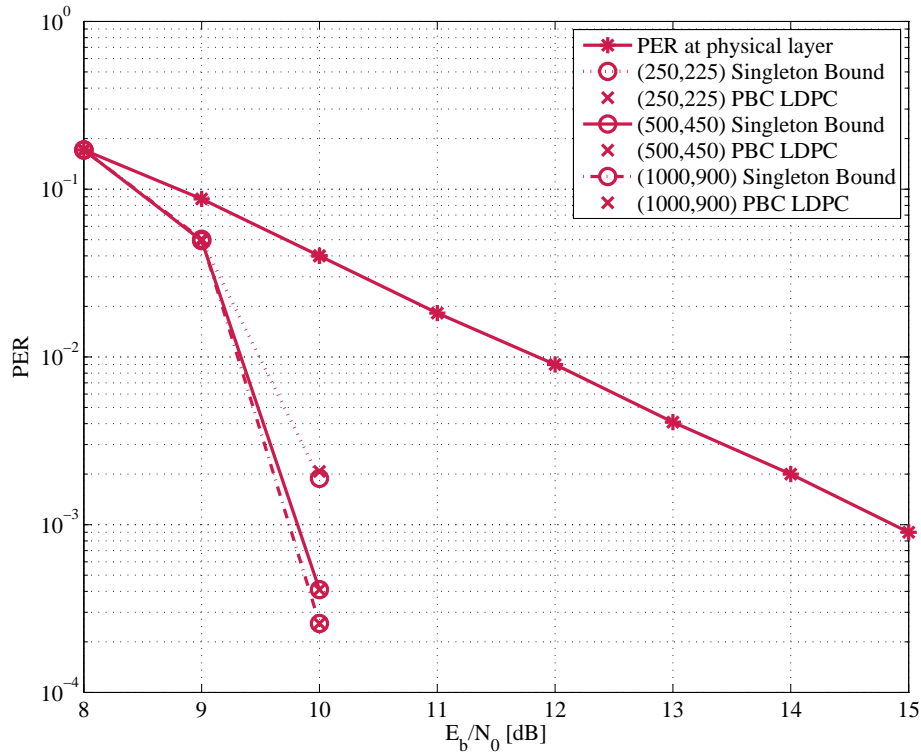


Figure 6.6: Packet error rate after physical layer decoding, and after the application of $R = 9/10$ packet level IRA codes (various block lengths).

lack of steepness in the curve. A $\text{PER} \simeq 10^{-2}$ is achieved at $E_b/N_0 = 12$ dB. Note that according to simulation parameters, the duration of a FL sub-frame is 2.5 ms, while the channel coherence time is roughly 50 ms. We hence applied different packet-level codes directly at the link layer (i.e., considering as encoding symbols the units encoded by the convolutional code). We selected code rates between 4/5 and 19/20, and block sizes of 250, 500 and 1000 symbols. Considering a frame duration of 5 ms (which includes both the FL and the RL sub-frames), the latency introduced by the packet-level codes spans from 1.25 s (for $n = 250$ symbols) to 5 s (for $n = 1000$ symbols), bringing sufficient time diversity to counteract moderate-short outages. The introduced latency is indeed acceptable for file delivery applications, while it is too large for delay-sensitive applications (such as voice communications).

PBCs have been considered, with $\Phi_2(x) = x^5$, which (for a reference rate $R = 9/10$) provides an iterative decoding threshold $\epsilon_{\text{IT}} = 0.0733$ and a ML one $\epsilon_{\text{ML}} = 0.0992$. No

outer code has been used.⁶ In Table 6.1, the performance in terms of PER after packet-level decoding is provided for several PBC IRA codes. The Singleton bound⁷ is provided as reference. The PBC codes attain in almost all the cases the Singleton bound. Figure 6.6 illustrates the PER vs. E_b/N_0 for different rate-9/10 PBC IRA codes of different lengths. Again, the performance achievable with idealized MDS codes (Singleton bound) is provided as reference. Already with a block length of 250 symbols, the PBC allows tightly approaching the bound. The gain at $\text{PER} \simeq 10^{-2}$ w.r.t. the curve without packet-level coding is ~ 2.5 dB.

Table 6.1: Packet error rates for various (n, k) PBC IRA codes compared with the Singleton bound (in brackets).

(n, k)	$E_b/N_0 = 8$ dB	$E_b/N_0 = 9$ dB	$E_b/N_0 = 10$ dB
-	$1.71 \cdot 10^{-1}$	$8.27 \cdot 10^{-2}$	$4.01 \cdot 10^{-2}$
(250, 225)	$1.71 \cdot 10^{-1}$ ($1.71 \cdot 10^{-1}$)	$4.93 \cdot 10^{-2}$ ($4.93 \cdot 10^{-2}$)	$2.20 \cdot 10^{-3}$ ($1.88 \cdot 10^{-3}$)
(500, 400)	$1.17 \cdot 10^{-1}$ ($1.17 \cdot 10^{-1}$)	$1.00 \cdot 10^{-2}$ ($1.00 \cdot 10^{-2}$)	-
(500, 450)	$1.71 \cdot 10^{-1}$ ($1.71 \cdot 10^{-1}$)	$4.93 \cdot 10^{-2}$ ($4.93 \cdot 10^{-2}$)	$4.10 \cdot 10^{-4}$ ($4.10 \cdot 10^{-4}$)
(1000, 800)	$1.22 \cdot 10^{-1}$ ($1.22 \cdot 10^{-1}$)	$4.25 \cdot 10^{-3}$ ($4.25 \cdot 10^{-3}$)	-
(1000, 900)	$1.71 \cdot 10^{-1}$ ($1.71 \cdot 10^{-1}$)	$5.02 \cdot 10^{-2}$ ($5.02 \cdot 10^{-2}$)	$2.57 \cdot 10^{-4}$ ($2.57 \cdot 10^{-4}$)
(1000, 950)	$1.71 \cdot 10^{-1}$ ($1.71 \cdot 10^{-1}$)	$6.25 \cdot 10^{-2}$ ($6.25 \cdot 10^{-2}$)	$1.45 \cdot 10^{-2}$ ($1.45 \cdot 10^{-2}$)

6.5 Summary

In this chapter, we introduced two algorithms for the on-line design of parity-check matrices for IRA codes. The proposed algorithms allow a fast design of parity-check matrices that are suitable for low-complexity ML decoding. The code ensembles generated by the proposed algorithms have been analyzed via extrinsic information transfer charts. One of the proposed constructions can attain codeword error rates as low as 10^{-5} without appreciable losses w.r.t. the performance of idealized MDS codes.

Furthermore, we applied the proposed techniques to a packet-level coding scheme for AeroMACS. The FL of AeroMACS constitutes a perfect application case, with large population of aircraft, broadcast nature of part of the traffic and demand of high reliability. Simulation results show large performance gains, proving the high efficiency and the flexibility of the approach.

⁶For high code rates (e.g., $R \geq 4/5$) the optimization of the degree distributions may leave place to the use of *sufficiently-dense* near-regular distributions. In fact, for high code rates near-regular distributions have IT thresholds close to the Shannon limit, allowing (in the finite length setting) approaching the Singleton bound while keeping the decoding complexity limited [93].

⁷The Singleton bound represents the performance of an idealized MDS code with a given block length, n , and code dimension k . More specifically, for each set of (n, k) parameters, we analyzed the sequence of packet erasures after physical layer decoding, and we assumed that in a block of n packets, $n - k$ or less have been erased, the entire block is recovered.

Chapter 7

Conclusions

In this thesis we analyzed the performance of the upcoming system for airport surface communications, i.e. the AeroMACS standard. The performance of AeroMACS shows a degradation in the scenarios characterized by NLOS condition with the control tower, moderate or no mobility and lack of diversity. Therefore, we investigated potential solutions increasing the diversity of the system and improving its performance. We analyzed techniques as multiple antennas, cooperative communications and packet level coding. The first two methods are based on spatial diversity¹, while the third one is based on time diversity. All the investigated methods provide large performance gains, and hence, represent appealing solutions. Though, they require different modifications to the base system and therefore, constitute interesting candidates for different phases of the AeroMACS upgrade plan. In the following section, we summarize the main pros and cons of each technique in the context of the airport communications. We provide hence recommendations on a potential upgrade plan of the AeroMACS standard. Finally, in the last section, we review the main achievements of this thesis.

7.1 Enhancements of AeroMACS

Multiple Antenna The performance gains attained by multiple antennas systems have been widely acknowledged. The case of airport communications doesn't represent an exception. Since the installation of more antennas on the aircraft is seen as critical, we focused on schemes which foresee multiple antennas only on the control tower. The simplest solution for the RL is a SIMO 1×2 scheme, which provides a diversity gain of order two (that corresponds to the maximum achievable with two antennas). Adopting a MRC receiver, as we proposed, we obtain also an additional array gain of 3 dB. Being obtained by the coherent sum of the signals this gain is independent from the channel (hence is present also in case of correlated channels). This scheme introduces a large performance improvement with a gain of almost 6 dB at $BER = 10^{-4}$. In this case, the unique modifications concern the base station, with the addition of a second antenna plus

¹Respectively, antenna diversity and cooperative diversity.

the maximal ratio combining receiver. The transmitter (i.e the aircraft), which constitutes the most sensitive part of the communication network to modifications, doesn't require any upgrade.

For the FL, we considered a MISO 2×1 STC scheme. Although STC doesn't benefit of array gain, we selected it for the airport communications because it doesn't require CSI at the transmitter (as the beamforming scheme), that is difficult to obtain. Also in this case, the diversity order is two, and the performance of AeroMACS is largely improved. Differently from the SIMO case, STC requires modifications at both the transmitter and receiver sides. At the control tower, the modifications concern the second antenna plus the frame composer (since the two antennas transmit two different signals). At the aircraft side, the STC decoder shall be implemented. Although this scheme requires modification also to the aircraft side, the 2×1 STC scheme has already been introduced in the last version (2009) of the WiMAX standard. Therefore, its implementation represents a minor issue.

The introduction of more antennas (also on the aircraft side) would provide even a larger gains. Having 4 antennas on the control tower, in case of SIMO, translates into a diversity gain of order 4 plus an array gain of 6 dB. Similar results could be obtained with a 2×2 MIMO scheme. However, the aeronautical world see as critical the installation of a second antenna on the aircraft, limiting the potential of MIMO.

Cooperative Techniques Cooperative communications provide spatial diversity, or more specifically cooperation diversity, even for single-antenna systems. They hence represent a potential solution for cases where the use of multiple antennas is not allowed (e.g. on the aircraft). The cooperation between users has a great potential in the airport context. The large population of aircrafts offers a large number of potential partners. Moreover, the aircrafts are provided with a large power supply, offering the possibility to perform even rather complex operations as coding, decoding, modulation, etc. Among the cooperation schemes, even the simpler ones, as amplify and forward and decode and forward, are able to provide large performance enhancements. More specifically, for the single-relay case, they are both able to attain a diversity of order two. This diversity order is the maximum achievable with a single relay, and is the same provided by a multiple antennas system with two antennas. Assuming the channel between the source and the relay as reliable², DF provides better performance than AF. In this condition, the relay system becomes equivalent to a 2×1 STC, providing basically the same performance. Although less performing, AF is more robust with respect to the channel condition on the source-relay link.

²This condition is fundamental for a DF scheme. If the channel between the source and the relay is unreliable, the relay may be not able to decode correctly the source message. As a consequence, it may forward a wrong codeword to the destination. This may lead to the degradation of the overall decoding error probability. Nevertheless, the use of a CRC validation test at the relay may be considered to detect a decoding failure. In this case, the relay may simply avoid forwarding any message to the destination.

Albeit simple, these schemes require major modifications of AeroMACS. Even for the DF scheme, where the relay-aircraft is already able to perform all the decode-and-re-encode operations, multiple access, signaling and protocols currently considered in the WiMAX standard shall be modified to allow the user cooperation. These aspects represent a main drawback of cooperative schemes in the aeronautical framework.

Cooperative schemes suffer also from a reduction of transmission efficiency. Considering a simple time-division scheme (as in our AF and DF implementation), where the transmission of the source and the one of the relay take place in two different time slots, the efficiency is reduced by a factor two. This is due to the fact that the transmission of a single message requires two time slots. Therefore, having assumed a code with rate $R = 1/2$ at the source, we obtain an overall rate of $1/4$. Nevertheless, the efficiency reduction problem can be solved using coding cooperation schemes, which allow to reach rates up to $1/2$ (that is the maximum for a system providing diversity two). Moreover, a new scheme (introduced in this thesis) named *unequal diversity coding* provides even higher rates. This appealing result is achieved by scarifying a low-priority part of the message, that obtains no diversity, while assuring diversity two to the high-priority segment of the message.

The drawbacks of these techniques (i.e., the need of deep modification to the AeroMACS standard) put some limits to a rapid deployment of cooperative communications in the airport environment. However, the large benefits and great potential of these methods constitute an appealing solution for AeroMACS, especially under the light of future higher demand of reliability and capacity. Hence, this techniques remains a valid solution for the long term evolution of AeroMACS. In order to provide a more detailed analysis on the use of cooperative communications in the airport, further investigations on different cooperation schemes, access schemes and cooperation protocols are required.

Packet Level Coding Packet level coding represents a simple yet effective mean to cope with slow-fading channels. Since a packet level code operates on symbols that are (in general) packets of fixed size, the packet-level coding sub-layer can be introduced on the higher layers of the protocol stack (e.g., at the application layer), rendering the introduction of packet-level coding almost transparent to the rest of the communication stack. Additionally, the inherent low complexity of erasure decoding allows implementing the packet-level encoders and decoders via simple software routines running on general purpose computing platforms. By this way, data rates of several hundred Mbps can be achieved. Thus, packet level coding is indeed a very-low complexity upgrade, that can be introduced in the system even after deploying the hardware infrastructure. As an added value, packet-level coding can be easily integrated with hybrid ARQ protocols by means of the fountain coding concept, allowing the delivery of broadcast content with nearly-optimum exploitation of the down link bandwidth. Packet level coding is especially efficient when the large blocks of data are processed by the packet level encoder.

More specifically, the encoded blocks shall be longer than a few channel coherence times to enjoy sufficient diversity. As a result, depending on the channel coherence time, large latencies may be expected. Thus, packet-level coding is not a panacea for every application. For certain applications (e.g., file delivery), large delays are indeed not a problem. However, for delay-critical services (such as voice communications) packet-level coding is not suitable.

7.1.1 Conclusions and Outlook

All the analyzed diversity techniques represent in principle appealing solutions to the diversity problem in the airport domain. Though, they imply modifications to the system and in some cases drawbacks as efficiency reduction or high delays. Focusing on the tradeoff between performance and costs, the multiple antennas schemes with two antennas on the control tower provide the best results, especially for the short-term AeroMACS upgrade. However, all the different techniques analyzed can be suitable for the airport communications. Each one represents indeed a good choice for different phases of the system development. Assuming the upgrade plan of the AeroMACS standard composed by three phases, the outcome of this work may be summarized as follow:

1. In the short term, simple multiple antenna schemes (SIMO 1×2 MRC for the RL and MISO 2×1 STC for the FL), which foresee only a second antenna at the base station, represent the best choice. They provide large performance gain, keeping at the minimum the modification required with respect to the single antenna baseline.
2. In the medium term, PLC techniques can be joined to the basic SIMO and MISO scheme to further enhance the performance of the system. This doesn't require hardware modifications and brings large benefits to broadcast/multicast services.
3. For the long term evolution, more sophisticated methods might be accounted to answer potential higher demand of reliability and capacity. MIMO schemes with more antennas and cooperative communications are thus appealing candidates. The presented cooperative schemes, especially unequal diversity coding, offer valid solutions in this context.

7.2 Thesis Achievements

The main contributions that have been achieved in this work are summarized as follow:

- We developed a **novel stochastic airport channel model** describing the main wireless propagation phenomena related to the airport environment. Multi-path and Doppler effects with the potentially resulting inter-symbol interference and inter-carrier interference have been taken into account, respectively. The channel model,

based on different scenarios, has parameters obtained from a measurement campaign carried out at the airport of Munich.

- We presented an analysis of the WiMAX (standard IEEE 802.16) profiles candidate to become the baseline for the future airport communication system. We showed the performance offered by the profiles based on the **OFDM waveform** and on the **OFDMA** one. The results have been obtained simulating the profiles over the developed airport channel model in four different scenarios.

The results are obtained assuming either perfect channel knowledge or actual channel estimation algorithms. We developed simple linear interpolation algorithms based on the pilot tones and tailored to the WiMAX structure (see Appendix A).

We selected as best candidate the **OFDMA profile**, which provides more flexibility and better performance in the airport environment and represents the most suitable WiMAX profile in this context.

- We evaluated the use of **multiple antennas** in the airport environment. After an overview of simple MIMO techniques, we focused on the schemes which foresee a second antenna only on the control tower. We implemented a **SIMO** 1×2 MRC scheme for the RL and a **MISO** 2×1 STC scheme for the FL, analyzing the resulting performance by simulations. We introduced a novel implementation of 2×1 STC which preserves the original framing structure of WiMAX and minimizes the modifications required to the system. We evaluated the proposed implementation by simulations and we compared the results with the ones obtained for the STC implementation proposed in the WiMAX standard.
- We investigated the use of simple single-relay cooperation strategies in the framework of airport communications, as an alternative/complement to system employing multiple antennas on the control tower only. We implemented two simple cooperation schemes, showing the corresponding performance. Amplify and forward represents the easiest form of cooperation. Nevertheless, it provides a large performance improvement and a diversity gain of order 2, which is the maximum allowed in the single-relay context. At the receiver, we implemented a MRC algorithm. Hence, it is necessary to estimate not only the channel resulting from the combination of the path source-relay-destination, but also the channel relative to the segment relay-destination. In order to properly estimate all the channels, we inserted some pilot tones at the relay before amplifying the signal, allowing the destination to coherently sum all the received signals and maximize the signal-to-noise ratio. The performance of the system with the application of an AF scheme is provided in different cooperation scenarios (i.e. considering different Rice factor values for the channels between source, relay and destination).

Decode and forward constitutes another simple cooperative scheme able to provide

large performance improvement. However, differently from AF, this scheme requires a sufficiently reliable link between the source and the relay, otherwise, the relay will propagate unreliable replicas of the transmitted signal. Differently from AF, this method doesn't require the receiver at the destination to estimate the channel between source and relay³. Simulation results showed the performance of AeroMACS with a DF scheme in different cooperation scenarios (i.e. generic case and worst case). Moreover, the results provided by AF and DF have been compared.

- We introduced the novel concept of **unequal diversity coding** for the relay channel. A novel class of high-rate **UD protograph** LDPC code ensembles have been proposed. Their performance over the quasi-static relay fading channel has been analyzed through a **novel PEXIT analysis**, which allows accurately predicting the error probability associated with different codeword fragments. Protograph ensemble exhibiting the UD feature has been proposed, which are obtained via simple (parallel) concatenation of IRA/RA protographs. The proposed schemes allow combining coding efficiency (through high coding rates) with diversity for the high-priority parts of the source messages.

We applied the unequal diversity coding concept to AeroMACS, showing that the method can effectively provide diversity of order two to the high-important segment, while offering high coding rates (higher than $1/2$). The simulation results illustrate in fact no diversity for the low-priority segment and diversity two for the high-priority message.

- Two algorithms for the on-line design of parity-check matrices for IRA codes have been introduced in the context of packet level coding for erasure recovery. The proposed algorithms allow a fast design of parity-check matrices that are suitable for low-complexity ML decoding over erasure channels. The code ensembles generated by the proposed algorithms have been analyzed via extrinsic information transfer charts. One of the proposed constructions can attain codeword error rates as low as 10^{-5} without appreciable losses w.r.t. the performance of idealized MDS codes.

The proposed techniques have been applied to a packet-level coding scheme for the upcoming AeroMACS standard, proving the high efficiency and the flexibility of the approach.

³The channel estimation for the $S - R$ link is done at the relay, indeed.

Appendix A

Channel Estimation

We adopted throughout this work channel estimation algorithms based on linear channel interpolation of the pilot tones and performed in frequency domain. In this section we illustrate the algorithms that we implemented. Since the WiMAX standard includes different frame structures (according to the profile, permutation mode, and subframe), we tailored each algorithm to a different frame structure.

A.1 OFDM Profile

The OFDM WiMAX profile includes a simple frame structure, with pilot tones equidistant and present in all the OFDM symbols. The linear interpolation algorithm, illustrated in Figure A.1, operates in frequency domain and in time direction. The computation of the

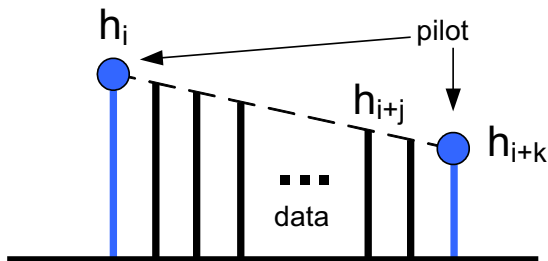


Figure A.1: provides a scheme of the channel interpolation algorithm.

channel coefficients¹ is based on reference channel coefficients, obtained in correspondence of the pilot tones (\hat{h}_i and \hat{h}_{i+d}), by dividing the received samples y_i by the transmitted ones x_i (Equation A.1). The transmitted samples are equals to the pilot boosting.

$$\begin{cases} \hat{h}_i = \frac{y_i}{x_i} \\ \hat{h}_{i+d} = \frac{y_{i+d}}{x_{i+d}} \end{cases} \quad (\text{A.1})$$

¹We indicate the estimated channel coefficients with \hat{h} .

Hence, the estimated channel coefficient are given by

$$\hat{h}_{i+j} = \hat{h}_i \cdot \left(\frac{d-j}{d}\right) + \hat{h}_{i+d} \cdot \left(\frac{j}{d}\right), \quad j = 1, \dots, d-1, \quad (\text{A.2})$$

where d is equal to 25 and indicates the distance (in number of subcarriers) between two pilot subcarriers.

A.2 OFDMA

The OFDMA profiles include different types of frame structures, depending on the chosen permutation mode. In our analysis, we focused on the PUSC permutation mode, that foresees FL and RL subframes based on the cluster and tile concepts, respectively (see Section 2.2). The next subsections illustrate in detail the algorithms developed for the FL and RL subframes.

A.2.1 Forward Link

In the forward link case, the frame structure is based on the cluster concept (see Section 2.2 and Figure 2.9). Therefore, the channel interpolation algorithm is tailored to this structure. The non-symmetrical pilot tone positions allow limited flexibility in the interpolation. We implemented three simple algorithms operating in the frequency domain. The simplest one interpolates the pilots just in frequency domain, as depicted in Figure A.1. Also the second interpolates the pilots only in frequency direction; though, it exploits also the pilots of the adjacent OFDM symbols. Since the channel is slow in time direction, we assumed the channel constant over two consecutive OFDM symbols and we used all the pilots available on the two OFDM symbols for performing a channel interpolation in frequency direction, as illustrated in Figure A.2. However, the channel is

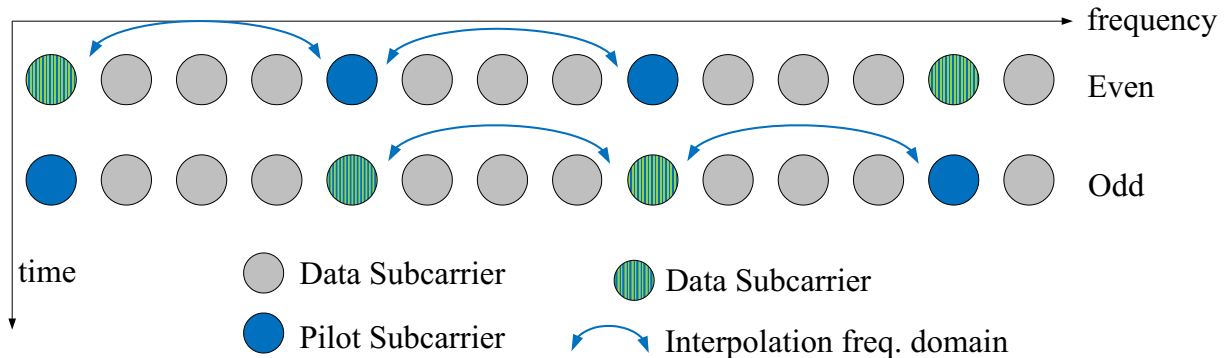


Figure A.2: Scheme of the channel interpolation algorithm for the cluster structure (second algorithm).

not perfectly constant over two OFDM symbols, and if we consider also the time direction, we can obtain a finer interpolation. We hence implemented a third algorithm, operating

in two steps. First, it performs an interpolation in time domain over the samples in correspondence of the pilot tones. In this way, additive pilot tones are obtained. Then, it interpolates all the pilot tones of the OFDM symbols (real and obtained ones) in the frequency direction, obtaining all the channel coefficients. Figure A.3.

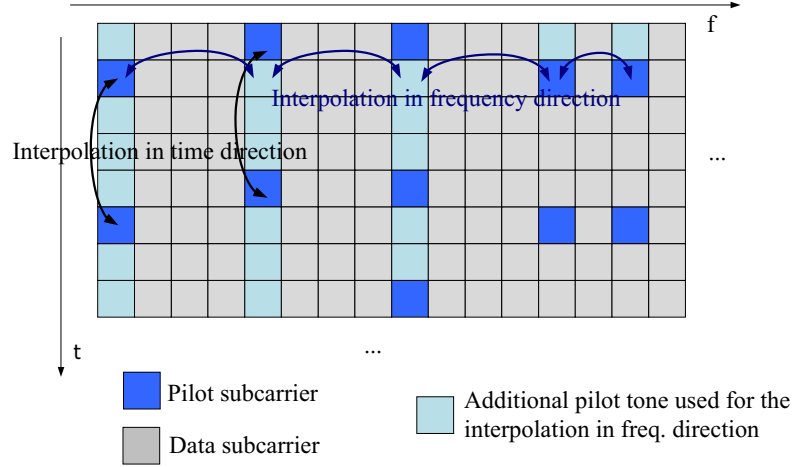


Figure A.3: Scheme of the channel interpolation algorithm in the FL (third algorithm).

A.2.2 Reverse Link

In the reverse link case, the subframe structure is based on the tile concept (see Chapter 2 and Figure 2.8). Hence, we tailored the channel interpolation algorithm to the tile structure. The channel estimation algorithm is based on pilot interpolation in frequency and time directions. The computation of the channel coefficients corresponding to OFDM symbols with pilot sub-carriers (odd symbols) is a simple frequency domain linear interpolation only in frequency direction (see Equation A.2 and A.1²). For the even symbols, without pilot sub-carriers, virtual pilot tones h^* are used instead of real pilot values. The virtual reference channel coefficients (\hat{h}_i^*) are obtained from an interpolation of the pilot values of the two adjacent odd symbols ($\hat{h}_{i,t}$, $\hat{h}_{i,t+2}$), according to Equations A.3 and A.4. In this way, the remaining channel coefficients may be computed with Equations A.2 and A.1, substituting the pilot values with the virtual reference coefficients ($\hat{h}_{i,t}^*$ and $\hat{h}_{i+d,t}^*$). Note that the estimated coefficient $\hat{h}_{i,t}$ represent values over the i^{th} subcarrier and the t^{th} OFDM symbol.

$$\hat{h}_{i,t}^* = \frac{1}{2} \cdot \hat{h}_{i,t-1} + \frac{1}{2} \cdot \hat{h}_{i,t+1} \quad (\text{A.3})$$

$$\hat{h}_{i+j,t} = \hat{h}_{i,t}^* \cdot \left(\frac{d-j}{d} \right) + \hat{h}_{i+d,t}^* \cdot \left(\frac{j}{d} \right), \quad j = 1, \dots, d-1. \quad (\text{A.4})$$

Figures A.2.2 and A.5 provide schemes of the channel coefficients interpolation.

²In this case, the distance between two pilot subcarriers in the frequency domain is 3 ($d = 3$).

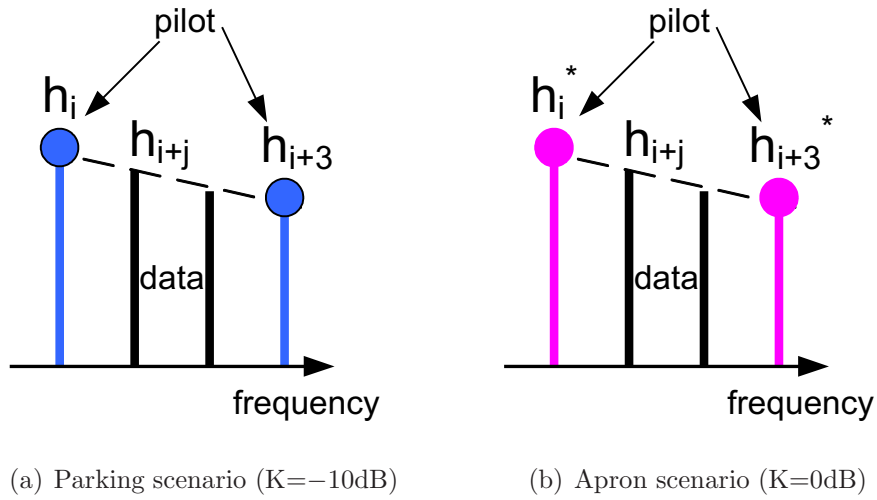


Figure A.4: RL channel interpolation scheme (frequency direction).

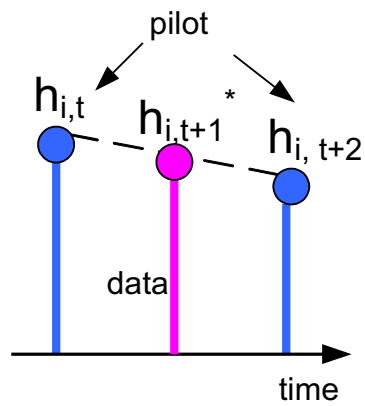


Figure A.5: RL channel interpolation scheme (time direction).

Appendix B

Low-Density Parity-Check Codes

The search of channel codes able to approach channel capacity has been an elusive target from more than fifty years, i.e. since the birth of information theory [102]. The revolution introduced by turbo codes [103] and the subsequent re-discovery of LDPC codes [104] provided the first practical mean to approach the Shannon limit over a number of communication channels. Curiously, the seed for this revolution was already present in the seminal work of R. Gallager [86]. While during most of the research on (block) channel codes in the 60s, 70s and 80s focused on algebraic constructions, LDPC codes have been neglected for more than 30 years (with a few exceptions, e.g. [105, 106]). We recall next some basic notation that will be used along the Chapter.

For a linear block code \mathcal{C} , encoding can be performed as

$$\mathbf{c} = \mathbf{u} \cdot \mathbf{G}, \quad (\text{B.1})$$

where \mathbf{u} is a vector of k bits, \mathbf{G} is the $k \times n$ binary generator matrix and \mathbf{c} is the encoded codeword of length n . The code rate is defined as the ratio

$$R = \frac{k}{n}. \quad (\text{B.2})$$

Denoting by \mathbf{H} the $m \times n$ parity-check matrix of the code \mathcal{C} , we have that for every $\mathbf{c} \in \mathcal{C}$

$$\mathbf{c} \cdot \mathbf{H}^T = \mathbf{0}, \quad (\text{B.3})$$

where $m = n - k$ if \mathbf{H} is full rank.

Considering a reference binary antipodal modulation, the n bits of \mathbf{c} are thus mapped to the channel symbols

$$x_i = 1 - 2 \cdot c_i, \quad i = 0, \dots, n - 1, \quad (\text{B.4})$$

and the received sample associated with the i -th element of \mathbf{c} is

$$r_i = x_i + n_i, \quad (\text{B.5})$$

where the received signal energy has been normalized to 1 and n_i (with $i = 0, \dots, n - 1$) are independent Gaussian random variables with zero mean and variance σ^2 .

In the following, we will introduce some basics on LDPC codes and on their (iterative) decoding algorithm.

B.1 Basics and Iterative Decoding

A LDPC code is a linear block code described by a sparse parity-check matrix \mathbf{H} . A LDPC code admits a graphical representation, usually referred to as the code *bipartite graph*, or equivalently as the code *Tanner graph* [106]. The bipartite (Tanner) graph has two set of nodes, $V = \{V_j\}_{j=0}^{n-1}$ and $C = \{C_i\}_{i=0}^{m-1}$, and a set of edges E . The nodes in V are referred to as VNs, whereas the nodes in C are referred to as CNs. An edge can connect a VN to a CN, but it cannot connect nodes withing the same set (i.e., it cannot connect two VNs, and it cannot connect two CNs). A length- l cycle is a closed path through the graph, constituted by l edges. The *degree*, d_v^j , of the variable node V_j is defined as the number of edges emanating from V_j . An analogous definition holds for the check node C_i and its degree d_c^i . Obviously d_v^j corresponds to the Hamming weight (i.e., the number of non-zero entries) of the j -th column of the parity-check matrix \mathbf{H} and d_c^i corresponds to the Hamming weight of the i -th row of \mathbf{H} .

Each check node is associated to a check equation, while each variable node refers to a codeword bit. An example of a bipartite graph is given in Fig. B.1.

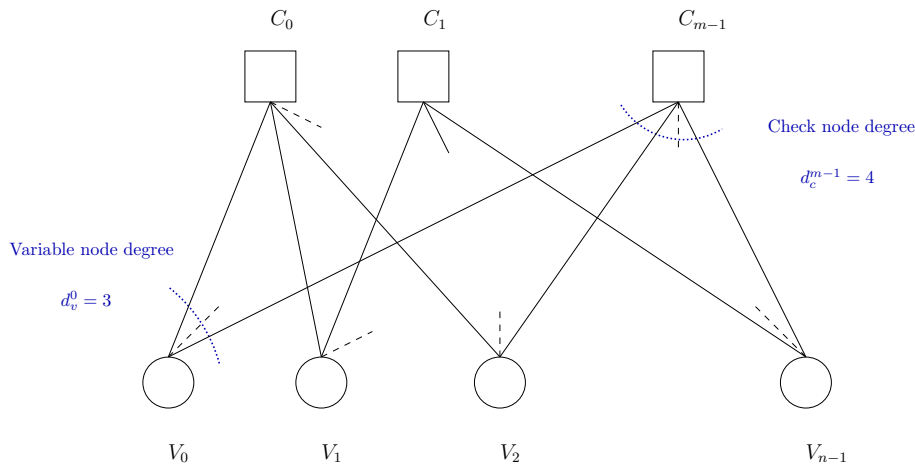


Figure B.1: Example of a bipartite (Tanner) graph for a LDPC code.

In their original setting [86], LDPC codes were based on graphs with constant variable node degree $d_v^j = d_v$ and constant check node degree $d_c^i = d_c$. Due to that, they are referred to as *regular* LDPC codes. On the contrary, *irregular* LDPC are based on graphs whose nodes possesses different degrees [107, 108]. More specifically, the VN degrees (as well as the CN degrees) are allowed to vary, accordingly to given *degree distributions*. The degree distributions are commonly given in polynomial form [107]. The VN degree distribution polynomial is denoted by $\lambda(x)$ and it is

$$\lambda(x) = \sum_{d=1}^{d_v} \lambda_d x^{d-1}, \quad (\text{B.6})$$

where λ_d is the fraction of edges connected to degree- d VNs (d_v is here the maximum

variable node degree). The check node degree distribution polynomial is

$$\rho(x) = \sum_{d=1}^{d_c} \rho_d x^{d-1}, \quad (\text{B.7})$$

where ρ_d is the fraction of edges connected to a check node of degree d and d_c is the maximum check node degree.

As an example, a (6, 3) regular LDPC code has a graph variable nodes having degree 3 and check nodes with degree equal to 6. Thus,

$$\lambda(x) = x^2, \quad \rho(x) = x^5. \quad (\text{B.8})$$

The average VN and CN degrees are denoted as \bar{d}_v , \bar{d}_c , and are given by

$$\bar{d}_v = \left[\sum_i \lambda_i \frac{1}{i} \right]^{-1} \quad (\text{B.9})$$

and

$$\bar{d}_c = \left[\sum_i \rho_i \frac{1}{i} \right]^{-1}. \quad (\text{B.10})$$

Since the overall number of edges in a graph is given by $n \cdot \bar{d}_v$ or equivalently by $m \cdot \bar{d}_c$, we have that $m/n = \bar{d}_v/\bar{d}_c$. If the parity-check matrix of the code is full-rank, the code rate is given by $R = 1 - m/n$ or in an equivalent manner by

$$R = 1 - \frac{\bar{d}_v}{\bar{d}_c}. \quad (\text{B.11})$$

The bipartite graph representation is particularly appealing from a decoding viewpoint. In fact, the iterative decoding algorithm for an LDPC code is based on a message-passing along the edges of the graph. The iterative decoder provides an estimation of the probability the i -th bit of the codeword \mathbf{c} is equal to 1, given the channel observation \mathbf{r} . This probability is usually referred to as the APP. Log-domain decoders compute an alternative metric, given by the a posteriori probability log-likelihood ratio (APP-LLR). Bearing in mind the antipodal modulation scheme that we consider as reference, the APP-LLR for i -th bit is given by

$$L^{(i)}(\mathbf{r}) = \ln \left(\frac{Pr(x_i = +1|\mathbf{r})}{Pr(x_i = -1|\mathbf{r})} \right), \quad (\text{B.12})$$

Once all the APP-LLR values have been computed, the final decision for each bit x_i is made following the rule

$$L^{(i)}(\mathbf{r}) \underset{-1}{\overset{+1}{\geq}} 0. \quad (\text{B.13})$$

For a graph without cycles, (B.12) can be derived exactly via message-passing along the graph edges via the sum-product algorithm (SPA). On the contrary, the SPA, applied to a bipartite graph with cycles, is sub-optimal, i.e., it gives an approximate evaluation of (B.12). Unfortunately, good LDPC codes rely on graphs with cycles. It follows that the SPA algorithm performs worse than ML decoding, which is nevertheless impractical already for moderate-length codes.

A typical way to reduce the sub-optimality of the SPA algorithm over graphs with cycles is to design codes whose bipartite graph avoids short cycles. Given a bipartite graph, its *girth* (g) is defined as the length of the shortest cycle present in the graph. Codes with bipartite graph possessing small values of girth (i.e., $g = 4$ or sometimes also $g = 6$) tend to perform poorly with SPA decoding. LDPC codes design techniques [109,110] have been introduced to enlarge the girth of the corresponding bipartite graphs.

Next, we review the log-domain version of the SPA.

B.1.1 The Log-Domain Sum-Product Algorithm

The iterative (log-domain) SPA decoder is based on four steps, i.e.

- Initialization
- VN processing
- CN processing
- APP-LLR evaluation and final decision.

Initialization

The decoder initialization proceeds as follows. At the i -th VN, the input message from the channel is given by

$$m_i^{ch} = \ln \left(\frac{Pr(x_i = +1|r_i)}{Pr(x_i = -1|r_i)} \right), \quad (\text{B.14})$$

which, for the binary-input AWGN channel, turn into

$$m_i^{ch} = \frac{2}{\sigma^2} r_i. \quad (\text{B.15})$$

Moreover, the messages that the CNs input to the VNs are initialized to 0, $m_{l,in}^{V_i} = 0$ for $i = 0, \dots, n$ and $l = 1, \dots, d_v^i$.

VN Processing

The i -th VN processing outputs on each edge connected to it, a message given by the sum of the channel observation, m_i^{ch} and of the $d_v^i - 1$ messages received by the VN on

the other edges,

$$m_{s,out}^{V_i} = \sum_{l=1, l \neq s}^{d_v^i} m_{l,in}^{V_i} + m_i^{ch}, \quad (\text{B.16})$$

with $s = 1 \dots d_v^i$, and d_v^i equal to the the i -th variable node degree. The messages evaluated by the VNs are used as soft-input by the check nodes. The representation of the message processing at the i -th variable node is depicted in Fig. B.2.

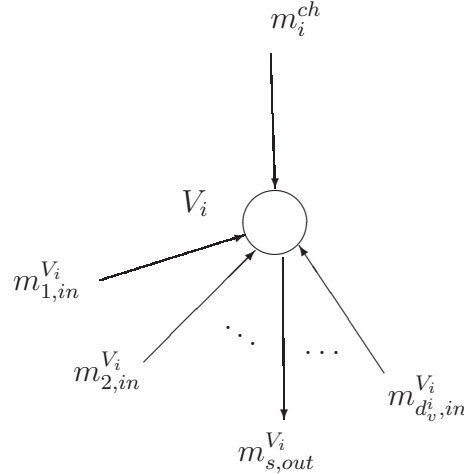


Figure B.2: Message processing at the i -th variable node.

CN Processing

To complete the each iteration, the CN processing takes place. CNs compute their soft-output given the messages received by their neighboring VNs. Denoting by $m_{l,in}^{C_j}$ the message received by the check node C_j from its l -th edge, the soft-output message that the check node sends on its s -th edge is given by

$$m_{s,out}^{C_j} = \left(\prod_{l=1, l \neq s}^{d_c^j} \alpha_l^j \right) \cdot \phi \left(\sum_{l=1, l \neq s}^{d_c^j} \phi(\beta_l^j) \right) \quad (\text{B.17})$$

where

$$\alpha_l^j = \text{sign} \left(m_{l,in}^{C_j} \right), \quad (\text{B.18})$$

$$\beta_l^j = \left| m_{l,in}^{C_j} \right| \quad (\text{B.19})$$

and

$$\phi(x) = \ln \left(\frac{e^x + 1}{e^x - 1} \right). \quad (\text{B.20})$$

Note that $s = 1 \dots d_c^j$, with d_c^j equal to the the j -th check node degree, and that $\phi(x) = \phi^{-1}(x)$. The representation of the message processing at the j -th check node is depicted in Figure B.3. The following iterations proceed with the message elaboration at the variable nodes, using as inputs the channel observations (Equation B.14) and the soft-outputs produced by the neighboring check nodes in the previous iteration (given by Equation

B.17). The VN and CN processing is iterated for a maximum number of iterations I_{max} , or it is stopped if the decoder converges to a codeword.

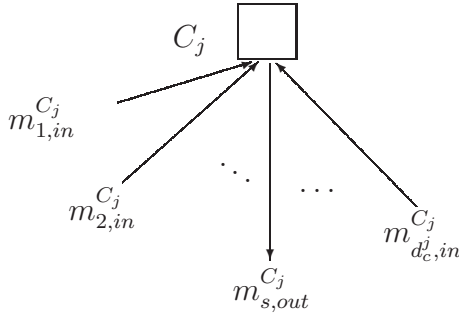


Figure B.3: Message processing at the j -th check node.

APP-LLR Evaluation and Final Decision.

The final APP-LLR for the i -th bit of the codeword is estimated as

$$L^{(i)}(\mathbf{r}) = \sum_{l=1}^{d_v^i} m_{l,in}^{V_i} + m_i^{ch}, \quad (\text{B.21})$$

and the final decision is taken according to Equation B.13.

B.2 Density Evolution Analysis

A simple yet efficient way to characterize the behavior of iterative decoding over bipartite graphs is provided by the DE analysis [111]. DE allows to derive from the degree distributions $\lambda(x)$, $\rho(x)$ a metric (the *iterative decoding threshold*, defined in the following) that anticipates how far a code (based on a graph with degrees according to $\lambda(x)$, $\rho(x)$) will perform from the Shannon limit. The key advantage of DE is that the calculation of the above-mentioned threshold is usually very fast. Thus, DE can be efficiently used in a preliminary code design phase to discard degree distributions that lead to poor performance. Additionally, DE can be placed in a loop with an optimization tool (e.g., differential evolution [112]) to derive degree distributions that allow approaching the Shannon limit.

DE analysis consists of the tracking of the probability density function (p.d.f.) of messages exchanged along the edges of a graph. The analysis is however complex for graphs with loops, since loops introduce correlation among messages, rendering the p.d.f. tracking problem unfeasible. Thus, the graph is commonly assumed to be *loop-free*. For a given degree distribution, large girths can be achieved by making the graph *sparser* which requires enlarging the graph. Thus, due to the loop-free assumption, DE provides an accurate prediction of the code performance for large blocks, $n \rightarrow \infty$. Thus, the DE analysis is often referred as an asymptotic analysis of the code performance. The loop-free assumption prevents the application of DE to predict the performance of short-block length codes. Nevertheless, for long or moderate block lengths (e.g., $n > 1000$),

degree distributions leading to good asymptotic performance allow construction codes with excellent performance in finite block length regime. The iterative decoding threshold (which is the metric derived by DE) is the lowest value of the signal-to-noise ratio E_b/N_0 , $(E_b/N_0)^*$, for which the iterative decoder of an infinite block length code (with a given degree distribution) converges successfully to a vanishing bit error probability, $P_b \rightarrow 0$, with an unbounded number of iterations.

A simplification of DE comes from modeling the messages exchanged along the graph edges as Gaussian random variables. In this way, instead of tracking a complete p.d.f., DE reduces to tracking the Gaussian distribution parameters (mean and variance). We will see next that the tracking problem can be further reduced to the tracking of a single parameter.

B.2.1 The Gaussian Approximation

The Gaussian approximation was introduced in [113,114] to perform a simplified and accurate density evolution analysis of iterative schemes. Since a Gaussian p.d.f. is completely characterized by its mean value and variance, the infinite-dimensional problem of tracking the evolution of a p.d.f. turns into a two-dimensional tracking problem, which further reduces to a one-dimensional problem if the p.d.f. is modeled as a *Gaussian symmetric* density [107]. A distribution $p(x)$ is referred to as *symmetric* if

$$p(x) = p(-x)e^x. \quad (\text{B.22})$$

When applying such a condition to a Gaussian distribution $p(x)$, the variance and the mean turn to be related by

$$\text{var}[X] = 2 \cdot \mathbb{E}[X]. \quad (\text{B.23})$$

Hence, given the mean (or the variance), the distribution is completely characterized, leading to a mono-dimensional analysis.

It happens that the log-likelihood ratios at the input of the log-domain decoder can be modeled with symmetric Gaussian distributions. In fact, the channel output m_i^{ch} is $m_i^{ch} = \frac{2}{\sigma^2}r_i$ with $r_i = x_i + n_i$ and $n_i \sim \mathcal{N}(0, \sigma^2)$. Assuming $x_i = +1, \forall i$ (all-0 codeword assumption), the mean of m_i^{ch} is

$$\mu_{ch} = E[m_i^{ch}] = \frac{2}{\sigma^2} \quad (\text{B.24})$$

while the variance is

$$\sigma_{ch}^2 = \text{var}\{m_i^{ch}\} = \frac{4}{\sigma^2} = 2\mu_{ch}. \quad (\text{B.25})$$

Therefore,

$$p(m_i^{ch}|x_i = +1) = \frac{1}{\sqrt{4\pi\mu_{ch}}} \exp\left[-\frac{(m_i^{ch} - \mu_{ch})^2}{4\mu_{ch}}\right]. \quad (\text{B.26})$$

Note that, considering the AWGN channel with BPSK signalling and channel coding with rate R , the following relation between the noise variance and the signal-to-noise ratio E_b/N_0

$$\frac{E_b}{N_0} = \frac{1}{2R\sigma^2} \quad (\text{B.27})$$

implies that

$$\sigma_{ch}^2 = \frac{4}{\sigma^2} = 8R\frac{E_b}{N_0}. \quad (\text{B.28})$$

The DE analysis (under the symmetric Gaussian assumption) proceeds as follows.

1. Assume the all-0 codeword transmitted ($x_i = +1$).
2. Set E_b/N_0 . Accordingly, the p.d.f. of the generic channel observation m_i^{ch} is given by (B.25), (B.26) and (B.28).
3. The evolution of the p.d.f.s associated to the messages exchanged along the edges of the graph, is evaluated iteration after iteration under the assumption of a loop-free graph.
4. If the densities of the messages tend to the point-mass at infinity, as the number of iterations increases, the error probability P_e associated to the messages tends to 0. If not, the decoder will not converge to a vanishing bit error probability.

The Gaussian approximation (GA) simplifies the tracking of evolution of the p.d.f.s, which reduces to the analysis of the evolution of a single parameter. In the GA DE analysis, the parameter to be tracked can be any parameter that characterizes a Gaussian symmetric distribution. For example, the parameters could be

- the mean
- the variance
- the message SNR, given by the ratio between the square of the mean and the variance
- the error probability associated binary detection of the message
- the mutual information between the message and the codeword bit associated to the message [73].

We will focus next on the last metric, which leads to the so-called EXIT analysis [73]. The main advantage of that approach relies on its universality (can be applied to a number of communication channels), on its accuracy [115] and on its implications (e.g., the Area Theorem [100]) from an information-theoretic viewpoint.

B.2.2 Extrinsic Information Transfer Charts

In [72], mutual information EXIT charts are employed to analyze the iterative decoding of LDPC codes. The mutual information between a binary random variable (r.v.) X , with $Pr(X = +\mu) = 1/2$ and $Pr(X = -\mu) = 1/2$, and a continuous r.v. Y with conditional p.d.f.

$$p_{Y|X}(y|x) = \frac{1}{\sqrt{4\pi\mu}} e^{-\frac{(y-x)^2}{4\mu}}, \quad (\text{B.29})$$

is defined as

$$J(\sigma) = I(Y; X) = H(Y) - H(Y|X), \quad (\text{B.30})$$

with $\sigma^2 = 2\mu$ for symmetric Gaussian assumption. In other words, $J(\sigma)$ returns the maximum mutual information between a binary r.v. $X \in \{\pm\mu\}$ and the r.v. Y defined by the superposition on X of a Gaussian noise sample with zero mean and variance $\sigma^2 = 2\mu$. $J(\sigma)$ represents the capacity of a binary-input additive Gaussian noise channel, and it is given by [73]

$$J(\sigma) = 1 - \int_{-\infty}^{+\infty} \frac{1}{\sqrt{2\pi\sigma^2}} e^{-\frac{(y-\sigma^2/2)^2}{2\sigma^2}} \cdot \log_2(1 + e^{-y}) dy. \quad (\text{B.31})$$

The mutual information EXIT function for variable nodes can be computed as follows. Consider the variable node processing, where

$$m_{s,out}^{V_i} = \sum_{l=1, l \neq s}^{d_v^i} m_{l,in}^{V_i} + m_i^{ch}. \quad (\text{B.32})$$

Assuming that the channel observation (conditioned to the related codeword bit $x_i = +1$) is distributed accordingly to (B.26), and considering the input messages $m_{l,in}^{V_i}$ ($l = 1 \dots d_v^i, l \neq s$), conditioned to the related codeword bit $x_i = +1$, as independent and identically-distributed Gaussian symmetric r.v.s

$$p(m_{l,in}^{V_i} | x_i = +1) = \frac{1}{\sqrt{4\pi\mu_l}} e^{-\frac{(m_{l,in}^{V_i} - \mu_l)^2}{4\mu_l}}, \quad (\text{B.33})$$

the output message $m_{s,out}^{V_i}$ will be distributed as

$$p(m_{s,out}^{V_i} | x_i = +1) = \frac{1}{\sqrt{4\pi\mu_s}} e^{-\frac{(m_{s,out}^{V_i} - \mu_s)^2}{4\mu_s}}, \quad (\text{B.34})$$

with

$$\mu_s = \sum_{l=1, l \neq s}^{d_v^i} \mu_l + \mu^{ch}. \quad (\text{B.35})$$

If the input messages $m_{l,in}^{V_i}$ ($l = 1 \dots d_v^i, l \neq s$) are identically distributed, i.e., if $\mu_l \equiv \mu_{IN}$, then

$$\mu_s = (d_v^i - 1) \cdot \mu_{IN} + \mu^{ch}. \quad (\text{B.36})$$

Recalling that, for Gaussian symmetric r.v.s, the variance is proportional to the mean value, we get

$$\sigma_s^2 = (d_v^i - 1) \cdot \sigma_{IN}^2 + \sigma_{ch}^2. \quad (\text{B.37})$$

If we define I_{Av} as the mutual information for the a priori knowledge available to the variable node (i.e., the mutual information between the input messages and the associated codeword bit),

$$I_{Av} = J(\sigma_{IN}). \quad (\text{B.38})$$

Therefore,

$$\sigma_s^2 = (d_v^i - 1) \cdot (J^{-1}(I_{Av}))^2 + \sigma_{ch}^2. \quad (\text{B.39})$$

The mutual information I_{Ev} between the output message and the associated codeword symbol will be

$$I_{Ev} = J(\sigma_s) = J\left(\sqrt{(d_v^i - 1) \cdot (J^{-1}(I_{Av}))^2 + \sigma_{ch}^2}\right). \quad (\text{B.40})$$

Recalling (B.28), the EXIT function for a degree- d_v variable node will be

$$I_{Ev}\left(I_{Av}, \frac{E_b}{N_0}\right) = J(\sigma_s) = J\left(\sqrt{(d_v - 1) \cdot (J^{-1}(I_{Av}))^2 + 8r \frac{E_b}{N_0}}\right). \quad (\text{B.41})$$

The EXIT function for a degree- d_c check node can be derived exploiting a dual property [72]. In this case, the EXIT curve for a $(d_c, d_c - 1)$ single parity-check (SPC) code can be obtained from the EXIT curve of a $(d_c, 1)$ repetition code. This property is exact on the binary erasure channel, while it is just an (accurate) approximation on the binary-input AWGN channel [72]. The EXIT function for a degree- d_c check node is therefore

$$I_{Ec}(I_{Ac}) \simeq 1 - J\left(\sqrt{d_c - 1} \cdot J^{-1}(1 - I_{Ac})\right). \quad (\text{B.42})$$

The inverse of (B.42) is given by

$$I_{Ac}(I_{Ev}) \simeq 1 - J\left(\frac{J^{-1}(1 - I_{Ev})}{\sqrt{d_c - 1}}\right). \quad (\text{B.43})$$

The EXIT chart for a regular (d_v, d_c) LDPC code ensemble is obtained by recalling that

$$I_{Av} = I_{Ec} \quad (\text{B.44})$$

$$I_{Ac} = I_{Ev} \quad (\text{B.45})$$

and plotting on the same chart $I_{Ev}\left(I_{Av}, \frac{E_b}{N_0}\right)$ and $I_{Ac}(I_{Ec})$.

The EXIT analysis can be applied to irregular LDPC codes too. In [72], the check-regular case (i.e., the check node degree is constant) is discussed. Denoting the set of possible degrees as $\{d_{v,i}\}$, with $i = 1 \dots D$, the fraction of edges incident to variable nodes

of degree $d_{v,i}$ is given by λ_i . The variable node EXIT function is then given by the average of the EXIT functions for each variable node type,

$$I_{Ev} \left(I_{Av}, \frac{E_b}{N_0} \right) = \sum_{i=1}^D \lambda_i \cdot J \left(\sqrt{(d_{v,i} - 1) \cdot (J^{-1}(I_{Av}))^2 + 8r \frac{E_b}{N_0}} \right). \quad (\text{B.46})$$

The EXIT chart for a check-regular LDPC code ensemble is then given again by the plots of $I_{Ev} \left(I_{Av}, \frac{E_b}{N_0} \right)$ and $I_{Ac}(I_{Ec})$.

B.2.3 The Area Theorem and Its Consequences

The EXIT analysis allows to derive some interesting properties of iteratively-decodable codes. Among them, the Area Theorem of [100] reveals to be extremely useful to define a trade-off between capacity-approaching performance and decoding complexity. We review next this result, focusing on the simplified case of EXIT charts for the BEC.

EXIT Charts on the Binary Erasure Channel

On the BEC, the EXIT analysis is exact. More importantly, it becomes simple and insightful. This is due to the fact that each edge in the code bipartite graph can transport two types of messages, i.e. the correct bit value or an erasure. Let's denote by p the probability that a message sent by a VN to a CN is an erasure, and q the probability that a message sent by a CN to a VN is an erasure. The MI at the output of VNs is given by

$$I_{Ev} = I_{Ac} = 1 - p, \quad (\text{B.47})$$

while at the output of CNs by

$$I_{Ec} = I_{Av} = 1 - q. \quad (\text{B.48})$$

If we denote by ϵ the channel erasure probability, the EXIT functions for degree- d VNs and CNs become

$$I_{Ev}(I_{Av}) = 1 - \epsilon(1 - I_{Av})^{d-1} \quad (\text{B.49})$$

and

$$I_{Ec}(I_{Ac}) = I_{Ac}^{d-1}. \quad (\text{B.50})$$

In the irregular LDPC case, we have

$$I_{Ev}(I_{Av}) = 1 - \epsilon \sum_d \lambda_d (1 - I_{Av})^{d-1} = 1 - \epsilon \lambda (1 - I_{Av}) \quad (\text{B.51})$$

and

$$I_{Ec}(I_{Ac}) = \sum_d \rho_d I_{Ac}^{d-1} = \rho(I_{Ac}). \quad (\text{B.52})$$

It has been shown that, remarkably, the EXIT functions over the erasure channel model quite well the EXIT functions over more general channel, e.g. the AWGN, the binary symmetric channel (BSC) or the Rayleigh channel [116–118]. Thus, the results achieved on the BEC are often extended to other channels.

The Area Theorem

Let's consider now the area lying below each EXIT function. We have that

$$A_v = \int_0^1 I_{Ev}(x) dx = 1 - \epsilon \sum_d \lambda_d \int_0^1 (1-x)^{d-1} dx = 1 - \epsilon \sum_d \lambda_d \frac{1}{d}. \quad (\text{B.53})$$

$$A_c = \int_0^1 I_{Ec}(x) dx = \sum_d \int_0^1 \rho_d x^{d-1} dx = \sum_d \rho_d \frac{1}{d}. \quad (\text{B.54})$$

By a simple inspection of the equations above, we can see that the area underlined by the EXIT function of a specific (n, k) component code equals 1 minus its code rate. This result is referred to as the *Area Theorem* [100]. For a degree- d VN we have that $A_v = 1 - \epsilon/d$. By posing $\epsilon = 1$ (thus evaluating only the extrinsic information contribution to the EXIT function), we have $A_v = (d-1)/d$, which is 1 minus the code rate of a length- d repetition code. Similarly, we have that for a degree- d CN, $A_c = 1/d$, which is 1 minus the code rate of a length- d single-parity-check code. Thus, the result we are going to derive next relates to every iterative decoding scheme relying on exchange of soft-information between two component decoders (thus, to most of the LDPC and the turbo code ensembles).

Figure B.4 shows the EXIT chart over the BEC at the decoding threshold, $\epsilon^* = 0.429$, for the $(3, 6)$ regular LDPC code ensemble (i.e., an LDPC code ensemble with constant variable node degree 3 and constant check node degree 6). The shaded areas represent the complements of the areas underlying the CN and the VN EXIT functions. When operating below (or at) the decoding threshold, the tunnel between the two curves has to be open. As a result, we have that

$$(1 - A_v) + (1 - A_c) \leq 1, \quad (\text{B.55})$$

leading, in the general LDPC code case, to

$$\epsilon^* \sum_d \lambda_d \frac{1}{d} + 1 - \sum_d \rho_d \frac{1}{d} \leq 1. \quad (\text{B.56})$$

After noticing that $\sum_d \lambda_d \frac{1}{d} = 1/\bar{d}_v$ and that $\sum_d \rho_d \frac{1}{d} = 1/\bar{d}_c$, where \bar{d}_v and \bar{d}_c are the average variable and check node degrees, we get to

$$\epsilon^* \frac{1}{\bar{d}_v} - \frac{1}{\bar{d}_c} \leq 0. \quad (\text{B.57})$$

and to

$$\epsilon^* \leq \frac{\bar{d}_v}{\bar{d}_c}, \quad (\text{B.58})$$

thus to

$$1 - \frac{\bar{d}_v}{\bar{d}_c} = r \leq 1 - \epsilon^* = C. \quad (\text{B.59})$$

This essentially proves the Shannon theorem on channel capacity for the BEC just using EXIT chart arguments: the coding rate of any LDPC code ensemble, R , cannot exceed the channel capacity of a BEC with erasure probability ϵ^* , given by $C = 1 - \epsilon^*$. It is now interesting to check what is the role of the white area (A_{gap} in the following) in Figure B.4. We have

$$\begin{aligned} A_{gap} &= 1 - (1 - A_v) - (1 - A_c) = 1 - \epsilon^* \frac{1}{d_v} - 1 + \frac{1}{d_c} \\ &= -\epsilon^* \frac{1}{d_v} + \frac{1}{d_c} = \frac{1}{d_v} [C - r]. \end{aligned} \quad (\text{B.60})$$

Hence, the gap area A_{gap} is proportional to the gap between the ensemble code rate and the channel capacity. This leads to the following considerations.

- I. A scheme which shall approach capacity under iterative decoding must rely on an EXIT chart having, at the threshold, a very narrow tunnel between the check and the variable node curves.
- II. Being the tunnel narrow for capacity-approaching ensembles, capacity can be approached only with a large number of iterations.
- III. A scheme with a wider tunnel between the variable and the check node EXIT functions will suffer for a loss compared with channel capacity, but may allow reaching low error probabilities with a lower number of iterations.

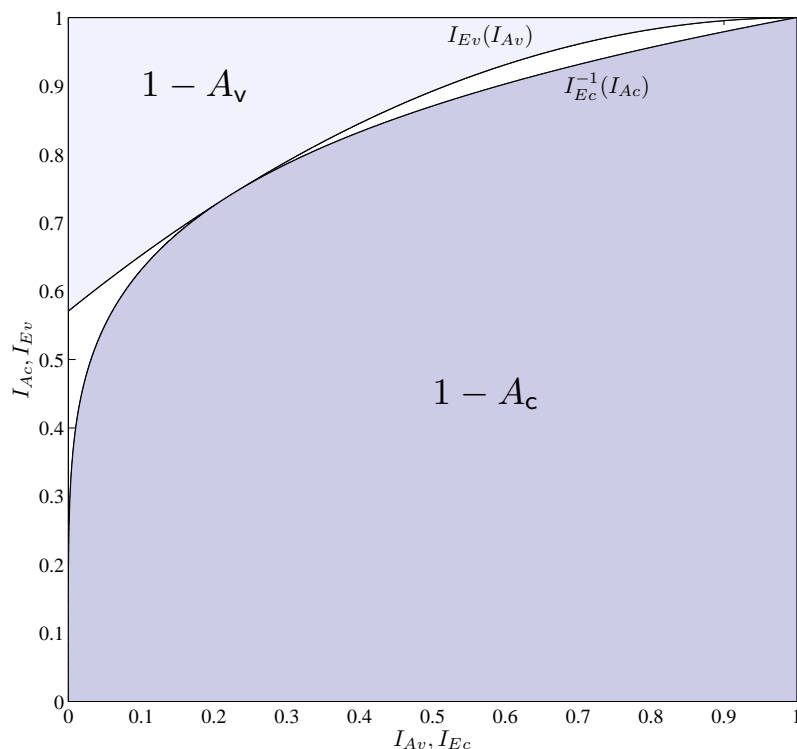


Figure B.4: Mutual information EXIT chart for the (3, 6) regular LDPC codes ensemble, at the threshold, over the BEC.

B.3 LDPC Code Designs

Since the rediscovery of LDPC codes in the 90s [104], several classes of LDPC codes have been introduced. We provide next a chronology of the main developments in this area. As reference, we will consider as finite-length benchmark on the code performance the RCB introduced by Gallager [119].

- The IRA codes (1998, [96]).
- Irregular LDPC codes (2000, [107, 108]).
- Finite Geometries LDPC codes (2001, [120]).
- Enhanced design of IRA codes (2004, [121]).
- Quasi-cyclic LDPC codes based on circulant permutation matrices (2004, [122]).
- multi-edge-type (MET) LDPC and protograph-based LDPC (2004 [60, 123, 124]).
- The class of accumulate-repeat-accumulate (ARA)-like codes (2005, [125, 126]).
- Terminated convolutional LDPC codes with spatial coupling (2008, [127–130]).

Threshold-optimized IRA codes and the irregular LDPC codes of [107, 108] achieve decoding thresholds that are extremely close to capacity. Nevertheless, they tend to show high error floors when the finite block size regime is considered [121]. The enhanced IRA design of [121] trades off threshold performance vs. error floor. The codes of [121] are able to perform within 1 dB from the RCB down to low error rates for $R \geq 1/2$, while they perform within 1.5 dB from the RCB for lower rates. The finite geometry approach of [120] leads to codes with highly regular structure and degree distributions, bringing to codes with extremely low error floors at the expense of a loss w.r.t. the RCB. A key limitation of the codes of [120] is that they cannot be constructed for arbitrary block lengths / code rates, being their design driven by geometric constructions on finite fields. The quasi-cyclic construction proposed in [122] has the merit of removing this lack of flexibility, maintaining a highly-structured parity-check matrix form while allowing more freedom in the code design. As a result, the architecture aware (AA) codes presented in [131], as well as the structured IRA design of [81] design rely on the construction of [122]. An actual breakthrough on the LDPC code design is given by the introduction of MET and protograph LDPC codes. These LDPC code classes introduced explicitly state (punctured) VNs in the code graph. Furthermore, they specify in careful manner the edge connectivity properties of a graph, with respect to the usual degree distribution pairs. Thanks to that, they allow achieving excellent iterative decoding thresholds while keeping low error floors. It is important to observe that the IRA codes of [121], as well as the quasi-cyclic construction of [122] are specific instances of protograph LDPC codes which do not use

state variable nodes. Also the ARA-like codes [125, 126] are protograph-based, but they exploit state variables to achieve a better tradeoff between error floor and waterfall performance. A review of recent protograph code designs can be found in [62, 69]. A class of codes amenable of protograph representation is the one of terminated convolutional LDPC codes [127–130]. Convolutional LDPC codes possess extremely close-to-capacity thresholds (via the so-called threshold saturation effect recently discovered in [129, 130]) as well as low error floors. Nevertheless, their appealing features emerge at rather large block lengths (in the order of 10^5 bits or more), and they require a large number of iterations to achieve the promised performance. Besides decoding performance, several classes of LDPC codes have been introduced which target efficient encoder implementations. Efficient encoding structures for LDPC codes can be classified according to two major classes, i.e.

A. Accumulator-based encoders.

B. Quasi-cyclic encoders.

In general, accumulator-based encoders have linear-time complexity. They are generally seen as the concatenation of two stages: in a first stage, the k information bits of \mathbf{u} are encoded through a low-density generator matrix. Here, the number of operations to produce each of the $n - k$ (intermediate) encoded bits (grouped in the \mathbf{v} vector) is limited to the XOR of a small constant number of information bits. The intermediate symbols are then processed by an accumulator which produces the $n - k$ parity bits of \mathbf{p} as $p_i = v_i + p_{i-1}$. Codes fulfilling this encoding process are general IRA/irregular LDPC codes, and accumulator-based protograph codes (e.g., ARA codes). Quasi-cyclic encoding can be in general applied to any code with parity-check matrix in block circulant form [122]. Thus, all AA LDPC codes admit a quasi-cyclic encoder [132]. In general, quasi-cyclic encoding requires the derivation of the generator matrix \mathbf{G} in block-circulant form. The calculation of the codeword \mathbf{c} is then give by $\mathbf{c} = \mathbf{u} \times \mathbf{G}$, where the generator matrix is in general a dense, block circulant matrix. Thus, the matrix multiplication $\mathbf{u} \times \mathbf{G}$ in general required a number of XORs per encoded bits that can be as large as $k/2$. However, the multiplication can be structured in hardware by performing it via long shift registers (thanks to the block circulant structure of \mathbf{G} , [122]). A more efficient approach can be obtained by exploiting the general efficient encoding method of [133], which works for any general LDPC code, modified to account for the block circulant structure of the parity-check matrix.

B.3.1 Protograph Designs

A protograph [60, 82, 123, 134] is a relatively small bipartite graph from which a larger graph can be obtained by a copy-and-permute procedure: the protograph is copied q times, and then the edges of the individual replicas are permuted among the q replicas (under

restrictions described below) to obtain a single, large graph. Suppose the protograph possesses N variable nodes and M check nodes. Then the *derived graph* will consist of $n = Nq$ variable nodes and $m = Mq$ check nodes.

Observe that the edge permutations cannot be arbitrary. In particular, the nodes of the protograph are labeled so that if variable node A is connected to check node B in the protograph, then variable node A in a replica can only connect to one of the q replicated B check nodes. Doing so preserves the iterative decoding properties of the protograph. If the edge permutations are organized in a cyclic manner such that the final parity-check matrix is in block-circulant form, the derived graph describes a code that can be put in quasi-cyclic form, as described in the previous section. A protograph can possess parallel edges, i.e. two nodes can be connected by more than one edge. The copy-and-permute procedure must eliminate such parallel connections in order to obtain a derived graph appropriate for a parity-check matrix.

Several well-known codes constructions are amenable to protograph representation. Note that this property is particularly appealing for high-throughput decoder implementations [60]. For quasi-cyclic LDPC codes, the protograph consist of the bipartite graph describing the base matrix \mathbf{H}_{base} . Regular LDPC codes possess simple protographs too: in Fig. B.5 two examples are provided.

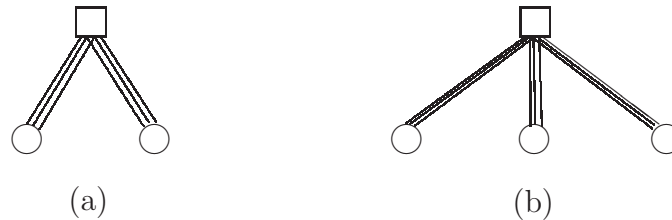


Figure B.5: Example of protographs for (a) regular rate-1/2 LDPC codes with $d_c = 6$ and $d_v = 3$ and (b) regular rate-2/3 LDPC codes with $d_c = 9$ and $d_v = 3$.

Instances of protographs provided in Figure B.6(a) for an IRA code with constant variable node degree equal to 4 for information bits, and Figure B.6(b) for an ARA [125] code with repetition rate equal to 4 (the dark circle correspond to a punctured variable node). Protograph-based codes represent instances of multi-edge type LDPC codes [123].

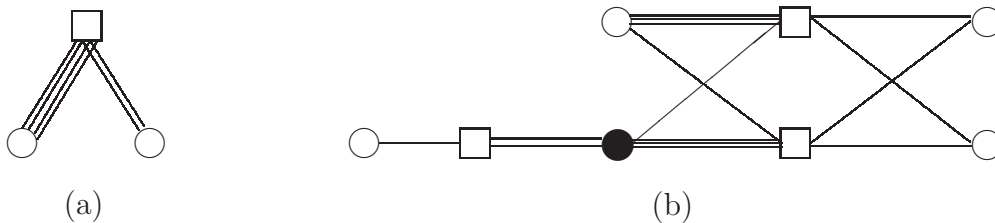


Figure B.6: Example of protographs for (a) rate-1/2 IRA code with $a = 4$ and information bits variable nodes with degree 4, and (b) rate-1/2 ARA codes with inner repetition rate equal to 4.

B.4 On Decoding Over Erasure Channels and PLC

As already mentioned, LDPC codes exhibit extraordinary performance under IT decoding over a wide range of communication channels.

A recent flurry of research activities [9, 15, 94, 135, 136] has been focused on the application of error control techniques to the protocol stack layers different from the physical one. Such coding techniques deal with the use of a (linear) block code applied to *encoding units* (symbols) that are usually packets with constant size. We will refer in the following to such coding techniques as *packet level coding*. The packet level encoder receives as input a set of k symbols (packets), and produces as output $n > k$ packets. At the receiver, after the physical layer decoding, a CRC test is performed, and the packets that have been validated are forwarded to the packet-layer decoder. The packets that are corrupted are marked as lost. Thus, the upper layers *see* packet erasures. The role of the packet-level decoder is therefore to recover the erased packets by use of the redundant packets introduced on the transmitter side.

An appealing application for packet level coding deals with file-based transmission, especially in the context of reliable multicast and broadcast mobile transmissions, where long outages (due to correlated fading) may jeopardize the correct reception of packets.

LDPC codes are extremely powerful erasure correcting codes. This is true under IT decoding and, remarkably, also under ML decoding, which over BEC becomes not only feasible, but also efficient. In fact, if the communication channel is a BEC, ML decoding is equivalent to solving the linear equation

$$\mathbf{x}_{\overline{K}} \mathbf{H}_{\overline{K}}^T = \mathbf{x}_K \mathbf{H}_K^T, \quad (\text{B.61})$$

where $\mathbf{x}_{\overline{K}}$ (\mathbf{x}_K) denotes the set of erased (correctly received) encoded bits and $\mathbf{H}_{\overline{K}}$ (\mathbf{H}_K) the submatrix composed of the corresponding columns of the parity-check matrix \mathbf{H} . Then, ML decoding for the BEC can be implemented as a Gaussian elimination performed on the binary matrix $\mathbf{H}_{\overline{K}}^T$: its complexity is in general $O(n^3)$, where n is the codeword length. It is obvious that for long block lengths ML decoding becomes impractical so that IT decoding is preferred. For LDPC codes, it is indeed possible to take advantage of both the ML and IT approach. To keep complexity low, a first decoding attempt is done in an iterative manner [92]. If not successful, the residual set of unknowns is processed by an ML decoder. Efficient ways of implementing ML decoders for LDPC codes can be found in [95], whose approach takes basically benefit from the sparse nature of the parity-check matrix of the code.

Efficient ML Decoding for LDPC Codes Over the Erasure Channel

The problem of Gaussian elimination (GE) over large sparse, binary matrices has been widely investigated in the past (see e.g. [95, 137]). A usual approach relies on structured GE with the purpose of converting the given system of sparse linear equations to a new

smaller system that can be solved afterwards by brute-force GE [95,137]. Here, we provide an simplified overview of the approach presented in [95].

For sake of clarity, we first apply column permutations to arrange the parity check matrix \mathbf{H} as in Equation B.61: the left part shall contain all the columns related to known variable nodes (\mathbf{H}_K), whereas the right part shall be made up of all the columns related to erased variable nodes ($\mathbf{H}_{\bar{K}}$). Thus, to solve the unknowns, we proceed as follows:

- Perform diagonal extension steps on $\mathbf{H}_{\bar{K}}$. This results in the sub-matrices \mathbf{B} , as well as \mathbf{P} that is in a lower triangular form, and columns that cannot be put in lower triangular form (columns of matrices \mathbf{A} and \mathbf{S}). The variable nodes corresponding to the former set of columns build up the so-called *pivots* (see Figure B.7(b)). All remaining unknown variable can be obtained by linear combination of the pivots and of the known variables.
- Zero the matrix \mathbf{B} by summing its rows with those of \mathbf{P} (Figure B.7(a)).
- Resolve the system by performing Gaussian elimination only on \mathbf{A}' . Out of the pivots, the unknown variables can be obtained iteratively by back-substitution thanks to the lower triangular structure of \mathbf{P} .

The main strength of this algorithm lies in the fact that GE is only performed on \mathbf{A}' and not on the entire set of unknown variables. Therefore, it is of great interest to keep the dimensions of \mathbf{A}' rather small. This can be obtained by sophisticated ways of choosing the pivots [95] and by a judicious code design [92].

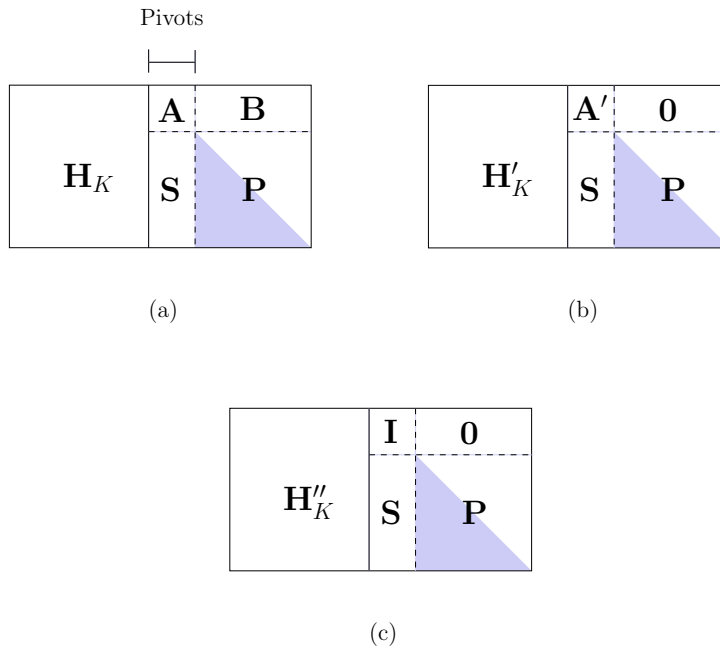


Figure B.7: ML decoder as in [95]. (a) Pivots selection within $\mathbf{H}_{\bar{K}}$. (b) Zeroing of matrix \mathbf{B} . (c) Gaussian Elimination on \mathbf{A}' .

Bibliography

- [1] IEEE standard 802.16-2004, “Local and Metropolitan Area Networks - Part 16: Air Interface for Fixed Broadband Wireless Access Systems,” Oct. 2004.
- [2] IEEE 802.16-2005, “Part 16: Air Interface for Fixed and Mobile Broadband Wireless Access Systems, Amendment 2: Physical and Medium Access Control Layers for Combined Fixed and Mobile Operation in Licensed Bands and Corrigendum 1,” Feb. 2006.
- [3] IEEE 802.16-2009, “Standard for Local and Metropolitan Area Networks - Part 16: Air Interface for Fixed Broadband Wireless Access Systems,” 2009.
- [4] “IEEE 802.16e System Profile Analysis for FCI’s Airport Surface Operation,” Sept. 2009, European Organization for the Safety of Air Navigation.
- [5] Air Navigation Commission, “Report on the Results of the ITU World Radiocommunication Conference (WRC-07),” 2007.
- [6] P. Pulini, G. Liva, and M. Chiani, “Protograph EXIT Analysis over Block Fading Channels with Application to Relays,” in *ICC’12*. Ottawa, CA: IEEE, June 2012.
- [7] M. Luby, M. Mitzenmacher, M. A. Shokrollahi, D. A. Spielman, and V. Stemann, “Practical loss-resilient codes,” in *Proc. 29th Symp. Theory Computing*, 1997, pp. 150–159.
- [8] J. Byers, M. Luby, and M. Mitzenmacher, “A digital fountain approach to reliable distribution of bulk data,” *IEEE Journal on Selected Areas in Communications*, vol. 20, no. 8, pp. 1528–1540, Oct. 2002.
- [9] M. Shokrollahi, “Raptor codes,” *IEEE Transactions on Information Theory*, vol. 52, no. 6, pp. 2551–2567, Jun. 2006.
- [10] M. Luby, M. Watson, T. Gasiba, T. Stockhammer, and W. Xu, “Raptor codes for reliable download delivery in wireless broadcast systems,” in *Proc. of IEEE Consumer Communications and Networking Conf.*, vol. 1, Jan. 2006, pp. 192–197.
- [11] G. Liva, E. Paolini, and M. Chiani, “Performance versus overhead for fountain codes over \mathbb{F}_q ,” *IEEE Comm. Letters.*, vol. 14, no. 2, pp. 178–180, 2010.

-
- [12] G. Faria, J. Henriksson, E. Stare, and P. Talmola, "DVB-H: Digital Broadcast Services to Handheld Devices," *Proceedings of the IEEE*, vol. 94, no. 1, pp. 194–209, Jan 2006.
- [13] "Framing structure, channel coding and modulation for Satellite Services to Handheld devices (SH) below 3GHz," 2007.
- [14] 3GPP TS 26.346 V6.1.0, "Technical specification group services and system aspects; multimedia broadcast/multicast service; protocols and codecs," Jun. 2005.
- [15] G. P. Calzolari, M. Chiani, F. Chiaraluce, R. Garello, and E. Paolini, "Channel coding for future space missions: New requirements and trends," *Proc. IEEE*, vol. 95, no. 11, pp. 2157–2170, Nov. 2007.
- [16] T. de Cola, H. Ernst, and M. Marchese, "Performance analysis of ccstds file delivery protocol and erasure coding techniques in deep space environments," *Comput. Netw.*, vol. 51, pp. 4032–4049, October 2007.
- [17] T. de Cola, E. Paolini, G. Liva, and G. P. Calzolari, "Reliability Options for Data Communications in the Future Deep-Space Missions," *Proc. IEEE*, 2011.
- [18] P. A. Bello, "Characterization of Randomly Time-Variant Linear Channels," *IEEE Trans. Comm.*, vol. 11, no. 4, pp. 360–393, Dec. 1963.
- [19] P. Pulini, G. Liva, and M. Chiani, "Unequal Diversity LDPC Codes for Relay Channels," *IEEE Transaction on Communications*, 2012, submitted.
- [20] G. Liva, P. Pulini, and M. Chiani, "On-Line Construction of Irregular Repeat Accumulate Codes for Packet Erasure Channels," *IEEE Transaction on Wireless Communications*, 2011, submitted.
- [21] P. Pulini and M. Chiani, "Improving the performance of AeroMACS by cooperative communications," in *Proc. Digital Avionics System Conference, DASC 30th*, Seattle, WG, US, October 2011.
- [22] G. Liva, P. Pulini, and M. Chiani, "Flexible On-line Construction of IRA Codes for Packet Erasure Correction with Application to Aeronautical Communications," in *Proc. IEEE Int. Conf. on Communications*, Kyoto, Japan, Jun. 2011.
- [23] P. Pulini and M. Chiani, "Improving the Forward Link of the Future Airport Data Link by Space-Time Coding," in *Proc. InOwO'10*, Hamburg, Germany, Sep. 2010.
- [24] P. Pulini, "Forward Link Performance Analysis for the Future IEEE 802.16-based Airport Data-Link," in *Proc. IEEE Int. Conf. on Communications*, Cape Town, South Africa, May 2010.

- [25] S. Gligorevic, and P. Pulini, "Simplified Airport Surface Channel Model Based on the WSSUS Assumption," in *ICNS'10*, Washington, US, May 2009.
- [26] P. Pulini, and S. Gligorevic, "WiMAX Performance in the Airport Environment," in *MCSS'09*, Hersching, Germany, May 2009.
- [27] EUROCONTROL, FAA, "Action Plan 17: Future Communications Study (Final Conclusions and Recommendations Report)," Nov. 2007.
- [28] Air Navigation Commission, "Report on the Results of the ITU World Radiocommunication Conference (WRC-07)," 2007.
- [29] S. Gligorevic, R. Zierhut, T. Jost, W. Wang, "Airport Channel Measurement at 5.2 GHz," in *Proc. EuCAP 2009*, Berlin, Germany, Mar. 2009.
- [30] R. H. Clarke, "A statistical theory of mobile-radio reception," *Bell Sys. Tech. J.*, vol. 47, no. 6, pp. 957–1000, July/Aug. 1968.
- [31] S. O. Rice, "Mathematical analysis of random noise," *Bell Sys. Tech. J.*, vol. 23, pp. 282–332, July 1944.
- [32] —, "Mathematical analysis of random noise," *Bell Sys. Tech. J.*, vol. 24, pp. 46–156, Jan. 1945.
- [33] P. Höher, *Kohärenter Empfang trelliscodierter PSK-Signale auf frequenzselektiven Mobilfunkkanälen; Entzerrung, Decodierung und Kanalparameterschätzung*. VDI-Verlag, Fortschritt-Berichte, 1990, vol. 147.
- [34] —, "A statistical discrete-time model for the wssus multipath channel," *IEEE Trans. Veh. Technol.*, vol. 41, no. 4, pp. 461–468, Nov. 1992.
- [35] H. Schulze, "Stochastische Modelle und digitale Simulation von Mobilfunkkanälen," in *Proc. Kleinheubacher Reports of the German PTT*, vol. 32, Darmstadt, Germany, Nov. 1989, pp. 473–483.
- [36] P. A. Bello, "Aeronautical channel characterization," *IEEE Trans. Inform. Theory*, vol. 21, pp. 548–563, May 1973.
- [37] A. Neul, "Modulation und Codierung im Aeronautischen Satellitenkanal," Ph.D. dissertation, University of the Federal Armed Forces Munich, Munich, Germany, Sep. 1989.
- [38] M. Pätzold, *Mobile Fading Channels*. Grimstad, Norway: Wiley, 2002.
- [39] H. Schulze, "Stochastische Modelle und digitale Simulation von Mobilfunkkanälen," in *Proc. Kleinheubacher Reports of the German PTT*, vol. 32, Darmstadt, Germany, Nov. 1989, pp. 473–483.

- [40] P. Höher, “Kohärenter Empfang trelliscodierter PSK-Signale auf frequenzselektiven Mobilfunkkanälen; Entzerrung, Decodierung und Kanalparameterschätzung,” *VDI-Verlag, Fortschritt-Berichte*, vol. 147, no. 10, 1990.
- [41] ———, “A statistical discrete-time model for the wssus multipath channel,” *IEEE Trans. Veh. Technol.*, vol. 41, no. 4, pp. 461–468, Nov. 1992.
- [42] “WiMAX Forum.”
- [43] D. Tse and P. Viswanath, *Fundamentals of wireless communication*. Cambridge University Press, 2005.
- [44] J. H. Winters, “Optimum combining in digital mobile radio with cochannel interference,” *IEEE Journal on Selected Areas on Communications*, vol. SAC-2, pp. 528–539, Jul. 1984.
- [45] M. Z. W. M. Chiani, “Multiple Antennas Systems from Optimum Combining to MIMO: an Approach Based on Random Matrix Theory,” Tutorial, ICC, Dresden, Germany, Jun. 2008.
- [46] M. Chiani, M. Z. Win, and A. Zanella, “On the capacity of spatially correlated MIMO Rayleigh fading channels,” *IEEE Transaction on Information Theory*, vol. 49, no. 10, pp. 2363–2371, Oct. 2003.
- [47] M. Chiani, M. Z. Win, “Error probability for optimum combining of M-ary PSK signals in the presence of interference and noise,” *IEEE Transaction on Communications*, vol. 51, no. 11, pp. 1949–1957, Nov. 2003.
- [48] M. Chiani, M. Z. Win, A. Zanella, R. K. Mallik, and J. H. Winters, “Bounds and approximations for optimum combining of signals in the presence of multiple co-channel interferers and thermal noise,” *IEEE Transaction on Communications*, vol. 51, no. 2, pp. 296–307, Feb. 2003.
- [49] G. J. Foschini, “Layered space-time architecture for wireless communication a fading environment when using multiple antennas,” *Bell Labs Tech. J.*, vol. 1, pp. 41–59, 1996.
- [50] G. J. Foschini and M. J. Gans, “On limits of wireless communications in a fading environment when using multiple antennas,” *IEEE Wireless Personal Communications*, vol. 6, pp. 311–335, Mar. 1998.
- [51] S. A. Alamouti, “A simple transmit diversity technique for wireless communications,” *IEEE Journal on Select Areas in Communications*, vol. 16, no. 8, Oct. 1998.
- [52] T. C. Cover, A. A. El Gamal, “Capacity theorems for the relay channel,” *IEEE Transaction on Information Theory*, vol. IT-25, pp. 572–584, Sept. 1979.

- [53] J. N. Laneman, G. W. Wornell, and D. Tse, "An efficient protocol for realizing cooperative diversity in wireless network," in *Proc. IEEE ISIT*, Washington, DC, US, Jun. 2001, p. 294.
- [54] A. Sedonaris, E. Erkip, B. Aazhang, "User Cooperation Diversity Part I," *IEEE Transaction on Communications*, vol. 51, no. 11, pp. 1927–48, Nov. 2003.
- [55] —, "User Cooperation Diversity Part II," *IEEE Transaction on Communications*, vol. 51, no. 11, pp. 1927–48, Nov. 2003.
- [56] J. N. Laneman, G. W. Wornell, "Distributed space-time-coded protocols for exploiting cooperative diversity in wireless networks," *IEEE Transaction on Information Theory*, vol. 49, no. 10, pp. 2415–25, Oct. 2003.
- [57] B. Zhao, M. C. Valenti, "Some new adaptive protocols for the wireless relay channel," in *Proceedings Allerton Conference Commun.*, Monticello, IL, US, Oct. 2003.
- [58] T. H. Hunter, A. Nosratinia, "Cooperative diversity through coding," in *Proceedings IEEE ISIT*, Lousanne, Switzerland, Jul. 2002, p. 220.
- [59] —, "Diversity through Coded Cooperation," *IEEE Transaction On Wireless Communications*, vol. 5, no. 2, Feb. 2006.
- [60] J. Thorpe, "Low-Density Parity-Check (LDPC) Codes Constructed from Protographs," JPL INP, Tech. Rep., Aug. 2003.
- [61] G. Liva and M. Chiani, "Protograph LDPC codes design based on EXIT analysis," in *Proc. IEEE Globecom*, Washington, D.C., USA, Nov. 2007.
- [62] G. Liva, S. Song, L. Lan, Y. Zhang, W. Ryan, and S. Lin, "Design of LDPC codes: A survey and new results," *J. Commun. Softw. Syst.*, vol. 2, no. 3, pp. 191–211, Sep. 2006, invited paper.
- [63] R. McEliece and W. Stark, "Channels with block interference," *IEEE Trans. Inform. Theory*, vol. 30, no. 1, pp. 44–53, Jan. 1984.
- [64] P. Razaghi, and W. Yu, "Bilayer Low-Density Parity-Check Codes for Decode-and-Forward in Relay Channels," *IEEE Trans. Inform. Theory*, vol. 53, no. 10, pp. 3723–3739, Oct. 2007.
- [65] T. V. Nguyen, A. Nosratinia, and D. Divsalar, "Bilayer protograph codes for half-duplex relay channels," in *Proc. IEEE International Symposium on Information Theory (ISIT)*, Austin, TX, Jun. 2010.

- [66] J. Boutros, A. G. i Fàbregas, and E. Calvanese, “Analysis of coding on non-ergodic block fading channels,” in *Proc. 42th Annu. Allerton Conf. on Communication, Control, and Computing*, Allerton, Illinois, Oct. 2005.
- [67] D. Duyck, D. Cahirone, J. Boutros, and M. Moeneclaey, “Analysis and construction of full-diversity joint network-LDPC codes for cooperative communications,” *EURASIP Journal on Wireless Communications and Networking*, pp. 1–16, 2010.
- [68] D. MacKay, “Relationships between sparse graph codes,” *Information-based Induction Sciences, Shizuoka, Japan*, 2000.
- [69] W. E. Ryan and S. Lin, *Channel Codes – Classical and Modern*. Cambridge University Press, 2009.
- [70] R. Tanner, “A recursive approach to low complexity codes,” *IEEE Transactions on Information Theory*, vol. 27, pp. 533–547, Sep. 1981.
- [71] M. Valenti and B. Zhao, “Distributed turbo codes: Towards the capacity of the relay channel,” in *Proc. IEEE Vehicular Tech. Conf. (VTC)*, Orlando, FL, Oct. 2003.
- [72] S. Ten Brink, G. Kramer, and A. Ashikhmin, “Design of low-density parity-check codes for modulation and detection,” *IEEE Transactions on Communications*, vol. 52, pp. 670–678, Apr. 2004.
- [73] S. Ten Brink, “Convergence behavior of iteratively decoded parallel concatenated codes,” *IEEE Transactions on Communications*, vol. 49, pp. 1727–1737, Oct. 2001.
- [74] S. Y. Chung, *On the construction of some capacity-approaching coding schemes*. Cambridge, MA: Ph.D. dissertation, M.I.T., 2000.
- [75] A. Ashikhmin, G. Kramer, and S. ten Brink, “Extrinsic Information Transfer Functions: Model and Erasure Channel Properties,” *IEEE Trans. Inform. Theory*, vol. 50, no. 11, pp. 2657–2673, Nov. 2004.
- [76] D. Divsalar, S. Dolinar, C. Jones, and K. Andrews, “Capacity-Approaching Protograph Codes,” *IEEE J. Select. Areas Commun.*, vol. 27, no. 6, pp. 876–888, Aug. 2009.
- [77] M. Lentmaier and D.V. Truhachev and K.Sh. Zigangirov and D.J. Costello, “An analysis of the block error probability performance of iterative decoding,” *IEEE Trans. Inform. Theory*, vol. 51, no. 11, pp. 3834 – 3855, Nov. 2005.
- [78] H. Jin and T. Richardson, “Block error iterative decoding capacity for LDPC codes,” in *Proc. of IEEE Int. Symp. on Information Theory*, Sep. 2005, pp. 52–56.

- [79] J. Boutros, A. Guillén i Fàbregas, E. Biglieri, and G. Zemor, “Low-Density Parity-Check Codes for Nonergodic Block-Fading Channels,” *IEEE Trans. Inform. Theory*, vol. 56, no. 9, pp. 4286–4300, Sep. 2010.
- [80] X.-Y. Hu, E. Eleftheriou, and D. Arnold, “Regular and irregular progressive edge-growth Tanner graphs,” *IEEE Trans. Inform. Theory*, vol. 51, no. 1, pp. 386–398, Jan. 2005.
- [81] Y. Zhang and W. E. Ryan, “Structured IRA codes: Performance analysis and construction,” *IEEE Trans. Commun.*, vol. 55, no. 5, pp. 837–844, May 2007.
- [82] R. Tanner, “On quasi-cyclic repeat-accumulate codes,” in *Proc. 37th Annu. Allerton Conf. on Communication, Control, and Computing*, Monticello, Illinois, Sep. 1999.
- [83] EUROCONTROL/FAA Future communications study operational concepts and requirements team, “Communications Operating Concept and Requirements for the Future Radio System,” Tech. Rep. Version 2.
- [84] J. Metzner, “An improved broadcast retransmission protocol,” *IEEE Trans. Commun.*, vol. 32, no. 6, pp. 679 – 683, jun 1984.
- [85] B. Matuz, G. Liva, E. Paolini, and M. Chiani, “Pivoting Algorithms for Maximum Likelihood Decoding of LDPC Codes over Erasure Channels,” in *Proc. IEEE Globecom*, Honolulu, USA, Nov. 2009.
- [86] R. Gallager, *Low-Density Parity-Check Codes*. Cambridge, MA: M.I.T. Press, 1963.
- [87] P. Elias, “Coding for two noisy channels,” in *In Proc Information Theory: Third London Symposium*. London: Butterworth Scientific, Ed. C. Cherry, 1955, pp. 61–74.
- [88] M. Luby, M. Mitzenmacher, M. Shokrollahi, and D. Spielman, “Efficient erasure correcting codes,” *IEEE Trans. Inform. Theory*, vol. 47, no. 2, pp. 569–584, Feb. 2001.
- [89] P. Oswald and M. A. Shokrollahi, “Capacity-achieving sequences for the erasure channel,” *IEEE Trans. Inform. Theory*, vol. 48, no. 12, pp. 364–373, Dec. 2002.
- [90] H. D. Pfister, I. Sason, and R. Urbanke, “Capacity-achieving ensembles for the binary erasure channel with bounded complexity,” *IEEE Transactions on Information Theory*, vol. 51, no. 7, pp. 2352–2379, Jul. 2005.
- [91] C. Di, D. Proietti, T. Richardson, E. Telatar, and R. Urbanke, “Finite length analysis of low-density parity-check codes on the binary erasure channel,” *IEEE Trans. Inform. Theory*, vol. 48, pp. 1570–1579, 2002.

- [92] E. Paolini, G. Liva, B. Matuz, and M. Chiani, "Generalized IRA erasure correcting codes for hybrid Iterative/Maximum Likelihood decoding," *IEEE Communications Letters*, vol. 12, no. 6, pp. 450–452, Jun. 2008.
- [93] E. Paolini, G. Liva, M. Varrella, B. Matuz, and M. Chiani, "Low-Complexity LDPC Codes with Near-Optimum Performance over the BEC," in *Proc. 4th Advanced Satellite Mobile Systems Conference*, Bologna, August 2008.
- [94] G. Liva, B. Matuz, Z. Katona, E. Paolini, and M. Chiani, "On Construction of Moderate-Length LDPC Codes over Correlated Erasure Channels," in *IEEE Int. Conf. on Communications*, Dresden, Germany, Jun. 2009.
- [95] D. Burshtein and G. Miller, "An efficient maximum likelihood decoding of LDPC codes over the binary erasure channel," *IEEE Transactions on Information Theory*, vol. 50, no. 11, nov 2004.
- [96] H. Jin, A. Khandekar, and R. McEliece, "Irregular repeat-accumulate codes," in *Proc. Int. Symp. on Turbo codes and Related Topics*, Sep. 2000, pp. 1–8.
- [97] G. Liva, E. Paolini, and M. Chiani, "Simple reconfigurable low-density parity-check codes," *IEEE Communications Letters*, vol. 9, no. 3, pp. 258–260, Mar. 2005.
- [98] R. Storn and K. Price, "Differential evolution - a simple and efficient heuristic for global optimization over continuous spaces," *Journal of Global Optimization*, vol. 11, no. 4, pp. 341–359, December 1997.
- [99] C. Measson, A. Montanari, T. Richardson, and R. Urbanke, "Life above threshold: From list decoding to area theorem and mse," in *Proc. IEEE Information Theory Workshop*, San Antonio, USA, October 2004.
- [100] A. Ashikhmin, G. Kramer, and S. ten Brink, "Extrinsic information transfer functions: Model and erasure channel properties," *IEEE Transactions on Information Theory*, vol. 50, no. 11, pp. 2657–2673, Nov. 2004.
- [101] E. Berlekamp, "The technology of error-correcting codes," *IEEE Proceedings*, vol. 68, pp. 564–593, 1980.
- [102] C. E. Shannon, "A mathematical theory of communication," *Bell System Tech. J.*, vol. 27, pp. 379–423, 623–656, 1948.
- [103] C. Berrou, A. Glavieux, and P. Thitimajshima, "Near Shannon limit error-correcting coding and decoding: Turbo-codes," in *Proc. IEEE Int. Conf. on Communications*, Geneva, Switzerland, May 1993.
- [104] D. J. C. MacKay, "Good error-correcting codes based on very sparse matrices," *IEEE Transactions on Information Theory*, vol. 45, no. 2, pp. 399–431, Mar 1999.

- [105] V. Zyablov and M. Pinsker, "Decoding complexity of low-density codes for transmission in a channel with erasures," *Problemy Peredachi Informatsii*, vol. 10, no. 1, pp. 15–28, 1974.
- [106] R. Tanner, "A recursive approach to low complexity codes," *IEEE Trans. Inform. Theory*, vol. 27, pp. 533–547, Sep. 1981.
- [107] T. Richardson, M. Shokrollahi, and R. Urbanke, "Design of capacity-approaching irregular low-density parity-check codes," *IEEE Trans. Inform. Theory*, vol. 47, no. 2, pp. 619–637, Feb. 2001.
- [108] M. Luby, M. Mitzenmacher, M. A. Shokrollahi, and D. A. Spielman, "Improved low-density parity-check codes using irregular graphs," *IEEE Trans. Inform. Theory*, vol. 47, no. 2, pp. 585–598, Feb. 2001.
- [109] X. Y. Hu, E. Eleftheriou, and D. M. Arnold, "Progressive edge-growth Tanner graphs," in *Proc. IEEE Globecom*, San Antonio, Texas, Nov. 2001, pp. 995–1001.
- [110] T. Tian, C. Jones, J. Villasenor, and R. D. Wesel, "Characterization and selective avoidance of cycles in irregular LDPC codes," in *Proc. IEEE Int. Conf. on Communications*, May 2003.
- [111] T. Richardson and R. Urbanke, "The capacity of low-density parity-check codes under message-passing decoding," *IEEE Transactions on Information Theory*, vol. 47, 2001.
- [112] A. Shokrollahi and R. Storn, "Design of efficient erasure codes with differential evolution," in *Proceedings of the IEEE International Symposium on Information Theory, ISIT 2000*, Sorrento, Italy, June 2000, p. 5.
- [113] H. El Gamal and A. R. Hammons, "Analyzing the turbo decoder using the Gaussian approximation," *IEEE Transactions on Information Theory*, vol. 47, pp. 671–686, Feb. 2001.
- [114] S.-Y. Chung, T. J. Richardson, and R. L. Urbanke, "Analysis of sum-product decoding of Low-Density Parity-Check Codes Using a Gaussian Approximation," *IEEE Transactions on Information Theory*, vol. 47, no. 2, pp. 657–670, Feb. 2001.
- [115] M. Tüchler, S. ten Brink, and J. Hagenauer, "Measures for tracing convergence of iterative decoding algorithms," in *Proc. 4th IEEE/ITG Conf. on Source and Channel Coding*, Berlin, Germany, Jan. 2002.
- [116] S. Chung, "On the construction of some capacity-approaching coding schemes," Ph.D. dissertation, Massachusetts Institute of Technology, 2000.

- [117] F. Peng, W. Ryan, and R. Wesel, "Surrogate-channel design of universal ldpc codes," *IEEE Commun. Lett.*, vol. 10, no. 6, pp. 480–482, 2006.
- [118] M. Franceschini, G. Ferrari, and R. Raheli, "Does the performance of ldpc codes depend on the channel?" *IEEE Trans. Commun.*, vol. 54, no. 12, pp. 2129–2132, 2006.
- [119] R. G. Gallager, *Information Theory and Reliable Communication*. New York: Wiley, 1968.
- [120] Y. Kou, S. Lin, and M. Fossorier, "Low-density parity-check codes based on finite geometries: a rediscovery and new results," *IEEE Transactions on Information Theory*, vol. 47, Nov. 2001.
- [121] M. Yang, Y. Li, and W. Ryan, "Design of efficiently encodable moderate-length high-rate irregular LDPC codes," *IEEE Trans. Commun.*, vol. 52, no. 4, pp. 564–571, Apr. 2004.
- [122] M. P. C. Fossorier, "Quasi-cyclic low-density parity-check codes from circulant permutation matrices," *IEEE Transactions on Information Theory*, vol. 50, pp. 1788–1793, Aug. 2004.
- [123] T. Richardson and R. Urbanke, "Multi-edge type LDPC codes," *IEEE Transactions on Information Theory*, 2008. [Online]. Available: <http://lthcwww.epfl.ch/>
- [124] G. Liva, W. E. Ryan, and M. Chiani, "Quasi-cyclic generalized ldpc codes with low error floors," *IEEE Trans. Commun.*, vol. 56, no. 1, pp. 49–57, Jan. 2008.
- [125] A. Abbasfar, K. Yao, and D. Divsalar, "Accumulate repeat accumulate codes," in *Proc. IEEE Globecom*, Dallas, Texas, Nov. 2004.
- [126] D. Divsalar, S. Dolinar, C. Jones, and K. Andrews, "Capacity-approaching protograph codes," *IEEE Journal on Selected Areas in Communications*, vol. 27, no. 6, pp. 876–888, august 2009.
- [127] M. Lentmaier, G. Fettweis, K. Zigangirov, and D. Costello, "Approaching capacity with asymptotically regular ldpc codes," in *UCSD Information Theory and Applications Workshop*, 2009, pp. 173–177.
- [128] M. Lentmaier, A. Sridharan, D. Costello, and K. Zigangirov, "Iterative decoding threshold analysis for ldpc convolutional codes," *IEEE Trans. Inform. Theory*, vol. 56, no. 10, pp. 5274–5289, 2010.
- [129] M. Lentmaier and G. Fettweis, "On the thresholds of generalized ldpc convolutional codes based on protographs," in *IEEE International Symposium on Information Theory Proceedings (ISIT)*, 2010, pp. 709–713.

-
- [130] S. Kudekar, T. Richardson, and R. Urbanke, “Threshold saturation via spatial coupling: Why convolutional ldpc ensembles perform so well over the bec,” *IEEE Trans. Inform. Theory*, vol. 57, no. 2, pp. 803–834, Feb. 2011.
- [131] M. Mansour and N. Shanbhag, “High-throughput ldpc decoders,” *IEEE Transactions on Very Large Scale Integration (VLSI) Systems*, vol. 11, no. 6, pp. 976–996, dec. 2003.
- [132] Z. Li, L. Chen, L. Lingqi, S. Lin, and W. Fong, “Efficient Encoding of Quasi-Cyclic Low-Density Parity Codes,” *IEEE Transactions on Communications*, vol. 54, pp. 71–81, Jan. 2006.
- [133] T. Richardson and R. Urbanke, “Efficient encoding of low-density parity-check codes,” *IEEE Transactions on Information Theory*, vol. 47, pp. 638–656, Feb. 2001.
- [134] J. Xu, L. Chen, L. Zeng, L. Lan, and S. Lin, “Construction of low-density parity-check codes by superposition,” *IEEE Transactions on Communications*, vol. 53, pp. 243–251, Feb. 2005.
- [135] M. Luby, “LT codes,” in *Proc. of the 43rd Annual IEEE Symposium on Foundations of Computer Science*, Vancouver, Canada, Nov. 2002, pp. 271–282.
- [136] N. Alon and M. G. Luby, “A linear-time erasure-resilient code with nearly optimal recovery,” *IEEE Transactions on Information Theory*, vol. 42, pp. 1732–1736, Nov. 1996.
- [137] A. M. Odlyzko, “Discrete logarithms in finite fields and their cryptographic significance,” in *Theory and Application of Cryptographic Techniques*, 1984, pp. 224–314.